Carbon supported nanomaterials for electrochemical energy applications

By

Sonali Panigrahy
CHEM11201804021

National Institute of Science Education and Research Bhubaneswar, Odisha – 752050

A thesis submitted to the
Board of Studies in Chemical Sciences
In partial fulfilment of requirements
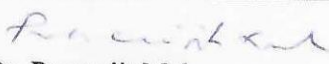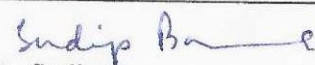*for the Degree of*
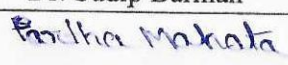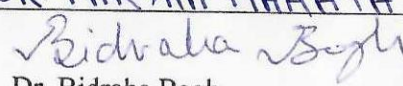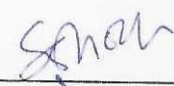
DOCTOR OF PHILOSOPHY

of

HOMI BHABHA NATIONAL INSTITUTE

Homi Bhabha National Institute

Recommendations of the Viva Voce Committee

As members of the Viva Voce Committee, we certify that we have read the dissertation prepared by **Sonali Panigrahy** entitled **"Carbon supported nanomaterials for electrochemical energy applications"** and recommend that it may be accepted as fulfilling the thesis requirement for the award of Degree of Doctor of Philosophy.

Chairman -		Date: 21/02/24
	Dr. Prasenjit Mal	
Guide / Convener -		Date: 21/02/2024
	Dr. Sudip Barman	
Examiner -		Date: 21/02/2024
	DR. PARTHA MAHATA	
Member 1 -		Date: 21/02/24
	Dr. Bidraha Bagh	
Member 2-		Date: 21/02/2024
	Dr. Subhadip Ghosh	
Member 3 -		Date: 21/2/24
	Dr. Dinesh Topwal	

Final approval and acceptance of this thesis is contingent upon the candidate's submission of the final copies of the thesis to HBNI.

I/We hereby certify that I/we have read this thesis prepared under my/our direction and recommend that it may be accepted as fulfilling the thesis requirement.

Date: 21/02/2024

Place: Bhubaneswar

(Dr. Sudip Barman)

Guide

ii

STATEMENT BY AUTHOR
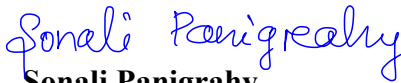
This dissertation has been submitted in partial fulfilment of requirements for an advanced degree at Homi Bhabha National Institute (HBNI) and is deposited in the library to be made available to borrowers under rules of the HBNI.

Brief quotations from this dissertation are allowable without special permission, provided that accurate acknowledgement of source is made. Requests for permission for extended quotation from or reproduction of this manuscript in whole or in part may be granted by the Competent Authority of HBNI when in his or her judgment the proposed use of the material is in the interests of scholarship. In all other instances, however, permission must be obtained from the author.

Sonali Panigrahy

DECLARATION

I, hereby declare that the investigation presented in the thesis has been carried out by me. The work is original and has not been submitted earlier as a whole or in part for a degree / diploma at this or any other Institution / University.

Sonali Panigrahy

List of Publications arising from the thesis

Journal Published

1. **Panigrahy, S**.; Samanta, R.; Panda, P.; Mishra, R.; Barman, S. *, RuO$_2$ as promoter in Pt-RuO$_2$-nanostructures/carbon composite, a pH-universal catalyst for hydrogen evolution/ oxidation reactions. *International Journal of Energy Research* **2022,** *46*, 6406–6420.

2. **Panigrahy, S**.; Mishra, R.; Panda, P.; Kempasiddaiah, M.; Barman, S. *, Carbon-Supported Ag Nanoparticle Aerogel for Electrocatalytic Hydrogenation of 5-(Hydroxymethyl)furfural to 2,5-Hexanedione Under Acidic Conditions. *ACS Applied Nano Materials* **2022,** *5*, 8314−8323.

3. **Panigrahy, S**.; Panda, P.; Shekhawat, A.; Barman, S. *, One-Dimensional Ni-MIL-77 Metal−Organic Framework as an Efficient Electrode Nanomaterial for Asymmetric Supercapacitors. *ACS Applied Nano Materials* **2023,** *6*, 3825−3834.

Under Preparation

1. Panigrahy, S.; Kempasiddaiah, M.; Samanta, R.; Barman, S. *, One-dimensional Bismuth Nanofibers as an Efficient Cathode Material for Electrochemical CO2 Conversion to Formate. (manuscript under preparation).

2. Panigrahy, S.; Barman, S. *, Palladium Oxide Nanoparticle for Electrocatalytic Oxidation of 5 (Hydroxymethyl)furfural. (manuscript under preparation).

3. Panigrahy, S.; Barman, S. *, Ag-Pt Nanostructures for Electrochemical Hydrogen Evolution and Oxygen Reduction Reaction in Alkaline medium. (manuscript under preparation).

4. Panigrahy, S.; Kempasiddaiah, M.; Barman, S. *, Carbon-Supported Ag Nanostructure for Electrochemical CO$_2$ Reduction. (manuscript under preparation).

Journals not included in thesis

1. Panda, P.; Mishra, R.; Panigrahy, S.; Barman, S. *, Design of Co1Al$_3$(OH)m/Carbon Nitride hybrid Nanostructure for Enhanced Capacitive Energy Storage in Alkaline Electrolyte. Materials Advances, 2021, 2, 7671.

2. Panda, P.; Mishra, R.; Panigrahy, S.; Barman, S. *, 3D Assembly of CoAl2O4 Spinel Nanosheets for Energy Storage. ACS Applied Nano Materials 2022, 5, 4, 5176–5186.

3. Sahu, P.; Mishra, R.; Panigrahy, S.; Panda, P.; Barman, S. *, Constructing micropore-rich nitrogen-doped carbon for high-performance supercapacitor and adsorption of carbon dioxide. International Journal of Energy Research 2022, 46, 13556- 13569.

4. Mishra, R.; Panigrahy, S.; Barman, S. *, Single-Source-Derived Nitrogen-Doped Soft Carbons for Application as Anode for Sodium-Ion Storage. Energy & Fuels 2022, 36, 6483-6491.

5. Mishra, R.; Panigrahy, S.; Barman, S. *, Rational Design of Sulfur-Doped Carbon with Expanded Inter-layer Spacing toward Anode Material of Sodium-Ion Batteries. Energy & Fuels 2022, 36, 12310–12318.

6. Kempasiddaiah, M.; Samanta, R.; Panigrahy, S.; Barman, S. *, Interface-Rich Highly Oxophilic Copper/Tin−Oxide Nanocomposite on Reduced Graphene Oxide for Efficient Electroreduction of CO2 to Formate. ACS Applied Energy Materials 2023, 6, 3020-3031.

7. Shekhawat, A.; Samanta, R.; Panigrahy, S.; Barman, S. *, Electrocatalytic Oxidation of Urea and Ethanol on Two-Dimensional Amorphous Nickel Oxide Encapsulated on N Doped Carbon Nanosheets. ACS Applied Energy Materials 2023, 6, 3135-3146.

Conferences and Presentation

1. Poster Presentation: 7th National Conference on " Recent Advancement in Material Science" (RAIMS-2022) (18th-19th November 2022) Department of Chemistry, Veer Surendra Sai University of Technology, Burla Sambalpur, Odisha, India.

2. Poster Presentation: 36th Annual Conference of Orissa Chemical Society & National Conference on "Advances in Materials Chemistry and Application" (AMCA-2022) (18th-19th December 2022) Department of Chemistry, Utkal University, Bhubaneswar, Odisha, India.

3. Poster Presentation: Emergent Materials for Energy and Environment (EMEE-2023) (04th-05th March 2023) Department of Chemistry, IIT Roorkee, Uttarakhand, India.

Sonali Panigrahy

Dedicated

to

My Family

ACKNOWLEDGEMENTS

my brother (Mr. Jagannath Panigrahy) for their support, patience, and ability to make me happy. I love you all.

Sonali Panigrahy

… **Sonali Panigrahy**

CONTENTS

Summary

The increasing global energy demand and the depletion of fossil fuels have propelled the exploration of renewable energy sources. Among various renewable energy technologies, water electrolyzers (WEs) and fuel cells (FCs) are pivotal for energy storage and conversion. Regenerative fuel cells involve four distinct reactions: hydrogen oxidation reaction (HOR) and oxygen reduction reaction (ORR) in FCs stacks, and hydrogen evolution reaction (HER) and oxygen evolution reaction (OER) in WEs stacks. Commercial Pt/C is the most active catalyst for HER, ORR, and HOR. However, its electrocatalytic stability, abundance, and energy efficiency are significantly limited, which hinders the practical application of FCs and WEs devices. In electrolyzers, various reactions such as HMF reduction, HMF oxidation, and CO_2 reduction can yield value-added products. For energy storage applications, supercapacitors bridge the gap between conventional capacitors and batteries. Our research focused on the

synthesis of diverse carbon-supported nanomaterials and explored their activity in HER, HOR, ORR, HMF reduction, HMF oxidation, CO_2 reduction reactions, and their potential as supercapacitor materials.

RuO_2-Pt/C exhibits approximately an order of magnitude higher catalytic activity for alkaline hydrogen evolution reaction/hydrogen oxidation reaction (HER/HOR) when compared to commercial Pt/C. Furthermore, RuO_2-Pt/C also displays superior HER/HOR performance in acidic conditions relative to commercial Pt/C. This thesis highlights the promotional role of RuO_2 in RuO_2-Pt/C for HOR/HER. This enhancement is attributed to RuO_2's ability to facilitate stronger OH^- adsorption. This factor significantly contributes to the remarkable improvement in alkaline HER/HOR via a bi-functional mechanism. The descriptors for alkaline HER/HOR, namely, oxophilicity (OHBE) and hydrogen binding energy (HBE), are crucial in elucidating this phenomenon. Additionally, our findings underscore that the exceptionally high electrochemical performance is a result of interface engineering, synergistic effects, and the porous structure of the catalyst.

The AgPt-CN_x catalyst, synthesized via a two-step procedure involving $NaBH_4$ reduction of Ag within CN_x, succeeded by the electrochemical deposition of Pt in Ag-CN_x, reveals its remarkable versatility as a bifunctional catalyst, effectively facilitating both HER and ORR. In the context of HER performance within a 1 M KOH electrolyte solution, AgPt-CN_x impressively outperforms the commercial Pt/C catalyst. Regarding ORR performance, both AgPt-CN_x and commercial Pt/C exhibit an onset potential near 0.942 V. However, the AgPt-CN_x catalyst exhibits a higher limiting current density in comparison to the commercial Pt/C catalyst, highlighting its superior ORR performance, particularly at higher current densities. This thesis underscores the synthesis of bifunctional catalysts, offering a novel pathway to provide versatile solutions for a wide array of applications.

The Ag-aerogel-CN$_x$ catalyst effectively catalysed the reduction of HMF to HD through a 6e$^-$ and 6H$^+$ ring-opening process. This reduction process was conducted under acidic conditions at room temperature, utilizing water as the source of hydrogen. Remarkably, the Ag-aerogel-CN$_x$ catalyst demonstrated a high Faradic efficiency of 78% and a selectivity of 77% in the production of HD when operated at -1.1 V vs. Ag/AgCl in a 0.5 M H$_2$SO$_4$ solution. The synthesized Ag-aerogel-CN$_x$ catalyst effectively mitigated the competing HER and efficiently facilitated the hydrogenation of HMF to HD. This direct conversion of HMF into HD opens up a novel avenue for generating valuable intermediates from biomass resources.

PdO/CN$_x$ emerged as a highly effective catalyst for the selective oxidation of HMF to FDCA within a 0.1 M KOH solution. Remarkably, the onset potential for HMF oxidation on the PdO/CN$_x$ catalyst was significantly lower than the potential required for the OER. The primary product resulting from the oxidation of HMF was identified as FDCA, and an impressive Faradaic efficiency of 78% was achieved for FDCA production using the PdO/CN$_x$ catalyst at an overpotential of 1.4 V vs. RHE in the 0.1 M KOH solution. This efficient conversion of HMF into FDCA presents an innovative pathway for generating valuable chemical intermediates from biomass resources.

Ag-CN$_x$ exhibited impressive efficacy in the reduction of CO$_2$, yielding CO as the primary product. Notably, Ag-CN$_x$ achieved its highest Faradaic efficiency for CO production, reaching 56.4%, at a potential of -1.4 V vs. Ag/AgCl. The study also delved into the influence of reduction time and catalyst loading on CO production. Optimal conditions were identified as a catalyst loading of 1 mg and a reduction time of 20 minutes. These findings emphasize the potential of Ag-CN$_x$ as a robust catalyst for CO$_2$ reduction reactions and underscore the significance of meticulous adjustment of experimental parameters to enhance the efficiency of CO production.

The electrospinning method was employed to create the Bi-Bi$_2$O$_3$-embedded CNF matrix. This catalyst's remarkable performance is ascribed to its high porosity and substantial electrochemically active surface area, providing an abundance of active sites for CO$_2$ reduction. This synthesized catalyst, Bi-Bi$_2$O$_3$@NF-600, serves as a cathode material, effectively suppressing HER and yielding formate as the primary CO$_2$ reduction product. Bi-Bi$_2$O$_3$@NF-600 demonstrates efficient CO$_2$ reduction to formate with a remarkable Faradaic efficiency of approximately 90% at -0.8 V vs. RHE. Consequently, this thesis holds the potential to pave the way for the development of a pathway to generate value-added products through CO$_2$ reduction, carrying significant implications for sustainable energy applications.

The synthesis of the 1D-Ni-MIL-77 composite through a straightforward one-step solvothermal method, resulting in specific surface area of 93.48 m^2 g^{-1} is discussed in this thesis. The 1D-Ni-MIL-77 electrode demonstrates a substantial specific capacitance of 1376 F g^{-1} at a current of 1 A g^{-1}, with an impressive 81% retention of its initial capacity even after 4000 charge-discharge cycles. In an asymmetric supercapacitor device, the 1D-Ni-MIL-77/activated carbon (AC) combination delivers a noteworthy energy density (ED) of 25 W h kg-1 at a power density (PD) of 750 W kg-1, maintaining 95% of its capacitance after 5000 cycles. This study presents an effective strategy for the development of one-dimensional metal-organic frameworks (MOFs) with enhanced conductivity and a multitude of active sites, particularly beneficial for energy storage applications.

LIST OF FIGURES

NPs/C and comm. Pt/C in 0.5M H_2SO_4.(c, d, e) current density, MA, SA of these catalysts at 0.07 V overpotential, (f) comparison of HER stability of RuO_2-Pt/C and comm. Pt/C catalyst in 0.5M H_2SO_4.

minutes.^{1}H NMR (400 MHz, 90% H_2O/ 10% D_2O): δ 8.02 (s, 1H). (Formate peak at 8.02 ppm).

LIST OF TABLES

LIST OF SCHEMES

Chapter 1

Overview of environmentally friendly electrochemical energy storage and conversion methods

1.1 ABSTRACT

The current chapter addresses the imperative need for converting and storing renewable, clean energy sources, taking into account our perceptions of both existing and future energy resources. It delves into the realm of conversion devices, including water electrolysers and fuel cells, as well as storage devices such as supercapacitors. This section offers a comprehensive overview of the reaction processes and kinetics associated with several fuel cell reactions, including the hydrogen oxidation reaction (HOR), oxygen reduction reaction (ORR), and key water electrolyser reactions such as the hydrogen evolution reaction (HER) and oxygen evolution reaction (OER). Additionally, it covers reactions like the HMF reduction reaction (HMFRR), HMF oxidation reaction (HMFOR), and electrochemical CO_2 reduction reaction. Furthermore, the thesis briefly elucidates the reaction mechanisms and contemporary trends for these reactions. Towards the conclusion of this chapter, the thesis outlines its objectives and goals, setting the stage for the subsequent research and exploration in the field of energy conversion and storage.

1.2 INTRODUCTION

Energy stands as a fundamental element in our everyday existence, playing an indispensable role in almost every facet of human endeavour. Nonetheless, we continue using energy for granted in some ways, even as the energy problem worsens. Despite decades of research into alternatives, fossil fuels currently constitute more than 80% of

worldwide energy usage (Figure 1.1).[1] In light of diminishing natural resources and escalating environmental concerns, the imperative task at hand involves devising a sustainable path for contemporary living predicated on renewable energy sources. This endeavour necessitates the development of dependable and secure approaches for energy conversion, storage, and utilization that can rival the traditional hydrocarbon fuels procured from the Earth. Global energy consumption is now 14 Terawatt hours (TWh) per year, based on the United States Energy Information Administration (US-EIA), and is expected to nearly double by 2050.[2] Fossil fuels are inefficient energy sources that will eventually run out. Furthermore, they are the source of significant emissions of hazardous gases that endanger human civilisation by depleting the ozone layer and adding to global warming. As a result, the temperature of our planet rises, threatening all life on it. Furthermore, as temperatures rise, the ice on the poles in the Arctic and Antarctica have been steadily melting, rising sea levels.[3, 4] While the most suitable strategies may vary depending on geographic factors and the availability of alternative energy-enabling resources, a prominent and recommended approach involves harnessing hydrogen as an energy carrier and employing hydrogen fuel cells as a principal method for converting energy into electrical power. The concept of a hydrogen economy represents an ambitious vision for a comprehensive societal system encompassing hydrogen production, storage, and utilization on a large scale.[5]

After careful analysis, hydrogen emerged as a promising ideal sustainable future energy carrier due to its excellent features.[6] For a long time, researchers have focused on hydrogen as a viable energy source for the future economy. Because of hydrogen's extremely low density, storage is a technical difficulty that must be resolved in order to develop a hydrogen-oriented economy.[7, 8]
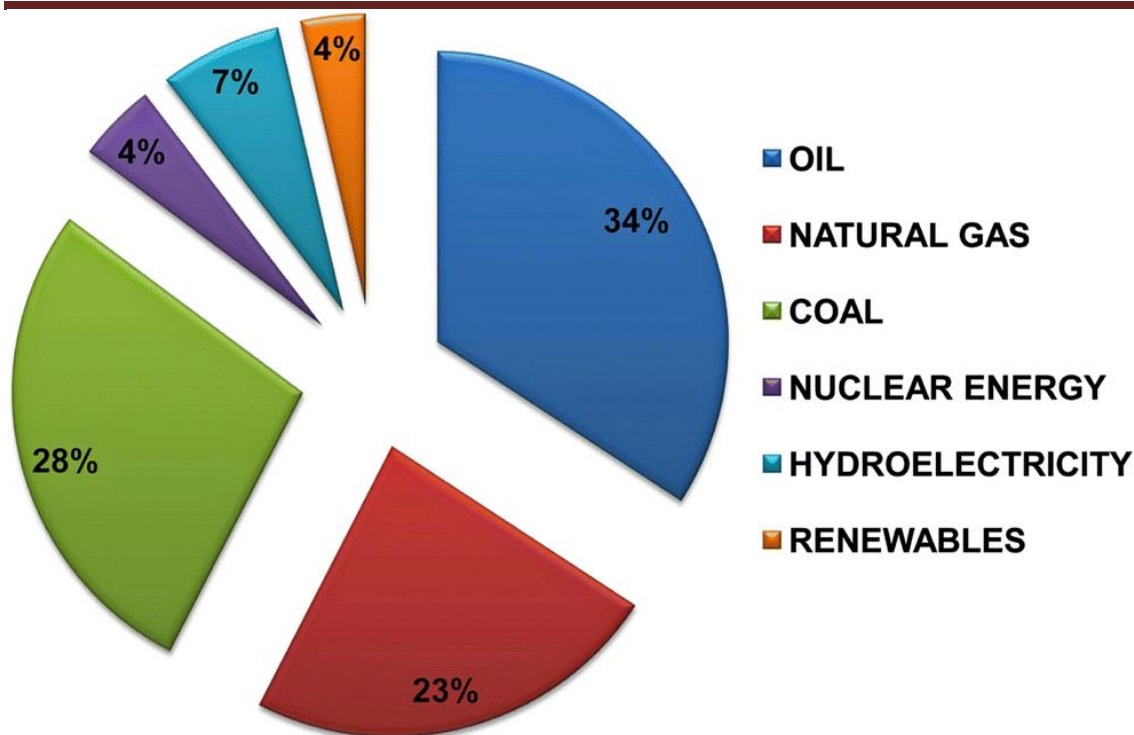
Figure 1.1. Various energy sources for global energy demand (Adopted from Environmental science and Pollution Research 2021, 28, 49327–49342 with permission of Spinger) [1]

Hydrogen is widely recognized as a promising, cost-effective, and eco-friendly fuel for the future economy, and this recognition is grounded in its multiple virtues. Firstly, it stands as the universe's most abundant element, constituting over 90% of all atoms. Secondly, it boasts the distinction of being the lightest element with the highest energy content among all known fuels. Thirdly, it is sustainable, ensuring long-term availability. Fourthly, it is non-toxic and poses no harm to health. Lastly, in contrast to traditional fuels like petroleum, natural gas, or coal, hydrogen serves as a clean energy carrier, promoting environmental well-being and generating only water as the sole byproduct during energy conversion.[9] Hydrogen has an incredible energy storage capability, and estimates suggest that the energy stored in 1 kg of hydrogen is around 120 MJ (=33.33

kWh), which is more than double that of most conventional fuels.[10, 11] Hydrogen can be produced using both renewable like solar, biomass, hydro, geothermal and wind, and also non-renewable like nuclear, natural gas, and coal energy sources. Once generated, hydrogen can be stored as a versatile fuel and deployed across various applications, including transportation, power generation systems employing fuel cells, and internal combustion engines or turbines.[12, 13] However, the largest source of hydrogen nowadays is the reforming of fossil fuels (oil, natural gas, and coal), which account for 96% of total production.[14] This is far from a sustainable energy solution. However, there is a more environmentally friendly and "green" way to manufacture hydrogen by employing water electrolysis by using renewable energy sources.

The advancement of sustainable systems and technologies for energy generation and storage is of paramount importance. This progress is essential for efficiently fulfilling the energy needs of both commercial and residential sectors and mitigating the substantial economic repercussions associated with intermittent energy sources.[15] In this chapter, our discussion will primarily revolve around two main segments: 1) electrochemical energy conversion and 2) electrochemical energy storage.

1.3. Electrochemical Energy Conversion

Energy conversion systems are primarily composed of two fundamental components: the electrolyser and the fuel cell. The water-energy cycle is essential and the main technologies for advancing a sustainable electrochemical energy conversion. The electrolyser is a crucial component designed for the conversion of electrical energy into chemical energy. Within this device, a diverse array of chemical reactions can occur. It operates through the process of electrolysis, wherein an electric current is applied to split a compound, typically water, into its constituent elements, such as hydrogen and oxygen.

This process involves a range of reactions at the electrode-electrolyte interface, including HER and OER that take place on the cathode and anode of a water electrolysis system, respectively.[16] Conversely, the fuel cell is another pivotal component that facilitates the conversion of chemical energy, typically stored in fuels like hydrogen, into electrical energy. The hydrogen produced can be used as an energy carrier in a fuel cell. Fuel cells employ the reverse process of electrolysis, with hydrogen and oxygen as reactants, to produce electricity. In this electrochemical process, HOR occurs at the anode, and ORR takes place at the cathode.[17] These reactions contribute to the generation of electrical energy. In essence, both the electrolyser and fuel cell are integral to energy conversion systems, with the electrolyser focusing on the generation of chemical energy from electrical energy, while the fuel cell centres on the conversion of chemical energy into electrical energy.
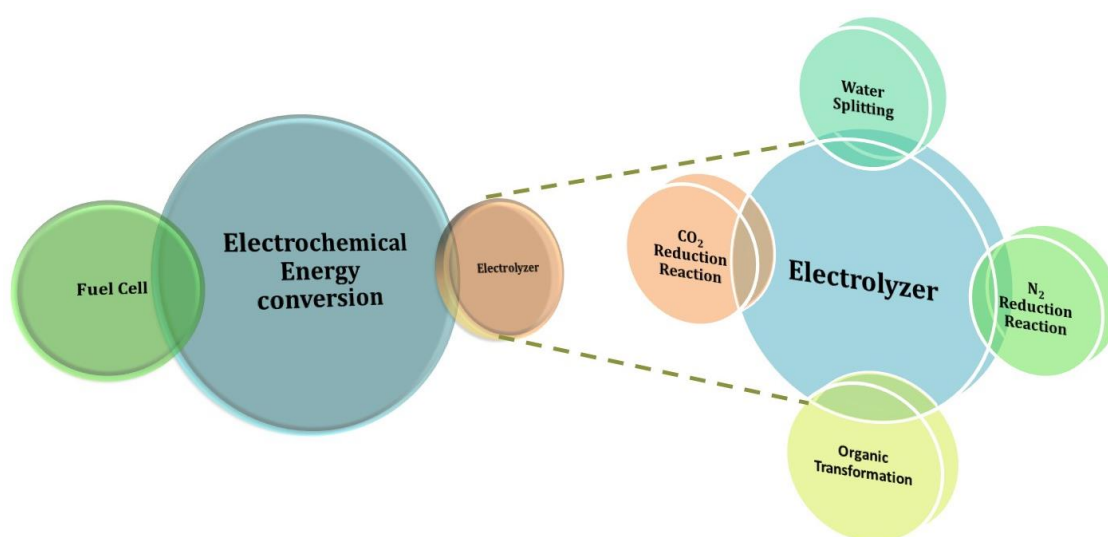
Figure 1.2. Various aspects of electrochemical energy conversion.

HER in an electrochemical water-splitting cell entails transferring two electrons to produce one mol of hydrogen gas. OER, on the other hand, uses a four-electron-transfer mechanism to produce 1 mol of oxygen gas. In a fuel cell, HOR is followed by

transferring two electrons to oxidise 1 mol of molecular hydrogen. ORR, on the other hand, requires four electrons to travel over the anode in order to reduce one mol of oxygen gas.[18]
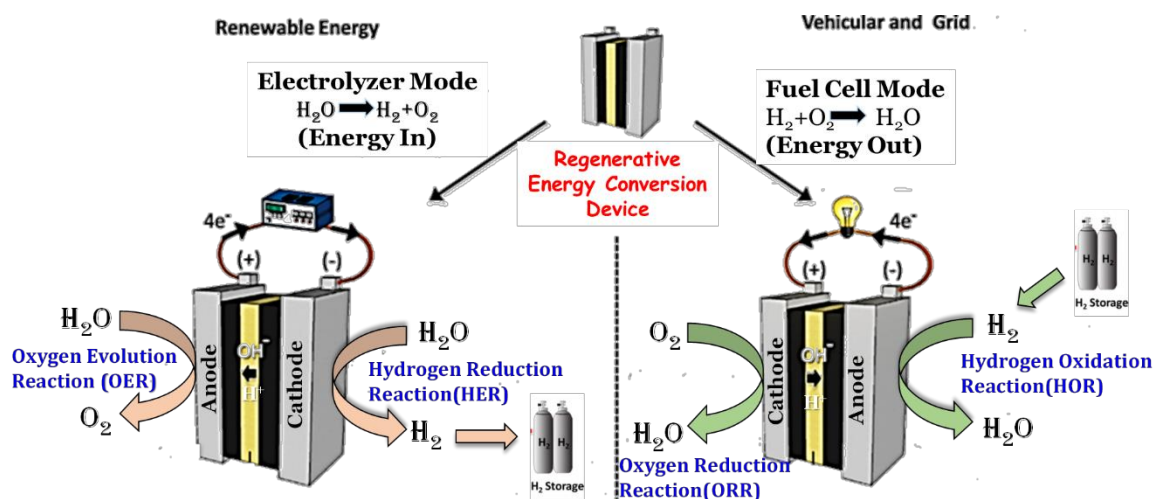
Figure 1.3 Diagram of an RFC illustrating its main components: Fuel Cell and Electrolyzer.

1.3.1. Fuel Cells

An electrochemical device that can transform chemical energy into electrical energy is a fuel cell through the catalysis of an electrochemical reaction at an electrode. Fuel cells offer an alternative energy solution. It is crucial to note, however, that it is not strictly necessary for the cell to be a renewable energy device until the fuel used in the cell comes from a renewable source, that much is evident. However, it is comparable to batteries, but compared to batteries, that are restricted in the capacity to produce energy by the amount of chemicals they can retain, fuel cells have the ability to produce energy constantly for as long as fuel is provided.[19] By electrochemically mixing hydrogen and oxygen, conventional fuel cells generate energy without burning. The supply of oxygen is air, whereas water can be easily converted to hydrogen using electricity. Fuel cell

technologies presently subject to extensive research scrutiny encompass polymer exchange membrane fuel cells, including both proton exchange membrane fuel cells (PEMFCs) and anion exchange membrane fuel cells (AEMFCs), in addition to solid oxide fuel cells, alkaline fuel cells, and molten carbonate fuel cells.[20]

Water has the potential to serve as a sustainable source in the electrolysis process for fuel production, and chemical bonds can function as a means to store electrical energy. Fuel cells consist of four essential components: a) Anode: The anode serves as the negative terminal in fuel cells. It captures electrons generated through the oxidation of hydrogen molecules and facilitates their movement through an external circuit. b) Cathode: Located on the positive side of fuel cells, the cathode produces oxygen in a reduced state and combines it with oxidized hydrogen to produce water. It is responsible for transferring electrons back into the external circuit. c) Electrolyte: This component, which can be either solid or liquid, plays a crucial role in facilitating the transfer of electric charge among the two electrodes. d) Catalyst: Catalysts are a distinct group of substances that accelerate the interaction between oxygen and hydrogen. Thin layers of platinum are commonly employed as catalyst surfaces on materials such as carbon paper or fabric.
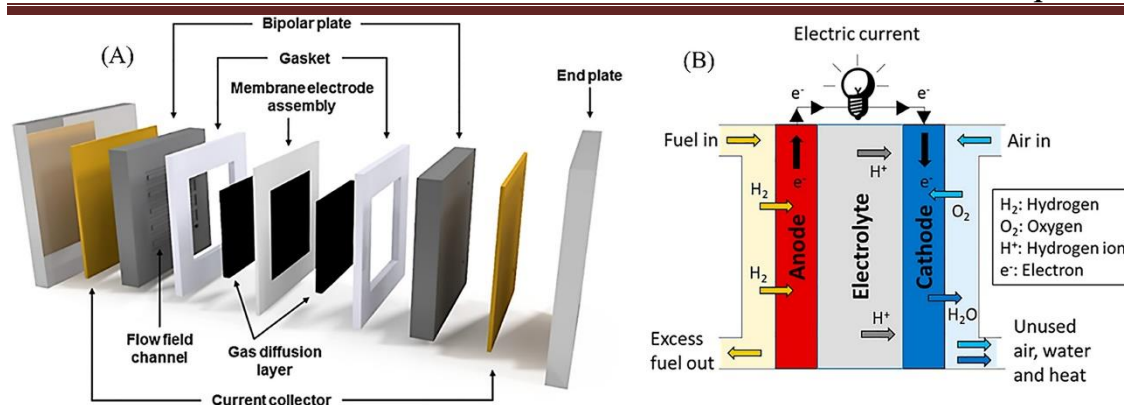
Figure 1.4. (a, b) A schematic diagram showing a proton exchange membrane fuel cell. (Adopted from International Journal of Hydrogen Energy 2022, 47, 41956-41973 with permission from ELSEVIER)

Renewable fuel cells (RFCs) are typically categorized into two groups: proton exchange membrane fuel cells (PEMFCs) and anion exchange membrane fuel cells (AEMFCs), depending on the composition of their electrolytes. In the standard acidic operating environment of a PEMFC system, the protons (H) generated by electrolytes or anodic reactions' products are transported between the anodic and cathodic compartments.[21] In an AEMFC system, hydroxyl anions are exchanged between the anodic and cathodic compartments, and this system performs optimally under alkaline electrolyte conditions with a higher pH level.[22]

Various Reactions Involved in RFCs

Within a fuel cell, hydrogen (H_2) and oxygen (O_2) function as the fuel and oxidant, with the principal reactions occurring as the HOR at the anode and the ORR at the cathode.[19]

1.3.2. Hydrogen Oxidation Reaction:

To generate renewable green electricity, hydrogen can be fed into PEMFCs, which are ecologically benign and extremely efficient energy converters that are not constrained by

the Carnot cycle.[23] Nonetheless, an effective catalyst is indispensable for this procedure; otherwise, it would require an extended duration and necessitate higher energy input. While a minimal amount of precious metal platinum (≤ 0.05 mg$_{Pt}$ cm^{-2}) can ensure a reasonably satisfactory HOR performance on the anode side of proton exchange membrane fuel cells (PEMFCs),[24] the ORR occurring at the cathode side necessitates a higher platinum loading (0.2-0.4 mg$_{Pt}$ cm^{-2}) due to its slow kinetics.[25] The limited availability of cathodic electrocatalysts that possess both high activity and stability at an affordable cost currently poses an obstacle to the extensive adoption of PEMFCs in commercial applications. On the other hand, alkaline polymer electrolyte fuel cells (APEFCs), which belong to a recently emerged category of fuel cells, are anticipated to effectively address these issues by employing cost-effective alkaline polymer membranes and functioning in relatively mild alkaline environments.[26] Alkaline environments offer highly active, cost-effective, and readily available transition metal catalysts for both the ORR and OER, making alkaline membrane fuel cells (AMFCs) and alkaline electrolyzers more promising alternatives to PEMFC-based technologies.[27,28] Another advantage of AMFCs over PEMFCs is the significantly enhanced stability of transition metal catalysts when subjected to the fundamental conditions of the ORR and OER.[29,30] In alkaline environments, the kinetics of the HOR are substantially lower by two orders of magnitude compared to acidic conditions, even when employing commercial Pt/C electrocatalysts. This persistent disparity presents a notable challenge for the scientific community. Consequently, in order to achieve a substantial level of activity, alkaline membrane fuel cells (AMFCs) require a significant quantity of platinum (Pt) at the anode.[26]
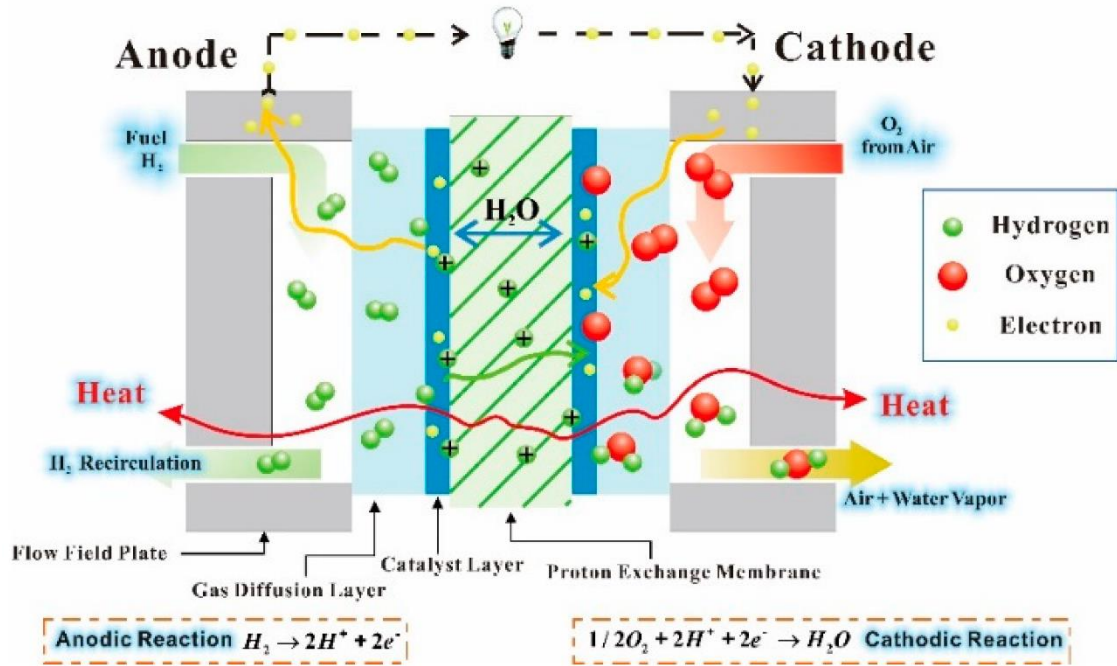
Figure 1.5. Schematic depiction of proton exchange membrane fuel cells (PEMFCs)[31]

Up to this point, the advancement of AMFCs and alkaline electrolyzers has significantly benefited from highly efficient HOR catalysts. In the pursuit of developing more effective catalysts for the HER and HOR in alkaline membrane fuel cells and alkaline electrolyzers, it becomes imperative to gain a comprehensive understanding of the underlying mechanisms in basic media. Presently, there exist conflicting interpretations for the diminished performance of HOR in alkaline environments, revolving around two key factors:[32-37] (1) the role of hydrogen binding energy (HBE) and (2) the impact of OH- adsorption on the metal (oxophilicity). In contrast, the HOR and HER occur in acidic conditions through either the Tafel-Volmer or Heyrovsky-Volmer mechanisms.[38, 39]

Tafel: $H_2 + M \leftrightarrow M\text{-}H_{ads}$

Volmer: $H_{ads}\text{-}M \leftrightarrow H^+ + e^- + M$

Heyrovsky: $H_2 + M \leftrightarrow H_{ads}\text{-}M + H^+ + e^-$
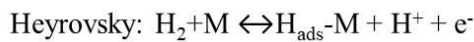
Consequently, the hydrogen oxidation reaction (HOR) can go through either the Tafel−Volmer or Heyrovsky−Volmer pathways. Since the formation of H_{ads} in both the Tafel and Heyrovsky steps, a fundamental prerequisite for efficient HOR catalysts lies in their substantial affinity for hydrogen chemisorption. Consequently, hydrogen binding energy (HBE) is commonly acknowledged as the pivotal determinant influencing HOR/HER kinetics [33, 40, 41].

In an alkaline environment, the reaction proceeds through the subsequent stages:

Tafel: $H_2 + M \leftrightarrow M\text{-}H_{ads}$

Heyrovsky: $H_2 + M + OH^- \leftrightarrow H_{ads}\text{-}M + H_2O + e^-$

Volmer: $H_{ads}\text{-}M + OH^- \leftrightarrow H_2O + e^- + M$

The role of the OH- ion in alkaline environments remains ambiguous. Some researchers have proposed that protons (H^+) are generated through the desorption of Had and subsequently rapidly combine with OH^- ions to form water.[42] (Figure 1.6 a, b).

$H_{ads}\text{-}M \leftrightarrow H^+ + e + M$

$H^+ + OH^- \leftrightarrow H_2O$
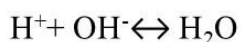
HBE serves as the predominant descriptor for the HOR/HER in alkaline media within this mechanism, much like in acidic conditions. Alternatively, there exists another possibility in this scenario: the catalyst's surface may adsorb OH^- ions, generating OH_{ads} species that can subsequently interact with adjacent H_{ads} species to form a water molecule.[42]

$OH^- + M \rightarrow M\text{-}OH_{ads}$

$M\text{-}OH_{ads} + M\text{-}H_{ads} \rightarrow H_2O + 2M$

(a)

(b)

(c)

(d)
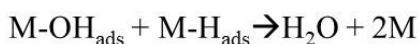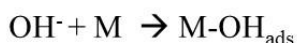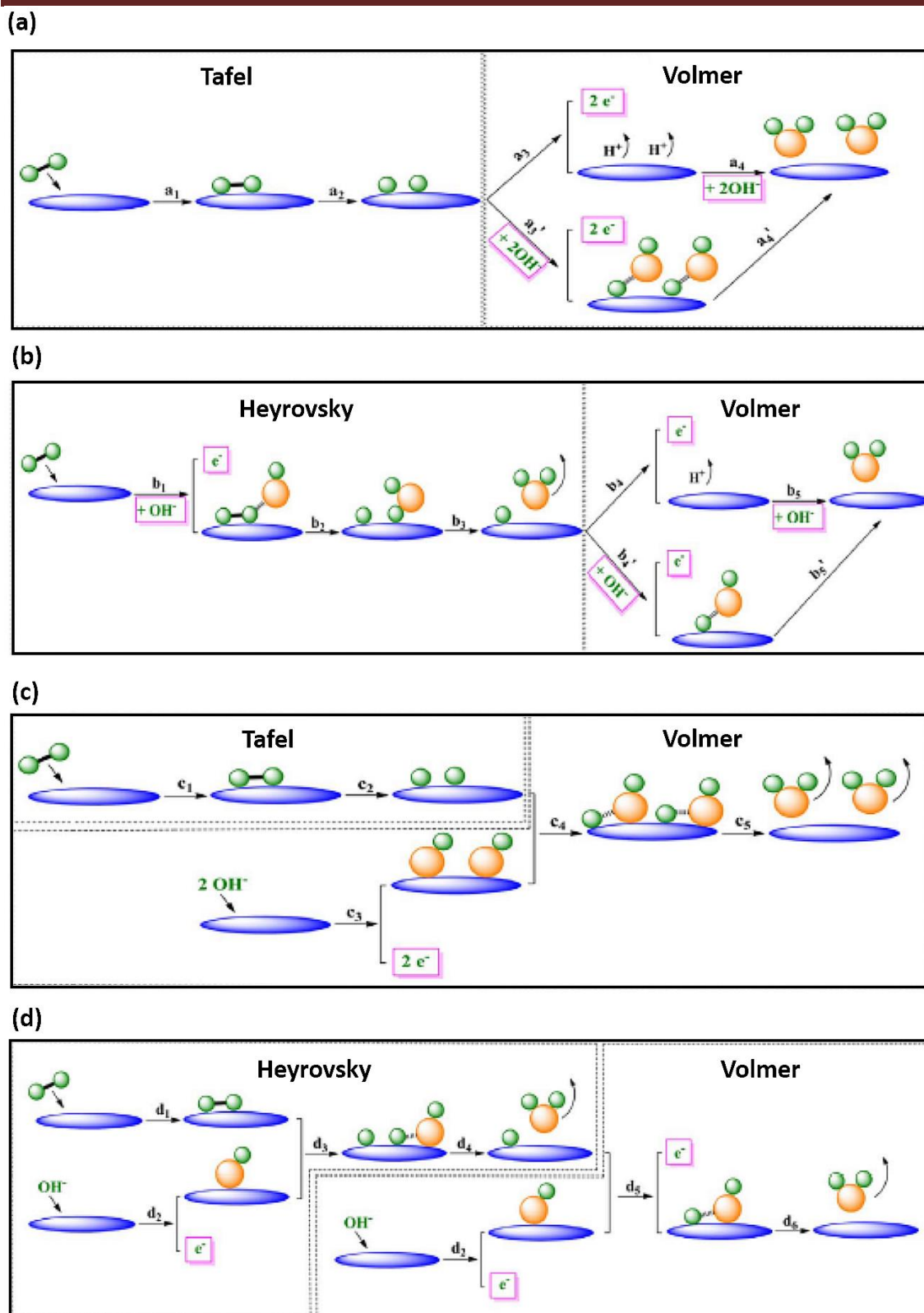
Figure 1.6. (a-b) Potential reaction mechanism of the HOR in an alkaline environment with the influence of OH⁻ ions in the electrolyte, and (c-d) the impact of adsorbed OH_{ad}

species on the catalyst surface (Adopted from Nano Energy 2018, 44, 288 with permission from ELSEVIER).

The bi-functional mechanism regulates the interaction between H_{ads} and OH_{ads} when the catalyst surface has adsorbed OH- ions. Consequently, enhanced OH^- adsorption on the surface of the catalyst causes an increase in hydrogen oxidation reaction (HOR) performance in alkaline media.[35, 43] (Figure 1.6 c and d). As a consequence, the primary feature of the HOR in alkaline conditions is determined by either HBE or the oxophilicity of the catalyst. When HBE and the HER/HOR performance of several monometallic metal surfaces are graphed, it results in volcano-shaped curves, as illustrated by Y. Yan et al.[33,44] Durst and his team have indicated that a higher HER/HOR performance in conventional media could potentially be associated with a lower hydrogen binding energy (HBE).[45]

Due to the reduction in the overall hydrogen binding energy (HBE), J. X. Wang et al.[46] have shown that Ru-Pt core-shell nanoparticles, when compared to bulk Pt, can substantially enhance the mass activity of the hydrogen oxidation reaction/hydrogen evolution reaction (HOR/HER) by several orders of magnitude. While platinum's onset potential for OH^- adsorption is inferior to that of ruthenium-platinum (PtRu), Wang and coworkers[47] have documented that the HOR activity of the PtRu composite material in alkaline environments surpasses that of pure platinum by a factor of two. This observation implies that the metal's oxophilicity does not appear to exert a substantial influence on the HOR activity. As indicated by S. S. Wong et al.,[48] the electrical influence exerted by ruthenium (Ru) on platinum (Pt) plays a crucial role in modulating HBE levels, which, in turn, govern the hydrogen oxidation reaction (HOR) activity.

Furthermore, our research team[38] has recently demonstrated that in basic conditions, bifunctional mechanism that is HBE and oxophilicity both play a significant role for HOR in the case of Pt-(PtO$_x$)-NSs/C composite materials. Nonetheless, as reported by D. Strmcnik et al.,[35] metal oxophilicity does indeed play a notable role in dictating the HER/HOR activity in alkaline environments. They proposed that the limited availability of OH$_{ads}$ species on the catalytic surface contributes to the sluggish hydrogen oxidation reaction (HOR) in alkaline media. Furthermore, their findings indicated that the incorporation of more oxophilic metals, such as nickel (Ni) and ruthenium (Ru), into platinum (Pt) can potentially boost hydrogen oxidation reaction (HOR) performance (Figure 1.6 c-d).[49]

1.3.3. Oxygen Reduction Reaction:

A critical cathodic half-cell process in fuel cells pertains to the electrochemical ORR. Research into the ORR has been concentrated upon due to its significance as a pivotal reaction within diverse electrochemical energy storage/conversion systems, encompassing applications like metal−air batteries, fuel cells, electrocatalytic processes, photocatalytic water splitting, and more.[50, 51] A delayed 4-electron transfer process with a significant intrinsic overpotential that results from the interaction of free-energy scaling correlations between the ORR intermediates adsorbed on catalysts defines the ORR inherently.[52]

Nanomaterials composed of platinum are efficient and long-lasting catalysts for the ORR, yet their cost is prohibitively high for widespread large-scale implementation.[53] To tackle the challenge of the elevated cost associated with platinum, two potential solutions have been proposed: (1) enhancing the utilization or efficiency of platinum catalysts to reduce the platinum requirement, or (2) entirely substituting platinum

catalysts with non-precious alternatives. The latter strategy, which involves a complete replacement of platinum with non-precious metal catalysts, is considerably more favourable in the long-term perspective, as it directly addresses the issue of limited global platinum supply. Simultaneously, transition metals like cobalt (Co), iron (Fe), and nickel (Ni) have garnered significant interest due to their cost-effectiveness and have demonstrated notable enhancements in oxygen reduction reaction (ORR) activity.[54]

The study revealed that the rate-determining step in the oxygen reduction reaction (ORR) involves the creation of O_{ads} and a hydroxide anion, originating from the electro-splitting of $O_{2,ads}$ species.[55] The alkaline environment proves to be an efficient system due to the inherently swifter kinetics of the ORR in basic conditions compared to acidic conditions. Additionally, alkaline media offer a less corrosive setting for both catalysts and electrodes. Rapid adsorption and desorption processes involving oxygen-containing groups like O_2^-, O, H_2O_2, OH^-, and HO_2^- from catalyst surfaces are necessary in alkaline environments, Essentially, a conducive pathway allowing oxide species to move smoothly can enhance reaction kinetics.[56] A significant cathodic process occurring within fuel cells is the electrochemical ORR. The ORR is a complex multi-step, multi-electron transfer mechanism encompassing numerous fundamental stages and intermediate species.

The following are the steps in a reaction in an acidic medium:

Direct 2e⁻ path	Direct 4e⁻ path	Indirect 4e⁻ path

Direct 2e⁻ path

$O_2 + M \rightarrow M\text{-}O_2^*$

$M\text{-}O_2^* + H^+ + e^- \rightarrow M\text{-}OOH$

$^*M\text{-}OOH^* + H^+ + e^- \rightarrow H_2O_2$

Direct 4e⁻ path

$O_2 + M \rightarrow M\text{-}O_2^*$

$M\text{-}O_2^* + M \rightarrow 2\,M\text{-}O^*$

$M\text{-}O^* + e^- + H^+ \rightarrow M\text{-}OH$

$M\text{-}OH^* + H^+ + e^- \rightarrow H_2O$

Indirect 4e⁻ path

$O_2 + M \rightarrow M\text{-}O_2^*$

$^*M\text{-}O_2^* + H^+ + e^- \rightarrow M\text{-}OOH^*$

$M\text{-}OOH^* \rightarrow M\text{-}O^* + M\text{-}OH^*$

$M\text{-}O^* + H^+ + e^- \rightarrow M\text{-}OH^*$

$M\text{-}OH^* + H^+ + e^- \rightarrow H_2O$
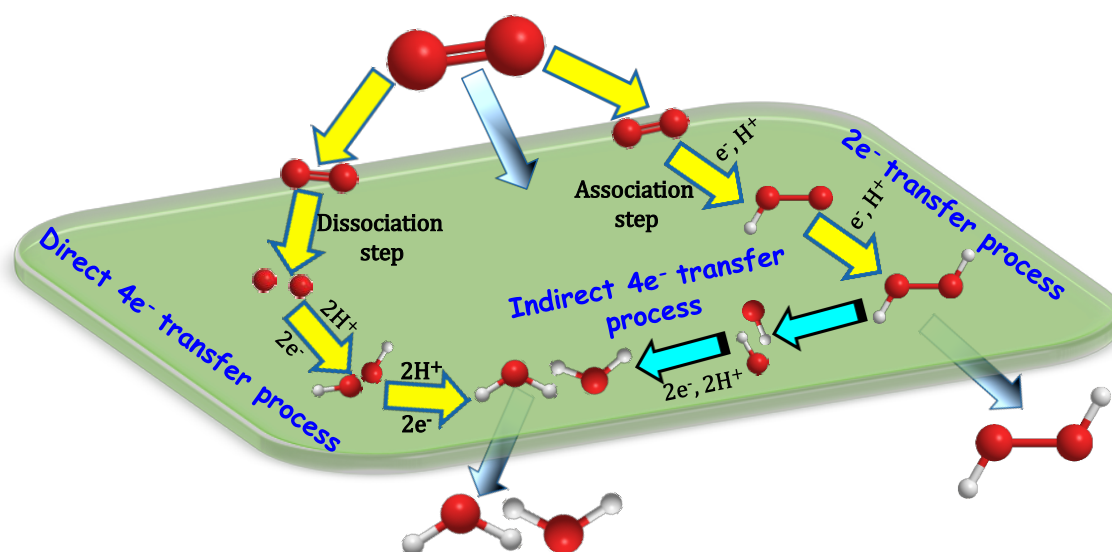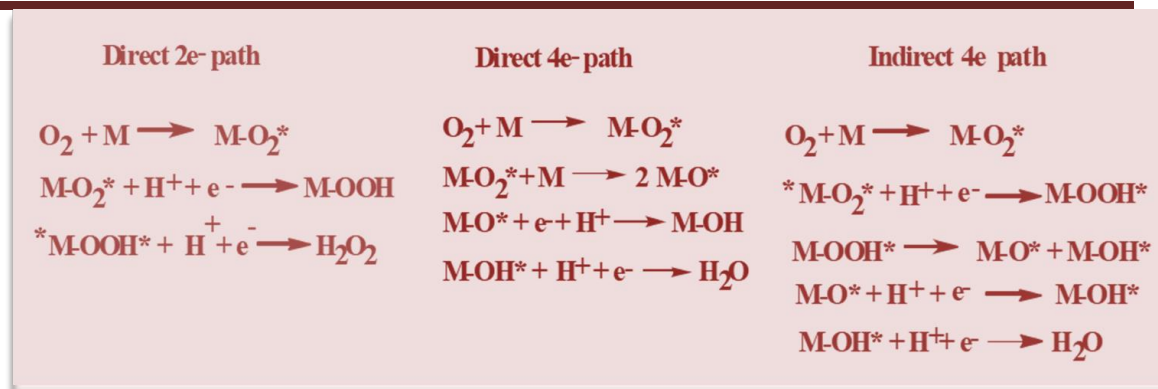
Figure 1.7. Schematic representation of direct and indirect path of ORR.

Oxygen can undergo electrochemical reduction to form water through three distinct pathways: direct 4-electron reduction ($O_2 + 2H_2O + 4e^- \rightarrow 4OH^-$), direct 2-electron reduction ($O_2 + 2H_2O + 2e^- \rightarrow H_2O^- + OH^-$), and the by formation of hydrogen peroxide (2+2 electron reduction, ($H_2O^- + H_2O + 2e^- \rightarrow OH^-$).[57] In the context of fuel cells, the formation of hydrogen peroxide (H_2O_2) is unfavourable as it can lead to the corrosion of the membranes employed in cell fabrication. Occasionally, in non-aqueous aprotic solvents or under alkaline conditions, an alternate pathway involves a one-electron process that generates superoxide species ($O_2^{\cdot-}$).[58] To mitigate the over-potential

associated with the ORR and reduce the production of H_2O_2, various initiatives have been pursued to develop catalysts based on noble metals.

1.3.4. Electrolyser:

In light of concerns about contamination and global warming, investigating more environmentally acceptable energy sources is urgently needed. Within this context, the production of hydrogen (H_2) through electrolysis, powered by sustainable energy sources like wind and solar power, emerges as a plausible strategy for shaping a future energy landscape. This approach holds the potential for sustainable and efficient generation of high-purity hydrogen, often referred to as "green hydrogen."[59] Electrolysis is the electrochemical method employed to facilitate a non-spontaneous chemical reaction. Within an electrolyser, electrical energy is harnessed to initiate water electrolysis, a process that disassembles water into its fundamental components, hydrogen and oxygen ($2H_2O \rightarrow 2H_2 + O_2$). An electrolyser generates exceptionally pure hydrogen suitable for energy production. With the exception of the reversal of the anode and cathode reactions, there exist few distinctions between an electrolyser and a hydrogen fuel cell. Hydrogen gas is produced at the cathode in an electrolyser, whereas in a fuel cell, hydrogen gas is consumed at the anode.

In the present era, two primary technologies exist in the domain of water electrolysis: alkaline electrolyser and proton exchange membrane electrolyser. Among the various devices capable of performing electrolysis, the most likely commercial methods for producing hydrogen in the foreseeable future are PEM electrolyzers. However, the widespread adoption of PEM electrolyzers faces challenges due to the use of noble metals with high commercial value as electrocatalysts in their electrodes. Specifically, platinum (Pt) is employed at the cathode for the HER, and ruthenium (Ru) or iridium (Ir) is used at the anode for the OER.[60] Despite the initial discovery of water splitting into H_2

and O_2 occurring in an acidic electrolyte, the practice of water electrolysis in basic environments has been commercially viable for more than a century, particularly for large-scale industrial implementations.[61] Alkaline electrolysis stands as the oldest and most established technology, having already been deployed in industrial-scale initiatives. Nevertheless, it necessitates the use of a corrosive electrolyte, yields gases at low pressure, and mandates a purification phase for the generated products.[62]

Electrolyzers, akin to batteries, possess positive (anode) and negative (cathode) terminals, as depicted in Figure 1.7. At the negative terminal, hydrogen gas (H_2) is produced, while at the positive terminal, oxygen gas (O_2) is generated (Figure 1.7). These gases can be accumulated in empty containers for subsequent utilization. In electrolyzers, the following reactions transpire:

Anode: $4H^+ + 4e^- \rightarrow 2H_2$

Cathode: $2H_2O \rightarrow O_2 + 4H^+ + 4e^-$

Overall: $2H_2O \ (l) + 4H^+ + 4e^- \rightarrow 2H_2 + O_2 + 4H^+ + 4e^-$
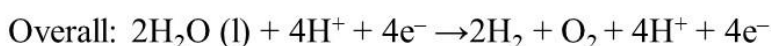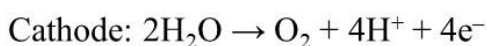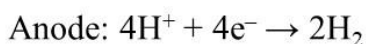
1.3.5. Hydrogen Evolution Reaction:

Hydrogen is regarded as one of the most environmentally friendly sources of fuel and energy. However, the production of pure hydrogen poses a considerable challenge. Electrocatalytic water splitting stands out as an eco-friendly method for generating pure H_2, with HER taking place at the cathode. Platinum (Pt) is indisputably the catalyst with the highest activity in acidic conditions. Nevertheless, Pt-based catalysts face significant drawbacks such as their high cost, limited availability, and diminished stability in acidic environments, which constrain their extensive utilization.[63] This limitation can be

surmounted by utilizing cost-effective transition metal catalysts, alloying combinations of transition and noble metals, or employing the minimal quantity of noble metal essential to attain the desired activity. [64, 65] To attain the desired level of hydrogen production while using a minimal quantity of catalyst, it is imperative to engineer platinum (Pt) nanostructured materials featuring diverse sizes and morphologies.
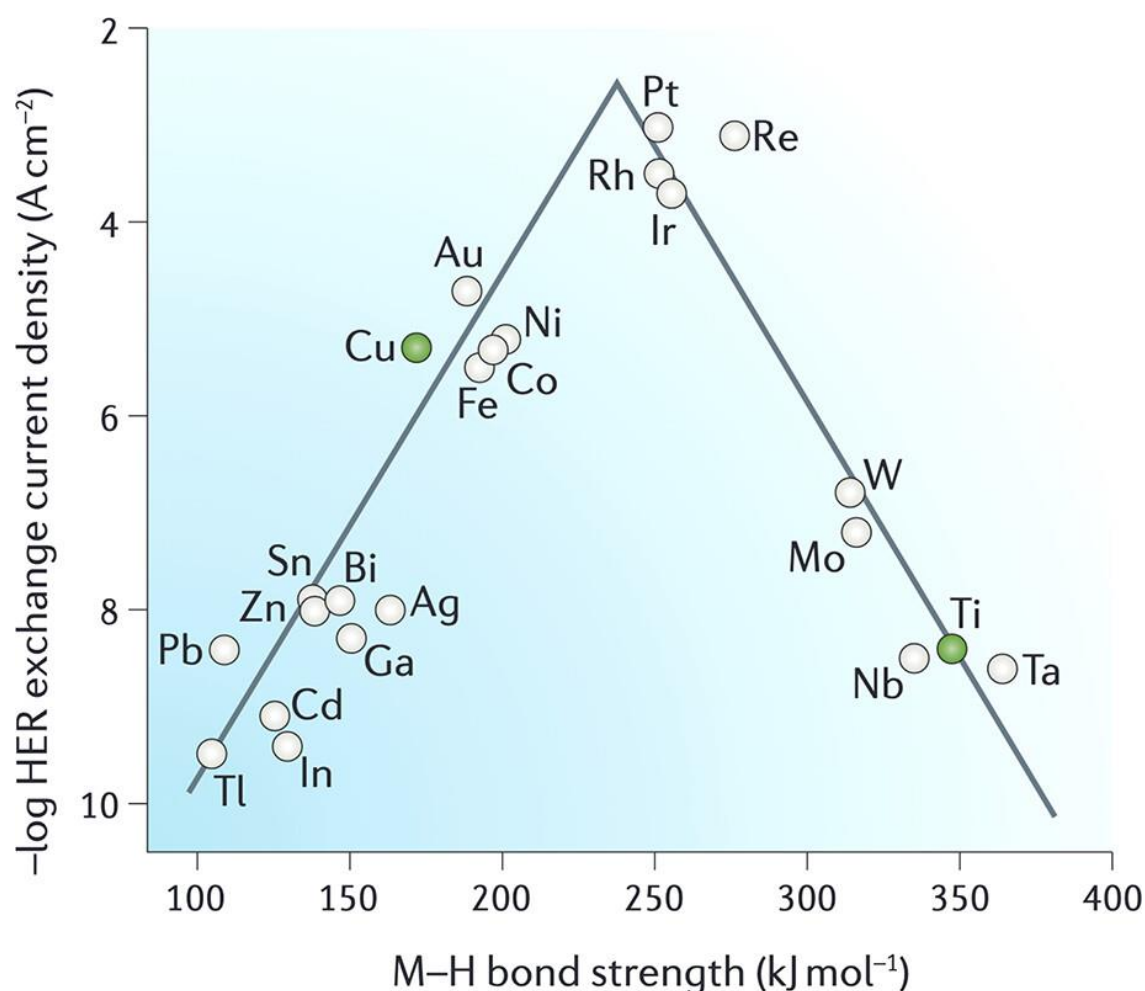
Figure 1.8. HER volcano plot correlating activity with M–H interaction energy.[60]

As per the Sabatier principle,[66] an effective catalyst for HER should exhibit an interaction with the adsorbed H* intermediate that is neither excessively strong nor excessively weak.[67] A pivotal source of inspiration for the search of new HER catalysts is provided

by the "volcano plots," which establish a correlation between the exchange current density and the chemisorption energy of hydrogen on various materials. This pattern was initially documented for metals by Trasatti in the 1970s,[68] with platinum (Pt) positioned near the peak of the volcano. While platinum supported on carbon is considered the most efficient catalyst in acidic conditions, its performance in alkaline environments is notably lower, exhibiting a reduction in activity by two orders of magnitude.[69] The reaction chemistry implies the existence of an additional energy barrier for HER in alkaline media, which the electrocatalyst must overcome.[70] Based on experimental observations, HER activity of a catalyst is enhanced in an alkaline environment when it incorporates an additional active component that facilitates the water dissociation process.[71] For example, the catalyst featuring $Ni(OH)_2$ decoration on platinum (Pt), as developed by the Markovic group,[49] has been demonstrated to elevate the HER activity of Pt by reducing the energy barriers associated with water dissociation. Numerous catalysts composed of single non-noble metals or combinations of non-noble and transition metals have garnered acknowledgment for their hydrogen evolution reaction (HER) performance in alkaline environments.[72]

The following are the HER response mechanisms:

HER mechanism in acidic condition:

1. Volmer step: $M + H_3O^+ + e^- \rightarrow M\text{-}H_{ads} + H_2O$

2. Heyrovsky step: $M\text{-}H_{ads} + H_3O^+ + e^- \rightarrow M + H_2 + H_2O$

3. Tafel step: $M\text{-}H_{ads} + M\text{-}H_{ads} \rightarrow 2M + H_2$

HER mechanism in alkaline condition:

1. Volmer step: $M + H_2O + e^- \rightarrow M\text{-}H_{ads} + OH^-$

2. Heyrovsky step: $M\text{-}H_{ads} + H_2O + e^- \rightarrow M + H_2 + OH^-$

3. Tafel step: $M\text{-}H_{ads} + M\text{-}H_{ads} \rightarrow 2M + H_2$

M is the catalyst surface.

1.3.6. Oxygen Evolution Reaction:

The mechanism governing the OER on anode catalysts is intricate and remains a subject of debate. The traditional OER mechanism, often referred to as the adsorbate evolution mechanism, encompasses numerous electron-proton coupled reactions. In this mechanism, hydroxide ions (OH⁻) are oxidized to produce oxygen molecules and water molecules within alkaline electrolytes.[73] The anodic OER encounters a complex four-electron oxidation process with sluggish kinetics, resulting in a significant electrochemical overpotential (η). Even the most effective OER catalysts still require an overpotential (η) exceeding 300 mV for OER to occur in basic medium, leading to substantial overall efficiency losses in water splitting.[62] To gain fundamental insights into the underlying active site for OER and to facilitate the prediction of more efficient OER catalysts, extensive efforts have been made to establish correlations between OER activity and specific descriptors. These descriptors include the bond energy between a

metal and OH (M-OH),[74, 75] and more.[76] In order to find new and highly active catalysts, a proper descriptor can create a volcano-like connection between OER performance and the descriptor.

1.4. Organic transformation

Inside the electrolyser, a diverse range of chemical reactions can take place, and among these reactions, organic transformations are one of the possibilities. In the context of an electrolyser, organic transformations may occur when organic compounds are introduced into the electrolyte or when the conditions within the electrolyser favour the conversion of organic molecules.
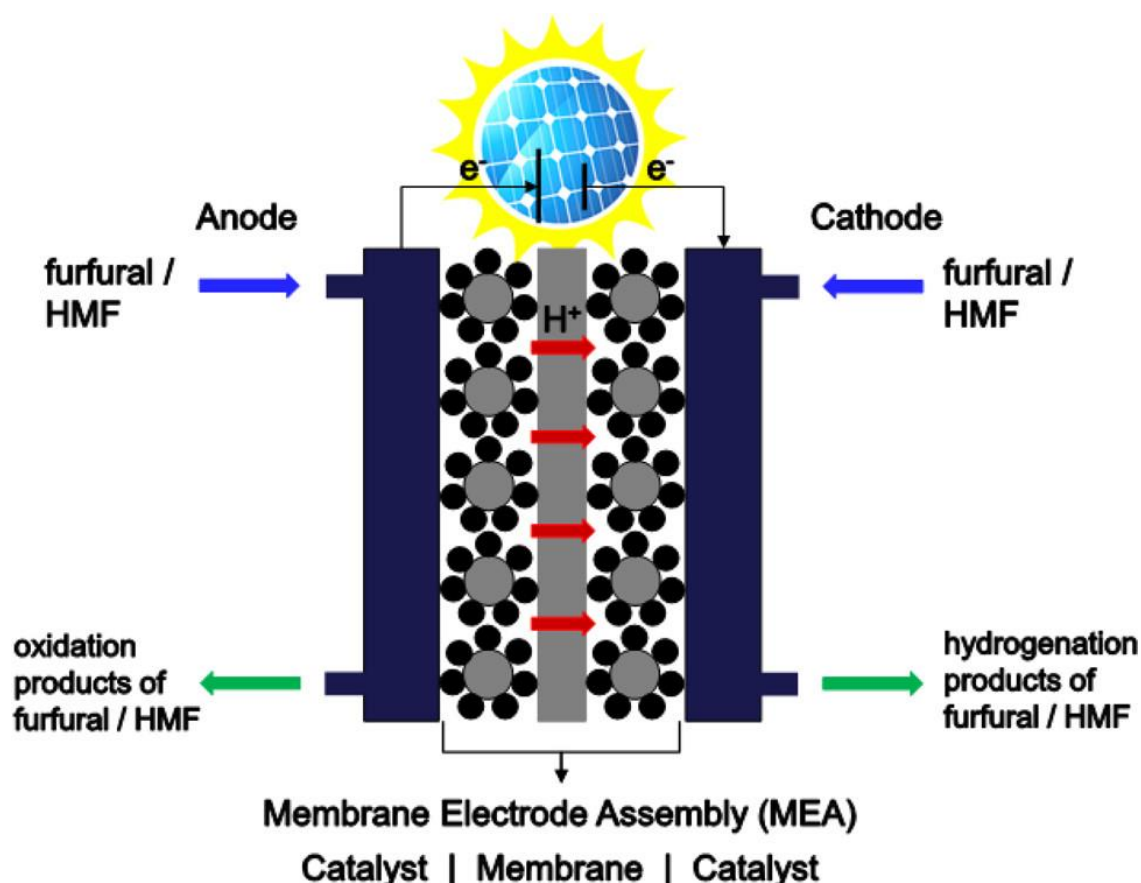
Figure 1.9. Schematic of a continuous electrocatalytic membrane reactor for furfural/HMF oxidation at the anode and hydrogenation at the cathode, driven by

renewable energy. (Adopted from ACS Catalysis 2016, 6, 6704−6717, with permission from ACS)

Due to the extremely desirable end products produced by the electrocatalytic transformation of furanic molecules, having a particular focus on 5-hydroxymethylfurfural (HMF), it has recently been clear that this method is a promising and scalable one for oxidation and hydrogenation processes. HMF serves as a versatile precursor amenable to electrochemical transformation into valuable compounds. Nonetheless, its practical industrial application faces challenges in terms of limited catalytic activity and product selectivity. As a result, a deeper comprehension of catalytic processes as well as a design approach for the catalyst might result in catalysts that can convert materials completely and only into the required products.

There are mainly two reactions for conversion of HMF

1. HMF reduction reaction (HMFRR)
2. HMF oxidation reaction (HMFOR)
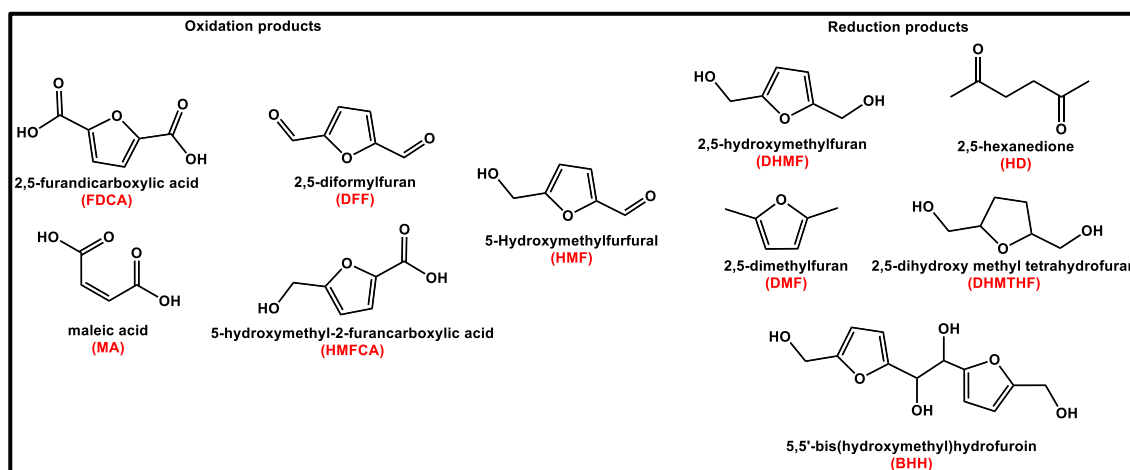
Figure 1.10. Different oxidation and reduction products of HMF.

The reduction of 5-hydroxymethylfurfural (HMF) yields precursors for various compounds, including ketones, ethers, polyesters, and polyurethanes. Notably, this process generates high-energy-density biofuels such as 2,5-dimethylfuran (DMF), 2,5-hexanedione (HD), and 5,5'-bis(hydroxymethyl) hydrofuroin (BHH), along with ethers and ketones. 2,5-furan dicarboxylic acid (FDCA), 5-hydroxymethyl-2-furan carboxylic acid (HMFCA), Maleic acid (MA), 2,5-diformyl furan (DFF), and other useful chemical compounds are produced from oxidation of HMF and are used as precursors or intermediates in the synthesis of polymers, chemicals, and pharmaceuticals.

1.4.1. HMF reduction reaction (HMFRR):

Thermocatalytic hydrogenation methods can be completely replaced by electrocatalytic reduction of chemicals produced from biomass. It also serves as a means to store renewable electrical energy in the form of chemical compounds and liquid organic fuels.[77] HMF has the potential for conversion into a diverse array of valuable compounds, encompassing transportation fuels suitable for internal combustion, compression ignition, and jet engines, as well as polymers and pharmaceuticals.[78] Alternate transportation fuels have received a lot of attention in recent years, including ethanol serving as a first-generation biofuel. Concerns regarding its elevated water solubility, diminished energy content, and competition with food resources, among other factors, have instigated the quest for advanced biofuels.[79] One promising contender is 2,5-Dimethylfuran (DMF), a compound that can be derived from the reduction of HMF. Historically, DMF has been synthesized through the hydrogenation and hydrogenolysis of HMF under elevated temperatures (393-573 K) and high hydrogen pressures (6.8-62 bar)[80, 81] DMF exhibits immiscibility with water and boasts a high-octane number of 119, along with an energy content that surpasses ethanol by 40%.[82] An additional candidate

for an alternative fuel source is methylcyclopentane, which boasts a higher octane number and energy content compared to gasoline while also exhibiting a lower level of hazard when compared to DMF. Recent findings have unveiled a method for synthesizing methylcyclopentane from 2,5-hexanedione (HD), itself a reduction product derived from HMF.[83] DHMF, which is another reduction product of HMF is utilized in a variety of products, including resins, polymers, and synthetic fibres, as well as an intermediary in drug manufacturing.[84]
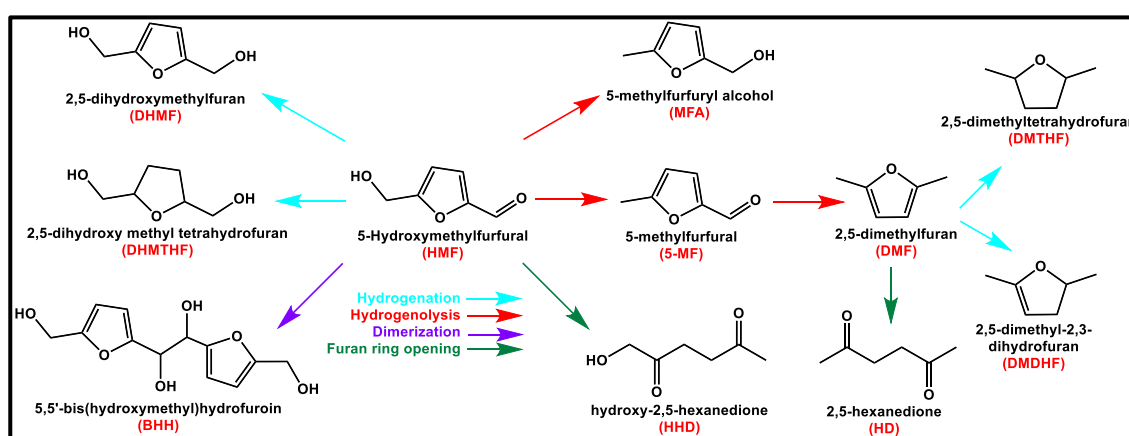
Figure 1.11. Various pathways for the reduction of HMF.

The reduction process of HMF can undergo by different ways shown in following figure

1. Hydrogenation of aldehyde group

2. Hydrogenolysis of aldehyde/ hydroxymethyl group

3. HMF dimerization

4. Hydrogenation of furan ring

5. Ring opening of furan

Numerous conventional techniques exist for HMF reduction, but electrocatalytic hydrogenation (ECH) has garnered considerable attention in recent years. ECH shares similarities with thermo-catalytic hydrogenation, with a key distinction being the

52

electrochemical generation of adsorbed hydrogen on the electrode surface through water reduction (Volmer reaction), rather than hydrogen dissociation. This electrochemical approach circumvents the substantial activation energy barrier associated with H_2 dissociation, allowing ECH to operate under mild conditions without the necessity for an external hydrogen supply or traditional hydrogenation catalysts such as Pd or Pt, among others.[85-87] The primary challenge in achieving high faradaic efficiency for HMF hydrogenation lies in the concurrent occurrence of the competitive HER at similar potentials. HER, as a competing reaction in ECH, consumes adsorbed hydrogen through Heyrovsky or Tafel reactions, potentially diminishing the faradaic efficiency of ECH. Therefore, the selection of an effective catalyst for HMF reduction, especially from the pool of less efficient H_2 evolution catalysts, becomes crucial for attaining high faradaic efficiency.

General mechanism of electrocatalytic HMF reduction reaction

The electrocatalytic hydrogenation of the aldehyde group within HMF has been extensively investigated; however, the precise mechanism of this reaction and the primary active species participating in it remain subjects of ongoing debate within the scientific community.[88] HMF ($C_6H_6O_3$) contains two functional groups connected to the furan ring (-OH and -C=O) and HMF reduction is highly pH sensitive. The onset potentials for HMF hydrogenation (-0.5 ± 0.2 V) on all metal catalysts in a neutral environment are relatively less negative compared to those observed for the HER. HER onset potentials range from -1 to -0.4 V vs. the reversible hydrogen electrode (V_{RHE}) on transition d metals and -1.5 to -1 V_{RHE} on post-transition sp metals. Since the HMF hydrogenation onset potentials are similar, there may not be much catalytic influence on the first electron transfer reaction. Consequently, it can be inferred that the initial

hydrogenation of HMF primarily undergoes directly through interactions with water molecules present in the electrolyte under neutral pH conditions, with only minor influence from the metal electrode.[85]

$$HMF + 2H_2O + 2e^- \leftrightarrow DHMF + 2OH^-$$
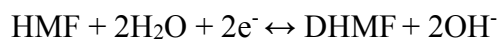
There is a noticeable shift in the onset potentials for HMF hydrogenation towards more positive values under acidic conditions. These potentials range from approximately -0.4 to 0 V vs. the V_{RHE} for transition d metals and from about -0.7 to -0.25 V_{RHE} for post-transition sp metals.[89] Furthermore, the onset potentials for HMF hydrogenation are closely correlated with the onset of the HER under acidic conditions. It's important to note that in acidic solution, the HER is generally more active compared to neutral or alkaline solutions. The formation of adsorbed hydrogen (H_{ads}) species occurs in both acidic and neutral/basic conditions, whether the source is H+ ions or H_2O.

$$H^+ + e^- \leftrightarrow H_{ads}$$

$$H_2O + e^- \leftrightarrow H_{ads} + OH^-$$
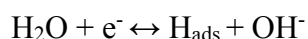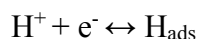
Ring opening of furan

HD, a significant product obtained from HMF reduction, is formed through a process that involves the reductive cleavage of the furan ring, as well as the reduction of HMF's aldehyde and hydroxymethyl functional groups, ultimately yielding an alkane compound. The conversion of HMF into HD necessitates the ring-opening and reduction of both terminal functional groups, such as the alcohol and aldehyde groups, with the consumption of $6H^+$ and $6e^-$. In traditional approaches, the production of HD from HMF requires the use of precious metals, hydrogen (H_2) gas, as well as elevated temperatures and pressures.[82, 90] HD is a critical intermediate derived from biomass that holds versatile

applications, serving as a precursor for various chemicals and biofuels (as depicted in Figure 1.12). For instance, HD plays a crucial role in the efficient synthesis of methylcyclopentane, a promising alternative fuel source (as shown in Figure 1.12).[83] Beyond its significance in alternative fuels, HD serves as a precursor for synthesizing isocarboxazid, an irreversible monoamine oxidase inhibitor (MAOI) employed in antidepressant medications. Additionally, HD can be utilized in the production of para-xylene, a key raw material for generating terephthalic acid, an essential component in the production of polyethylene terephthalate (PET).
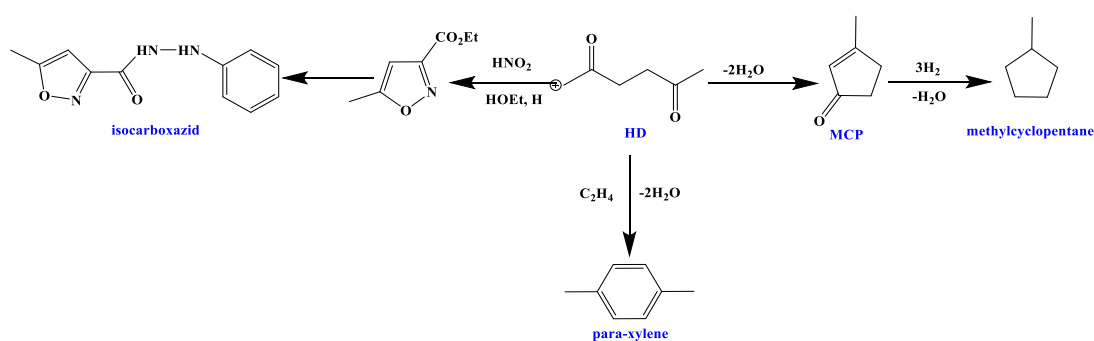
Figure 1.12. Conversion and potential applications of HD.

The production of HD from HMF goes through Clemmensen reduction[91] to convert aldehyde or ketone to hydrocarbon, which consumes 4 electrons and 4 protons, and by removing an H_2O molecule. As a result, aldehyde or ketone groups are reduced to corresponding hydrocarbons. The reductive ring opening of HMF to HD goes through a concerted mechanism; that is, the Clemmensen reaction and acid-catalyzed ring-opening are going through a coupled manner[79]. The formation of HD from 5-methylfurfural (5-MF) is also tested . 5-MF is similar to 5-HMF, which has a furan ring and a formyl group; however, it lacks a terminal alcohol group. The reduction showed that HD was detected as the only product from the reduction of 5-MF. This proves lack of an alcohol group is not affecting the reduction and ring-opening process of HMF. If the hydrogenolysis of

HMF occurs prior to the Clemmensen reduction, the outcome is the formation of HD, as illustrated in the figure. Conversely, when HMF undergoes reduction without hydrogenolysis, the Clemmensen reaction produces HHD, which keeps the hydroxymethyl functional group from the starting material, HMF.[79] This reaction contributes to the simplification of the biomass-based compound refinery by demonstrating electrochemical ring-opening reduction of HMF.
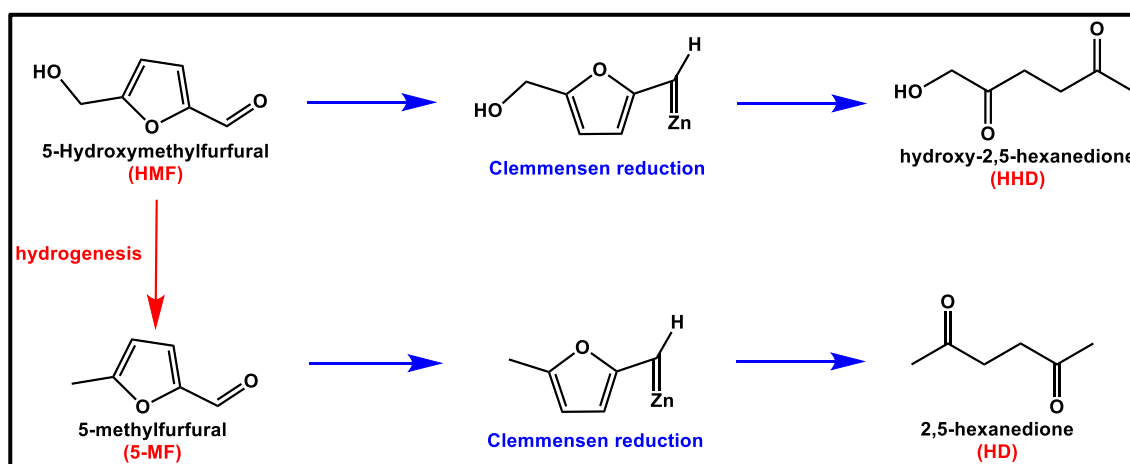
Figure 1.13. Plausible mechanism of production of HD from HMF through reductive ring opening.

1.4.2. HMF oxidation reaction (HMFOR):

Biomass represents a readily available and sustainable non-fossil carbon source with the potential to offer the most environmentally viable alternative to conventional fuels and organic compounds derived from fossil fuels.[92] Within the array of platform chemicals attainable through biomass conversion, 2,5-furandicarboxylic acid (FDCA) emerges as a pivotal near-market platform chemical with the potential to serve as a viable substitute for terephthalic acid in numerous polyesters, including polyethylene terephthalate (PET). FDCA can also be used as an intermediary in the production of other key polymers, fine chemicals, medicines, and agrochemicals.[93] Although HMF oxidation to produce FDCA

has been researched, the majority of reported techniques necessitate extreme circumstances (environmental hazard chemical oxidants, elevataed air pressure, and high temperature) as well as expensive catalysts (Pt, Au, and Pd).[94, 95] The energy-intensive and expensive upgrading procedures necessitate the exploration of alternative methods that ideally rely on cost-effective catalysts and can function under ambient conditions. In this context, electrocatalysis stands as a favourable approach because it is entirely regulated by electrochemical potential and eliminates the need for chemical oxidants.[96]

The use of electrocatalytic water splitting (which involves HER at the cathode and OER at the anode) with renewable energy input has been identified as a promising method for producing clean H_2 fuel.[97] However, its widespread use is hampered by the high cost of catalysts, high activation barrier, sluggish kinetics and the low total energy conversion efficiency of OER.[98] In fact, the OER which produces O_2, is not a valuable chemical and is the kinetic barrier of water splitting.[99] As a result, replacing OER with alternative oxidation reactions that are not only more thermodynamically and kinetically more feasible but also capable of producing highly valued products, such as bioproducts from biomass valorisation, is appealing. HMFOR can potentially be integrated with the HER to produce H_2 with a lower energy input.[100] Due to its lower standard potential of 0.3 V vs. RHE in contrast to the OER with a potential of 1.23 V vs. RHE, the electrocatalytic oxidation of HMF presents a thermodynamically more viable and economically advantageous substitute to the OER.[101] As a result, substituting HMFOR for OER lowers electrolytic cell voltage while producing more useful value-added anodic compounds than O_2.[102] A good catalyst must, therefore, be constructed with an emphasis on the electrocatalytic processing of HMF, encompassing both electrocatalytic oxidation and electrocatalytic reduction, as well as pathways, mechanisms, and principles.
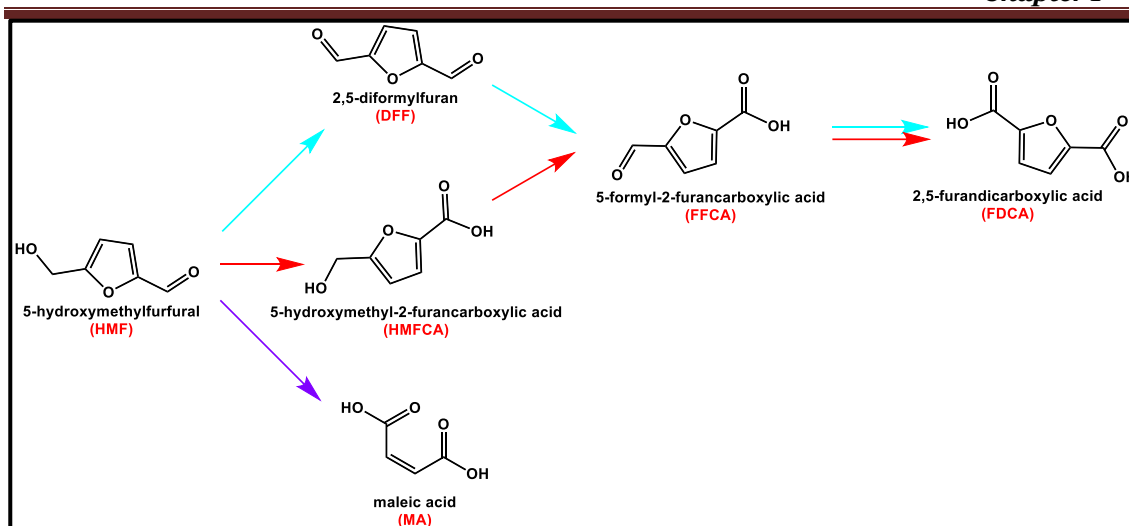
Figure 1.14. Various paths for HMF oxidation reaction.

The molecular composition of HMF consists of a furan ring, an aldehyde group, and a hydroxymethyl group, each of which has the potential for oxidation. Both the hydroxymethyl and aldehyde groups can undergo oxidation, resulting in the ultimate product, FDCA, featuring carboxyl groups.[88] By considering the stepwise oxidation of these functional groups, the conversion of HMF into FDCA can be readily divided into two distinct pathways.[103] Pathway 1 (indicated by the blue arrow) involves the predominant oxidation of the hydroxymethyl group, leading to the formation of DFF, as illustrated in Figure 1.14. In contrast, Pathway 2 (indicated by the red arrow) primarily involves the oxidation of the aldehyde group in HMF, resulting in the generation of a carboxyl group and the formation of the intermediate HMFCA. Subsequently, both the aldehyde and hydroxymethyl groups in DFF and HMFCA undergo oxidation, ultimately yielding 5-formyl-2-furancarboxylic acid (FFCA). This is then oxidised to produce its final product FDCA. In an acid electrolyte, HMF can also perform oxidative ring-opening to MA, as seen in Figure 1.14. (purple colour arrow).[104]

Factors affecting HMFOR

1. pH of the electrolyte

The HMFOR is strongly influenced by the OH^- concentration of the electrolyte. The current density was dramatically increased at the same potential when the KOH concentration was increased from 0.1 to 2 M, indicating a boost in HMFOR activity.[105] Given the heightened reactivity of the aldehyde group in a highly alkaline setting, it predominantly attaches to the electrode's surface and subsequently engages in a further reaction with H_2O to produce a geminal diol through alkaline catalysis.[106] A substantial OH concentration in the electrolyte enhances HMFOR activity and promotes the formation of intermediates responsible for oxidizing HMF into FDCA. Consequently, a majority of studies have employed a 1.0 M KOH solution as the electrolyte for HMFOR, yielding high FDCA yields.[107]

However, the base-induced polymerization of HMF, which results in the creation of insoluble humins, causes the stability of HMF to drastically decline as pH increases.[108] HMF stability was assessed under room temperature and atmospheric pressure conditions at both pH 13 and 14. At pH 14, the degradation of HMF becomes notable as the HMF concentration or the duration of exposure to the pH 14 solution increases. This suggests that pH 14 may not be a practical condition for industrial-scale processes involving large volumes of highly concentrated HMF solutions that need to remain in solution for extended periods. It's important to note that these stability tests were conducted with stationary HMF solutions. The degradation of HMF through polymerization would be accelerated under agitation, as is typical in most reaction settings. Although complete prevention of HMF degradation was not achieved at pH 13, the loss of HMF can be significantly mitigated, even for a 0.5 M HMF solution over an 8-hour period.[92, 109, 110] The instability of HMF in alkaline solutions poses a significant

practical challenge for selective HMFOR, as electrolytes with a pH ≥13 are not suitable for assessing the catalytic activity of HMFOR.[111] This finding implies that identifying electrocatalysts capable of performing effectively at pH≤13 is necessary for the development of practical electrochemical methods for HMF oxidation.

2. Concentration of reactant HMF

Increasing the initial HMF concentrations in the HMFOR reaction can provide a greater number of substrate molecules for the reaction, leading to higher current densities. This is evident from the gradual rise in current density at a constant potential, indicating enhanced activity as the HMF concentration is increased.[112],[113] Elevated concentrations of HMF, conversely, have the potential to impede the electrochemical oxidation process due to excessive adherence to the electrode. During both direct and indirect oxidation of HMF, HMF and OH^- adsorption transpires concurrently at the electrode's surface. An excessive adsorption of HMF can mask active sites, hinder OH adsorption, and lead to a reduced presence of *OH or obstruct the formation of high-valence intermediates. Both of these consequences are detrimental to both the direct and indirect oxidation processes.[88] The correlation between the initial HMF concentration and current density reveals that HMFOR follows a diffusion-limited reaction mechanism.[113] A continual rise in HMF concentration has been observed to decrease both the selectivity and Faradaic efficiency (FE) for FDCA, alongside HMF conversion.[114, 115] Moreover, elevating the HMF concentration enhances the probability of humin formation. Humins have the tendency to adhere to catalyst surfaces, leading to catalyst deactivation and reduced catalytic activity. The presence of humins adds complexity to the purification of the desired product, FDCA, posing challenges in achieving high product purity.[88]

1.5. Electrocatalytic CO₂ reduction reaction

With rising worldwide energy consumption and accompanying environmental issues, particularly carbon dioxide (CO_2) emissions, the development of energy systems that are more efficient is unavoidable in order to provide reliable, affordable, and sustainable energy to all. Through the recycling of CO2 from various sources into feedstock materials for the production of fuels and chemicals, electrochemical CO2 reduction has the potential to ultimately close the anthropogenic carbon cycle. The world remains entrenched in a fossil fuel-based economy, primarily because fossil energy sources have historically and still play a significant role in global economic expansion, technological advancement, and the ongoing industrial revolution.[116] The excessive use of these non-renewable fossil fuels leads to excessive CO_2 emissions and has significantly impacted anthropogenic climate change.[117, 118] Hence, the problem of an anthropogenic carbon cycle, where humans can produce our own feedstocks and fuels from CO_2, has existed for a very long time and still does now.[119] The ability to use industrial CO_2 is currently incredibly limited. The one reason for that is, the continuous reliance on plentiful, reasonably priced fossil fuel-based oil sources for more than a century; and another reason is that there is currently no technology that can economically replace oil.[120] There is not yet a totally sustainable system that completely recycles the CO_2 that a particular system produces. Naturally, the energy needed to carry out this recycling should essentially come from a source that does not produce its own CO_2; as a result, we must either use nuclear energy or some renewable energy (geothermal, solar, hydro, wind, etc.) to do so. The problem discussed here only makes sense if it is implemented without using fossil fuel-based power sources, as our power grid still significantly depends on CO_2-producing sources like coal.
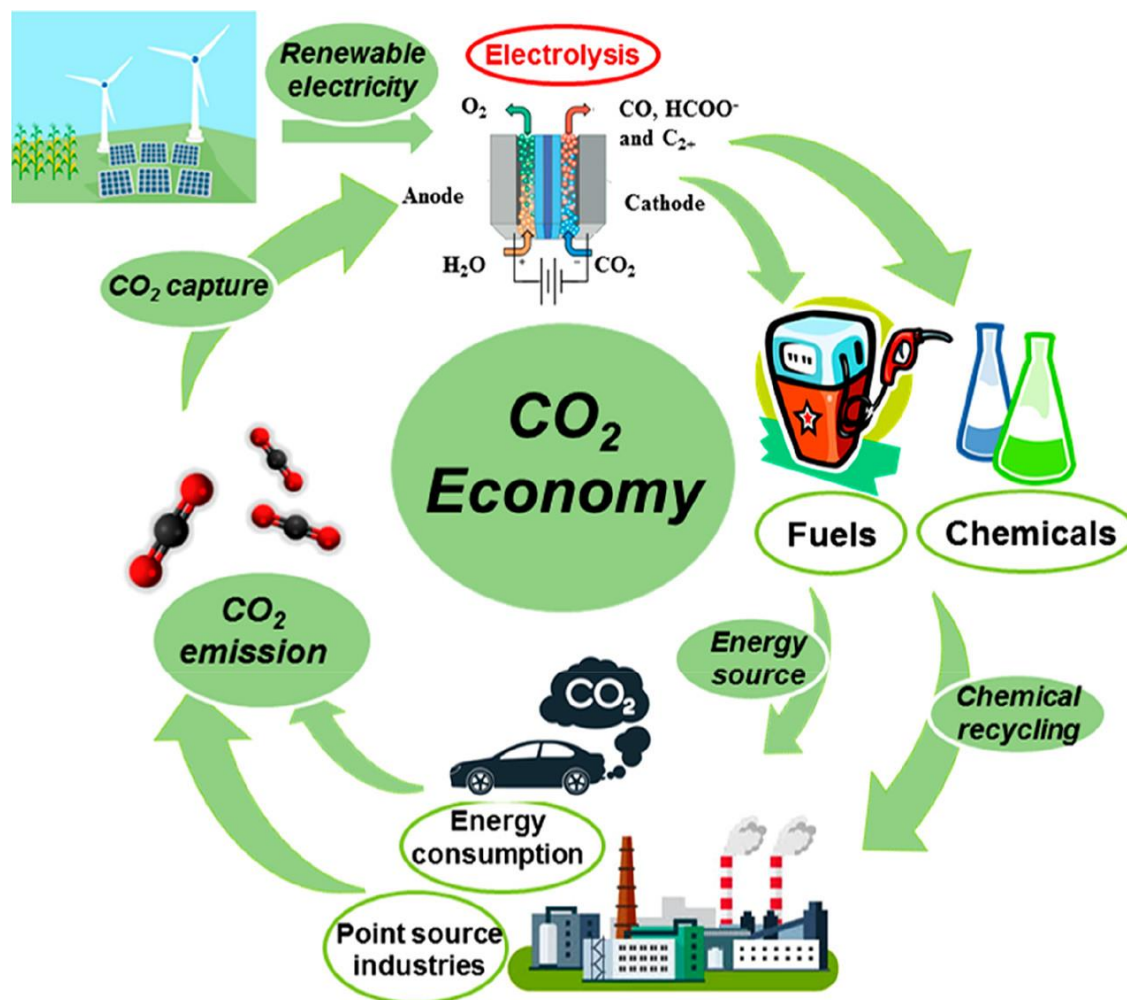
Figure 1.15. Diagram showing an instance of the anthropogenic Carbon Cycle utilizing electrolysis technologies for a Carbon-Neutral economy (adopted from ACS Nano 2021, 15, 7975−8000, with permission from ACS)

The utilization of electrochemical CO_2 reduction represents one avenue for generating renewable fuels and chemicals, but it is not the exclusive approach. Another potential route to renewable energy is thermochemical CO_2 conversion. Under elevated temperatures and pressures, CO_2 has the capacity to react with H_2, yielding long-chain hydrocarbons through a process known as the Fischer-Tropsch reaction[121]. The primary

challenge in creating renewable fuels and chemicals through thermochemical pathways is the production of hydrogen from a sustainable source. Currently, ninety-nine percent of the hydrogen available in the market is obtained from fossil fuels, mainly through methane reforming. Water electrolysis emerges as a highly viable method for generating renewable hydrogen. However, similar to the situation with CO_2 reduction reactions, the practical production of hydrogen via electrolysis demands effective catalysts for the HER. There is a need for research into both thermochemical and electrochemical CO_2RR approaches; however, the electrochemical technique may provide significant advantages. The reaction could possibly be completed in a single step at ambient environmental conditions without the use of high temperatures or pressure. Aqueous electrolyte-driven CO_2 reduction will use H_2O as a proton source which will not need stored H_2. This would reduce the process's infrastructure costs. CO_2 reduction could be done in tiny, portable devices, allowing for more scattered manufacturing than thermochemical processing allows.[116]

1.5.1. Mechanism of Electrochemical CO_2 Reduction Reaction

Carbon dioxide is a chemically stable, non-polar molecule characterized by two double bonds measuring 1.17 angstroms in length between oxygen and carbon atoms. In CO_2, carbon atoms exhibit a +4 oxidation state.[122] The process of converting CO_2 into artificial fuels such as hydrocarbons requires a large amount of energy to start the processes.[123] CO_2 molecules are thermodynamically stable, but they exhibit slow mass transport and reaction kinetics.[124] As a result, a single electron reduction reaction requires a large amount of negative energy to activate, i.e., E° = 1.90 V.[125] Another notable challenge involves the OER, which occurs at the anode during the CO_2RR and involves a four-electron process. This reaction requires substantial overpotentials to proceed, thereby

diminishing the overall efficiency of the CO_2RR..[126, 127] Moreover, the OER generates oxygen (O_2) as a product, which lacks significant value, and it produces reactive oxygen species (ROS) as byproducts. These ROS can potentially damage the electrolyser membrane, leading to premature failure of the electrolyser.[128] Overall, the CO_2RR's practical cell voltage is always significantly greater than its thermodynamic potential.[129]
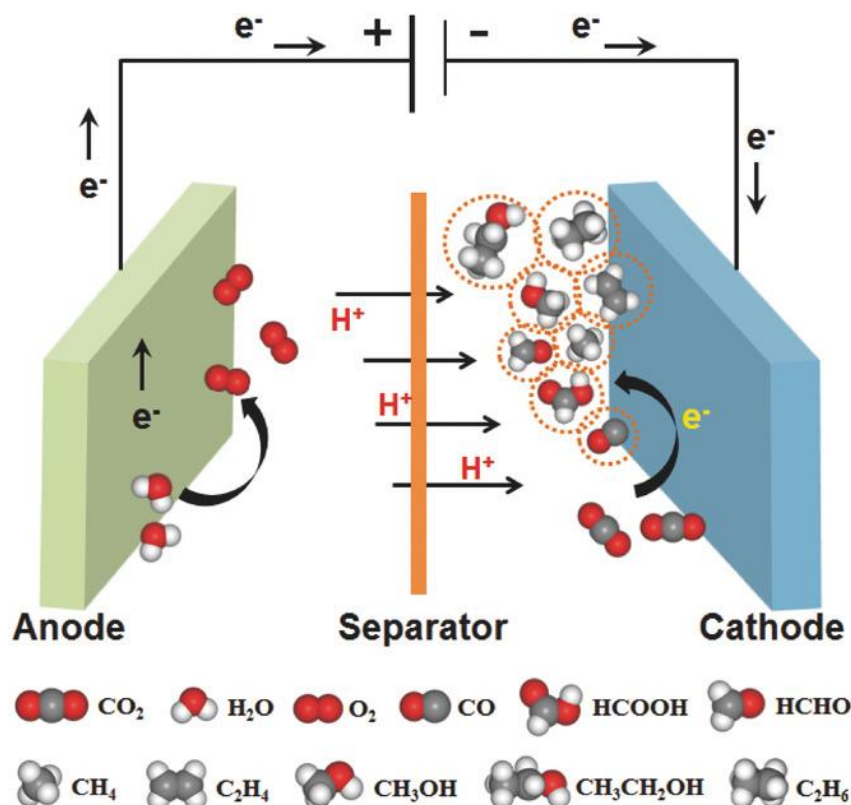
Figure 1.16. Visual representation of the electrochemical CO_2 reduction process and potential products produced within an electrochemical reaction cell.[130]

CO_2 reduction reactions can be categorized into two main types: i) single-electron reduction reactions and ii) multi-electron reduction reactions coupled with proton transfer. The resulting CO_2 reduction products fall into two primary categories: i) C1 chemicals, including carbon monoxide, formate, formaldehyde, and methanol,[131, 132] and ii) catalytic organic synthesis processes that utilize CO_2 as a carbon source for various chemical compounds.[133, 134] The reduction of CO_2 into various products involves several

sequential steps, including the generation and transfer of electrons and protons within the reaction. This process necessitates a more negative potential than the theoretical voltage to initiate the reduction reaction.[135, 136] Overpotential can be detrimental since it reduces efficiency and selectivity.[137]

The multi-electron transfer nature of the CO_2 reduction reaction is influenced by the highly oxidized form of carbon in CO_2. This complexity leads to the generation of various products through diverse pathways (as illustrated in Figure 1.16 and detailed in the following table, Figure 1.17), resulting in the CO_2RR's limited selectivity for a single product.[138-141] While numerous nanostructured materials have demonstrated remarkable efficiency in converting CO_2 to CO, with good efficiency, such as noble-metal nanocrystals[142, 143], single-atom catalysts[144], and metal complexes[145], the production of more reduced multi-carbon products with greater energy density and broader usability, such as oxygenates and hydrocarbons, remains constrained by challenges such as limited selectivity, slow production rates, a scarcity of suitable catalyst options, and reduced energy conversion efficiency.[146]

Possible half-reactions of electrochemical CO_2 reduction	Electrode potentials (V vs SHE) at pH 7
$CO_2 (g) + e^- \rightarrow {*}COO^-$	−1.90
$CO_2 (g) + 2H^+ + 2e^- \rightarrow HCOOH (l)$	−0.61
$CO_2 (g) + H_2O (l) + 2e^- \rightarrow HCOO^- (aq) + OH^-$	−0.43
$CO_2 (g) + 2H^+ + 2e^- \rightarrow CO (g) + H_2O (l)$	−0.53
$CO_2 (g) + H_2O (l) + 2e^- \rightarrow CO (g) + 2OH^-$	−0.52
$CO_2 (g) + 4H^+ + 2e^- \rightarrow HCHO (l) + H_2O (l)$	−0.48
$CO_2 (g) + 3H_2O (l) + 4e^- \rightarrow HCHO (l) + 4OH^-$	−0.89
$CO_2 (g) + 6H^+ (l) + 6e^- \rightarrow CH_3OH (l) + H_2O (l)$	−0.38
$CO_2 (g) + 5H_2O (l) + 6e^- \rightarrow CH_3OH (l) + 6OH^-$	−0.81
$CO_2 (g) + 8H^+ + 8e^- \rightarrow CH_4 (g) + 2H_2O (l)$	−0.24
$CO_2 (g) + 6H_2O (l) + 8e^- \rightarrow CH_4 (g) + 8OH^-$	−0.25
$2CO_2 (g) + 12H^+ + 12e^- \rightarrow C_2H_4 (g) + 4H_2O (l)$	0.06
$2CO_2 (g) + 8H_2O (l) + 12e^- \rightarrow C_2H_4 (g) + 12OH^-$	−0.34
$2CO_2 (g) + 12H^+ + 12e^- \rightarrow CH_3CH_2OH (l) + 3H_2O (l)$	0.08
$2CO_2 (g) + 9H_2O (l) + 12e^- \rightarrow CH_3CH_2OH (l) + 12OH^- (l)$	−0.33

Figure 1.17. Electrochemical potentials for CO_2 reduction reactions in aqueous solutions to generate various hydrocarbon fuels.[130]

For an extended period, scientists have been investigating the electrochemical CO2 reduction mechanism, primarily aiming to comprehend the factors that cause various metals to yield distinct compounds.[147-149] There has been extensive research going on to understand CO_2 reduction on different metallic electrodes.[146] Scheme 1 displays the numerous CO_2 reduction paths that can be followed depending on the electrode material. Multiple proton-coupled electron transfer (PCET) steps are involved in the electrochemical CO_2 reduction reaction (eCO2RR). To induce this uphill reaction at sufficient rates, a large overpotential is frequently necessary. Operating at such a reduced potential within an aqueous electrolyte, the electrochemical CO_2 reduction reaction

(eCO$_2$RR) faces the challenge of contending with the HER, which leads to decreased efficiency in CO$_2$ conversion. The rate limiting step in CO$_2$ reduction reaction is usually the first step, that is formation of CO$_2^{\cdot-}$ radical, is crucial since it decides whether the 2e$^-$ reduction result will be CO or formate.[150] The CO$_2^{\cdot-}$ radical intermediate has a high energy (2.21 V vs. SCE)[151] and rapidly interacts with water (to generate formate or CO) or anything else in solution, even another CO$_2$ molecule. When compared to the initial step, subsequent reduction steps occur nearly instantly[120]. Stabilisation of this high energy intermediate is thus critical to creating a rapid and energy-efficient CO$_2$ reduction process. Metal electrodes for CO$_2$ reduction are commonly classified into three types depending on their ability to bind the CO$_2^{\cdot-}$ intermediate and reduce CO. Group 1 includes those metals that cannot reduce CO because they do not bind the CO$_2^{\cdot-}$ intermediate. Group 2 metals have the tendency to bind the CO$_2^{\cdot-}$ intermediate but are incapable of reducing CO. Group 3 metal (generally copper) binds the CO$_2^{\cdot-}$ intermediate and has the ability to reduce CO. Another category of metals strongly binds hydrogen, hence cannot reduce CO$_2$ in aqueous conditions.[120]

Group 1 metals encompass elements such as Bi, Sn, Pb, In, Cd, and Hg. These metals exhibit such weak binding with the CO$_2^{\cdot-}$ intermediate that the CO$_2$ reduction process is hypothesized to proceed through an outer-sphere mechanism, ultimately producing formate (or formic acid) as the end product.[120] Group 2 consists of metals like Au, Ag, Zn, and Ga, which exhibit varying degrees of binding affinity with the CO2$^{\cdot-}$ intermediate but lack the capability to reduce CO[152], hence CO is usually the main result of CO$_2$ reduction for these metals.[120] Copper is the only metal in group 3 that is commonly investigated for CO$_2$ reduction, binding the CO$_2^{\cdot-}$ intermediate, and can even reduce CO[153] to give higher carbon derivative products.[154]
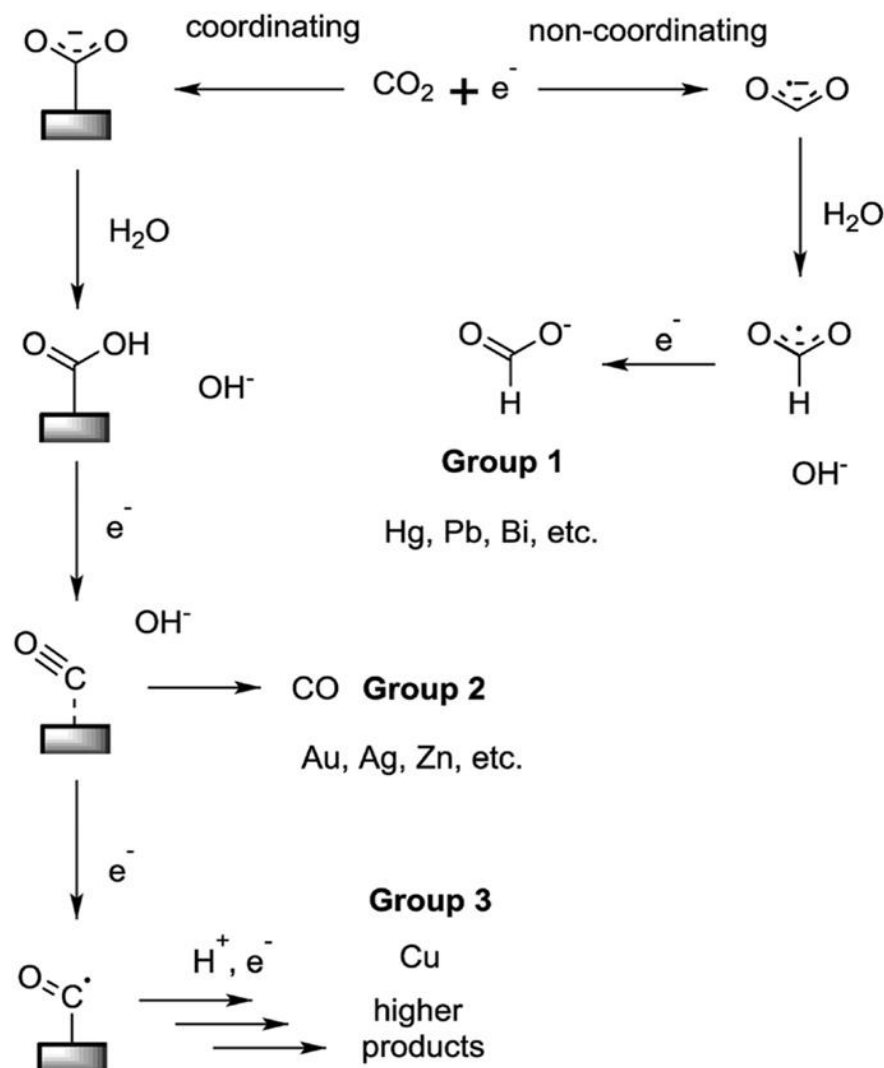
Figure 1.18. Diverse pathways for CO_2 reduction and classification of various metals. (adopted from Israel Journal of Chemistry 2014, 54, 1451-1466, with permission from Wiley)

Although these metal classes can provide general ideas, environmental factors can drastically influence product selectivity on a given electrode.[155] Because CO_2 reduction is frequently performed in aqueous conditions, the hydrogen evolution process (HER), which is more feasible in aqueous media for most of the metals, is in competition with CO_2 reduction, must also be considered. In reality, most CO_2 reduction catalysts are generally chosen for their significant HER overpotentials rather than their capacity to

catalyse CO_2 reduction. Sn, Pb, and Bi are frequently employed electrochemical CO_2 reduction catalysts for formate production, and they consistently display notable HER overpotentials.[156] One of the primary challenges in electrochemical CO2 reduction reactions lies in the interaction between CO_2 and water. The introduction of CO2 into an aqueous environment triggers a intricate sequence of reversible processes, as depicted in Figure 1.18.[120] The proportions of these compounds can be modified by adjusting the pH level, which increases the concentration of carbonate species in the solution. Although this may seem like a straightforward method to achieve higher CO_2 concentrations in aqueous solutions, it is well-established that it is dissolved CO_2 (referred to as CO_2 (aq) in Figure 1.18) and not carbonate species that can undergo electrochemical reduction on metal electrodes.[157] As a result, electrochemical CO2 reduction is a balancing act between creating an electrode material that is active enough to efficiently and rapidly reduce CO_2 to a specified product but inactive for competitive reactions, mainly HER. Conducting CO_2 reduction in an aqueous setting requires careful management of the solution's pH, as it directly influences both the HER and the solubility of CO_2. Moreover, a comprehensive understanding of the mechanism governing CO_2 reduction on metal surfaces is essential for the design of effective catalysts capable of addressing existing challenges.

1.6. Energy storage system

The global demand for energy generation and storage using renewable sources such as solar, wind, and hydro is primarily motivated by the extensive consumption of finite fossil fuels. Regrettably, the intermittent availability of these renewable energy sources renders them inadequate to meet the continually growing energy demand.[158] An analysis of power distribution reveals that around 30% of generated energy is lost due to

69

inadequate energy storage capabilities. Hence, the development of high-capacity, superior energy storage systems (ESS) is imperative to address these issues.[159] In the contemporary landscape, there is a growing focus on electrochemical energy devices, particularly electrochemical capacitors (ECs) and batteries. These energy storage systems have garnered substantial interest across industrial sectors and find application in various domains, including automotive applications such as electric vehicles and military usage.[160] Within the different electrochemical ESS available, batteries are particularly well-suited for applications requiring high energy density (ED), although they may have limited capabilities when it comes to delivering high power output. As a result, both batteries and capacitors fall short when it comes to applications that demand both high energy and power levels concurrently. This has led to extensive research into advanced ESS known as electrochemical capacitors (EC) or supercapacitors (SCs).[160]

1.6.1. Supercapacitor

Supercapacitors, alternatively referred to as ultracapacitors, stand out as prominent contenders amid the array of energy storage devices for forthcoming generations. Their appeal lies in their ability to offer superior specific capacitance, high power density, extended operational longevity, rapid charge-discharge rates, exceptional cycling performance, cost-effectiveness, and inherent safety.[161] In comparison to other rechargeable batteries, supercapacitors demonstrate the capability to store energy at a rate ranging from 10 to 100 times higher per unit volume and boast an extensive lifespan of approximately 500,000 cycles. Moreover, unlike conventional electrolytic capacitors, supercapacitors provide a flexible range of capacitance values, spanning from 1 to 2700 F. They are also characterized by substantially reduced equivalent series resistance, roughly one-tenth of that observed in electrolytic capacitors, and demonstrate

exceptional long-term stability over numerous charge-discharge cycles. Consequently, supercapacitors serve as a valuable intermediary between traditional capacitors and secondary ion batteries.[162, 163] Batteries can give an ED of up to 150 Wh kg^{-1}, which is approximately tenfold higher than that achievable with an EC. However, the power density (PD) of batteries generally reaches its maximum at approximately 200 W kg^{-1}, which signifies a power output roughly twenty times lower than that of an EC.[164] There are three distinct groups in which SC can be divided: pseudocapacitors, electrical double-layer capacitors (EDLCs), and hybrid supercapacitors.[165]
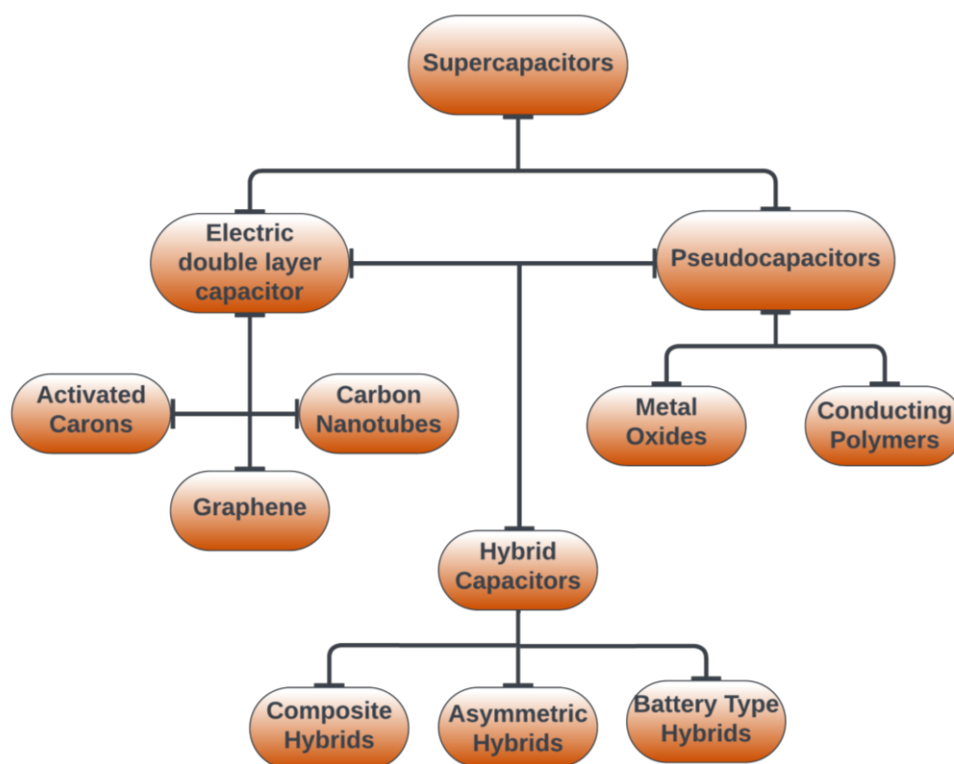
Figure 1.19. Classification of Supercapacitors.[164]

1.6.2. EDLCs

Energy is stored through a non-Faradaic process in EDLC, where charge separation takes place at the interface between the electrode and electrolyte. This interface is known as the electrical double layer (EDL) or Helmholtz double layer. This ES mechanism closely resembles the operation of conventional parallel capacitors. Moreover, it has the

capability to store a relatively advanced amount of energy on the electrode compared to conventional capacitors.[160] One notable feature of this process is the absence of Faradaic redox reactions, which imparts excellent stability to EDLCs and enables them to achieve rapid charge and discharge rates. The swift movement of ions to and from the electrodes facilitates this highly responsive storage mechanism. Electric charges collect on the electrode surfaces upon the application of voltage across the electrodes. As a result of these potential differences, opposite charges are attracted to each other, leading to the migration of ions from the electrolyte into the pores of the oppositely charged electrodes.[164, 166] Therefore, an electrical double layer forms on the electrodes with opposing charges, and this process occurs without significant interfacial charge transfer between the electrode and the electrolyte in the EDLC mechanism.

1.6.3. Pseudocapacitors

Pseudocapacitors, also known as Faradaic supercapacitors, are distinguished by their charge storage mechanism, which involves reversible Faradaic redox mechanism. This mechanism enables the attainment of a substantial specific capacitance without relying solely on electrostatic principles, consequently achieving a higher energy density compared to EDLCs. During the Faradaic redox process initiated by applying voltage, electrode materials undergo oxidation and reduction reactions, which facilitate charge flow across the double layer and result in Faradaic current generation within the SC cell.[167] The pseudocapacitor reaction encompasses a reversible charge transfer process that takes place in the place of interface between the electrolyte and electrode, leading to distinct redox peaks that can be observed in CV curves. Due to the slower nature of the redox reaction in comparison to the formation of the electrical double layer, Pseudocapacitors can attain an energy density nearly twice that of EDLCs. Nonetheless,

it is important to recognize that pseudocapacitors typically display lower PD and demonstrate reduced cyclic stability compared to EDLCs. Frequently employed materials for pseudocapacitive electrodes encompass transition metal oxides (e.g., RuO_2, MnO_2, and Fe_2O_3), transition metal hydroxides, and conducting polymers.[168-170]

1.6.4. Hybrid supercapacitor

EDLCs demonstrate remarkable cyclic stability and a notable PD, whereas pseudocapacitors give a higher energy density and significant specific capacitance. The concept of a hybrid SC has gained popularity as an effort to increse ED, resulting in significantly higher specific capacitance and operating potential. This can be 2 to 3 times greater than that of pseudocapacitors, EDLCs, and traditional capacitors, primarily due to its asymmetric behaviour. This hybrid design combines the benefits of both electrical double-layer capacitors and pseudocapacitors, offering an extended operating voltage range and enhanced energy storage capacity while maintaining power density.[171, 172]

1.7. Aim of the present thesis:

(i) The design and synthesis of carbon-supported nanomaterials using diverse chemical methodologies.

(ii) Thorough characterization of the carbon-supported nanomaterials through techniques including powder X-ray diffraction (p-XRD), X-ray photoelectron spectroscopy (XPS), physisorption analysis, and infrared (IR) spectroscopy.

(iii) Extensive morphological investigations of the composite materials using field-emission scanning electron microscopy (FE-SEM) and transmission electron microscopy (TEM).

(iv) The application of the synthesized composite materials as electrocatalysts in various electrocatalytic processes for energy conversion, particularly in fuel cells and electrolyzers.

(v) Exploration of different types of electrochemical reactions, including the hydrogen evolution reaction (HER), hydrogen oxidation reaction (HOR), oxygen reduction reaction (ORR), as well as the reduction and oxidation reactions of 5-hydroxymethylfurfural (HMF), and the reduction of carbon dioxide (CO_2).

(vi) In-depth analysis of the mechanistic pathways governing the electrocatalytic behaviours of various electrocatalysts.

(vii) The assessment of the ability of the material for its applications in energy storage, particularly as cathode electrode materials for supercapacitors designed for use in aqueous environments.

1.8. Scopes and Challenges of the Present Thesis:

The preceding discussion highlights the growing emphasis on investigating carbon-supported nanomaterials, primarily owing to their significant applicative potential in electrochemical energy conversion, storage, and environmental contexts. The central theme of the present thesis centres on the systematic design, synthesis, and comprehensive characterization of diverse carbon-supported nanomaterials. Furthermore, it explores the various ways these materials can potentially serve as electrocatalysts in the field of energy conversion and storage. One noteworthy cornerstone of this thesis is the development of a facile synthetic procedure for fabricating carbon-supported nanomaterials that exhibit highly effective electrochemical properties. Consequently, these findings may pave the way for the development of more

efficient and sustainable energy conversion and storage systems, contributing to the ongoing pursuit of environmentally friendly and renewable energy solutions.

1.9. References:

(1) Maurya, P. K.; Mondal, S.; Kumar, V.; Singh, S. P. Roadmap to sustainable carbon-neutral energy and environment: can we cross the barrier of biomass productivity? *Environmental Science and Pollution Research* **2021**, *28* (36), 49327-49342.

(2) Whitesides, G. M.; Crabtree, G. W. Don't Forget Long-Term Fundamental Research in Energy. *Science* **2007**, *315* (5813), 796-798.

(3) Dresselhaus, M. S.; Thomas, I. L. Alternative energy technologies. *Nature* **2001**, *414* (6861), 332-337.

(4) Jacobson, M. Z. Review of solutions to global warming, air pollution, and energy security. *Energy Environ. Sci.* **2009**, *2* (2), 148-173, 10.1039/B809990C.

(5) Baum, Z. J.; Diaz, L. L.; Konovalova, T.; Zhou, Q. A. Materials Research Directions Toward a Green Hydrogen Economy: A Review. *ACS Omega* **2022**, *7* (37), 32908-32935.

(6) Ren, J.; Musyoka, N. M.; Langmi, H. W.; Mathe, M.; Liao, S. Current research trends and perspectives on materials-based hydrogen storage solutions: A critical review. *International Journal of Hydrogen Energy* **2017**, *42* (1), 289-311.

(7) Durbin, D. J.; Malardier-Jugroot, C. Review of hydrogen storage techniques for on board vehicle applications. *International Journal of Hydrogen Energy* **2013**, *38* (34), 14595-14617.

(8) Eftekhari, A.; Fang, B. Electrochemical hydrogen storage: Opportunities for fuel storage, batteries, fuel cells, and supercapacitors. *International Journal of Hydrogen Energy* **2017**, *42* (40), 25143-25165.

(9) Abe, J. O.; Popoola, A. P. I.; Ajenifuja, E.; Popoola, O. M. Hydrogen energy, economy and storage: Review and recommendation. *International Journal of Hydrogen Energy* **2019**, *44* (29), 15072-15086.

(10) Becherif, M.; Ramadan, H. S.; Cabaret, K.; Picard, F.; Simoncini, N.; Bethoux, O. Hydrogen Energy Storage: New Techno-Economic Emergence Solution Analysis. *Energy Procedia* **2015**, *74*, 371-380.

(11) Teichmann, D.; Arlt, W.; Wasserscheid, P. J. I. j. o. h. e. Liquid Organic Hydrogen Carriers as an efficient vector for the transport and storage of renewable energy. **2012**, *37* (23), 18118-18132.

(12) Hwang, H. T.; Varma, A. Hydrogen storage for fuel cell vehicles. *Current Opinion in Chemical Engineering* **2014**, *5*, 42-48.

(13) Rosen, M. A.; Koohi-Fayegh, S. The prospects for hydrogen as an energy carrier: an overview of hydrogen energy and hydrogen energy systems. *Energy, Ecology and Environment* **2016**, *1* (1), 10-29.

(14) Santos, A. L.; Cebola, M.-J.; Santos, D. M. F. Towards the Hydrogen Economy—A Review of the Parameters That Influence the Efficiency of Alkaline Water Electrolyzers. In *Energies*, 2021; Vol. 14.

(15) Tomy, M.; Ambika Rajappan, A.; Vm, V.; Thankappan Suryabai, X. Emergence of Novel 2D Materials for High-Performance Supercapacitor Electrode Applications: A Brief Review. *Energy & Fuels* **2021**, *35* (24), 19881-19900.

(16) Jin, H.; Guo, C.; Liu, X.; Liu, J.; Vasileff, A.; Jiao, Y.; Zheng, Y.; Qiao, S.-Z. Emerging Two-Dimensional Nanomaterials for Electrocatalysis. *Chemical Reviews* **2018**, *118* (13), 6337-6408.

(17) Vij, V.; Sultan, S.; Harzandi, A. M.; Meena, A.; Tiwari, J. N.; Lee, W.-G.; Yoon, T.; Kim, K. S. Nickel-Based Electrocatalysts for Energy-Related Applications: Oxygen Reduction, Oxygen Evolution, and Hydrogen Evolution Reactions. *ACS Catalysis* **2017**, *7* (10), 7196-7225.

(18) Lu, H.; Tournet, J.; Dastafkan, K.; Liu, Y.; Ng, Y. H.; Karuturi, S. K.; Zhao, C.; Yin, Z. Noble-Metal-Free Multicomponent Nanointegration for Sustainable Energy Conversion. *Chemical Reviews* **2021**, *121* (17), 10271-10366.

(19) Etesami, M.; Mehdipour-Ataei, S.; Somwangthanaroj, A.; Kheawhom, S. Recent progress of electrocatalysts for hydrogen proton exchange membrane fuel cells. *International Journal of Hydrogen Energy* **2022**, *47* (100), 41956-41973.

(20) Bakangura, E.; Wu, L.; Ge, L.; Yang, Z.; Xu, T. Mixed matrix proton exchange membranes for fuel cells: State of the art and perspectives. *Progress in Polymer Science* **2016**, *57*, 103-152.

(21) Kraytsberg, A.; Ein-Eli, Y. Review of Advanced Materials for Proton Exchange Membrane Fuel Cells. *Energy Fuels* **2014**, *28* (12), 7303-7330.

(22) Gottesfeld, S.; Dekel, D. R.; Page, M.; Bae, C.; Yan, Y.; Zelenay, P.; Kim, Y. S. Anion exchange membrane fuel cells: Current status and remaining challenges. *J. Power Sources* **2018**, *375*, 170-184.

(23) Zhou, M.; Wang, H.-L.; Guo, S. Towards high-efficiency nanoelectrocatalysts for oxygen reduction through engineering advanced carbon nanomaterials. *Chemical Society Reviews* **2016**, *45* (5), 1273-1307, 10.1039/C5CS00414D.

(24) Zheng, J.; Zhou, S.; Gu, S.; Xu, B.; Yan, Y. Size-Dependent Hydrogen Oxidation and Evolution Activities on Supported Palladium Nanoparticles in Acid and Base. *Journal of The Electrochemical Society* **2016**, *163* (6), F499.

(25) Chen, J.; Lim, B.; Lee, E. P.; Xia, Y. Shape-controlled synthesis of platinum nanocrystals for catalytic and electrocatalytic applications. *Nano Today* **2009**, *4* (1), 81-95.

(26) Yao, Z.-C.; Tang, T.; Jiang, Z.; Wang, L.; Hu, J.-S.; Wan, L.-J. Electrocatalytic Hydrogen Oxidation in Alkaline Media: From Mechanistic Insights to Catalyst Design. *ACS Nano* **2022**, *16* (4), 5153-5183.

(27) Safizadeh, F.; Ghali, E.; Houlachi, G. Electrocatalysis developments for hydrogen evolution reaction in alkaline solutions – A Review. *Int. J. Hydrogen Energy* **2015**, *40* (1), 256-274.

(28) Pu, Z.; Liu, Q.; Asiri, A. M.; Sun, X. Tungsten phosphide nanorod arrays directly grown on carbon cloth: a highly efficient and stable hydrogen evolution cathode at all pH values. *ACS Appl. Mater. Interfaces* **2014**, *6* (24), 21874-21879.

(29) Guo, S.; Zhang, S.; Wu, L.; Sun, S. Co/CoO Nanoparticles Assembled on Graphene for Electrochemical Reduction of Oxygen. *Angew. Chem. Int. Ed.* **2012**, *51* (47), 11770-11773.

(30) Liang, Y.; Li, Y.; Wang, H.; Zhou, J.; Wang, J.; Regier, T.; Dai, H. Co3O4 nanocrystals on graphene as a synergistic catalyst for oxygen reduction reaction. *Nat. Mater.* **2011**, *10* (10), 780-786, 10.1038/nmat3087.

(31) Yuan, Y.; Qu, Z.; Wang, W.; Ren, G.; Hu, B. Illustrative Case Study on the Performance and Optimization of Proton Exchange Membrane Fuel Cell. *ChemEngineering* **2019**, *3* (1).

(32) Sheng, W.; Gasteiger, H. A.; Shao-Horn, Y. Hydrogen Oxidation and Evolution Reaction Kinetics on Platinum: Acid vs Alkaline Electrolytes. *J. Electrochem. Soc.* **2010**, *157* (11), B1529-B1536.

(33) Zheng, J.; Sheng, W.; Zhuang, Z.; Xu, B.; Yan, Y. Universal dependence of hydrogen oxidation and evolution reaction activity of platinum-group metals on pH and hydrogen binding energy. *Sci. Adv.* **2016**, *2* (3), e1501602.

(34) Sheng, W.; Zhuang, Z.; Gao, M.; Zheng, J.; Chen, J. G.; Yan, Y. Correlating hydrogen oxidation and evolution activity on platinum at different pH with measured hydrogen binding energy. **2015**, *6*, 5848.

(35) Strmcnik, D.; Uchimura, M.; Wang, C.; Subbaraman, R.; Danilovic, N.; van der, V.; Paulikas, A. P.; Stamenkovic, V. R.; Markovic, N. M. Improving the hydrogen oxidation reaction rate by promotion of hydroxyl adsorption. *Nat. Chem.* **2013**, *5* (4), 300-306.

(36) Guo, S.; Wang, E. Noble metal nanomaterials: Controllable synthesis and application in fuel cells and analytical sensors. *Nano Today* **2011**, *6* (3), 240-264.

(37) Zhu, H.; Zhang, S.; Huang, Y.-X.; Wu, L.; Sun, S. Monodisperse MxFe3–xO4 (M = Fe, Cu, Co, Mn) Nanoparticles and Their Electrocatalysis for Oxygen Reduction Reaction. *Nano Lett.* **2013**, *13* (6), 2947-2951.

(38) Kundu, M. K.; Bhowmik, T.; Mishra, R.; Barman, S. Platinum Nanostructure/Nitrogen-Doped Carbon Hybrid: Enhancing its Base Media HER/HOR Activity through Bi-functionality of the Catalyst. *ChemSusChem* **2018**, *11* (14), 2388-2401.

(39) Kundu, M. K.; Mishra, R.; Bhowmik, T.; Barman, S. Rhodium metal–rhodium oxide (Rh–Rh2O3) nanostructures with Pt-like or better activity towards hydrogen evolution and oxidation reactions (HER, HOR) in acid and base: correlating its HOR/HER activity with hydrogen binding energy and oxophilicity of the catalyst. *Journal of Materials Chemistry A* **2018**, *6* (46), 23531-23541.

(40) Sheng, W.; Zhuang, Z.; Gao, M.; Zheng, J.; Chen, J. G.; Yan, Y. Correlating hydrogen oxidation and evolution activity on platinum at different pH with measured hydrogen binding energy. *Nat. Commun.* **2015**, *6*, 5848-5854, Article.

(41) Lu, S.; Zhuang, Z. Investigating the Influences of the Adsorbed Species on Catalytic Activity for Hydrogen Oxidation Reaction in Alkaline Electrolyte. *J. Am. Chem. Soc.* **2017**, *139* (14), 5156-5163.

(42) Cong, Y.; Yi, B.; Song, Y. Hydrogen oxidation reaction in alkaline media: From mechanism to recent electrocatalysts. *Nano Energy* **2018**, *44*, 288-303.

(43) Wang, G.; Parrondo, J.; He, C.; Li, Y.; Ramani, V. Pt/C/Ni(OH)2 Bi-Functional Electrocatalyst for Enhanced Hydrogen Evolution Reaction Activity under Alkaline Conditions. *J. Electrochem. Soc.* **2017**, *164* (13), F1307-F1315.

(44) Sheng, W.; Myint, M.; Chen, J. G.; Yan, Y. Correlating the hydrogen evolution reaction activity in alkaline electrolytes with the hydrogen binding energy on monometallic surfaces. *Energy Environ. Sci.* **2013**, *6* (5), 1509-1512, 10.1039/C3EE00045A.

(45) Durst, J.; Simon, C.; Hasché, F.; Gasteiger, H. A. Hydrogen Oxidation and Evolution Reaction Kinetics on Carbon Supported Pt, Ir, Rh, and Pd Electrocatalysts in Acidic Media. *J. Electrochem. Soc.* **2015**, *162* (1), F190-F203.

(46) Elbert, K.; Hu, J.; Ma, Z.; Zhang, Y.; Chen, G.; An, W.; Liu, P.; Isaacs, H. S.; Adzic, R. R.; Wang, J. X. Elucidating Hydrogen Oxidation/Evolution Kinetics in Base and Acid by Enhanced

Activities at the Optimized Pt Shell Thickness on the Ru Core. *ACS Catal.* **2015**, *5* (11), 6764-6772.

(47) Wang, Y.; Wang, G.; Li, G.; Huang, B.; Pan, J.; Liu, Q.; Han, J.; Xiao, L.; Lu, J.; Zhuang, L. Pt-Ru catalyzed hydrogen oxidation in alkaline media: oxophilic effect or electronic effect? *Energy Environ. Sci.* **2015**, *8* (1), 177-181.

(48) Scofield, M. E.; Zhou, Y.; Yue, S.; Wang, L.; Su, D.; Tong, X.; Vukmirovic, M. B.; Adzic, R. R.; Wong, S. S. Role of Chemical Composition in the Enhanced Catalytic Activity of Pt-Based Alloyed Ultrathin Nanowires for the Hydrogen Oxidation Reaction under Alkaline Conditions. *ACS Catal.* **2016**, *6* (6), 3895-3908.

(49) Strmcnik, D.; Uchimura, M.; Wang, C.; Subbaraman, R.; Danilovic, N.; van der Vliet, D.; Paulikas, A. P.; Stamenkovic, V. R.; Markovic, N. M. Improving the hydrogen oxidation reaction rate by promotion of hydroxyl adsorption. *Nature Chemistry* **2013**, *5* (4), 300-306.

(50) Patel, P. P.; Datta, M. K.; Jampani, P. H.; Hong, D.; Poston, J. A.; Manivannan, A.; Kumta, P. N. High performance and durable nanostructured TiN supported Pt50–Ru50 anode catalyst for direct methanol fuel cell (DMFC). *Journal of Power Sources* **2015**, *293*, 437-446.

(51) Patel, P. P.; Datta, M. K.; Velikokhatnyi, O. I.; Jampani, P.; Hong, D.; Poston, J. A.; Manivannan, A.; Kumta, P. N. Nanostructured robust cobalt metal alloy based anode electro-catalysts exhibiting remarkably high performance and durability for proton exchange membrane fuel cells. *Journal of Materials Chemistry A* **2015**, *3* (26), 14015-14032.

(52) Lim, J.; Shin, K.; Bak, J.; Roh, J.; Lee, S.; Henkelman, G.; Cho, E. Outstanding Oxygen Reduction Reaction Catalytic Performance of In–PtNi Octahedral Nanoparticles Designed via Computational Dopant Screening. *Chemistry of Materials* **2021**, *33* (22), 8895-8903.

(53) Huang, L.; Zaman, S.; Tian, X.; Wang, Z.; Fang, W.; Xia, B. Y. Advanced Platinum-Based Oxygen Reduction Electrocatalysts for Fuel Cells. *Accounts of Chemical Research* **2021**, *54* (2), 311-322.

(54) Zhang, J.; Zhou, Z.; Wang, F.; Li, Y.; Jing, Y. Two-Dimensional Metal Hexahydroxybenzene Frameworks as Promising Electrocatalysts for an Oxygen Reduction Reaction. *ACS Sustainable Chemistry & Engineering* **2020**, *8* (19), 7472-7479.

(55) Roche, I.; Chaînet, E.; Chatenet, M.; Vondrák, J. Carbon-Supported Manganese Oxide Nanoparticles as Electrocatalysts for the Oxygen Reduction Reaction (ORR) in Alkaline Medium: Physical Characterizations and ORR Mechanism. *The Journal of Physical Chemistry C* **2007**, *111* (3), 1434-1443.

(56) Shi, M.; Tong, X.; Li, W.; Fang, J.; Chen, L.; Ma, C.-a. Enhanced Electrocatalytic Oxygen Reduction on NiWOx Solid Solution with Induced Oxygen Defects. *ACS Applied Materials & Interfaces* **2017**, *9* (40), 34990-35000.

(57) Costa de Oliveira, M. A.; D'Epifanio, A.; Ohnuki, H.; Mecheri, B. Platinum Group Metal-Free Catalysts for Oxygen Reduction Reaction: Applications in Microbial Fuel Cells. In *Catalysts*, 2020; Vol. 10.

(58) Hayyan, M.; Hashim, M. A.; AlNashef, I. M. Superoxide Ion: Generation and Chemical Implications. *Chemical Reviews* **2016**, *116* (5), 3029-3085.

(59) Hou, J.; Wu, Y.; Zhang, B.; Cao, S.; Li, Z.; Sun, L. Rational Design of Nanoarray Architectures for Electrocatalytic Water Splitting. *Advanced Functional Materials* **2019**, *29* (20), 1808367.

(60) Ramírez, A. M. R.; Heidari, S.; Vergara, A.; Aguilera, M. V.; Preuss, P.; Camarada, M. B.; Fischer, A. Rhenium-Based Electrocatalysts for Water Splitting. *ACS Materials Au* **2023**, *3* (3), 177-200.

(61) Ursua, A.; Gandia, L. M.; Sanchis, P. Hydrogen Production From Water Electrolysis: Current Status and Future Trends. *Proceedings of the IEEE* **2012**, *100* (2), 410-426.

(62) Yu, Z.-Y.; Duan, Y.; Feng, X.-Y.; Yu, X.; Gao, M.-R.; Yu, S.-H. Clean and Affordable Hydrogen Fuel from Alkaline Water Splitting: Past, Recent Progress, and Future Prospects. *Advanced Materials* **2021**, *33* (31), 2007100.

(63) Yang, H.; Ji, Y.; Shao, Q.; Zhu, W.; Fang, M.; Ma, M.; Liao, F.; Huang, H.; Zhang, Y.; Yang, J.; et al. Metastable-phase platinum oxide for clarifying the Pt–O active site for the hydrogen evolution reaction. *Energy & Environmental Science* **2023**, *16* (2), 574-583.

(64) Sial, M. A. Z. G.; Mateen, M.; Naz, R.; Abbas, M.; Abbas, N.; Talib, S. H.; Janjua, M. R. S. A.; Qamar, M. Alloying platinum single atoms with nickel iron nanoalloys for high performance hydrogen evolution reaction. *International Journal of Hydrogen Energy* **2023**.

(65) Zhang, H.; Guo, X.; Liu, W.; Wu, D.; Cao, D.; Cheng, D. Regulating surface composition of platinum-copper nanotubes for enhanced hydrogen evolution reaction in all pH values. *Journal of Colloid and Interface Science* **2023**, *629*, 53-62.

(66) Sabatier, P. Hydrogénations et déshydrogénations par catalyse. *Berichte der deutschen chemischen Gesellschaft* **1911**, *44* (3), 1984-2001.

(67) Yu, P.; Wang, F.; Shifa, T. A.; Zhan, X.; Lou, X.; Xia, F.; He, J. Earth abundant materials beyond transition metal dichalcogenides: A focus on electrocatalyzing hydrogen evolution reaction. *Nano Energy* **2019**, *58*, 244-276.

(68) Trasatti, S. Work function, electronegativity, and electrochemical behaviour of metals: III. Electrolytic hydrogen evolution in acid solutions. *Journal of Electroanalytical Chemistry and Interfacial Electrochemistry* **1972**, *39* (1), 163-184.

(69) Zheng, J.; Sheng, W.; Zhuang, Z.; Xu, B.; Yan, Y. Universal dependence of hydrogen oxidation and evolution reaction activity of platinum-group metals on pH and hydrogen binding energy. *Sci. Adv.* **2016**, *2* (3).

(70) Mahmood, N.; Yao, Y.; Zhang, J.-W.; Pan, L.; Zhang, X.; Zou, J.-J. Electrocatalysts for Hydrogen Evolution in Alkaline Electrolytes: Mechanisms, Challenges, and Prospective Solutions. *Adv. Sci.* **2018**, *5* (2), 1700464.

(71) Schwämmlein, J. N.; Stühmeier, B. M.; Wagenbauer, K.; Dietz, H.; Tileli, V.; Gasteiger, H. A.; El-Sayed, H. A. Origin of Superior HOR/HER Activity of Bimetallic Pt-Ru Catalysts in Alkaline Media Identified via Ru@Pt Core-Shell Nanoparticles. *Journal of The Electrochemical Society* **2018**, *165* (5), H229.

(72) Bhunia, K.; Chandra, M.; Kumar Sharma, S.; Pradhan, D.; Kim, S.-J. A critical review on transition metal phosphide based catalyst for electrochemical hydrogen evolution reaction: Gibbs free energy, composition, stability, and true identity of active site. *Coordination Chemistry Reviews* **2023**, *478*, 214956.

(73) Suen, N.-T.; Hung, S.-F.; Quan, Q.; Zhang, N.; Xu, Y.-J.; Chen, H. M. Electrocatalysis for the oxygen evolution reaction: recent development and future perspectives. *Chemical Society Reviews* **2017**, *46* (2), 337-365.

(74) Morales-Guio, C. G.; Liardet, L.; Hu, X. Oxidatively Electrodeposited Thin-Film Transition Metal (Oxy)hydroxides as Oxygen Evolution Catalysts. *Journal of the American Chemical Society* **2016**, *138* (28), 8946-8957.

(75) Subbaraman, R.; Tripkovic, D.; Chang, K.-C.; Strmcnik, D.; Paulikas, A. P.; Hirunsit, P.; Chan, M.; Greeley, J.; Stamenkovic, V.; Markovic, N. M. Trends in activity for the water electrolyser reactions on 3d M(Ni,Co,Fe,Mn) hydr(oxy)oxide catalysts. *Nature Materials* **2012**, *11* (6), 550-557.

(76) Man, I. C.; Su, H.-Y.; Calle-Vallejo, F.; Hansen, H. A.; Martínez, J. I.; Inoglu, N. G.; Kitchin, J.; Jaramillo, T. F.; Nørskov, J. K.; Rossmeisl, J. Universality in Oxygen Evolution Electrocatalysis on Oxide Surfaces. *ChemCatChem* **2011**, *3* (7), 1159-1165.

(77) Sanghez de Luna, G.; Ho, P. H.; Sacco, A.; Hernández, S.; Velasco-Vélez, J.-J.; Ospitali, F.; Paglianti, A.; Albonetti, S.; Fornasari, G.; Benito, P. AgCu Bimetallic Electrocatalysts for the Reduction of Biomass-Derived Compounds. *ACS Applied Materials & Interfaces* **2021**, *13* (20), 23675-23688.

(78) van Putten, R.-J.; van der Waal, J. C.; de Jong, E.; Rasrendra, C. B.; Heeres, H. J.; de Vries, J. G. Hydroxymethylfurfural, A Versatile Platform Chemical Made from Renewable Resources. *Chemical Reviews* **2013**, *113* (3), 1499-1597.

(79) Roylance, J. J.; Choi, K.-S. Electrochemical reductive biomass conversion: direct conversion of 5-hydroxymethylfurfural (HMF) to 2,5-hexanedione (HD) via reductive ring-opening. *Green Chemistry* **2016**, *18* (10), 2956-2960.

(80) Román-Leshkov, Y.; Barrett, C. J.; Liu, Z. Y.; Dumesic, J. A. Production of dimethylfuran for liquid fuels from biomass-derived carbohydrates. *Nature* **2007**, *447* (7147), 982-985.

(81) Binder, J. B.; Raines, R. T. Simple Chemical Transformation of Lignocellulosic Biomass into Furans for Fuels and Chemicals. *Journal of the American Chemical Society* **2009**, *131* (5), 1979-1985.

(82) Chidambaram, M.; Bell, A. T. A two-step approach for the catalytic conversion of glucose to 2,5-dimethylfuran in ionic liquids. *Green Chemistry* **2010**, *12* (7), 1253-1262.

(83) Sacia, E. R.; Deaner, M. H.; Louie, Y. L.; Bell, A. T. Synthesis of biomass-derived methylcyclopentane as a gasoline additive via aldol condensation/hydrodeoxygenation of 2,5-hexanedione. *Green Chemistry* **2015**, *17* (4), 2393-2397.

(84) Roylance, J. J.; Kim, T. W.; Choi, K.-S. Efficient and Selective Electrochemical and Photoelectrochemical Reduction of 5-Hydroxymethylfurfural to 2,5-Bis(hydroxymethyl)furan using Water as the Hydrogen Source. *ACS Catalysis* **2016**, *6* (3), 1840-1847.

(85) Kwon, Y.; de Jong, E.; Raoufmoghaddam, S.; Koper, M. T. M. Electrocatalytic Hydrogenation of 5-Hydroxymethylfurfural in the Absence and Presence of Glucose. *ChemSusChem* **2013**, *6* (9), 1659-1667.

(86) Chadderdon, X. H.; Chadderdon, D. J.; Matthiesen, J. E.; Qiu, Y.; Carraher, J. M.; Tessonnier, J.-P.; Li, W. Mechanisms of Furfural Reduction on Metal Electrodes: Distinguishing Pathways for Selective Hydrogenation of Bioderived Oxygenates. *Journal of the American Chemical Society* **2017**, *139* (40), 14120-14128.

(87) Suastegui, M.; Matthiesen, J. E.; Carraher, J. M.; Hernandez, N.; Rodriguez Quiroz, N.; Okerlund, A.; Cochran, E. W.; Shao, Z.; Tessonnier, J.-P. Combining Metabolic Engineering and Electrocatalysis: Application to the Production of Polyamides from Sugar. *Angewandte Chemie International Edition* **2016**, *55* (7), 2368-2373.

(88) Gao, Y.; Ge, L.; Xu, H.; Davey, K.; Zheng, Y.; Qiao, S.-Z. Electrocatalytic Refinery of Biomass-Based 5-Hydroxymethylfurfural to Fine Chemicals. *ACS Catalysis* **2023**, *13* (17), 11204-11231.

(89) Kwon, Y.; Birdja, Y. Y.; Raoufmoghaddam, S.; Koper, M. T. M. Electrocatalytic Hydrogenation of 5-Hydroxymethylfurfural in Acidic Solution. *ChemSusChem* **2015**, *8* (10), 1745-1751.

(90) Liu, F.; Audemar, M.; De Oliveira Vigier, K.; Clacens, J.-M.; De Campo, F.; Jérôme, F. Palladium/Carbon Dioxide Cooperative Catalysis for the Production of Diketone Derivatives from Carbohydrates. *ChemSusChem* **2014**, *7* (8), 2089-2093.

(91) Brewster, J. H. Reductions at Metal Surfaces. II. A Mechanism for the Clemmensen Reduction1. *Journal of the American Chemical Society* **1954**, *76* (24), 6364-6368.

(92) Nam, D.-H.; Taitt, B. J.; Choi, K.-S. Copper-Based Catalytic Anodes To Produce 2,5-Furandicarboxylic Acid, a Biomass-Derived Alternative to Terephthalic Acid. *ACS Catalysis* **2018**, *8* (2), 1197-1206.

(93) Hu, L.; Zhao, G.; Hao, W.; Tang, X.; Sun, Y.; Lin, L.; Liu, S. Catalytic conversion of biomass-derived carbohydrates into fuels and chemicals via furanic aldehydes. *RSC Advances* **2012**, *2* (30), 11184-11206.

(94) Davis, S. E.; Houk, L. R.; Tamargo, E. C.; Datye, A. K.; Davis, R. J. Oxidation of 5-hydroxymethylfurfural over supported Pt, Pd and Au catalysts. *Catalysis Today* **2011**, *160* (1), 55-60.

(95) Villa, A.; Schiavoni, M.; Campisi, S.; Veith, G. M.; Prati, L. Pd-modified Au on Carbon as an Effective and Durable Catalyst for the Direct Oxidation of HMF to 2,5-Furandicarboxylic Acid. *ChemSusChem* **2013**, *6* (4), 609-612.

(96) Jiang, N.; You, B.; Boonstra, R.; Terrero Rodriguez, I. M.; Sun, Y. Integrating Electrocatalytic 5-Hydroxymethylfurfural Oxidation and Hydrogen Production via Co–P-Derived Electrocatalysts. *ACS Energy Letters* **2016**, *1* (2), 386-390.

(97) You, B.; Jiang, N.; Sheng, M.; Bhushan, M. W.; Sun, Y. Hierarchically Porous Urchin-Like Ni2P Superstructures Supported on Nickel Foam as Efficient Bifunctional Electrocatalysts for Overall Water Splitting. *ACS Catalysis* **2016**, *6* (2), 714-721.

(98) Cook, T. R.; Dogutan, D. K.; Reece, S. Y.; Surendranath, Y.; Teets, T. S.; Nocera, D. G. Solar Energy Supply and Storage for the Legacy and Nonlegacy Worlds. *Chemical Reviews* **2010**, *110* (11), 6474-6502.

(99) Shekhawat, A.; Samanta, R.; Panigrahy, S.; Barman, S. Electrocatalytic Oxidation of Urea and Ethanol on Two-Dimensional Amorphous Nickel Oxide Encapsulated on N-Doped Carbon Nanosheets. *ACS Applied Energy Materials* **2023**, *6* (5), 3135-3146.

(100) Tang, C.; Zheng, Y.; Jaroniec, M.; Qiao, S.-Z. Electrocatalytic Refinery for Sustainable Production of Fuels and Chemicals. *Angewandte Chemie International Edition* **2021**, *60* (36), 19572-19590.

(101) Verevkin, S. P.; Emel'yanenko, V. N.; Stepurko, E. N.; Ralys, R. V.; Zaitsau, D. H.; Stark, A. Biomass-Derived Platform Chemicals: Thermodynamic Studies on the Conversion of 5-Hydroxymethylfurfural into Bulk Intermediates. *Industrial & Engineering Chemistry Research* **2009**, *48* (22), 10087-10093.

(102) Chen, Y. X.; Lavacchi, A.; Miller, H. A.; Bevilacqua, M.; Filippi, J.; Innocenti, M.; Marchionni, A.; Oberhauser, W.; Wang, L.; Vizza, F. Nanotechnology makes biomass electrolysis more energy efficient than water electrolysis. *Nature Communications* **2014**, *5* (1), 4036.

(103) Ge, R.; Wang, Y.; Li, Z.; Xu, M.; Xu, S.-M.; Zhou, H.; Ji, K.; Chen, F.; Zhou, J.; Duan, H. Selective Electrooxidation of Biomass-Derived Alcohols to Aldehydes in a Neutral Medium: Promoted Water Dissociation over a Nickel-Oxide-Supported Ruthenium Single-Atom Catalyst. *Angewandte Chemie International Edition* **2022**, *61* (19), e202200211.

(104) Wang, C.; Bongard, H.-J.; Weidenthaler, C.; Wu, Y.; Schüth, F. Design and Application of a High-Surface-Area Mesoporous δ-MnO2 Electrocatalyst for Biomass Oxidative Valorization. *Chemistry of Materials* **2022**, *34* (7), 3123-3132.

(105) Zhou, Z.; Chen, C.; Gao, M.; Xia, B.; Zhang, J. In situ anchoring of a Co3O4 nanowire on nickel foam: an outstanding bifunctional catalyst for energy-saving simultaneous reactions. *Green Chemistry* **2019**, *21* (24), 6699-6706.

(106) Lu, Y.; Liu, T.; Huang, Y.-C.; Zhou, L.; Li, Y.; Chen, W.; Yang, L.; Zhou, B.; Wu, Y.; Kong, Z.; et al. Integrated Catalytic Sites for Highly Efficient Electrochemical Oxidation of the Aldehyde and Hydroxyl Groups in 5-Hydroxymethylfurfural. *ACS Catalysis* **2022**, *12* (7), 4242-4251.

(107) Park, M.; Gu, M.; Kim, B.-S. Tailorable Electrocatalytic 5-Hydroxymethylfurfural Oxidation and H2 Production: Architecture–Performance Relationship in Bifunctional Multilayer Electrodes. *ACS Nano* **2020**, *14* (6), 6812-6822.

(108) Ait Rass, H.; Essayem, N.; Besson, M. Selective Aerobic Oxidation of 5-HMF into 2,5-Furandicarboxylic Acid with Pt Catalysts Supported on TiO2- and ZrO2-Based Supports. *ChemSusChem* **2015**, *8* (7), 1206-1217.

(109) Cai, M.; Zhang, Y.; Zhao, Y.; Liu, Q.; Li, Y.; Li, G. Two-dimensional metal–organic framework nanosheets for highly efficient electrocatalytic biomass 5-(hydroxymethyl)furfural (HMF) valorization. *Journal of Materials Chemistry A* **2020**, *8* (39), 20386-20392.

(110) Latsuzbaia, R.; Bisselink, R.; Anastasopol, A.; van der Meer, H.; van Heck, R.; Yagüe, M. S.; Zijlstra, M.; Roelands, M.; Crockatt, M.; Goetheer, E.; et al. Continuous electrochemical oxidation of biomass derived 5-(hydroxymethyl)furfural into 2,5-furandicarboxylic acid. *Journal of Applied Electrochemistry* **2018**, *48* (6), 611-626.

(111) Zhou, Y.; Shen, Y.; Luo, X. Critical practices in conducting electrochemical conversion of 5-hydroxymethylfurfural. *Catalysis Science & Technology* **2021**, *11* (14), 4882-4888, 10.1039/D1CY00692D.

(112) Zhang, M.; Liu, Y.; Liu, B.; Chen, Z.; Xu, H.; Yan, K. Trimetallic NiCoFe-Layered Double Hydroxides Nanosheets Efficient for Oxygen Evolution and Highly Selective Oxidation of Biomass-Derived 5-Hydroxymethylfurfural. *ACS Catalysis* **2020**, *10* (9), 5179-5189.

(113) Pang, X.; Bai, H.; Zhao, H.; Fan, W.; Shi, W. Efficient Electrocatalytic Oxidation of 5-Hydroxymethylfurfural Coupled with 4-Nitrophenol Hydrogenation in a Water System. *ACS Catalysis* **2022**, *12* (2), 1545-1557.

(114) Gao, L.; Gan, S.; Ma, J.; Sun, Z.; Liu, Z.; Zhong, L.; Zhou, K.; Han, F.; Wang, W.; Han, D.; et al. Titanium Oxide-Confined Manganese Oxide for One-Step Electrocatalytic Preparation of 2,5-Furandicarboxylic Acid in Acidic Media. *ChemElectroChem* **2020**, *7* (20), 4251-4258.

(115) Liu, W.-J.; Dang, L.; Xu, Z.; Yu, H.-Q.; Jin, S.; Huber, G. W. Electrochemical Oxidation of 5-Hydroxymethylfurfural with NiFe Layered Double Hydroxide (LDH) Nanosheet Catalysts. *ACS Catalysis* **2018**, *8* (6), 5533-5541.

(116) Xiao, C.; Zhang, J. Architectural Design for Enhanced C2 Product Selectivity in Electrochemical CO2 Reduction Using Cu-Based Catalysts: A Review. *ACS Nano* **2021**, *15* (5), 7975-8000.

(117) Long, C.; Li, X.; Guo, J.; Shi, Y.; Liu, S.; Tang, Z. Electrochemical Reduction of CO2 over Heterogeneous Catalysts in Aqueous Solution: Recent Progress and Perspectives. *Small Methods* **2019**, *3* (3), 1800369.

(118) Higgins, D.; Hahn, C.; Xiang, C.; Jaramillo, T. F.; Weber, A. Z. Gas-Diffusion Electrodes for Carbon Dioxide Reduction: A New Paradigm. *ACS Energy Letters* **2019**, *4* (1), 317-324.

(119) Jiang, X.; Nie, X.; Guo, X.; Song, C.; Chen, J. G. Recent Advances in Carbon Dioxide Hydrogenation to Methanol via Heterogeneous Catalysis. *Chemical Reviews* **2020**, *120* (15), 7984-8034.

(120) Jones, J.-P.; Prakash, G. K. S.; Olah, G. A. Electrochemical CO2 Reduction: Recent Advances and Current Trends. *Israel Journal of Chemistry* **2014**, *54* (10), 1451-1466.

(121) Maitlis, P. M. What is Fischer–Tropsch? In *Greener Fischer-Tropsch Processes for Fuels and Feedstocks*, 2013; pp 1-15.

(122) Jhong, H.-R. M.; Ma, S.; Kenis, P. J. A. Electrochemical conversion of CO2 to useful chemicals: current status, remaining challenges, and future opportunities. *Current Opinion in Chemical Engineering* **2013**, *2* (2), 191-199.

(123) Schlager, S.; Dibenedetto, A.; Aresta, M.; Apaydin, D. H.; Dumitru, L. M.; Neugebauer, H.; Sariciftci, N. S. Biocatalytic and Bioelectrocatalytic Approaches for the Reduction of Carbon Dioxide using Enzymes. *Energy Technology* **2017**, *5* (6), 812-821.

(124) Qiao, J.; Liu, Y.; Hong, F.; Zhang, J. A review of catalysts for the electroreduction of carbon dioxide to produce low-carbon fuels. *Chemical Society Reviews* **2014**, *43* (2), 631-675, 10.1039/C3CS60323G.

(125) Kumar, B.; Brian, J. P.; Atla, V.; Kumari, S.; Bertram, K. A.; White, R. T.; Spurgeon, J. M. New trends in the development of heterogeneous catalysts for electrochemical CO2 reduction. *Catalysis Today* **2016**, *270*, 19-30.

(126) Zhou, L. Q.; Ling, C.; Zhou, H.; Wang, X.; Liao, J.; Reddy, G. K.; Deng, L.; Peck, T. C.; Zhang, R.; Whittingham, M. S.; et al. A high-performance oxygen evolution catalyst in neutral-pH for sunlight-driven CO2 reduction. *Nature Communications* **2019**, *10* (1), 4081.

(127) Zheng, X.; Zhang, B.; De Luna, P.; Liang, Y.; Comin, R.; Voznyy, O.; Han, L.; García de Arquer, F. P.; Liu, M.; Dinh, C. T.; et al. Theory-driven design of high-valence metal sites for water oxidation confirmed using in situ soft X-ray absorption. *Nature Chemistry* **2018**, *10* (2), 149-154.

(128) You, B.; Sun, Y. Innovative Strategies for Electrocatalytic Water Splitting. *Accounts of Chemical Research* **2018**, *51* (7), 1571-1580.

(129) Zhao, X.; Du, L.; You, B.; Sun, Y. Integrated design for electrocatalytic carbon dioxide reduction. *Catalysis Science & Technology* **2020**, *10* (9), 2711-2720.

(130) Zhang, W.; Hu, Y.; Ma, L.; Zhu, G.; Wang, Y.; Xue, X.; Chen, R.; Yang, S.; Jin, Z. Progress and Perspective of Electrocatalytic CO2 Reduction for Renewable Carbonaceous Fuels and Chemicals. *Advanced Science* **2018**, *5* (1), 1700275.

(131) Jadhav, S. G.; Vaidya, P. D.; Bhanage, B. M.; Joshi, J. B. Catalytic carbon dioxide hydrogenation to methanol: A review of recent studies. *Chemical Engineering Research and Design* **2014**, *92* (11), 2557-2567.

(132) Lee, S.; Speight, J. G.; Loyalka, S. K. *Handbook of alternative fuel technologies*; crc Press, 2014.

(133) Tamura, M.; Ito, K.; Honda, M.; Nakagawa, Y.; Sugimoto, H.; Tomishige, K. J. S. r. Direct copolymerization of CO2 and diols. **2016**, *6* (1), 24038.

(134) Lephoto, M. L.; Nakano, K.; Appavoo, D.; Owaga, B. O.; Nozaki, K.; Darkwa, J. J. C. Pyrazole supported zinc (II) benzoates as catalysts for the ring opening copolymerization of cyclohexene oxide and carbon dioxide. **2016**, *6* (1), 17.

(135) Simakov, D. S. *Renewable synthetic fuels and chemicals from carbon dioxide: fundamentals, catalysis, design considerations and technological challenges*; Springer, 2017.

(136) Jhong, H.-R. M.; Tornow, C. E.; Smid, B.; Gewirth, A. A.; Lyth, S. M.; Kenis, P. J. A. A Nitrogen-Doped Carbon Catalyst for Electrochemical CO2 Conversion to CO with High Selectivity and Current Density. *ChemSusChem* **2017**, *10* (6), 1094-1099.

(137) Zhao, K.; Liu, Y.; Quan, X.; Chen, S.; Yu, H. CO2 Electroreduction at Low Overpotential on Oxide-Derived Cu/Carbons Fabricated from Metal Organic Framework. *ACS Applied Materials & Interfaces* **2017**, *9* (6), 5302-5311.

(138) Nam, D.-H.; De Luna, P.; Rosas-Hernández, A.; Thevenon, A.; Li, F.; Agapie, T.; Peters, J. C.; Shekhah, O.; Eddaoudi, M.; Sargent, E. H. Molecular enhancement of heterogeneous CO2 reduction. *Nature Materials* **2020**, *19* (3), 266-276.

(139) Jouny, M.; Hutchings, G. S.; Jiao, F. Carbon monoxide electroreduction as an emerging platform for carbon utilization. *Nature Catalysis* **2019**, *2* (12), 1062-1070.

(140) Todorova, T. K.; Schreiber, M. W.; Fontecave, M. Mechanistic Understanding of CO2 Reduction Reaction (CO2RR) Toward Multicarbon Products by Heterogeneous Copper-Based Catalysts. *ACS Catalysis* **2020**, *10* (3), 1754-1768.

(141) Huang, J.; Buonsanti, R. Colloidal Nanocrystals as Heterogeneous Catalysts for Electrochemical CO2 Conversion. *Chemistry of Materials* **2019**, *31* (1), 13-25.

(142) Zhang, B. A.; Ozel, T.; Elias, J. S.; Costentin, C.; Nocera, D. G. Interplay of Homogeneous Reactions, Mass Transport, and Kinetics in Determining Selectivity of the Reduction of CO2 on Gold Electrodes. *ACS Central Science* **2019**, *5* (6), 1097-1105.

(143) Yuan, X.; Zhang, L.; Li, L.; Dong, H.; Chen, S.; Zhu, W.; Hu, C.; Deng, W.; Zhao, Z.-J.; Gong, J. Ultrathin Pd–Au Shells with Controllable Alloying Degree on Pd Nanocubes toward

Carbon Dioxide Reduction. *Journal of the American Chemical Society* **2019**, *141* (12), 4791-4794.

(144) Liu, J.; Kong, X.; Zheng, L.; Guo, X.; Liu, X.; Shui, J. Rare Earth Single-Atom Catalysts for Nitrogen and Carbon Dioxide Reduction. *ACS Nano* **2020**, *14* (1), 1093-1101.

(145) Wei, L.; Li, H.; Chen, J.; Yuan, Z.; Huang, Q.; Liao, X.; Henkelman, G.; Chen, Y. Thiocyanate-Modified Silver Nanofoam for Efficient CO2 Reduction to CO. *ACS Catalysis* **2020**, *10* (2), 1444-1453.

(146) Nitopi, S.; Bertheussen, E.; Scott, S. B.; Liu, X.; Engstfeld, A. K.; Horch, S.; Seger, B.; Stephens, I. E. L.; Chan, K.; Hahn, C.; et al. Progress and Perspectives of Electrochemical CO2 Reduction on Copper in Aqueous Electrolyte. *Chemical Reviews* **2019**, *119* (12), 7610-7672.

(147) Tsujiguchi, T.; Kawabe, Y.; Jeong, S.; Ohto, T.; Kukunuri, S.; Kuramochi, H.; Takahashi, Y.; Nishiuchi, T.; Masuda, H.; Wakisaka, M.; et al. Acceleration of Electrochemical CO2 Reduction to Formate at the Sn/Reduced Graphene Oxide Interface. *ACS Catalysis* **2021**, *11* (6), 3310-3318.

(148) Zhu, Q.; Sun, X.; Yang, D.; Ma, J.; Kang, X.; Zheng, L.; Zhang, J.; Wu, Z.; Han, B. Carbon dioxide electroreduction to C2 products over copper-cuprous oxide derived from electrosynthesized copper complex. *Nature Communications* **2019**, *10* (1), 3851.

(149) Xi, W.; Ma, R.; Wang, H.; Gao, Z.; Zhang, W.; Zhao, Y. Ultrathin Ag Nanowires Electrode for Electrochemical Syngas Production from Carbon Dioxide. *ACS Sustainable Chemistry & Engineering* **2018**, *6* (6), 7687-7694.

(150) Delacourt, C.; Ridgway, P. L.; Newman, J. Mathematical Modeling of CO2 Reduction to CO in Aqueous Electrolytes: I. Kinetic Study on Planar Silver and Gold Electrodes. *Journal of The Electrochemical Society* **2010**, *157* (12), B1902.

(151) Lamy, E.; Nadjo, L.; Saveant, J. M. Standard potential and kinetic parameters of the electrochemical reduction of carbon dioxide in dimethylformamide. *Journal of Electroanalytical Chemistry and Interfacial Electrochemistry* **1977**, *78* (2), 403-407.

(152) Hori, Y.; Murata, A.; Takahashi, R.; Suzuki, S. Electrochemical Reduction of Carbon Monoxide to Hydrocarbons at Various Metal Electrodes in Aqueous Solution. *Chemistry Letters* **1987**, *16* (8), 1665-1668.

(153) Hori, Y.; Koga, O.; Yamazaki, H.; Matsuo, T. Infrared spectroscopy of adsorbed CO and intermediate species in electrochemical reduction of CO2 to hydrocarbons on a Cu electrode. *Electrochimica Acta* **1995**, *40* (16), 2617-2622.

(154) Hori, Y.; Takahashi, R.; Yoshinami, Y.; Murata, A. Electrochemical Reduction of CO at a Copper Electrode. *The Journal of Physical Chemistry B* **1997**, *101* (36), 7075-7081.

(155) Pei, Y.; Zhong, H.; Jin, F. A brief review of electrocatalytic reduction of CO2—Materials, reaction conditions, and devices. *Energy Science & Engineering* **2021**, *9* (7), 1012-1032.

(156) Zhang, X.; Guo, S.-X.; Gandionco, K. A.; Bond, A. M.; Zhang, J. Electrocatalytic carbon dioxide reduction: from fundamental principles to catalyst design. *Materials Today Advances* **2020**, *7*, 100074.

(157) Paik, W.; Andersen, T. N.; Eyring, H. Kinetic studies of the electrolytic reduction of carbon dioxide on the mercury electrode. *Electrochimica Acta* **1969**, *14* (12), 1217-1232.

(158) Kumar, K. S.; Choudhary, N.; Jung, Y.; Thomas, J. Recent Advances in Two-Dimensional Nanomaterials for Supercapacitor Electrode Applications. *ACS Energy Letters* **2018**, *3* (2), 482-495.

(159) Theerthagiri, J.; Senthil, R. A.; Nithyadharseni, P.; Lee, S. J.; Durai, G.; Kuppusami, P.; Madhavan, J.; Choi, M. Y. Recent progress and emerging challenges of transition metal sulfides based composite electrodes for electrochemical supercapacitive energy storage. *Ceramics International* **2020**, *46* (10, Part A), 14317-14345.

(160) Najib, S.; Erdem, E. Current progress achieved in novel materials for supercapacitor electrodes: mini review. *Nanoscale Advances* **2019**, *1* (8), 2817-2827.

(161) Raghavendra, K. V. G.; Vinoth, R.; Zeb, K.; Muralee Gopi, C. V. V.; Sambasivam, S.; Kummara, M. R.; Obaidat, I. M.; Kim, H. J. An intuitive review of supercapacitors with recent progress and novel device applications. *Journal of Energy Storage* **2020**, *31*, 101652.

(162) Revankar, S. T. Chapter Six - Chemical Energy Storage. In *Storage and Hybridization of Nuclear Energy*, Bindra, H., Revankar, S. Eds.; Academic Press, 2019; pp 177-227.

(163) Gautham Prasad, G.; Shetty, N.; Thakur, S.; Rakshitha; Bommegowda, K. B. Supercapacitor technology and its applications: a review. *IOP Conference Series: Materials Science and Engineering* **2019**, *561* (1), 012105.

(164) Iro, Z. S.; Subramani, C.; Dash, S. S. A Brief Review on Electrode Materials for Supercapacitor. *International Journal of Electrochemical Science* **2016**, *11* (12), 10628-10643.

(165) Tan, Y. B.; Lee, J.-M. Graphene for supercapacitor applications. *Journal of Materials Chemistry A* **2013**, *1* (47), 14814-14843.

(166) Sahu, P.; Mishra, R.; Panigrahy, S.; Panda, P.; Barman, S. Constructing micropore-rich nitrogen-doped carbon for high-performance supercapacitor and adsorption of carbon dioxide. *International Journal of Energy Research* **2022**, *46* (10), 13556-13569.

(167) Halper, M. S.; Ellenbogen, J. C. J. T. M. C., McLean, Virginia, USA. Supercapacitors: A brief overview. **2006**, *1*.

(168) Hui, C.-y.; Kan, C.-w.; Mak, C.-l.; Chau, K.-h. Flexible Energy Storage System—An Introductory Review of Textile-Based Flexible Supercapacitors. In *Processes*, 2019; Vol. 7.

(169) Oh, S. M.; Hwang, S.-J. Recent advances in two-dimensional inorganic nanosheet-based supercapacitor electrodes. *Journal of the Korean Ceramic Society* **2020**, *57* (2), 119-134.

(170) Muralee Gopi, C. V. V.; Vinodh, R.; Sambasivam, S.; Obaidat, I. M.; Kim, H.-J. Recent progress of advanced energy storage materials for flexible and wearable supercapacitor: From design and development to applications. *Journal of Energy Storage* **2020**, *27*, 101035.

(171) Liu, H.; Liu, X.; Wang, S.; Liu, H.-K.; Li, L. Transition metal based battery-type electrodes in hybrid supercapacitors: A review. *Energy Storage Materials* **2020**, *28*, 122-145.

(172) Muzaffar, A.; Ahamed, M. B.; Deshmukh, K.; Thirumalai, J. A review on recent advances in hybrid supercapacitors: Design, fabrication and applications. *Renewable and Sustainable Energy Reviews* **2019**, *101*, 123-145.

Chapter 2

Comprehensive Approaches and Methodologies in Experimental Research

2.1. INTRODUCTION

An overview of the basic principles underlying the instruments utilized in the current thesis is provided in this chapter. Additionally, it provides a concise overview of the experimental methodologies employed throughout the thesis.

2.2. Materials:

The precursors utilized in this thesis were acquired from commercially available materials, without the need for further purification. **Table 2.1** provides a compilation of the chemicals employed in the thesis, along with their respective formulas.

Table 2.1. Materials employed in the experimental work, including their chemical formulas and supplier names.

Name of Chemicals	Chemical formula	Company name
Formamide	$HCONH_2$	Spectrochem
Ruthenium (III) chloride	$RuCl_3$	Spectrochem
Chloroplatinic acid	H_2PtCl_6	Spectrochem
Sodium borohydride	$NaBH_4$	Spectrochem
40% Platinum on carbon	Comm. Pt/C	Sigma Aldrich
Perchloric acid	$HClO_4$	Merck
Sulfuric acid	H_2SO_4	Merck
Sodium borohydride	$NaBH_4$	Merck
Potassium hydroxide	KOH	CDH
Silver (I) nitrate	$AgNO_3$	Sigma Aldrich
Potassium sulfate	K_2SO_4	Sigma Aldrich

5-hydroxymethylfurfural	$C_6H_6O_3$	Spectrochem
Boric acid	H_3BO_4	Sigma Aldrich
Sodium bicarbonate	$NaHCO_3$	Merck
Phosphate buffer solution	PBS	Merck
2,5-hexanedione	$C_6H_{10}O_2$	Spectrochem
2,5-bis(hydroxymethyl)furan	$C_6H_8O_3$	Cayman
Glutaric acid	$C_5H_8O_4$	Sigma Aldrich
Nickel acetate tetrahydrate	$C_4H_6NiO_4$	Sigma Aldrich
Sodium hydroxide	NaOH	Merck
Bismuth (III) nitrate pentahydrate	$Bi(NO_3)_3. 5H_2O$	Spectrochem
Polyacrylonitrile	$(C_3H_3N)_n$	Spectrochem
N,N-Dimethylformamide	C_3H_7NO	Spectrochem
Potassium bicarbonate	$KHCO_3$	CDH
Palladium (II) chloride	$PdCl_2$	Sigma Aldrich
2,5-furandicarboxylic acid	$C_6H_4O_5$	Sigma Aldrich

2.3. INSTRUMENTAL TECHNIQUES

X-ray diffraction (XRD): [1]

X-ray diffraction (XRD) is an analytical technique used for identifying the crystalline phases of materials. It provides valuable insights into the unit cell structure of these materials. XRD relies on the interaction of X-rays, which have nanometre-scale wavelengths, with the material's atomic arrangement. The X-ray source in XRD is typically an X-ray tube, which consists of a heated tungsten filament encased in a transparent ceramic container serving as the cathode, and a cooled copper target as the anode. In this setup, electrons emitted from the heated tungsten filament are accelerated toward the copper target, which is actively cooled by water. This process causes the emission of electrons from the inner shells of copper atoms, resulting in the displacement

of valence electrons to lower energy levels and the generation of X-rays. These X-rays are then employed for scattering experiments in XRD. The copper source generates X-rays with two distinct wavelengths, known as Cu Kα (λ = 0.154 nm) and Cu Kβ (λ = 0.139 nm). To ensure accurate diffraction patterns, it is crucial to use monochromatic X-rays. This is achieved by utilizing a nickel channel to selectively emit only the Kβ wavelength. In XRD, a detector is employed to capture the scattered X-ray beam, which originates from the sample's interaction with the incident X-ray beam. The angle 2θ is defined as the angle between the direction of the incoming X-ray beam and the direction of the outgoing scattered X-ray beam. This angle is a key parameter in XRD analysis.

The determination of the angle 2θ is employed to calculate the interplanar distance (d-spacing) between two crystal planes using Bragg's diffraction equation, (Figure 2.1):

$$n\lambda = 2d \, sin\theta$$

In this equation, "n" represents the interference order, "θ" stands for the angle between the lattice plane and the incident ray, and "λ" denotes the wavelength of the incident beam.
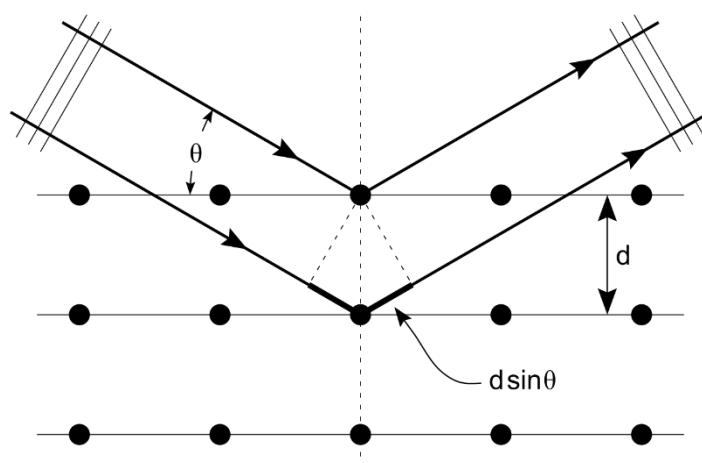
Figure 2.1. Illustrative representation of X-ray scattering (adopted from Wikipedia).

To obtain the X-ray spectra for this thesis, a Bruker diffractometer (DAVINCI D8 ADVANCE) was employed, utilizing Cu Kα radiation with a wavelength (λ) of 0.154 nm.

Transmission Electron Microscope (TEM): [2, 3]

Transmission electron microscopy (TEM) is frequently employed to investigate a variety of materials, including nanowires, quantum dots, and various types of nanoparticles, along with their characteristics such as size, shape, and density in the field of materials science. It can also be used to examine defects, composition, and structure of semiconductors. TEM operates on a concept similar to that of a microscope, with the key difference being the use of electrons instead of light. The instrument features an electron gun that generates a monochromatic electron beam. Condenser lenses are responsible for focusing this beam into a narrow, coherent stream. The condenser aperture further refines the beam by excluding high-angle electrons. Upon interaction with the specimen, a portion of the energy is transmitted, the extent of which depends on the thickness and transparency of the sample. The transmitted component is then converted into an image by the objective lens. The image is subsequently relayed down the column, progressively magnified at each stage, through intermediate and projection lenses.

The fluorescent screen is responsible for receiving the image and emitting light. In the image, darker regions indicate fewer electron interactions, while brighter areas indicate more frequent interactions. Depending on the operational mode, this setup can be useful for generating images or diffraction patterns. In the case of high-resolution transmission electron microscopy (HRTEM), both scattered and transmitted electron beams are utilized to create an interference pattern, revealing the sample's image. For characterizing point defects, dislocations, and surface structures, one can analyse lattice

imperfections and crystal structures in various materials with atomic-level precision. The indices obtained from the selected area electron diffraction (SAED) pattern enable the determination of crystal d-spacing, while the pattern itself provides information about the crystallinity of the samples. According to Bragg's law, crystal planes in the sample that are parallel to the path of the electron beam will undergo diffraction. The generation of this diffraction pattern involves applying a Fourier transformation to the periodic electron potential. Subsequently, the interference between these diffracted electrons and the primary electrons leads to a back transformation, known as the inverse Fourier transform, which ultimately produces an image.

The JEOL F200 model, operating at a voltage of 200 kV is utilized to investigate the material morphologies in this study, we.

Field Emission Scanning Electron Microscope (FESEM):[4, 5]

High-resolution three-dimensional morphological images are generated using Field Emission Scanning Electron Microscopy (FESEM). In FESEM, electrons are emitted from the cathode of the electron gun and subsequently accelerated by the anode within a high-vacuum environment. The vacuum environment is crucial to prevent any unwanted interactions between atoms and molecules in the column and the electron beam, ensuring the integrity of the acquired images. Condenser lenses are employed to tightly focus the electron beam, while a generated magnetic field facilitates its precise back-and-forth deflection. Following this, the beam is meticulously focused onto a very small area, typically ranging from 1 to 5 nanometres. Surface samples are systematically scanned in a raster pattern, with emphasis on these compact regions of interest. The interaction between a primary electron and an atom on the sample's surface leads to the emission of secondary electrons, which are detected and utilized to construct the final

image. The angles and velocities of these secondary electrons are intricately linked to the surface's structural characteristics, allowing for the creation of detailed images that reveal the surface morphology with exceptional precision.
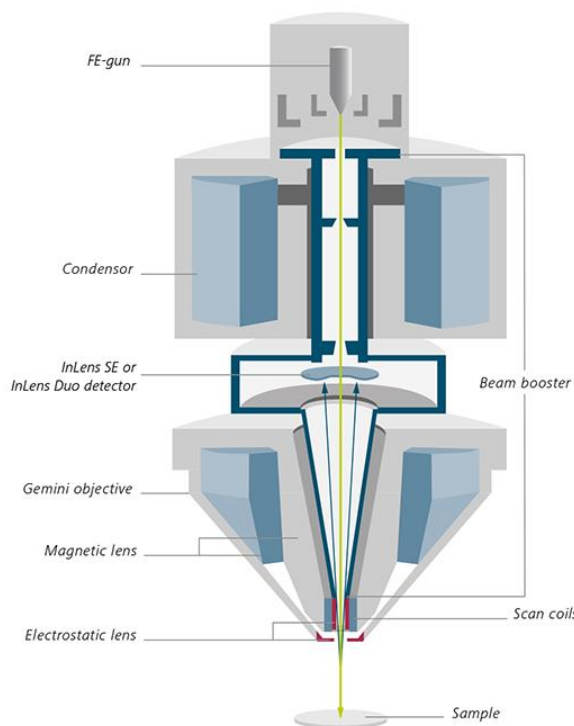
Figure 2.2. Schematic diagram of FE-SEM (adopted from ZEISS).

The data employed in this thesis are derived from a FESEM manufactured by Carl Zeiss in Germany, with the model name 'igma'.

Energy-Dispersive X-ray spectroscopy (EDS):

EDS is employed for the identification and analysis of elemental composition. EDS is an integral component of both SEM and TEM instruments, eliminating the necessity for a separate device. When the sample interacts with incident X-rays, it generates electron-hole pairs. Upon applying a high bias voltage across the crystal, these electrons and holes migrate towards opposing electrodes, producing a charge signal that is subsequently processed. The amplitude of this signal is directly proportional to the energy of the incident X-rays, allowing for the determination of X-ray energy based on the generated current.

Samples for energy-dispersive spectroscopy (EDS) analysis were obtained using the Carl Zeiss spectrometer, manufactured in Germany, with the model name ∑igma.

X-ray photoelectron spectroscopy (XPS):[6, 7]

XPS technique is used for surface analysis, allowing the collection of qualitative and chemical data from the material. This technique provides information about the substance's empirical formula, electronic state, and elemental composition. The X-ray emission source that leads to photoelectron emission from the sample surface is Al K X-rays. By measuring the photoelectron energy (binding energy) and the intensity of the photoelectron peak, one can determine the chemical state and quantity of elements present. It's important to note that the information obtained from XPS measurements originates from a depth of approximately 10 nm below the surface.
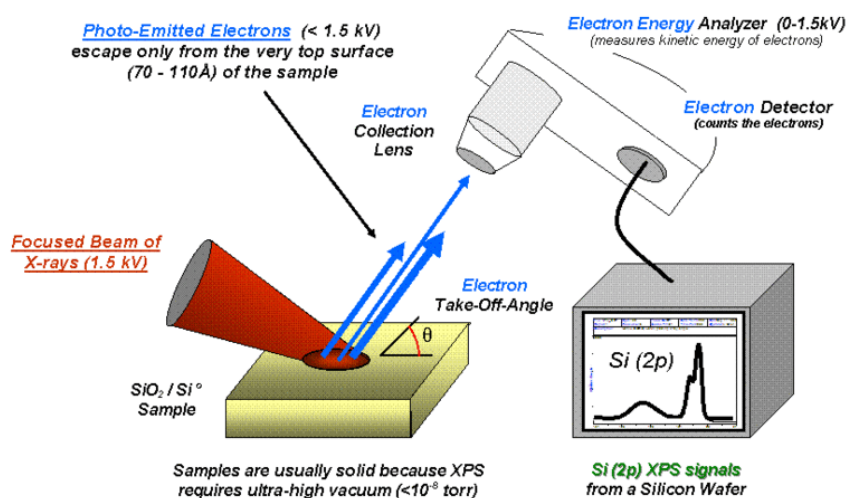
Figure 2.3. Diagram illustrating the operational concept of XPS (adapted from Wikipedia).[5]

XPS measurements were conducted under ultra-high vacuum conditions using the Kratos Axis Ultra and VG Microtech instruments, both equipped with a monochromatic Al K X-ray source for this thesis.

Nuclear Magnetic Resonance (NMR):[8]

NMR spectroscopy is a powerful analytical technique used for studying the nuclear environments of atoms within molecules. The core instrument for NMR spectroscopy is the NMR spectrometer. This spectrometer generates a strong magnetic field and is equipped with various probes and detectors suitable for different types of NMR experiments. The NMR spectrometer maintains a constant and homogeneous magnetic field, typically generated by superconducting magnets. The Radiofrequency (RF) transmitter is responsible for producing the radiofrequency pulses used to excite the nuclear spins of the sample. These pulses are carefully tuned to match the resonance frequencies of the specific nuclei of interest, such as protons (^{1}H) or carbon-13 (^{13}C). The sample probe is an essential component that holds the NMR sample. It is designed to fit within the NMR spectrometer and is equipped with a coil for transmitting RF pulses and receiving NMR signals. Sample probes are available in various configurations to accommodate different sample types and volumes. Achieving a homogeneous magnetic field is crucial for obtaining high-quality NMR spectra. The spectrometer is equipped with a shimming system that fine-tunes the magnetic field to minimize field inhomogeneities.

In this thesis, NMR was done with Bruker 400 MHz for all the samples.

Inductive Coupled Plasma-Optical Emission Spectroscopy (ICP-OES):[9]

ICP-OES is an analytical method employed to identify and quantify elemental components, making it valuable for detecting trace amounts of metals in various substances, including food and water. It relies on a high-temperature flame with temperatures ranging from 6000 to 10,000 K. The ICP-OES instrument comprises two main components: the atomizer and the analyser. The inductive coupled plasma (ICP) serves as the atomizer, while optical emission spectroscopy functions as the analyser.

Argon gas, acting as a carrier gas, is used to transport the sample through a differential vacuum interface in this technique. As the argon cools down, it emits emission rays. These emission rays are directed into the optical emission chamber, where they are separated based on their wavelengths. The element being analysed is identified by the location of the emitted photons, while the concentration is determined by their intensity. ICP-OES offers several advantages over other analytical methods: (a) It allows for the simultaneous measurement of multiple elements. (b) It is less susceptible to ionization and chemical interferences. (c) The technique boasts high sensitivity, capable of detecting elements at the parts per billion level. (d) It provides consistent and reliable results.

The ICP-OES analysis in this study was conducted using the Thermo Scientific iCAP 7000 Series instrument.

Electrochemical measurement:[10]

All electrochemical performance tests in this study followed a conventional three-electrode configuration, and data acquisition was conducted using an electrochemical workstation (Autolab, Metrohm, PGSTAT 302N) as depicted in Figure 2.4. The counter and reference electrodes employed were platinum wire/mesh and Ag/AgCl in 3 M KCl, and Hg/HgO in 1 M KOH. The working electrode was either a glassy carbon electrode (GC) with diameters of 3 mm or 5 mm, Ni foam and carbon cloth, depending on the specific experiment. The GC electrode underwent a polishing process using a suspension of alumina powder (0.3 micron) in deionized water, performed on a nylon polishing pad (Metrohm). Subsequently, after each polishing step the GC electrode was rinsed with deionized water and further sonicated in ethanol for two minutes. All recorded potentials were referenced to either the reversible hydrogen electrode (RHE) or Ag/AgCl scale, and the reported current density was normalized by the geometrical area of the working

electrode for HER, HOR, ORR, and OER measurements. The Nernst equation, $E_{RHE} = E_{Ag/AgCl} + E^0_{Ag/AgCl} + 0.059$ pH, was employed to convert the potentials measured with respect to Ag/AgCl to RHE. In this equation, EAg/AgCl represents the working potential, and $E^0_{Ag/AgCl} = 0.197$ at 25°C. Several commonly used techniques are outlined below:

Figure 2.4. Photograph of conventional three electrode setup of Autolab instrument.[10]

Voltammetry:[11]

Voltammetry entails systematically varying the potential at a fixed rate while concurrently measuring the resulting current. It is a sensitive surface technique that offers insights into the charge exchange occurring at the interfaces between the electrode and electrolyte. Two primary variants of voltammetry are commonly employed to elucidate electrochemical processes:

(a) Cyclic Voltammetry (CV): In CV, the potential progresses linearly from one specified potential (V1) to another (V2), and subsequently reverses from V2 back to V1, as illustrated in Figure 2.5.a.

(b) Linear Sweep Voltammetry (LSV): In LSV, the potential varies linearly between two designated values, V1 and V2, without returning to the initial potential V1, as depicted in Figure 2.5.b.
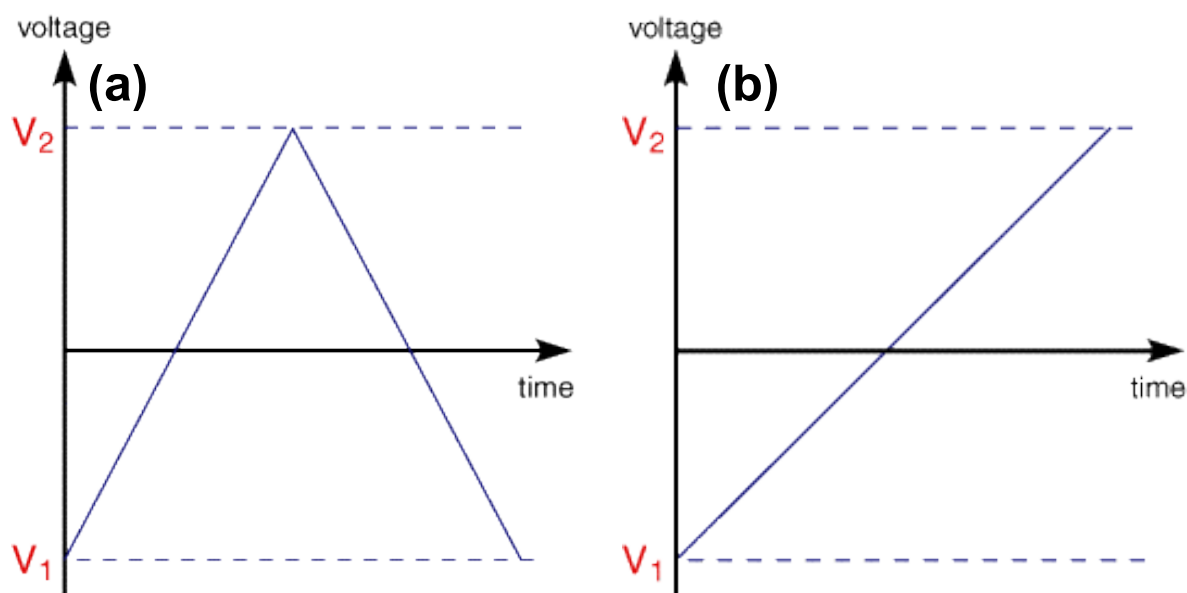
Figure 2.5. Graphs depicting the Voltage vs. Time profiles for (a) cyclic voltammetry and (b) linear sweep voltammetry.

Chronoamperometry (CA):

The CA technique constantly monitors the current at a constant voltage throughout time. This method is useful for calculating the Tafel slope and assessing the stability of electrocatalysts. It also enables for the quantitative study of data, like the total charge passed via the electrode, by combining the current during a predetermined time interval.

Chronopotentiometry (CP):

CP is a galvanostatic technique in which the applied potential required to maintain a constant current varies with time. CP is also employed to assess the stability of electrocatalysts.

Galvanostatic charge discharge (GCD):

The GCD technique measures the duration of charging and discharging cycles within a defined potential range and at a constant current. GCD is valuable for calculating specific capacitance values and determining energy density and power density based on the collected data.

Gas chromatography:[12]

GC is a technique used for the separation and analysis of a mixture of components. The separation occurs in a column containing a stationary phase (liquid or solid), and it relies on the unique retention properties of each component in the mixture. GC systems typically comprise three key components: an injector, a column, and a detector. The column is housed in an oven and is positioned between the injector and detector. Depending on the requirements of the samples, the oven, column, and injector can be heated to various temperatures. A carrier gas, typically argon (Ar), flows continuously through the column at a specific flow rate (standard cubic centimetres per minute, sccm).

To analyse the headspace of the electrochemical cell, a gas-tight syringe is used to inject the sample into the injection port. The carrier gas then sweeps the sample through the column. Due to their distinct retention properties, the analytes in the sample reach the detector at different times and in separate streams. For gas phase analysis, a Thermal Conductivity Detector (TCD) is employed, with argon (Ar) serving as the carrier gas. The Thermo Scientific Trace 1110 GC instrument, equipped with a TCD detector and utilizing argon as the carrier gas, was utilized for this study.

Double layer capacitance:

The catalyst's C_{dl} was determined by analysing its CV plot, which was recorded within a non-faradic potential window. The working electrode underwent 20 CV cycles within a specific potential range to stabilize it before acquiring charging-discharging CV plots at various scan rates. To calculate C_{dl}, we plotted the linear relationship between

current density (mA cm^{-2}) at a specific potential (RHE) and the scan rate (mF cm^{-2}). Additionally, the materials' roughness factor (R_f) was obtained using C_{dl}, employing the formula $R_f = C_{dl}/C_s$, where C_s represents the double-layer capacitance per unit area on an atomically flat planar surface under the same conditions. In this case, we utilized bare GC electrodes as the planar surface, and the C_s value for a bare GC electrode is 0.082 mF cm^{-2}.

Electrochemical Surface Area (ECSA) calculation using the Under-Potential Hydrogen Desorption (UPD-H$_{des}$) method:

The ECSA was assessed using the hydrogen desorption peak observed in the CV plots, with subsequent double-layer correction applied. ECSA was calculated using the formula:

ECSA = (S/m) x (v/c)

Where:

- ECSA represents the electrochemically active surface area.

- S is the double-layer corrected area under the hydrogen desorption curve.

- m is the Pt loading on the electrode surface.

- v is the scan rate (mV/s).

- c is the required charge (0.21 mC cm^{-2}) to oxidize a monolayer of hydrogen on the platinum surface.

This calculation allows for the determination of the ECSA based on the observed CV data and the known charge required for hydrogen monolayer oxidation on the platinum surface.

CO stripping measurement:[13]

The electrode potential was initially maintained at 0.1 V (RHE) for the CO stripping analysis to achieve complete monolayer adsorption of CO on the metal surface.

Subsequently, the dissolved CO in the solution was purged using N_2. Following this, a CV scan was performed at a scan rate of 30 mV/s, with the forward scan corresponding to CO stripping under different pH conditions.

2.4. References:

(1) Holder, C. F.; Schaak, R. E. Tutorial on Powder X-ray Diffraction for Characterizing Nanoscale Materials. *ACS Nano* **2019**, *13* (7), 7359-7365.

(2) Franken, L. E.; Grünewald, K.; Boekema, E. J.; Stuart, M. C. A. A Technical Introduction to Transmission Electron Microscopy for Soft-Matter: Imaging, Possibilities, Choices, and Technical Developments. *Small* **2020**, *16* (14), 1906198.

(3) Graham, L.; Orenstein, J. M. Processing tissue and cells for transmission electron microscopy in diagnostic pathology and research. *Nature Protocols* **2007**, *2* (10), 2439-2450.

(4) Lewczuk, B.; Szyryńska, N. Field-Emission Scanning Electron Microscope as a Tool for Large-Area and Large-Volume Ultrastructural Studies. In *Animals*, 2021; Vol. 11.

(5) Po, R.; Corso, G.; Cominetti, A.; Carbonera, C.; Bernardi, A.; Di Paola, E.; Carati, C.; Bonoldi, L. Field emission scanning electron microscopy (FESEM): an easy way to characterize morphologies of P3HT:PCBM coated and printed solar cells. *Flexible and Printed Electronics* **2019**, *4* (3), 034001.

(6) Greczynski, G.; Haasch, R. T.; Hellgren, N.; Lewin, E.; Hultman, L. X-ray photoelectron spectroscopy of thin films. *Nature Reviews Methods Primers* **2023**, *3* (1), 40.

(7) Greczynski, G.; Hultman, L. X-ray photoelectron spectroscopy: Towards reliable binding energy referencing. *Progress in Materials Science* **2020**, *107*, 100591.

(8) Simpson, A. J.; Simpson, M. J.; Soong, R. Nuclear Magnetic Resonance Spectroscopy and Its Key Role in Environmental Research. *Environmental Science & Technology* **2012**, *46* (21), 11488-11496.

(9) Khan, S. R.; Sharma, B.; Chawla, P. A.; Bhatia, R. Inductively Coupled Plasma Optical Emission Spectrometry (ICP-OES): a Powerful Analytical Technique for Elemental Analysis. *Food Analytical Methods* **2022**, *15* (3), 666-688.

(10) Xia, D.-H.; Deng, C.-M.; Macdonald, D.; Jamali, S.; Mills, D.; Luo, J.-L.; Strebl, M. G.; Amiri, M.; Jin, W.; Song, S.; et al. Electrochemical measurements used for assessment of corrosion and protection of metallic materials in the field: A critical review. *Journal of Materials Science & Technology* **2022**, *112*, 151-183.

(11) Elgrishi, N.; Rountree, K. J.; McCarthy, B. D.; Rountree, E. S.; Eisenhart, T. T.; Dempsey, J. L. A Practical Beginner's Guide to Cyclic Voltammetry. *Journal of Chemical Education* **2018**, *95* (2), 197-206.

(12) Eiceman, G. A.; Gardea-Torresdey, J.; Overton, E.; Carney, K.; Dorman, F. Gas Chromatography. *Analytical Chemistry* **2002**, *74* (12), 2771-2780.

(13) Ciapina, E. G.; Santos, S. F.; Gonzalez, E. R. Electrochemical CO stripping on nanosized Pt surfaces in acid media: A review on the issue of peak multiplicity. *Journal of Electroanalytical Chemistry* **2018**, *815*, 47-60.

RuO₂ as promoter in Pt-RuO₂-Nanostructures/Carbon composite, a pH-universal Catalyst for Hydrogen Evolution/Oxidation Reactions

Chapter 3

Chapter 3

RuO₂ as promoter in Pt-RuO₂-Nanostructures/Carbon composite, a pH-universal Catalyst for Hydrogen Evolution/Oxidation Reactions

3.1 ABSTRACT

The development of new catalysts for Hydrogen evolution reaction/Hydrogen oxidation reaction (HER/HOR) is of crucial importance for the commercialization of Proton-exchange membrane/ Anion-exchange membrane based renewable technologies. The sluggish HER/HOR kinetic (in base) and poor HER/HOR stability (in acid) of commercial Pt/C are the main obstacles. Interface engineering in multi-component nanostructures is a method for enhanced electrochemical performances. This chapter discuses the interfaces-engineered RuO_2-Pt/C as a pH-independent catalyst for Hydrogen oxidation reaction/Hydrogen evolution reaction applications. The Hydrogen oxidation reaction/Hydrogen evolution reaction activity of RuO_2-Pt/C is one order magnitude higher than commercial Pt/C in base and 2.5 fold higher in acid. It shows excellent stability in acid and base. It exhibits excellent pH tolerant HOR behavior. The $i_{0,m}$ of RuO_2-Pt/C in base is ~ 1833 $A.g^{-1}_{RuPt}$ which is 8 fold higher than commercial Pt/C. The RuO_2 in RuO_2-Pt/C makes it more active towards HER/HOR in base. Although it has similar activity in acid, its basic activity is 29 fold higher than Ru-Pt-NPs/C. Hydrogen binding energy and OH binding energy are two equivalent descriptors for HOR/HER in base. HOR/HER activity of this catalyst in different 0.1M electrolyte decreases in the sequence of $Li^+>Na^+>K^+$ but improved HER and decreased HOR is observed with increasing Li^+ ions. The $[(H_2O)_x-AM^+-(OH)_{ad}]$ in double-layer influences HOR/HER performance of RuO_2-Pt/C. This catalyst has great potential for application in PEM/AEM-based devices.

RuO₂ as promoter in Pt-RuO₂-Nanostructures/Carbon composite, a pH-universal Catalyst for Hydrogen Evolution/Oxidation Reactions

Chapter 3

3.2 INTRODUCTION

With rapidly increasing environmental issues and energy demand, the search for renewable energy technologies is gaining importance recently[1-4]. Electrolyzer is the device for energy storage systems[5] and Fuel Cell is the device for energy conversion systems[6, 7]. In Electrolyzers, energy is stored as molecular hydrogen via Hydrogen evolution reaction (HER) [8-10] whereas, in fuel cells, the chemical energy of H_2 molecule is converted into electricity through Hydrogen oxidation reaction (HOR)[11, 12]. The proton exchange membrane fuel cells (PEMFCs) have very high energy and power density, high energy conversion efficiency. Platinum (Pt) catalysts are highly active towards HOR/HER in acidic environment[13-16], however, poor durability of commercial (comm) Pt/C catalyst in the acid media is the main obstacle for its commercial applications in PEMFCs and PEMELs[17, 18]. Therefore, it is important to develop new active as well as durable catalyst for acidic HER/HOR. On the other hand, alkali exchange membrane fuels (AEMFCs) and alkali membrane electrolyzers (AEMELs) are considered as an affordable alternative to PEMFCs and PEMELs because non-precious ORR[19, 20] and OER [21-24] catalysts for alkaline media are available. Like acid media, Pt is also a good catalyst for alkaline HOR/HER. However, a large amount of Pt is required for AEMFCs or AEMELs due to its sluggish HOR/HER activity in alkaline environment[25, 26]. The HOR or HER on Pt catalyst is 2 to 3 times lower in base than its acid media activity [27]. Thus, highly active HOR/HER catalysts for alkaline media are essential for their application in AEMFCs and AEMELs. The HOR in acid goes through two simple steps: the Tafel step (dissociative H_2 adsorption as H_{ad}) followed by H_{ad} oxidation into H^+ ions[28]. In alkaline media, 1st step is the same and the second step is either H_{ad} combine with OH^- from the solution or H_{ad} combine with adsorbed OH (OH_{ad}) to form H_2O. The two contrasting mechanisms are known for alkaline HOR - (i) Hydrogen binding energy

RuO₂ as promoter in Pt-RuO₂-Nanostructures/Carbon composite, a pH-universal Catalyst for Hydrogen Evolution/Oxidation Reactions

Chapter 3

(HBE) theory[28-33] and (ii) OH_{ad} theory[34-38]. Understanding the alkaline HER/HOR mechanism is crucial for the development of new HER/HOR catalysts. In recent literatures, either HBE or OH adsorption was discussed as the sole descriptor for alkaline HER/HOR. Several groups reported that poor HOR/HER performance was linked with HBE of the metals in alkaline solution and indicated that HBE is a single descriptor for HOR/HER in basic solution[29, 39]. The HER performance vs HBE plot of different monometallic metals was volcano-shaped indicating that HBE is the key descriptor for alkaline HOR/HER[40]. Wang et al.[31] indicated HBE is the main descriptor, not oxophilicity, based on their HOR studies of PtRu alloy catalyst in alkaline solution. Gasteiger and coworkers [28] proposed that HBE was the main descriptor for alkaline HOR. In contrast, Strmcnik et al.[35] proposed that OH adsorption was another descriptor for HER when Pt was functionalized with $Ni(OH)_2$. The enhanced alkaline HER activity was explained by a bi-functional mechanism. Koper et al.[41] raised the potential of zero free charge (pzfc) theory and mentioned that reorganization of water at the interface is a descriptor for HER on Platinum electrode. S. Mukherjee and co-workers[42] proposed 2B theory combining the bifunctional mechanism and hard-soft-acid-base (HSAB) theory mechanism for alkaline HOR/HER behavior of Pt catalysts.

Here, in this chapter, we have discussed a simple synthesis method of RuO_2-Pt/C composite for electrochemical hydrogen oxidation and evolution reactions in various pH solutions. The HOR/HER activity of RuO_2-Pt/C is about 8-10 and 2.4 times better than comm Pt/C in basic and acidic medium respectively. We demonstrate the role of RuO_2 in RuO_2-Pt/C on HBE and OH adsorption and the effect of HBE and OH adsorption on HOR/HER performances. The RuO_2 acts as a promoter in the RuO_2-Pt/C catalyst for alkaline HOR/HER. We have also discussed that the HOR/HER performance of RuO_2-Pt/C is sensitive to the nature of alkali metal ions (AM^+) in alkaline electrolyte and also

RuO₂ as promoter in Pt-RuO₂-Nanostructures/Carbon composite, a pH-universal Catalyst for Hydrogen Evolution/Oxidation Reactions

Chapter 3

depends on the alkali metal ions concentration in the electrolyte solution. We have demonstrated the role of OH adsorption on the catalyst surface (catalyst-OH_{ad}) and in the double layer region, $[(H_2O)_{x-}AM^+-OH_{ad}]$ species modify HER/HOR activity in alkaline media as per HSAB theory.

3.3 EXPERIMENTAL SECTION

Materials:

Ruthenium (III) chloride ($RuCl_3$) 98+% assay), Chloroplatinic acid (H_2PtCl_6, $6H_2O$, 38-40% assay), sodium borohydride ($NaBH_4$) was purchased from Spectrochem (India). 40% Platinum on carbon (comm. Pt/C), Formamide ($HCONH_2$) was bought from Sigma-Aldrich. Perchloric acid ($HClO_4$), Sulfuric acid (H_2SO_4, 98%) and potassium hydroxide (KOH) was purchased from Merck (Germany). All these chemicals were used as they received without further purification. CO, H_2, N_2 and gases (99.99 % purity) were bought from Sigma Aldrich. Mili-Q water was obtained from ultrafiltration system (Mili-Q, Millipore) and the measured conductivity was 35 mho.cm^{-1} at 25 ^{0}C.

Synthesis of nitrogen-doped carbon:

First of all, nitrogen doped carbon (CN_x) was formed by microwave heating of Formamide ($HCONH_2$), which was reported recently by our group. A 30 ml volume of $HCONH_2$ was treated to a microwave irradiation at 180^{0}C for 2h. Then a brown coloured solution was formed. After that, the resulting solution was evaporated by vacuum in a rotary evaporator at 180^{0}C to form nitrogen-doped carbon. In the end, product was filtrated and thoroughly washed with the help of distilled water and vacuum dried to form a solid, dry nitrogen-doped carbon.

Preparation of the Ru-Pt-NPs/C composite:

Ru-Pt-NPs/C composite was formed by reducing ruthenium (III) chloride and chloroplatinic acid with the help of $NaBH_4$ followed by ultrasonic treatment. Initially,

RuO₂ as promoter in Pt-RuO₂-Nanostructures/Carbon composite, a pH-universal Catalyst for Hydrogen Evolution/Oxidation Reactions

Chapter 3

123 mg of chloroplatinic acid and 30 mg of ruthenium (III) chloride was dispersed well in 5 ml water by sonicating for 30 minutes. In another beaker, 7.5 mg of as prepared of CN_x was taken and dispersed in 2 ml water by sonication in a bath-sonicator for some time. Then two solutions are mixed together and sonicated for 30 minutes. Then with constant sonication, 150 mg of $NaBH_4$ was added to the mixed solution. At last, resultant black solution was sonicated for 3 hours using the bath sonicator. A black mass precipitated out from the solution after ultrasound treatment. The black precipitate was collected by centrifugation at 3600 rpm for 30 minutes and washed with deionized water & ethanol repeatedly. Then the product was kept in vacuum for drying.

Synthesis of the RuO₂-Pt/C nanostructures:

After obtaining solid Ru-Pt-NPs/C product, RuO₂-Pt/C was synthesized by thermal heating of Ru-Pt-NPs/C. Ru-Pt-NPs/C composite was taken in an alumina crucible and calcinated at 450°C in a tube furnace with a temperature accuracy ±2 °C for 90 minutes. Then, it was cooled down to room temperature normally & a black solid product was collected carefully. For comparison purpose we have synthesized RuO₂-Pt/C with different Pt, Ru ratio, only Pt-450/C, Ru-450/C and only RuO₂-Pt sample without using any carbon support, following the same synthesis procedure. This composite is termed as RuO₂-Pt.

Characterizations:

MAS-II microwave synthesizer was used for the synthesis of CN_x and was bought from SINEO Microwave Technology Company (Shanghai, China). Ultrasound treatment was carried out by SINEO UWave-1000 (Shanghai, China) with 28 kHz frequency. Field-emission scanning electron microscope (FESEM) system (Carl Zeiss, Germany make, Model: ∑igma) was used for taking FESEM images. FESEM samples were prepared by casting a drop on a Si-wafer and dried at air around 45^0C. The powder x-ray diffraction

RuO₂ as promoter in Pt-RuO₂-Nanostructures/Carbon composite, a pH-universal Catalyst for Hydrogen Evolution/Oxidation Reactions

Chapter 3

pattern (p-XRD) of samples was performed by Bruker DAVINCI D8 ADVANCE diffractometer equipped with Cu Kα radiation (λ= 0.15406 nm). Transmission Electron Microscopy (TEM, JEOL F200) operated at 200 kV, was used to investigate surface morphology and also used to take High-Resolution TEM (HRTEM) images. For TEM sample preparation, 10 µl solution was taken from a stock solution of 4×10^{-5} mg/l and dried at air around 45^0C. CHNS was analyzed by using Euro Vector (Euro EA analyzer 3000). XPS measurements were done by VG Microtech where monochromatic source was Mg K_α X-ray. XPS was taken from the sample deposited on Si wafer. And all the electrochemical measurements were performed with an Electrochemical Workstation (Autolab, Metrohm, PGSTAT 320N), equipped with rotating disk electrode (RDE). A conventional 3 electrode system, platinum wire as a counter electrode, glassy carbon as a working electrode and Ag/AgCl as a reference electrode were used. Smoothing was applied in chronoamperometric responses where needed to reduce noise in chronoamperometric measurements due to bubble accumulation. pH of the working solution was measured before experiment using Hanna (HI 2209) pH meter.

Electrochemical measurements:

All the electrochemical measurements were performed in a conventional three-electrode system at an Autolab 302 N electrochemical station using glassy carbon (GC) as a working electrode, Pt wire as counter electrode and Ag/AgCl (3M KCl) as reference electrode. The working GC electrode was polished with 1.0, 0.1 and 0.05 mm alumina slurry on Buehler micro cloth polishing cloth. After that the electrode was rinsed with copious water and then sonicated in distilled water about 10 min. In order to make a stock solution for HER in 1M KOH and 0.5M KOH, 1 mg of synthesized composite was dissolved in 1 ml water. 2.5 µl of aqueous stock solution was drop-casted and evaporated on cleaned glassy carbon electrode to prepare RuO₂-Pt/C electrode. The loading of RuPt

RuO₂ as promoter in Pt-RuO₂-Nanostructures/Carbon composite, a pH-universal Catalyst for Hydrogen Evolution/Oxidation Reactions

Chapter 3

metal on the GC electrode was 1.425 μg. For stability measurement 10 μl 5 wt% nafion solution was used to make the stock solution. 5 μl of aqueous stock solution (i.e 2.85 μg of RuPt) was evaporated on GC only for potentiometric study in KOH medium. For all the experiment, the amount of comm. Pt/C and comm. RuPt/C was also kept same for comparison.10 μl ethanol and 10 μl 5% nafion was used to make the stock solution of comm. Pt/C and comm. RuPt/C. By using the general formula $E_{RHE} = E_{Ag/AgCl} + E^0_{Ag/AgCl} + (0.059 \times pH)$, potential obtained from Ag/AgCl reference electrode was converted to RHE, where $E^0_{Ag/AgCl} = 0.1976$ at 25^0C (3M KCl) and $E_{Ag/AgCl}$ is the working potential. Before experiment pH was also measured for all electrolytes. And the HER measurements were carried out in both basic and acidic medium after degassing with nitrogen using LSV at a scan rate 10 mV/sec. HOR in different pH solutions was done in a H_2 saturated environment with the help of linear sweep voltammetry (LSV) at a scan rate 10 mV.sec^{-1} scan rate. For CV in different pH, 30 mv/sec scan rate was used with N_2 saturated medium. In CO stripping measurement, for full monolayer adsorption of CO on metal surface, first the electrode potential was held at 0.1 V (RHE). Then N_2 was flowed for some minutes to remove the dissolved CO from the solution. After that, CV scan was performed at 30 mV/sec where the forward scan represents the CO stripping. The stability of the electrode was measured by chronopotentiometric measurement by applying constant current for certain time. AC impedance measurements were performed in the identical system with a constant AC voltage in the frequency range 10^5 Hz to 10^{-1} Hz. Cell (solution) resistance was calculated by linearly extrapolating the intercept of impedance spectra with real axis and this value was used for iR correction. All HOR polarization curves in different pH were iR corrected.

3.4 RESULTS AND DISCUSSION

Morphology and characterization:

RuO₂ as promoter in Pt-RuO₂-Nanostructures/Carbon composite, a pH-universal Catalyst for Hydrogen Evolution/Oxidation Reactions

Chapter 3

The RuO_2-Pt/C was obtained by heating of carbon-supported Ru-Pt-nano-composite (Ru-Pt-NPs/C) at 450^0C for 90 minutes in the air (the details is in experimental section). The Ru-Pt-NPs/C was synthesized by ultra-sonication-assisted BH_4^- reduction of $RuCl_3$ and H_2PtCl_6 in the presence of N-doped carbon (N@C) support. The X-ray diffraction (XRD) data of Ru-450/C, Pt-450/C, and RuO_2-Pt/C composites were given in Figure 3.1a. These diffraction patterns were compared with standard JCPDS data of face-centered cubic (fcc) Pt metal and rutile RuO_2. The diffraction peaks at 39.55, 45.99, 67.1, and 80.9 in RuO_2-Pt/C composite are assigned as (111), (200), (202), (311) crystalline planes of fcc Pt metal (JCPDS No. 04-0802). In addition, the peaks at 28.05, 35.08, 39.6, 54.3 correspond to (110), (101), (111), (210) planes of RuO_2 (JCPDS No. 88-0322), which assured the existence of RuO_2 and metallic Pt in RuO_2-Pt/C composite. The morphology and structure of RuO_2-Pt/C were studied by Transmission Electron Microscopy (TEM). The TEM images of RuO_2-Pt/C are displayed in Figure (3.1(b-d), S3.1(a, b)). This shows the nano-particles are supported on carbon sheets.

RuO₂ as promoter in Pt-RuO₂-Nanostructures/Carbon composite, a pH-universal Catalyst for Hydrogen Evolution/Oxidation Reactions

Chapter 3
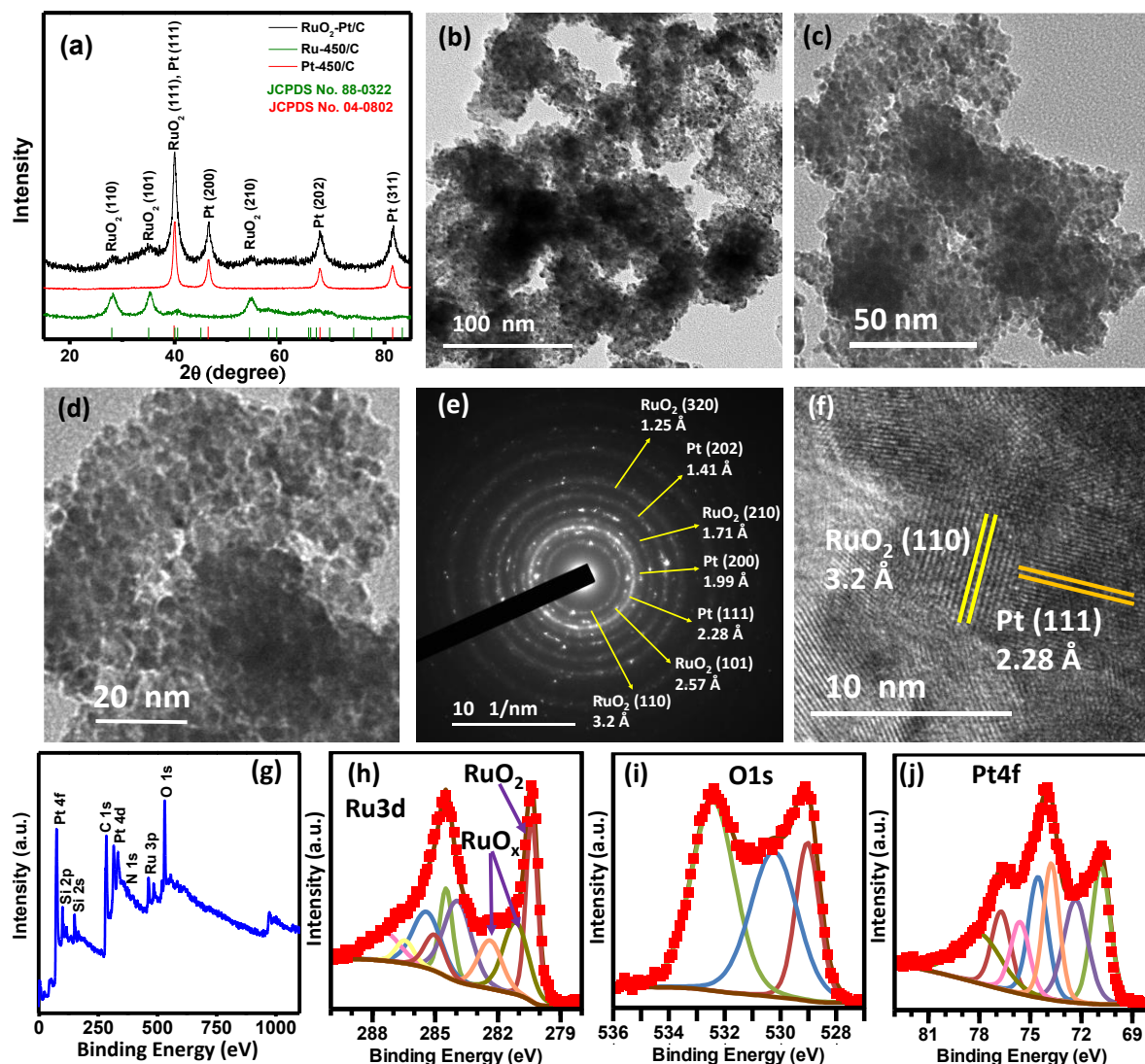
Figure 3.1. (a) p-XRD of Pt-450/C, Ru-450/C, RuO₂-Pt/C. (b, c, d) TEM images, (e) SAED image, (f) HRTEM image of RuO₂-Pt/C, (g) XPS survey scan of RuO₂-Pt/C, High resolution XPS spectra of (h) Ru 3d/C 1s, (i) O 1s, (j) Pt 4f.

The average size of nanoparticles varies from 5 to 8 nm and they are interconnected. In Figure 3.1e, the SAED image of RuO₂-Pt/C indicates a polycrystalline nature of the catalyst. The d-spacings, measured from the SAED image, are found to be 2.28, 1.99, 1.41 Å corresponding to (111), (200), and (202) planes of Pt and 3.2, 2.57, 1.71, and 1.25 corresponding to (110), (101), (210), and (320) planes of RuO₂ respectively. Figure 3.1f

117

RuO₂ as promoter in Pt-RuO₂-Nanostructures/Carbon composite, a pH-universal Catalyst for Hydrogen Evolution/Oxidation Reactions

Chapter 3

shows the high resolution (HR) TEM image of RuO_2-Pt/C catalyst. The d spacing values of 2.28 Å and 3.2 Å corresponding to the Pt (111) and RuO_2 (110) lattice planes confirmed the existence of Pt and RuO_2 in the catalyst. The elemental mapping images of RuO_2-Pt/C composite displayed that Pt and Ru are well dispersed over the whole composite as shown in Figure 3.2. The p-XRD, TEM images, and elemental mapping images of Ru-Pt-NPs/C catalyst are also given in Figure S3.2(2, 3). These suggest small nanoparticles of Ru and Pt are dispersed on carbon sheets. The elemental mapping suggests the uniform distribution of Ru and Pt nanoparticles. On heating of Ru-Pt-NPs/C composite at 450^0C, growth of Pt nanoparticles and formation of RuO_2 occurs, leads to the formation of plenty of interfaces due to interface engineering. The interfaces among different phases may play an important role to enhance catalytic reactions. The HRTEM images (Figure 3.1f and S3.1(c, d)) show the abundance of interfaces that may act as active catalytic sites for electrochemical reactions. The XPS survey scan spectrum of RuO_2-Pt/C hybrid was provided in Figure 3.1g. This indicates the presence of ruthenium (Ru), platinum (Pt), oxygen (O), carbon(C), and little amount of nitrogen (N) atom. Nine peaks were used to fit Ru3d/C1s XPS spectra of RuO_2-Pt/C catalyst (Figure 3.1h). The peaks at 284.0, 285.4, and 287.95 eV can be assigned to C1s peak of sp^2 carbon and carbon containing oxygen based functional groups whereas peaks at 280.39, 281, and 282.2 eV can be assigned to RuO_2 and RuO_x respectively. The O1s XPS spectrum of RuO_2-Pt/C composite was also deconvoluted into three peaks in Figure 3.1i. The O1s peak of RuO_2-Pt/C at 529.08, 530.3, and 532.4 eV are assigned to Ru-O-Ru, Ru-OH, and H_2O respectively. The high-resolution Pt4f XPS spectra of RuO_2-Pt/C are shown in Figure 3.1j. It was fitted by 7 peaks. The peaks at 70.8, 74.4 eV; 72.3, 75.5 eV; 73.7, 76.7 eV are due to $4f_{7/2}$ and $4f_{5/2}$ of Pt (0), Pt (II) and Pt (IV) species respectively. The accurate wt% of metal present in RuO_2-Pt/C and Ru-Pt-NPs/C was found to be 56.3% and 58%

RuO₂ as promoter in Pt-RuO₂-Nanostructures/Carbon composite, a pH-universal Catalyst for Hydrogen Evolution/Oxidation Reactions

Chapter 3

respectively by ICP-OES measurements. The electrochemical property of the RuO_2-Pt/C composite was studied by the cyclic voltammetry (CV) measurements. The hydrogen adsorption and desorption and OH adsorption or oxide formation can be explored from the CV measurements. The H_{ad} and OH_{ad} species are vital because these may serve as an intermediate for many electrochemical reactions. The CV in 0.1M KOH solution of RuO_2-Pt/C shows the proton adsorption−desorption peaks below 0.4 V (Figure S3.4). The two characteristic H-desorption peaks can be assigned to Pt (100) (at higher overpotential) and Pt (110) (at lower overpotential) respectively. The OH adsorption and Pt-oxidation peak of RuO_2-Pt/C are also seen in Figure S3.4. The CO-stripping experiments were used to calculate the ECSA (electrochemical Surface area) of all these catalysts (Figure S3.5). The ECSA values of RuO_2-Pt/C catalyst were found to be 101, 138 $m^2/g_{Pt,Ru}$ in 0.1M KOH and 0.1M $HClO_4$ whereas for Ru-Pt-NPs/C, it was 32 and 147 $m^2/g_{Pt,Ru}$ in 0.1M KOH and 0.1M $HClO_4$ and for comm Pt/C catalyst, it was 43 and 50 m^2/g_{Pt} in 0.1M KOH and 0.1M $HClO_4$ respectively.
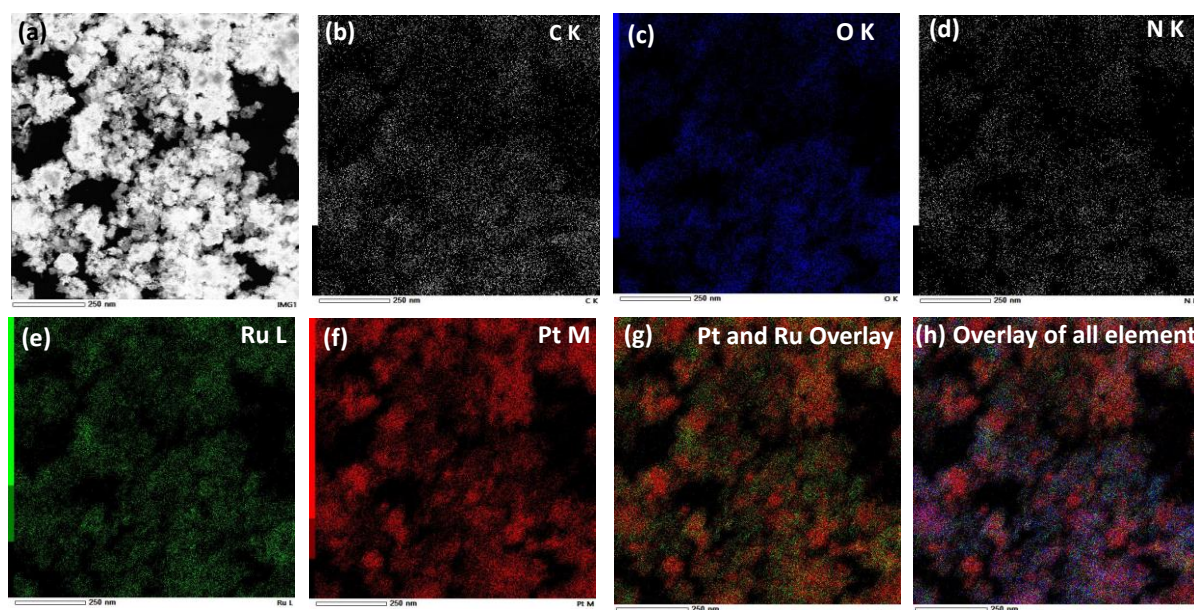
Figure 3.2. (a) STEM, (b-h) elemental mapping of RuO_2-Pt/C.

RuO₂ as promoter in Pt-RuO₂-Nanostructures/Carbon composite, a pH-universal Catalyst for Hydrogen Evolution/Oxidation Reactions

Chapter 3

HER of RuO$_2$-Pt/C in different pH electrolyte:

The electrochemical HER performances of as-synthesized RuO$_2$-Pt/C catalyst were studied in the base as well as acid medium. The linear sweep voltammogram (LSV) with 1600 rpm and a scan speed of 10 mV/sec in three-electrode systems was used. Figure 3.3a showed the comparison of HER (current vs. voltage) curves of RuO$_2$-Pt/C composite with other catalysts such as comm Pt/C, Pt-450/C, Ru-Pt-NPs/C, and Ru-450/C in 1M KOH. All the curves are iR corrected expect the tafel slope. The non iR corrected HER plots of all catalysts are also given in Figure S3.6a. As shown in Figure 3.3a and Table 3.S1, RuO$_2$-Pt/C catalyst exhibited the best HER performance among all catalysts in 1M KOH solution. The overpotential needed to reach 10 mA/cm^2 current density is only 20 mV for RuO$_2$-Pt/C whereas the over-potentials of 73 and 86 mV are required for Ru-Pt-NPs/C and comm Pt/C respectively. The HER Tafel slope can be obtained from log |j| vs. overpotential plot (Figure 3.3b). The Tafel slope values for RuO$_2$-Pt/C, comm Pt/C and Ru-Pt-NPs/C are 33.4, 100 and 45.8 mV.dec^{-1} respectively. This low value of Tafel slope compared to other catalysts suggests the very fast HER kinetic with Tafel-Volmer mechanism and desorption of hydrogen (Tafel Step) is the slow rate-determining step in alkaline solution. The fast kinetics for HER at the RuO$_2$-Pt/C electrode was also demonstrated by electrochemical impedance spectroscopy (EIS) studies. The EIS of all catalysts is compared in Figure S3.6(c, d). The R$_{ct}$ (charge-transfer resistance) value of RuO$_2$-Pt/C is 15.9 Ω which is much lower than comm Pt/C (253 Ω) and Ru-Pt-NPs/C (30 Ω). This confirmed the fast electron transfer for electrochemical reactions that is beneficial for high electrocatalytic activity.

RuO₂ as promoter in Pt-RuO₂-Nanostructures/Carbon composite, a pH-universal Catalyst for Hydrogen Evolution/Oxidation Reactions

Chapter 3
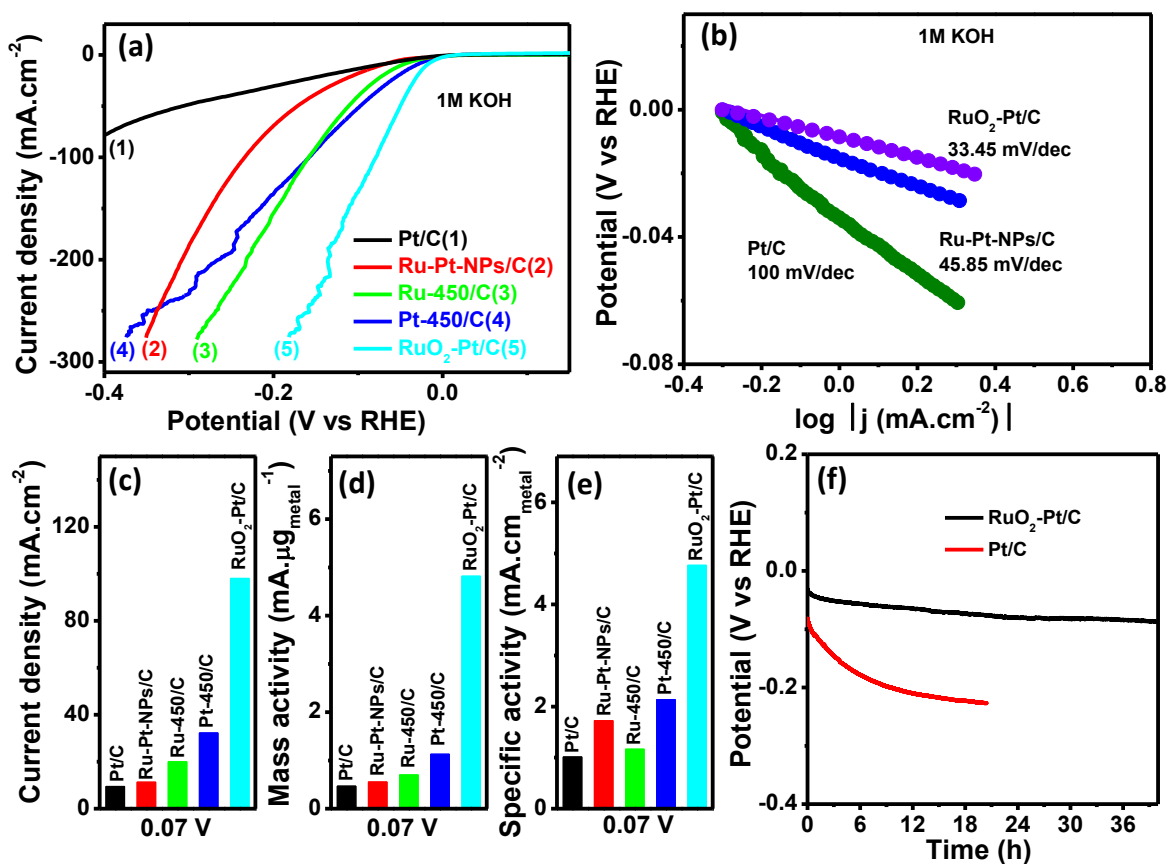
Figure 3.3. The HER polarization curves for RuO_2-Pt/C, Ru-450/C, Ru-Pt-NPs/C, Pt-450/C and commercial Pt/C in (a) 1.0M KOH, (b) Tafel plot of RuO_2-Pt/C, Ru-Pt-NPs/C and comm. Pt/C in 1.0M KOH, (c, d, e) current density, MA, SA of these catalysts at 0.07 V overpotential, (f) comparison of HER stability of RuO_2-Pt/C and comm. Pt/C catalyst in 1M KOH.

The current density (geometric), MA (mass activity), and SA (surface specific activity) of all the catalysts are compared in Figure 3.3c, 3d, and 3e respectively. The current density (J, 98.1 mA/cm^2), MA (4819 mA/mg) of RuO_2-Pt/C catalyst is 10 folds higher over comm Pt/C. The SA value for RuO_2-Pt/C and comm Pt/C are 4.77 mA/cm$^2_{PtRu}$, and 1.014 mA/cm$^2_{Pt}$ respectively. The stability test of RuO_2-Pt/C and comm. Pt/C catalysts were done by chronopotentiometric measurements at the current density of 10 mA/cm^2 (Figure 3.3f). The RuO_2-Pt/C shows almost the same potential after 40 hours of stability

RuO₂ as promoter in Pt-RuO₂-Nanostructures/Carbon composite, a pH-universal Catalyst for Hydrogen Evolution/Oxidation Reactions

Chapter 3

but, the 40% increase in overpotential was observed for comm Pt/C under the same experimental conditions suggesting excellent stability of this catalyst. The RuO_2-Pt/C showed much higher stability over commercial Pt/C. After stability, we have characterized the composite by p-XRD, TEM, SAED, and HRTEM image (Figure S3.7).
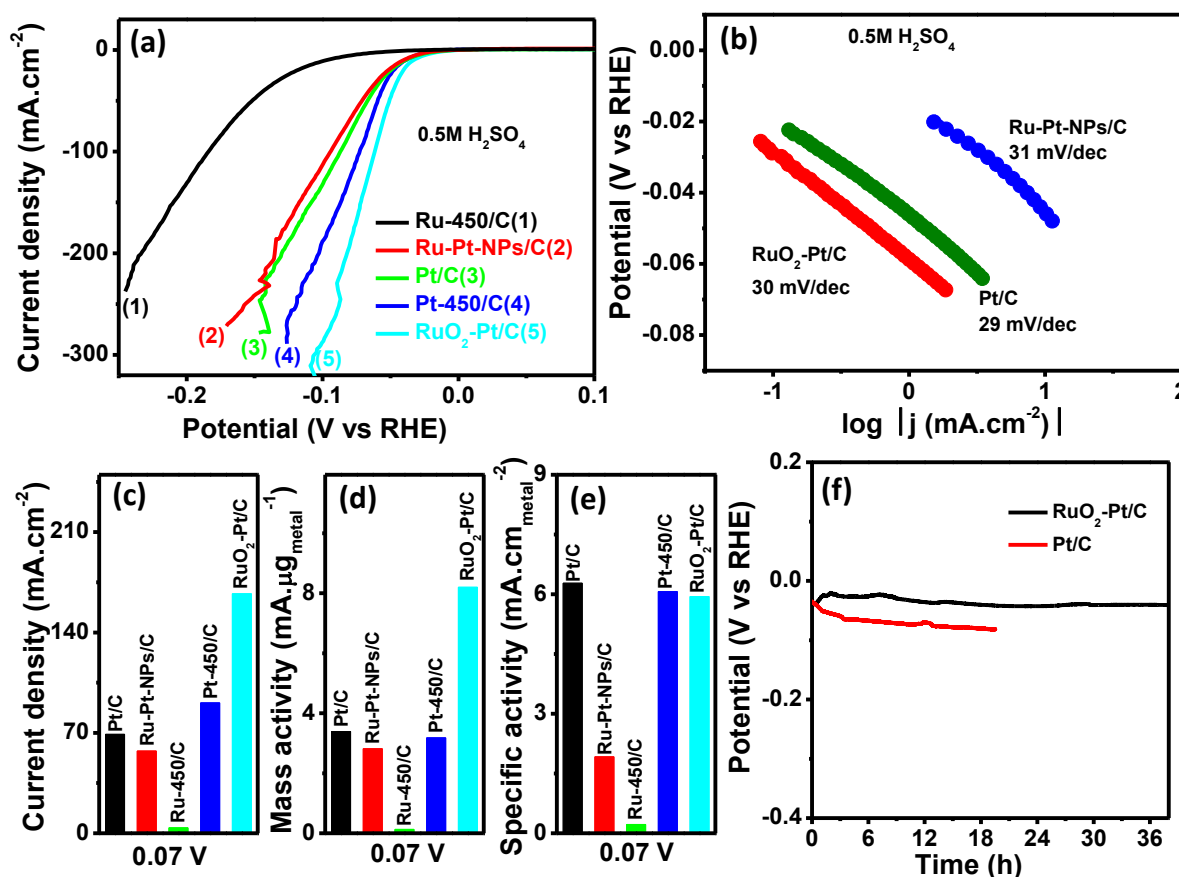
Figure 3.4. (a) The HER polarization curves of RuO_2-Pt/C, Ru-450/C, Ru-Pt-NPs/C, Pt-450/C and commercial Pt/C in 0.5M H_2SO_4, (b) Tafel plot of RuO_2-Pt/C, Ru-Pt-NPs/C and comm. Pt/C in 0.5M H_2SO_4.(c, d, e) current density, MA, SA of these catalysts at 0.07 V overpotential, (f) comparison of HER stability of RuO_2-Pt/C and comm. Pt/C catalyst in 0.5M H_2SO_4.

This shows the structure and morphology of the compound retains almost the same after the stability test. The HER activities of RuO_2-Pt/C with varying loading and varying Ru

RuO₂ as promoter in Pt-RuO₂-Nanostructures/Carbon composite, a pH-universal Catalyst for Hydrogen Evolution/Oxidation Reactions

Chapter 3

and Pt ratios are shown in Figure S3.8. The HER activity of the catalyst is also studied

in a different concentration of KOH solutions (Figure S3.9). This shows susceptibility of

HER activity towards OH^- concentration. The HER performance parameters such as

overpotential, Tafel slope value, etc. of RuO_2-Pt/C hybrid are compared with reported

noble metal-based catalysts as given in Table 3.S3. This shows, the RuO_2-Pt/C catalyst

is better or comparable to the recently reported catalysts[43-49]. The HER behavior of RuO_2-

Pt/C hybrid was also studied in acid media (Figure 3.4). The iR-corrected and non iR-

corrected HER curves of RuO_2-Pt/C, Ru-Pt-NPs/C, Ru-450/C and comm Pt/C in 0.5M

H_2SO_4 solution are presented in Figure 3.4a and S3.6b. The Tafel slope values for comm

Pt/C and RuO_2-Pt/C are 29 and 30 mV/dec respectively suggesting, the Tafel step is the

slowest (rate-determining) step (Figure 3.4b). The RuO_2-Pt/C composite showed 2.4

times better activity (HER) than comm Pt/C (Figure 3.4c-e). Although the SA value of

comm Pt/C and RuO_2-Pt/C are comparable, J (167 mA.cm^{-2}) and MA (8200 mA/mg $_{metal}$)

of RuO_2-Pt/C is 2.4 fold higher than comm. Pt/C at 0.07V. The stability of RuO_2-Pt/C

was studied by chronopotentiometric measurement at 10 mA.cm^{-2} constant current

density in 0.5M H_2SO_4. This suggested that RuO_2-Pt/C catalyst is more stable than comm

Pt/C in H_2SO_4 medium (Figure 3.4f). The comparison table of HER parameters of RuO_2-

Pt/C with other catalysts is shown in Table 3.S1 suggesting its very high activity.

pH universal HOR/HER activities of RuO₂-Pt/C catalyst:

The catalytic HOR performances of the RuO_2-Pt/C catalyst were examined by using RDE

(rotating disk electrode) method. The HOR polarization curves of RuO_2-Pt/C at different

rotations in H_2-saturated 0.1M KOH solutions is shown in Figure S3.10a. The HOR

polarization curves reach H_2 mass transport controlled limiting current densities at a

certain voltage and the limiting current densities (*j$_l$*) are gradually increased with the

RuO₂ as promoter in Pt-RuO₂-Nanostructures/Carbon composite, a pH-universal Catalyst for Hydrogen Evolution/Oxidation Reactions

Chapter 3

rotation speeds. The kinetic current density (j_k) can be executed from the Koutecky-Levich (K-L) equation (1) [32].

$$\frac{1}{j_l} = \frac{1}{j_k} + \frac{1}{j_d} = \frac{1}{j_k} + \frac{1}{BC_0\ \omega^{1/2}}$$

(1)

Where the concentration of H_2 is C_0, the rotation speed (rpm) is ω. BC_0 is a constant that relates to the diffusivity and concentration of the gas, the electrolyte kinematic viscosity, and the no. of electron transfers in the reaction. The K-L (J_l^{-1} *vs.* $\omega^{-1/2}$) plot shows a straight line that passes through the origin (Figure S3.10b). This confirmed that HOR kinetics on RuO_2-Pt/C hybrid is fully controlled by H_2 mass diffusion. The BC_0 values of RuO_2-Pt/C calculated from the plot was 0.0697 mA/(cm^2(diskrpm)$^{1/2}$) in 0.1M KOH, whereas other reported[32] value is (0.0678 mA/(cm^2(diskrpm)$^{1/2}$)). The HOR polarization curve of RuO_2-Pt/C at a rotation speed of 1600 rpm was compared with comm Pt/C, Ru-Pt-NPs/C, Pt-450/C, Ru-450/C catalysts in H_2 saturated base medium with 6 µg/cm^2 metal loading. The HOR branch follow Nernstian diffusion potential and we corrected HOR diffusion overpotential by using the following equation (2)

$$\eta_{diffusion} = -(RT/F)\ \ln(1 - j/j_l)$$

(2)

The kinetic current densities (j_k) were calculated from the HOR polarization curves of these different catalysts by using the first-order K-L correction (equation (3)). [50]

$$j_k = j(j_{lim}/(j_{lim} - j))$$

(3)

Where j and j_{lim} are the measured and diffusion limited current density (mA.cm^{-2}) respectively. Under pure diffusion condition, j_d (maximum HOR current) is related to HER/HOR diffusion overpotential as equation (4)

RuO₂ as promoter in Pt-RuO₂-Nanostructures/Carbon composite, a pH-universal Catalyst for Hydrogen Evolution/Oxidation Reactions

Chapter 3

$j_d = j \left(1 - \exp(-2F\eta/RT)\right)$ (4)

The kinetic parameters such as exchange current density (i_0) and transfer coefficient (α) of HOR/HER are generally determined from the j_k vs overpotential (η) plot. These parameters were obtained from this plot by fitting the Butler-Volmer (B-V) equation (5)

$$j_k = i_0 \left[e^{\left[\frac{\alpha F}{RT}\right]\eta} - e^{-\left[\frac{(\alpha-1)F}{RT}\right]\eta}\right]$$ (5)

Where the Faraday constant (F) is 96,485 C/mol, the universal gas constant (R) is 8.314 J.mol^{-1}.K^{-1}, and T (temperature) is in Kelvin.

The comparison of HOR/HER curves of different catalyst in H_2 saturated base media is given in Figure 3.5a. The j_k vs. potential plot and the corresponding B−V fitting of comm. Pt/C, Ru-Pt-NPs/C, Pt-450/C and RuO_2-Pt/C in 0.1M KOH solution are given in Figure 3.5b. All the fitting parameters are also given in Table 3.S2. The experimental data of RuO_2-Pt/C was fitted well by B−V fitting with $\alpha_a = 0.52$ and $\alpha_c = 0.48$ in 0.1M KOH. The calculated geometric exchange current density (i_0) of RuO_2-Pt/C obtained from B−V fitting was found to be 11 mA/cm^2 in 0.1M KOH (Table 3.S2). The geometric exchange current was then normalized by surface area (electrochemical) and mass of catalyst to obtain surface specific exchange current ($i_{0, s}$) and mass specific exchange current ($i_{0, m}$). The calculated $i_{0,m}$ and $i_{0,s}$ values for RuO_2-Pt/C in 0.1M KOH are shown in Figure 3.5c and 5d respectively. The $i_{0,m}$ and $i_{0,s}$ values for RuO_2-Pt/C in 0.1M KOH are 1833 mA/mg$_{Pt,Ru}$ and 1.8 mA/cm$^2_{Pt,Ru}$ respectively. The HOR activity of RuO_2-Pt/C was far better over Pt-based reported catalysts in base media[51-59]. For example, J. Zheng et al. [60] reported i_0 value for Pt disk electrode was 0.21 mA.cm^{-2} in 0.1M KOH. The $i_{0,m}$ value of RuO_2-Pt/C in 0.1M KOH is 29 and 8 fold higher than Ru-Pt-NPs/C and comm Pt/C respectively. We also compared the MA at 20 mV of all catalysts for HOR in 0.1M KOH solution as shown in Figure 3.5e. The HOR activity of RuO_2-Pt/C catalyst in acid and

RuO₂ as promoter in Pt-RuO₂-Nanostructures/Carbon composite, a pH-universal Catalyst for Hydrogen Evolution/Oxidation Reactions

Chapter 3

base are almost equal suggesting pH universal behavior of RuO_2-Pt/C, whereas HOR of Ru-Pt-NPs/C is significantly different in acid and base. The HOR activity of Ru-Pt-NPs/C in 0.1M KOH medium is 29 fold lower than RuO_2-Pt/C. The comparison of HOR activity parameters in base media is provided in Table 3.S4, this suggests that RuO_2-Pt/C is one of the best HOR catalysts. The HOR measurements of RuO_2-Pt/C and Ru-Pt-NPs/C were carried out in different buffer (pH) solutions to know the pH effect on HOR of the catalysts.
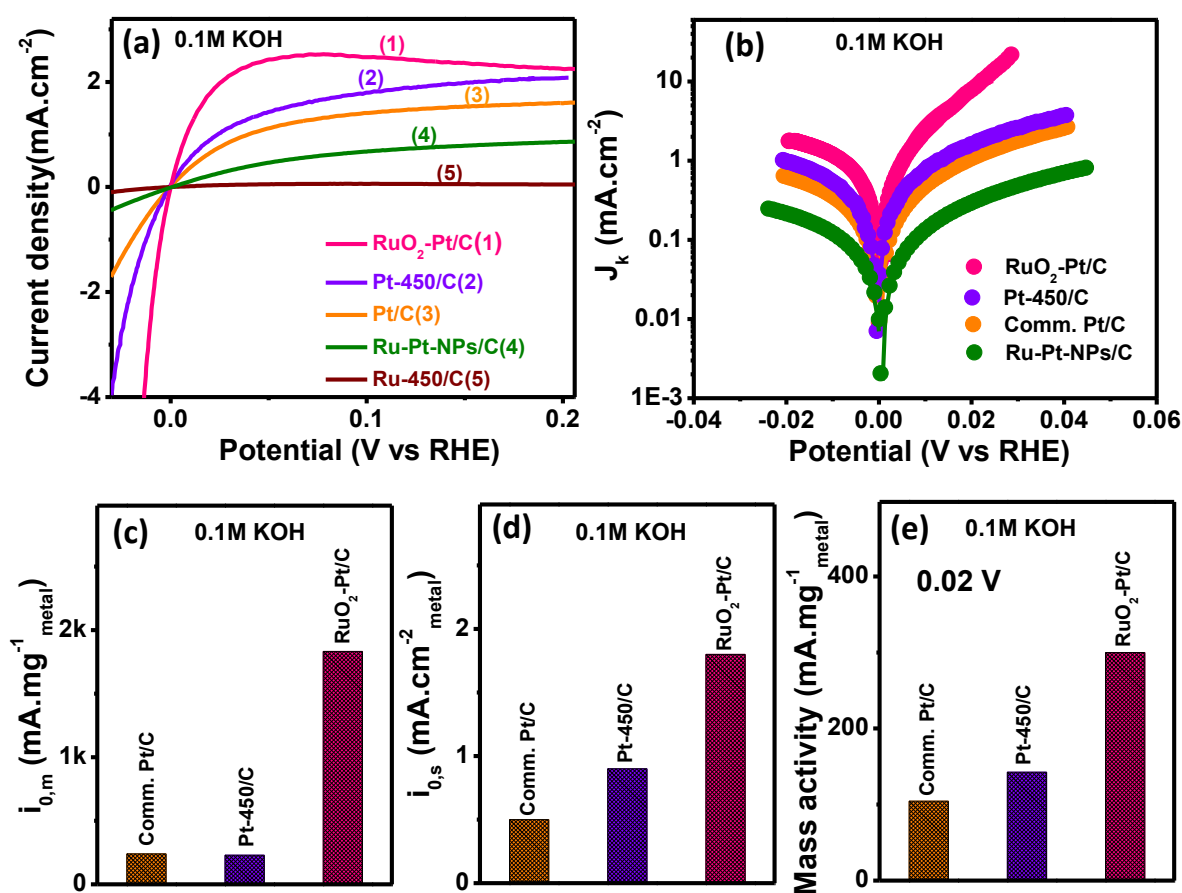
Figure 3.5. (a) HER/HOR polarization curves of RuO_2-Pt/C, Ru-450/C, Pt-450/C, Ru-Pt-NPs/C and comm. Pt/C in base. (b) The B-V fitting of all catalysts in base. The (c) $i_{0,m}$ (mA/mg$_{metal}$) (d) i_0,s (mA/cm$^2_{metal}$) (e) MA (mA/mg$_{metal}$) of all the catalysts.

RuO₂ as promoter in Pt-RuO₂-Nanostructures/Carbon composite, a pH-universal Catalyst for Hydrogen Evolution/Oxidation Reactions

Chapter 3

The HOR plots of RuO_2-Pt/C and Ru-Pt-NPs/C in different pH solutions at 1600 rpm rotation speed are given in Figure S3.11(a, b). Figure 3.6a and 3.6b show the normalized HOR polarization curves of RuO_2-Pt/C and Ru-Pt-NPs/C for different pH solutions. The half-wave potentials ($0.5i_{lim}$) of the two catalysts at various pH are compared in Figure 3.6c whereas overpotential at $1mA/cm^2$ for HOR and also for HER of RuO_2-Pt/C and Ru-Pt-NPs/C are plotted at various pH in Figure 3.6d. Below pH 7, the HOR/HER activity of these two catalysts is close and the high overpotential for HOR/HER and high $0.5i_{lim}$ of Ru-Pt-NPs/C suggested poor HOR/HER of this catalyst in alkaline media. Both the Figures suggested that HOR activities of RuO_2-Pt/C at all pH solutions are almost equal, but HOR/HER performance of Ru-Pt-NPs/C are highly sensitive to the solution pH and activity decreases with increasing pH. The HOR of Ru-Pt-NPs/C is more pH-sensitive than RuO_2-Pt/C and their HOR performance in 0.1M KOH solution is 29 fold lower in comparison to RuO_2-Pt/C catalyst.

RuO₂ as promoter in Pt-RuO₂-Nanostructures/Carbon composite, a pH-universal Catalyst for Hydrogen Evolution/Oxidation Reactions

Chapter 3
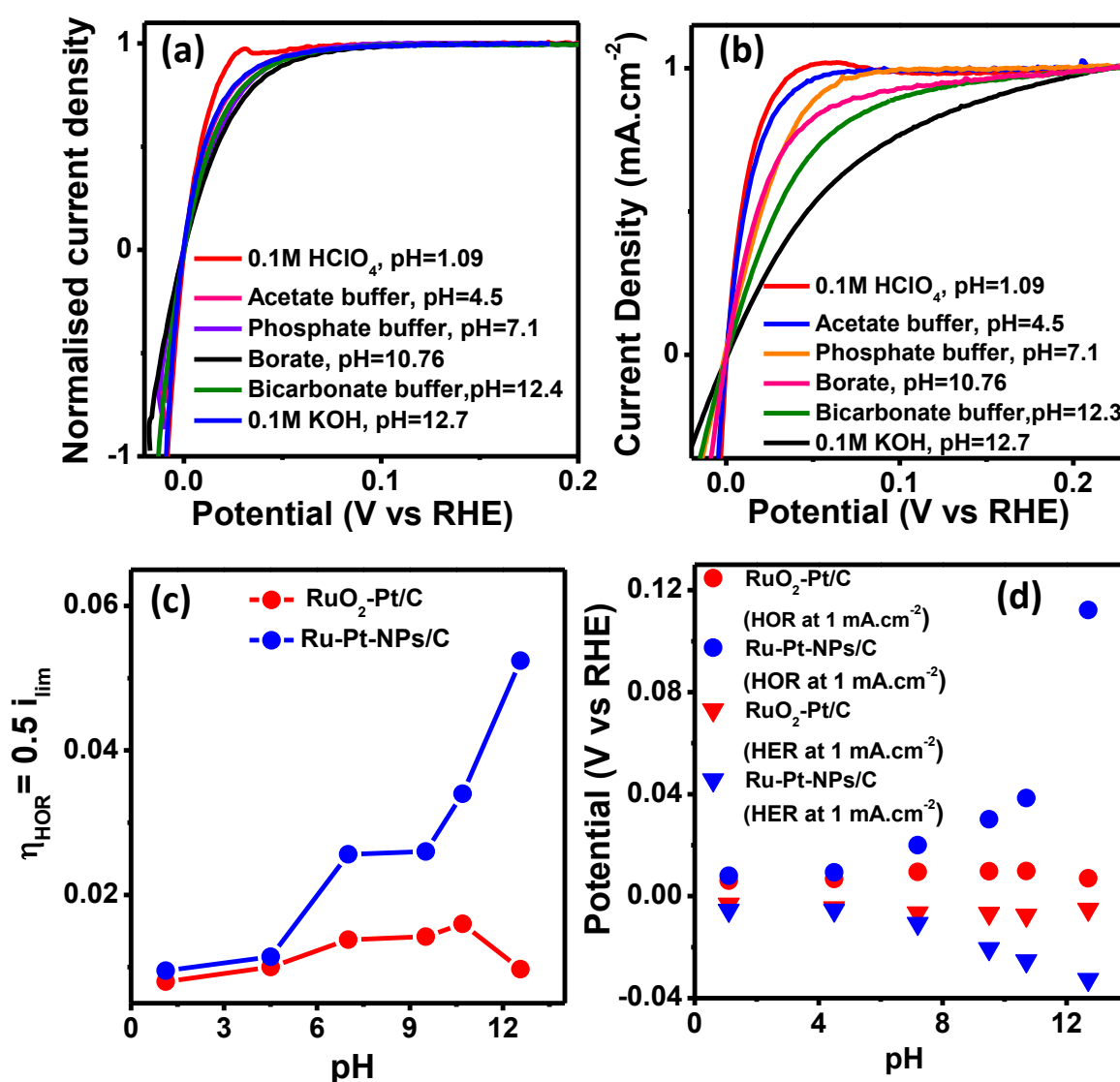
Figure 3.6. (a, b) HOR normalized curves RuO_2-Pt/C and Ru-Pt-NPs/C in different pH solutions, (c) Comarison of potential at $0.5i_{lim}$ vs. pH of RuO_2-Pt/C and Ru-Pt-NPs/C (d) Over-potential for HOR and HER current density of 1 mA/cm^2 at various solution pH for Ru-Pt-NPs/C and RuO_2-Pt/C.

RuO₂ as promoter in Pt-RuO₂-Nanostructures/Carbon composite, a pH-universal Catalyst for Hydrogen Evolution/Oxidation Reactions

Chapter 3

We examined the CV and CO striping experiments for RuO_2-Pt/C and Ru-Pt-NPs/C at various buffer (pH) solutions to know HOR mechanism in base. The CVs of RuO_2-Pt/C and Ru-Pt-NPs/C in different buffer (pH 1-13) solutions are presented in Figure 3.7a and 3.7b. The two H_{UPD} peaks corresponding to Pt(100) and Pt(110) for RuO_2-Pt/C and one H_{UPD} peak for Pt(110) of Ru-Pt-NPs/C are observed at all pH values. The position of H_{UPD} peaks (E_{peak}) for both composites moves to positive potentials with increasing solution pH. The HBE is related to E_{peak} of Pt catalyst as $\Delta H = -FE_{peak}$.
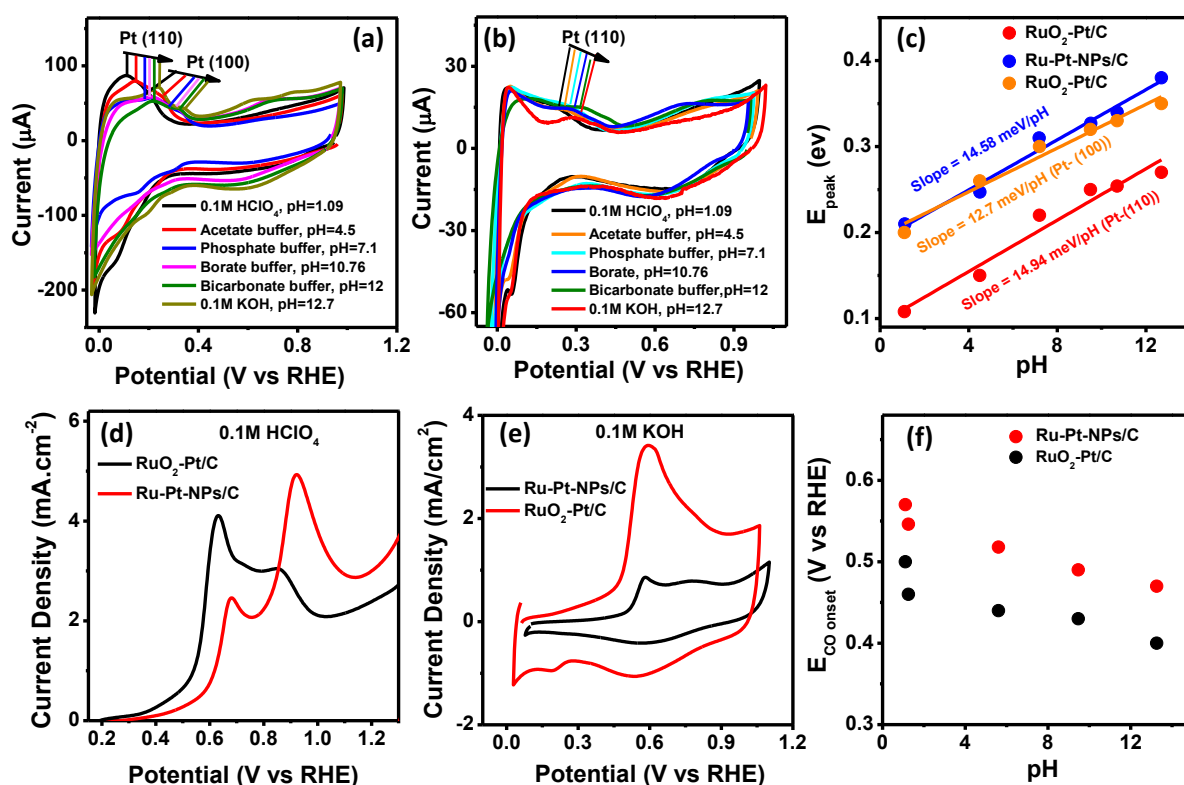
Figure 3.7. (a, b) CVs at different pH solutions of RuO_2-Pt/C and Ru-Pt-NPs/C, (c) E_{peak} (H_{UPD}) vs. pH plot (d, e) CO onset comparison of RuO_2-Pt/C and Ru-Pt-NPs/C in 0.1M $HClO_4$ and 0.1M KOH and (f) E_{CO} vs. pH plot for Ru-Pt-NPs/C and RuO_2-Pt/C.

The E_{peak} for Ru-Pt-NPs/C and RuO_2-Pt/C were shifted linearly with a slope of 14.58 meV/pH and 14.94 meV/pH respectively (Figure 3.7c). Although the HBE of both catalysts increase linearly, their HOR behaviors in different pH solutions are different.

RuO₂ as promoter in Pt-RuO₂-Nanostructures/Carbon composite, a pH-universal Catalyst for Hydrogen Evolution/Oxidation Reactions

Chapter 3

RuO_2-Pt/C showed pH tolerant HOR behavior whereas Ru-Pt-NPs/C showed poor HOR activity in base (about 30 times lower HOR activity in base than acid). The HOR of RuO_2-Pt/C in acid and base are almost equal whereas HOR of Ru-Pt-NPs/C in base is much lower than its acid media HOR activity. In addition, HOR of RuO_2-Pt/C in base is 29 times higher than Ru-Pt-NPs/C although their activities are almost the same in acid. This pH-independent HOR of RuO_2-Pt/C and pH-sensitive HOR behavior of Ru-Pt-NPs/C, can't be explained only with HBE. The CO stripping plots for RuO_2-Pt/C and Ru-Pt-NPs/C with a variation of pH is given in Figure S3.12 and S3.13. The CO stripping onset comparison of these two catalysts in 0.1M $HClO_4$ and 0.1M KOH solution is shown in Figure 3.7d and 3.7e and corresponding CO-onset potentials of these solutions are shown in Figure 3.7f respectively. The CO stripping curves reflect the potentials for adsorption of OH on the catalyst. This showed that adsorption of OH^- on both composites is increased with increasing solution pH. The RuO_2-Pt/C is more oxophilic than Ru-Pt-NPs/C. Thus, the presence of RuO_2 in RuO_2-Pt/C created more oxophilic (interfaces of between RuO_2/Pt) sites for OH adsorption. Adsorption of OH^- increases with increasing the pH. The improved HOR of RuO_2-Pt/C in comparison to Ru-Pt-NPs/C can be due to very high OH adsorption of RuO_2-Pt/C suggesting that OH_{ads} is another important intermediate for HOR in alkaline solution. The OH adsorption and HBE both are equally important for alkaline HOR/HER. We can explain enhanced HOR of RuO_2-Pt/C in base by bi-functionality [27]. The RuO_2 creates oxophilic sites for OH^- adsorption in RuO_2-Pt/C while Pt and the interfaces may act as H adsorption (Pt-H_{ad}) site. The molecular H_2 dissociates at Pt sites to form Pt-H_{ad} intermediate. In the interfaces, OH adsorption takes place to form (Pt/RuO_2)-OH_{ad}. Finally, H_{ad} and OH_{ad}, two intermediates combine to produce H_2O. Like HOR, the HER performance of the RuO_2-Pt/C hybrid is also enhanced by RuO_2 through the bi-functional mechanism. The RuO_2-Pt/C is 10 fold

RuO₂ as promoter in Pt-RuO₂-Nanostructures/Carbon composite, a pH-universal Catalyst for Hydrogen Evolution/Oxidation Reactions

Chapter 3

higher HER active than the Ru-Pt-NPs/C catalyst in alkaline solution. The HER/HOR of RuO_2-Pt/C catalyst in KOH, NaOH, and LiOH electrolyte solutions were studied. The HOR/HER polarization curves of the RuO_2-Pt/C hybrid in various alkali metal electrolyte are given in Figure 3.8(a, b). The HOR as well as HER are altered with different electrolyte although the concentrations of OH^- ions are same in all these solutions. Several groups reported the H_{UPD} peaks or H desorption peak of Pt catalyst are shifted toward negative potential in different electrolyte solutions[41, 61]. We have also performed CV measurements of RuO_2-Pt/C electrode in the three different electrolyte solutions (Figure 3.8c). The E_{peak} (H_{UPD}) peak of the catalyst is moved to positive potential when 0.1M LiOH solution is changed to either 0.1M NaOH or KOH electrolyte. This observed change of potential is due to the non-covalent interaction of hydrated alkali metal (AM^+) ions with adsorbed OH (OH_{ad}). We propose that the OH_{ad} and AM^+ are attached to form $[(H_2O)_x$-AM^+-$OH_{ad}]$ species and there is an indication of adsorption of AM^+ on either RuO_2 or Pt site. Hence we can write the Volmer step as (1) $[AM^+$-$(H_2O)_x]$ + H_2O ↔ $[OH_{ad}$-AM^+-$(H_2O)_x]$ + H_{ad} and (2) $[OH_{ad}$-AM^+-$(H_2O)_x]$ + e^- ↔ $[OH^-$-AM^+-$(H_2O)_x]$. The OH_{ad} and the OH^- are Lewis soft and hard base, whereas AM^+ is a hard acid. The hard−soft-acid−base (HSAB) theory [62] suggested that the binding between AM^+ and OH^- is strong and binding between AM^+ and OH_{ad} is weak. The interaction energy between OH_{ad} and $[(H_2O)_x$-$AM^+]$ in $[(H_2O)_x$-AM^+-$OH_{ad}]$ are decreased and interaction between $[(H_2O)_x$-$AM^+]$ and OH^- is increased in $[(H_2O)_x$-AM^+-$OH^-]$ in the sequence of $K^+ < Na^+ < Li^+$ because the hardness of AM^+ decreases in this $Li^+ > Na^+ > K^+$ sequence. Therefore, the interaction energy difference between $[(H_2O)_x$-AM^+-$OH^-]$ and $[(H_2O)_x$-AM^+-$OH_{ad}]$ becomes smaller in the sequence of $Li^+ > Na^+ > K^+$. The tendency for desorption of OH_{ad} species is increased in this $K^+ < Na^+ < Li^+$ order.

RuO₂ as promoter in Pt-RuO₂-Nanostructures/Carbon composite, a pH-universal Catalyst for Hydrogen Evolution/Oxidation Reactions

Chapter 3
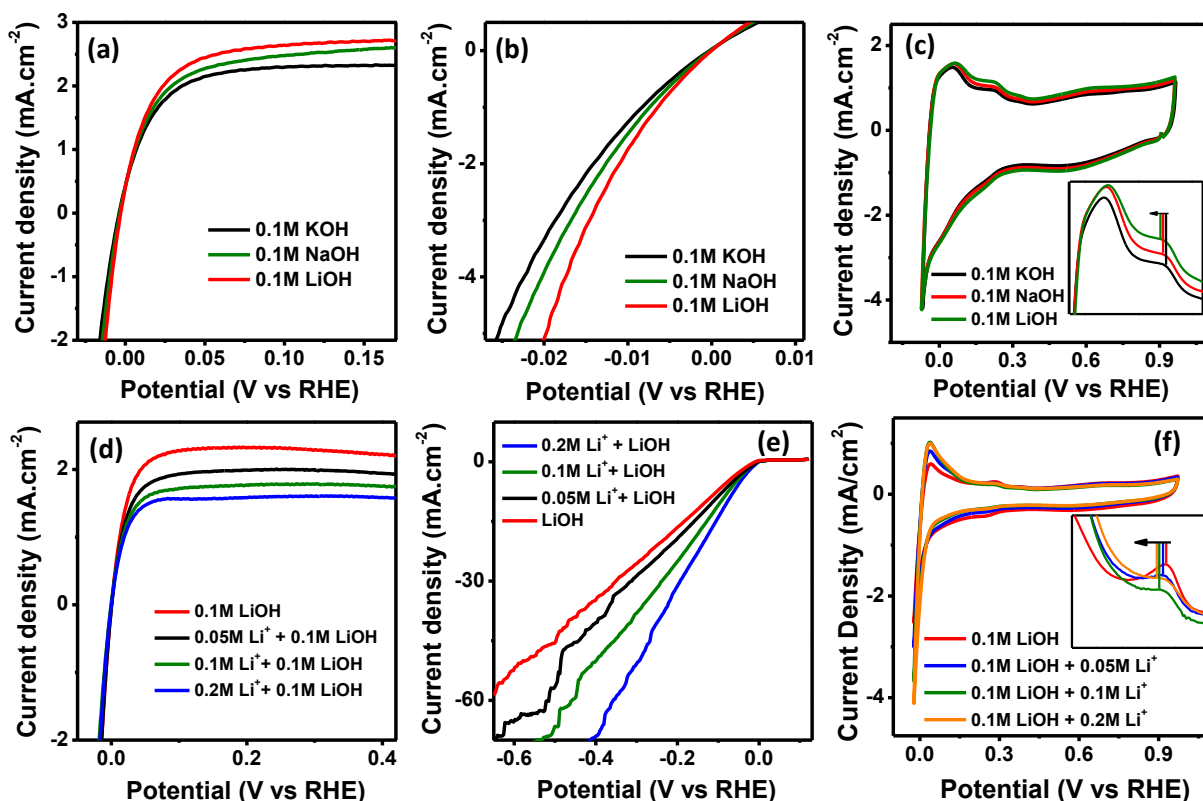
Figure 3.8. (a) HOR, (b) HER curves (c) CVs (inset: UPD-H region) of RuO_2-Pt/C in 0.1M LiOH, NaOH and KOH solutions. (d) HOR, (e) HER (f) CVs (inset: UPD-H region) of RuO_2-Pt/C in LiOH containing different amount of Li^+ ions.

Thus, the HER of RuO_2-Pt/C hybrid is increased in the sequence of KOH<NaOH<LiOH, (Figure 3.8b). The improved HER property of RuO_2-Pt/C in alkaline solution is probably due to the existence of $[(H_2O)_x\text{-}AM^+\text{-}OH_{ad}]$ species in the electrochemical double layer region. This indicated that the HER activity enhancement can be achieved with an increasing number of $[(H_2O)_x\text{-}AM^+\text{-}OH_{ad}]$ and this is possible by increasing either AM^+ ions /OH_{ad} or AM^+ ions and OH_{ad} both. The high HER of RuO_2-Pt/C composite relative to Ru-Pt-NPs/C catalyst can be explained based on the existence of more number of OH_{ad} species in the electrode surface and $[(H_2O)_x\text{-}AM^+\text{-}OH_{ad}]$ in the double layer region. The HER/HOR activity of RuO_2-Pt/C in an electrolyte solution containing different Li^+ ions concentrations was also examined. The HER of this RuO_2-Pt/C hybrid improved when

RuO₂ as promoter in Pt-RuO₂-Nanostructures/Carbon composite, a pH-universal Catalyst for Hydrogen Evolution/Oxidation Reactions

Chapter 3

the concentration of Li^+ ions was increased. The amount of $[(H_2O)_x\text{-}AM^+\text{-}OH_{ad}]$ in the electrochemical double layer increased with Li^+ ions concentration. Thus, the number of modified $(RuO_2/Pt)\text{-}OH_{ad}$ bonds increased which enhances HER activity of RuO_2-Pt/C due to the presence of more Li^+ ions in the solution. The HOR behaviour of the RuO_2-Pt/C composite is also strongly influenced when different concentrations of Li^+ ions are present. The HOR and HER curves of RuO_2-Pt/C in 0.1M LiOH containing different Li^+ ions concentrations are given in Figure 3.8d and 3.8e respectively. The HOR limiting current density of RuO_2-Pt/C catalyst decreased when the amount of Li^+ ions in solution increased. This indicates HOR performance of this composite is diminished due to the presence of Li^+ ions. As shown in Figure 3.8a, the HOR performance of RuO_2-Pt/C is increased in the sequence of KOH< NaOH< LiOH. We can explain this behaviour based on 2B theory. The HOR/HER mechanism on RuO_2-Pt/C electrode in alkaline solution involving $[(H_2O)_x\text{-}AM^+\text{-}OH_{ad}]$ species is provided in Figure 3.9.
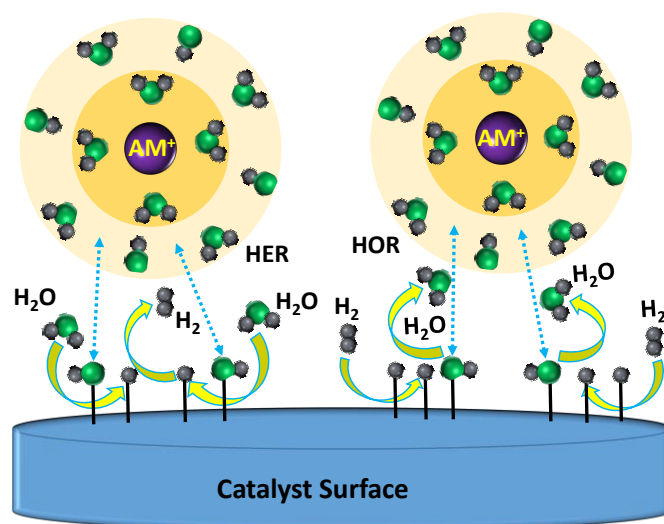
Figure 3.9. HER and HOR mechanism of RuO_2-Pt/C for alkaline medium.

RuO₂ as promoter in Pt-RuO₂-Nanostructures/Carbon composite, a pH-universal Catalyst for Hydrogen Evolution/Oxidation Reactions

Chapter 3

The $[(H_2O)_x$-AM^+-$OH_{ad}]$ species in the double layer region modifies the property of OH_{ad} and the (Pt/RuO_2)-OH_{ad} binding energy is changed by AM^+ ions as $[(H_2O)_x$-AM^+-$OH_{ad}]$ species formed. The AM^+ ions help desorption of OH_{ad} into the bulk; AM^+ ions cause the weakening of (Pt/RuO_2)-OH_{ad} bond as per HSAB theory. The weakening effect of (Pt/RuO_2)-OH_{ad} bond by K^+ ions is highest, whereas this weakening effect in Li^+ ions solution is small. The higher HOR activity of RuO_2-Pt/C in LiOH solution in comparison to KOH solution is now explained. The CO-stripping experiments in the different electrolyte are shown in Figure S3.14 (a-c). The CO stripping onset potential is shifted toward a negative direction when 0.1M KOH solution is replaced with 0.1M LiOH electrolyte. This indicated that desorption of OH_{ad} was affected by AM^+ ions. It was reported[63] that HOR performance of Pt/C catalyst was declined when Li^+ ions concentration was increased whereas the HOR remained same for the bimetallic catalyst of Pt and another oxophilic metal such as Ir, Ni, Ru. The H_{ad} and OH_{ad}, both the intermediates compete for the same catalytic site in Pt/C. Reduction of HOR performance of Pt/C with the increment of Li^+ ions was reported.
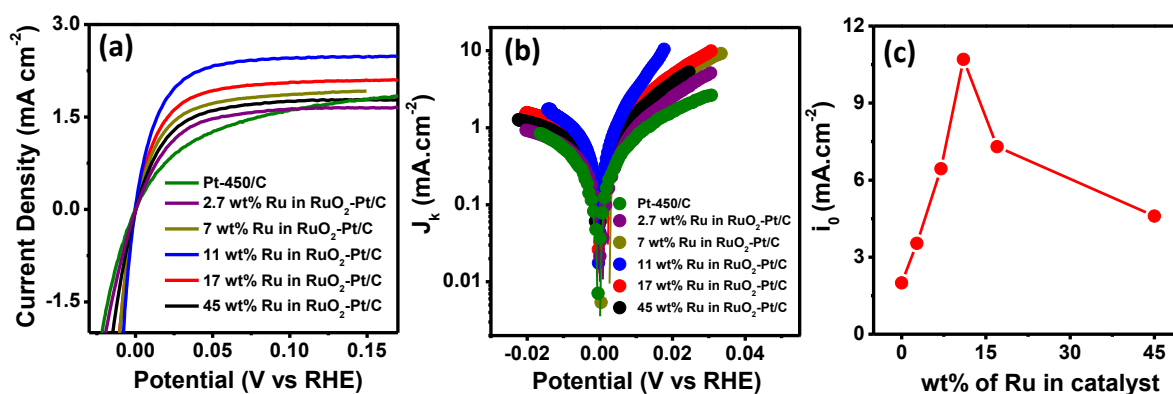
Figure 3.10. (a) HOR plots of RuO_2-Pt/C with different wt% of Ru, and (b) their corresponding Butler-Volmer, (c) i_0 (mA/cm^2) vs. wt% of Ru in RuO_2-Pt/C in 0.1M KOH.

RuO₂ as promoter in Pt-RuO₂-Nanostructures/Carbon composite, a pH-universal Catalyst for Hydrogen Evolution/Oxidation Reactions

Chapter 3

But in the case of bimetallic Pt-catalysts, OH_{ad} and H_{ad} adsorb on oxophilic metal and Pt metal sites respectively, thus HOR performance remained unaltered in different Li^+ ions concentrations. The H_{UPD} peak intensity of RuO_2-Pt/C in LiOH solution with increasing Li^+ ions does not decrease (Figure 3.8f) indicating that adsorption of Li^+ ions is not taking place on electrode surface. We observed that HOR of RuO_2-Pt/C is reduced when Li^+ ions are increased in the solution. The interfaces between Pt/RuO_2 are active sites for the intermediates (OH_{ad} and H_{ad}), thus OH_{ad} and H_{ad} generally compete for these active sites (interface of RuO_2/Pt) in RuO_2-Pt/C. The CO onset potential of CO stripping curves with increasing concentration of Li^+ ions is shifted towards the positive side indicating that Li^+ ions make destabilization of the OH_{ad}. The OH^- adsorption in RuO_2-Pt/C was delayed due to the weakening of the (Pt-RuO_2)-OH_{ad} bond, induced by AM^+ ions. This hinders the removal of H_{ad} and HOR performance of RuO_2-Pt/C thus decreases. We also measured the HOR of RuO_2-Pt/C hybrid with different amounts of Ru loading (Figure 3.10a) and their corresponding butler-volmer plots were given in Figure 3.10b. The HOR performance of RuO_2-Pt/C is enhanced when Ru wt% in RuO_2-Pt/C is increased and the HOR activity is highest when Ru loading in RuO_2-Pt/C is 11wt%. A small amount of RuO_2 enhances the electrochemical HOR/HER activity of RuO_2-Pt/C dramatically. The RuO_2 acts as a promoter in RuO_2-Pt/C for HOR/HER in alkaline electrolytes. The exchange current density (i_0) is plotted against wt% of Ru in the catalyst in Figure 3.10c. We have also done H_{UPD} (CV) and CO stripping experiments of RuO_2-Pt/C in alkaline media (Figure 3.11(a, b)). E_{peak} (UPD-H), and E_{onset} (CO) is plotted against wt% of Ru in the catalyst in Figure 3.11 (c, d) respectively. This suggests the catalytic activity of RuO_2-Pt/C is increased up to a certain Ru loading in the catalyst, after that it decreases gradually.

RuO₂ as promoter in Pt-RuO₂-Nanostructures/Carbon composite, a pH-universal Catalyst for Hydrogen Evolution/Oxidation Reactions

Chapter 3
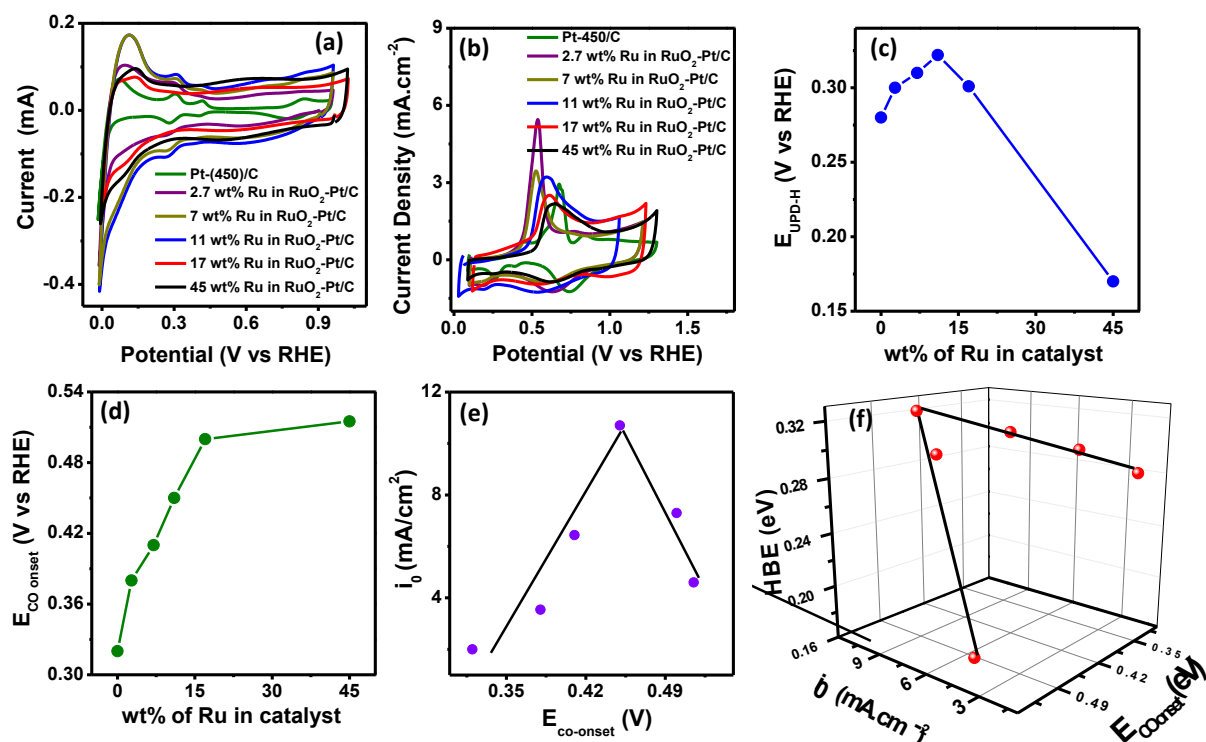
Figure 3.11. (a, b) CVs and CO-stripping voltammogram of RuO_2-Pt/C with different wt% of Ru HOR, (c)) E_{peak} (UPD-H) vs. wt% of Ru in RuO_2-Pt/C, (d) CO onset potential vs. wt% of Ru in RuO_2-Pt/C, (e) i_0 (mA/cm²) vs. CO onset potential of RuO_2-Pt/C, (f) i_0 (mA/cm²) vs. E_{peak} (UPD-H) or CO onset potential of RuO_2-Pt/C.

The i_0 vs. $E_{onset,}$ and i_0 vs. E_{peak} or E_{onset} plot is volcanic type as shown in Figure 3.11 (e, f) suggesting that OH_{ad} and H_{ad} are two main descriptors for alkaline HOR. The optimal HBE and OHBE are probably the main characteristic of a good electrocatalyst for alkaline HOR/HER. The RuO_2 in RuO_2-Pt/C helps to form more Pt/RuO_2-OH_{ad} intermediates and the Pt/RuO_2-OH_{ad} bonding is altered by [OH_{ad}–AM^+-$(H_2O)_x$] species leading increase of HOR/HER in alkaline media. The RuO_2-Pt/C catalyst is a three-component composite where every component has different roles: Pt metal offers the catalytic sites for H_{ad} intermediate and RuO_2 created catalytic sites for OH_{ad} intermediate and carbon layer is a conducting support. The strong synergistic interactions among three components in RuO_2-Pt/C could be one of the reasons for its superior electrochemical

RuO₂ as promoter in Pt-RuO₂-Nanostructures/Carbon composite, a pH-universal Catalyst for Hydrogen Evolution/Oxidation Reactions

Chapter 3

activity. We have done electrochemical EIS measurements of different catalysts. The EIS Nyquist plot of RuO_2-Pt/C, Physical mixture, Pt-450/C, and Ru-450/C was shown in Figure 3.12a. The charge transfer resistance (R_{ct}) of RuO_2-Pt/C, Pt-450/C, Ru-450/C, and their physical mixture are 15.9, 31.4, 311, and 889 Ω respectively. The R_{ct} value of RuO_2-Pt/C is much lower than that of either Pt-RuO_2 or carbon support. This indicated that strong interaction between three components (catalyst-support) exists in RuO_2-Pt/C catalyst.
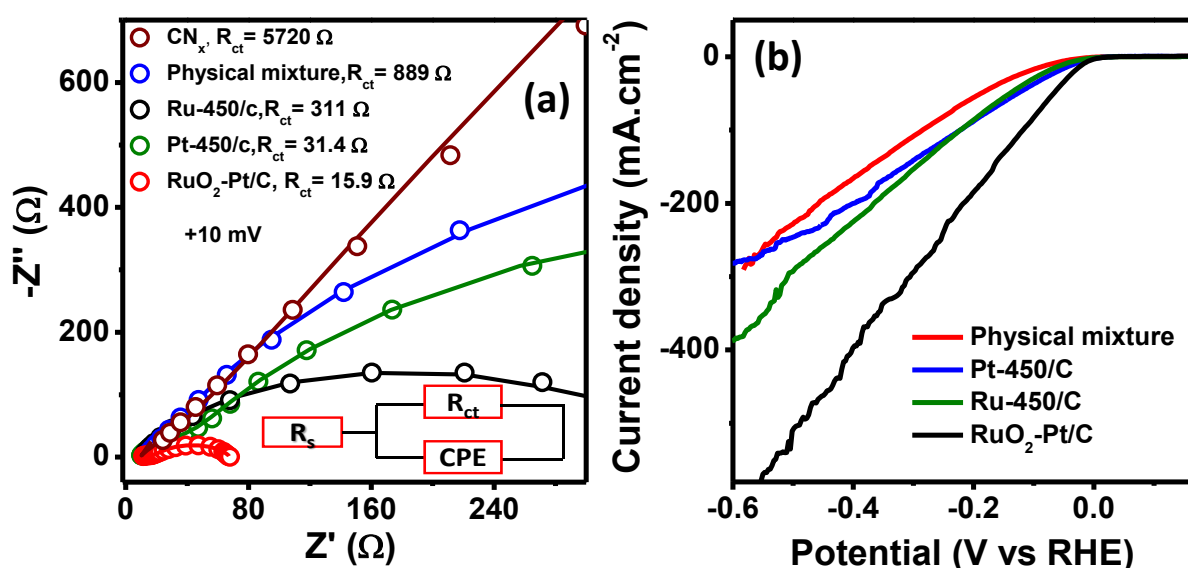
Figure 3.12. (a) Nyquist plots of RuO_2-Pt/C, Pt-450/C, Ru-450/C, Physical mixture and CNx, (b) their HER comparison plots.

This synergistic interaction was again proved by electrochemical HER studies of these three compounds (Figure 3.12b) showing that HER activity of RuO_2-Pt/C is much better in comparison to Pt-450/C, Ru-450/C, or their physical mixture. The high ESCA of RuO_2-Pt/C could also be another reason for the high electrochemical activity of the catalyst. The ESCA values of RuO_2-Pt/C are 138 and 101 m²/g in acid and base respectively, these values are much higher than that of commercial Pt/C. The high surface of this catalyst is probably originated from the presence of plenty of interfaces

RuO₂ as promoter in Pt-RuO₂-Nanostructures/Carbon composite, a pH-universal Catalyst for Hydrogen Evolution/Oxidation Reactions

Chapter 3

and its porous morphology. The TEM images showed that RuO_2-Pt/C composite is composed of plenty of interfaces and defects which generally act as active sites for catalytic reactions. There is also some nitrogen atom present in this RuO_2-Pt/C composite and the interaction between N atoms and proton helps to improve charge transfer kinetics leading to the improvement of catalytic activity.

3.5 CONCLUSIONS:

In summary, we demonstrated a two-step method for the synthesis of interface engineered RuO_2-Pt/C hybrid. This RuO_2-Pt/C showed one order magnitude higher alkaline HER/HOR activity compared to comm Pt/C. The HER/HOR activity of RuO_2-Pt/C in acid is also higher than comm Pt/C. We demonstrated that RuO_2 acts as a promoter in RuO_2-Pt/C for HOR/HER. The RuO_2 offers stronger OH^- adsorption and $[(H_2O)_x\text{-}AM^+\text{-}OH_{ad}]$ in the double layer region that plays a significant role in the dramatic enhancement of alkaline HER/HOR through the bi-functional mechanism. The oxophilicity (i.e. OHBE) and HBE are descriptors for alkaline HER/HOR. We also demonstrate that the very high electrochemical behavior is due to the interface engineering, synergistic effect, and porous structure of the catalyst. The excellent HER/HOR performance and stability of RuO_2-Pt/C is making this catalyst a future active catalyst for renewable energy technologies.

RuO₂ as promoter in Pt-RuO₂-Nanostructures/Carbon composite, a pH-universal Catalyst for Hydrogen Evolution/Oxidation Reactions

Chapter 3

3.6 REFERENCES:

(1) Cabán-Acevedo, M.; Stone, M. L.; Schmidt, J. R.; Thomas, J. G.; Ding, Q.; Chang, H.-C.; Tsai, M.-L.; He, J.-H.; Jin, S. Efficient hydrogen evolution catalysis using ternary pyrite-type cobalt phosphosulphide. *Nature Materials* **2015**, *14* (12), 1245-1251.

(2) Cobo, S.; Heidkamp, J.; Jacques, P. A.; Fize, J.; Fourmond, V.; Guetaz, L.; Jousselme, B.; Ivanova, V.; Dau, H.; Palacin, S.; et al. A Janus cobalt-based catalytic material for electro-splitting of water. *Nat Mater* **2012**, *11* (9), 802-807.

(3) Zhu, J.; Hu, L.; Zhao, P.; Lee, L. Y. S.; Wong, K.-Y. Recent Advances in Electrocatalytic Hydrogen Evolution Using Nanoparticles. *Chemical Reviews* **2020**, *120* (2), 851-918.

(4) Dresselhaus, M. S.; Thomas, I. L. Alternative energy technologies. *Nature* **2001**, *414* (6861), 332-337.

(5) Zou, X.; Zhang, Y. Noble metal-free hydrogen evolution catalysts for water splitting. *Chemical Society Reviews* **2015**, *44* (15), 5148-5180.

(6) Davydova, E. S.; Mukerjee, S.; Jaouen, F.; Dekel, D. R. Electrocatalysts for Hydrogen Oxidation Reaction in Alkaline Electrolytes. *ACS Catalysis* **2018**, *8* (7), 6665-6690.

(7) Ramaswamy, N.; Mukerjee, S. Alkaline Anion-Exchange Membrane Fuel Cells: Challenges in Electrocatalysis and Interfacial Charge Transfer. *Chemical Reviews* **2019**, *119* (23), 11945-11979.

(8) Winter, M.; Brodd, R. J. What Are Batteries, Fuel Cells, and Supercapacitors? *Chemical Reviews* **2004**, *104* (10), 4245-4270.

(9) Benck, J. D.; Hellstern, T. R.; Kibsgaard, J.; Chakthranont, P.; Jaramillo, T. F. Catalyzing the Hydrogen Evolution Reaction (HER) with Molybdenum Sulfide Nanomaterials. *ACS Catalysis* **2014**, *4* (11), 3957-3971.

(10) Fei, H.; Dong, J.; Arellano-Jiménez, M. J.; Ye, G.; Dong Kim, N.; Samuel, E. L. G.; Peng, Z.; Zhu, Z.; Qin, F.; Bao, J.; et al. Atomic cobalt on nitrogen-doped graphene for hydrogen generation. *Nature Communications* **2015**, *6* (1), 8668.

RuO₂ as promoter in Pt-RuO₂-Nanostructures/Carbon composite, a pH-universal Catalyst for Hydrogen Evolution/Oxidation Reactions

Chapter 3

(11) Cong, Y.; Yi, B.; Song, Y. Hydrogen oxidation reaction in alkaline media: From mechanism to recent electrocatalysts. *Nano Energy* **2018**, *44*, 288-303.

(12) Omasta, T. J.; Park, A. M.; LaManna, J. M.; Zhang, Y.; Peng, X.; Wang, L.; Jacobson, D. L.; Varcoe, J. R.; Hussey, D. S.; Pivovar, B. S.; et al. Beyond catalysis and membranes: visualizing and solving the challenge of electrode water accumulation and flooding in AEMFCs. *Energy & Environmental Science* **2018**, *11* (3), 551-558.

(13) Seh, Z. W.; Kibsgaard, J.; Dickens, C. F.; Chorkendorff, I.; Nørskov, J. K.; Jaramillo, T. F. Combining theory and experiment in electrocatalysis: Insights into materials design. *Science (New York, N.Y.)* **2017**, *355* (6321).

(14) Gasteiger, H. A.; Marković, N. M. Chemistry. Just a dream--or future reality? *Science (New York, N.Y.)* **2009**, *324* (5923), 48-49.

(15) Park, S.-K.; Chung, D. Y.; Ko, D.; Sung, Y.-E.; Piao, Y. Three-dimensional carbon foam/N-doped graphene@MoS2 hybrid nanostructures as effective electrocatalysts for the hydrogen evolution reaction. *Journal of Materials Chemistry A* **2016**, *4* (33), 12720-12725.

(16) Ma, Z.; Chen, C.; Cui, X.; Zeng, L.; Wang, L.; Jiang, W.; Shi, J. Hydrogen Evolution/Oxidation Electrocatalysts by the Self-Activation of Amorphous Platinum. *ACS Applied Materials & Interfaces* **2021**, *13* (37), 44224-44233.

(17) Esposito, D. V.; Hunt, S. T.; Stottlemyer, A. L.; Dobson, K. D.; McCandless, B. E.; Birkmire, R. W.; Chen, J. G. Low-cost hydrogen-evolution catalysts based on monolayer platinum on tungsten monocarbide substrates. *Angewandte Chemie* **2010**, *49* (51), 9859-9862.

(18) Cheng, Y.; Lu, S.; Liao, F.; Liu, L.; Li, Y.; Shao, M. Rh☐MoS2 Nanocomposite Catalysts with Pt-Like Activity for Hydrogen Evolution Reaction. *Advanced Functional Materials* **2017**, *27* (23), 1700359.

(19) Zhang, G.; Xu, Y.; Wang, L.; Wang, J.; Kuang, Y.; Sun, X. Rational design of graphene oxide and its hollow CoO composite for superior oxygen reduction reaction. *Science China Materials* **2015**, *58* (7), 534-542.

RuO₂ as promoter in Pt-RuO₂-Nanostructures/Carbon composite, a pH-universal Catalyst for Hydrogen Evolution/Oxidation Reactions

Chapter 3

(20) Lee, G.; Kang, G.-S.; Jang, J.-H.; Yoo, S. J.; Joh, H.-I.; Lee, S. Upcycling waste tires to affordable catalysts for the oxygen reduction reaction. *International Journal of Energy Research* **2021**, 46(4):4645-4654.

(21) Kim, J.; Yin, X.; Tsao, K.-C.; Fang, S.; Yang, H. Ca2Mn2O5 as Oxygen-Deficient Perovskite Electrocatalyst for Oxygen Evolution Reaction. *Journal of the American Chemical Society* **2014**, *136* (42), 14646-14649.

(22) Hu, J.; Li, S.; Chu, J.; Niu, S.; Wang, J.; Du, Y.; Li, Z.; Han, X.; Xu, P. Understanding the Phase-Induced Electrocatalytic Oxygen Evolution Reaction Activity on FeOOH Nanostructures. *ACS Catalysis* **2019**, *9* (12), 10705-10711.

(23) Deokate, R. J.; Chavan, H. S.; Bulakhe, S. C.; Tanwade, S. B.; Mujawar, S. H.; Mali, S. S.; Hong, C. K.; Im, H.; Inamdar, A. I. Electrodeposited bimetallic microporous MnCu oxide electrode as a highly stable electrocatalyst for oxygen evolution reaction. *International Journal of Energy Research* **2021**, 46(4):5269-5279.

(24) Kim, Y.; Karuppannan, M.; Lee, D.; Bae, H. E.; Luong, Q. T.; Kang, S. Y.; Sung, Y.-E.; Cho, Y.-H.; Kwon, O. J. (Fe, Ni, Co)9S8@CS catalyst decorated on N-doped carbon as an efficient electrocatalyst for oxygen evolution reaction. *International Journal of Energy Research* **2021**, *n/a* (n/a).

(25) Raja Sulaiman, R. R.; Wong, W. Y.; Loh, K. S. Recent developments on transition metal–based electrocatalysts for application in anion exchange membrane water electrolysis. *International Journal of Energy Research* **2021**, *n/a* (n/a).

(26) Jiao, L.; Liu, E.; Hwang, S.; Mukerjee, S.; Jia, Q. Compressive Strain Reduces the Hydrogen Evolution and Oxidation Reaction Activity of Platinum in Alkaline Solution. *ACS Catalysis* **2021**, *11* (13), 8165-8173.

(27) Danilovic, N.; Subbaraman, R.; Strmcnik, D.; Chang, K.-C.; Paulikas, A. P.; Stamenkovic, V. R.; Markovic, N. M. Enhancing the Alkaline Hydrogen Evolution Reaction Activity through the Bifunctionality of Ni(OH)2/Metal Catalysts. *Angewandte Chemie International Edition* **2012**, *51* (50), 12495-12498.

RuO₂ as promoter in Pt-RuO₂-Nanostructures/Carbon composite, a pH-universal Catalyst for Hydrogen Evolution/Oxidation Reactions

Chapter 3

(28) Durst, J.; Siebel, A.; Simon, C.; Hasché, F.; Herranz, J.; Gasteiger, H. A. New insights into the electrochemical hydrogen oxidation and evolution reaction mechanism. *Energy & Environmental Science* **2014**, *7* (7), 2255-2260.

(29) Zheng, J.; Zhuang, Z.; Xu, B.; Yan, Y. Correlating Hydrogen Oxidation/Evolution Reaction Activity with the Minority Weak Hydrogen-Binding Sites on Ir/C Catalysts. *ACS Catalysis* **2015**, *5* (7), 4449-4455.

(30) Zheng, J.; Sheng, W.; Zhuang, Z.; Xu, B.; Yan, Y. Universal dependence of hydrogen oxidation and evolution reaction activity of platinum-group metals on pH and hydrogen binding energy. *Science advances* **2016**, *2* (3), e1501602.

(31) Wang, Y.; Wang, G.; Li, G.; Huang, B.; Pan, J.; Liu, Q.; Han, J.; Xiao, L.; Lu, J.; Zhuang, L. Pt–Ru catalyzed hydrogen oxidation in alkaline media: oxophilic effect or electronic effect? *Energy & Environmental Science* **2015**, *8* (1), 177-181.

(32) Sheng, W.; Zhuang, Z.; Gao, M.; Zheng, J.; Chen, J. G.; Yan, Y. Correlating hydrogen oxidation and evolution activity on platinum at different pH with measured hydrogen binding energy. *Nature Communications* **2015**, *6* (1), 5848.

(33) Bhowmik, T.; Kundu, M. K.; Barman, S. Palladium Nanoparticle–Graphitic Carbon Nitride Porous Synergistic Catalyst for Hydrogen Evolution/Oxidation Reactions over a Broad Range of pH and Correlation of Its Catalytic Activity with Measured Hydrogen Binding Energy. *ACS Catalysis* **2016**, *6* (3), 1929-1941.

(34) Li, J.; Ghoshal, S.; Bates, M. K.; Miller, T. E.; Davies, V.; Stavitski, E.; Attenkofer, K.; Mukerjee, S.; Ma, Z.-F.; Jia, Q. Experimental Proof of the Bifunctional Mechanism for the Hydrogen Oxidation in Alkaline Media. *Angewandte Chemie International Edition* **2017**, *56* (49), 15594-15598.

(35) Strmcnik, D.; Uchimura, M.; Wang, C.; Subbaraman, R.; Danilovic, N.; van der Vliet, D.; Paulikas, A. P.; Stamenkovic, V. R.; Markovic, N. M. Improving the hydrogen oxidation reaction rate by promotion of hydroxyl adsorption. *Nature Chemistry* **2013**, *5* (4), 300-306.

(36) Koper, M. T. M. A basic solution. *Nature Chemistry* **2013**, *5* (4), 255-256.

RuO₂ as promoter in Pt-RuO₂-Nanostructures/Carbon composite, a pH-universal Catalyst for Hydrogen Evolution/Oxidation Reactions

Chapter 3

(37) Zhang, B.; Zhao, G.; Zhang, B.; Xia, L.; Jiang, Y.; Ma, T.; Gao, M.; Sun, W.; Pan, H. Lattice-Confined Ir Clusters on Pd Nanosheets with Charge Redistribution for the Hydrogen Oxidation Reaction under Alkaline Conditions. *Advanced Materials* **2021**, *33* (43), 2105400.

(38) Tran, D. S.; Park, H.; Kim, H.; Kim, S.-K. Electrodeposited NiRh alloy as an efficient low-precious metal catalyst for alkaline hydrogen oxidation reaction. *International Journal of Energy Research* **2021**, *45* (4), 5325-5336.

(39) Scofield, M. E.; Zhou, Y.; Yue, S.; Wang, L.; Su, D.; Tong, X.; Vukmirovic, M. B.; Adzic, R. R.; Wong, S. S. Role of Chemical Composition in the Enhanced Catalytic Activity of Pt-Based Alloyed Ultrathin Nanowires for the Hydrogen Oxidation Reaction under Alkaline Conditions. *ACS Catalysis* **2016**, *6* (6), 3895-3908.

(40) Sheng, W.; Myint, M.; Chen, J. G.; Yan, Y. Correlating the hydrogen evolution reaction activity in alkaline electrolytes with the hydrogen binding energy on monometallic surfaces. *Energy & Environmental Science* **2013**, *6* (5), 1509-1512.

(41) Chen, X.; McCrum, I. T.; Schwarz, K. A.; Janik, M. J.; Koper, M. T. M. Co-adsorption of Cations as the Cause of the Apparent pH Dependence of Hydrogen Adsorption on a Stepped Platinum Single-Crystal Electrode. **2017**, *56* (47), 15025-15029.

(42) Jia, Q.; Liu, E.; Jiao, L.; Li, J.; Mukerjee, S. Current understandings of the sluggish kinetics of the hydrogen evolution and oxidation reactions in base. *Current Opinion in Electrochemistry* **2018**, *12*, 209-217.

(43) Li, Y.; Zhang, L. A.; Qin, Y.; Chu, F.; Kong, Y.; Tao, Y.; Li, Y.; Bu, Y.; Ding, D.; Liu, M. Crystallinity Dependence of Ruthenium Nanocatalyst toward Hydrogen Evolution Reaction. *ACS Catalysis* **2018**, *8* (7), 5714-5720.

(44) Huang, J.-F.; Wu, Y.-C. Making Ag Present Pt-like Activity for Hydrogen Evolution Reaction. *ACS Sustainable Chemistry & Engineering* **2018**, *6* (7), 8285-8290.

(45) Zhang, X.; Shao, B.; Sun, Z.; Gao, Z.; Qin, Y.; Zhang, C.; Cui, F.; Yang, X. Platinum Nanoparticle-Deposited Ti3C2Tx MXene for Hydrogen Evolution Reaction. *Industrial & Engineering Chemistry Research* **2020**, *59* (5), 1822-1828.

RuO₂ as promoter in Pt-RuO₂-Nanostructures/Carbon composite, a pH-universal Catalyst for Hydrogen Evolution/Oxidation Reactions

Chapter 3

(46) Li, Y.; Guo, Y.; Yang, S.; Li, Q.; Chen, S.; Lu, B.; Zou, H.; Liu, X.; Tong, X.; Yang, H. Mesoporous RhRu Nanosponges with Enhanced Water Dissociation toward Efficient Alkaline Hydrogen Evolution. *ACS Applied Materials & Interfaces* **2021**, *13* (4), 5052-5060.

(47) Ferri, M.; Elliott, J. D.; Camellone, M. F.; Fabris, S.; Piccinin, S. CuFeO2–Water Interface under Illumination: Structural, Electronic, and Catalytic Implications for the Hydrogen Evolution Reaction. *ACS Catalysis* **2021**, *11* (4), 1897-1910.

(48) Kwon, I. S.; Kwak, I. H.; Kim, J. Y.; Debela, T. T.; Park, Y. C.; Park, J.; Kang, H. S. Concurrent Vacancy and Adatom Defects of Mo1–xNbxSe2 Alloy Nanosheets Enhance Electrochemical Performance of Hydrogen Evolution Reaction. *ACS Nano* **2021**, *15* (3), 5467-5477.

(49) Kundu, M. K.; Mishra, R.; Bhowmik, T.; Barman, S. Rhodium metal–rhodium oxide (Rh–Rh2O3) nanostructures with Pt-like or better activity towards hydrogen evolution and oxidation reactions (HER, HOR) in acid and base: correlating its HOR/HER activity with hydrogen binding energy and oxophilicity of the catalyst. *Journal of Materials Chemistry A* **2018**, *6* (46), 23531-23541.

(50) Zheng, J.; Yan, Y.; Xu, B. Correcting the Hydrogen Diffusion Limitation in Rotating Disk Electrode Measurements of Hydrogen Evolution Reaction Kinetics. *Journal of The Electrochemical Society* **2015**, *162* (14), F1470-F1481.

(51) Hamo, E. R.; Singh, R. K.; Douglin, J. C.; Chen, S.; Hassine, M. B.; Carbo-Argibay, E.; Lu, S.; Wang, H.; Ferreira, P. J.; Rosen, B. A.; et al. Carbide-Supported PtRu Catalysts for Hydrogen Oxidation Reaction in Alkaline Electrolyte. *ACS Catalysis* **2021**, *11* (2), 932-947.

(52) Zhao, T.; Wang, G.; Gong, M.; Xiao, D.; Chen, Y.; Shen, T.; Lu, Y.; Zhang, J.; Xin, H.; Li, Q.; et al. Self-Optimized Ligand Effect in L12-PtPdFe Intermetallic for Efficient and Stable Alkaline Hydrogen Oxidation Reaction. *ACS Catalysis* **2020**, *10* (24), 15207-15216.

(53) Zhao, L.; Liu, H.; Liu, Y.; Han, X.; Xu, J.; Xing, W.; Guo, W. Correction to "Mechanistic Insights into the Hydrogen Oxidation Reaction on PtNi Alloys in Alkaline Media: A First-Principles Investigation". *ACS Applied Materials & Interfaces* **2020**, *12* (45), 51133-51133.

RuO₂ as promoter in Pt-RuO₂-Nanostructures/Carbon composite, a pH-universal Catalyst for Hydrogen Evolution/Oxidation Reactions

Chapter 3

(54) Stühmeier, B. M.; Selve, S.; Patel, M. U. M.; Geppert, T. N.; Gasteiger, H. A.; El-Sayed, H. A. Highly Selective Pt/TiOx Catalysts for the Hydrogen Oxidation Reaction. *ACS Applied Energy Materials* **2019**, *2* (8), 5534-5539.

(55) Mao, J.; He, C.-T.; Pei, J.; Liu, Y.; Li, J.; Chen, W.; He, D.; Wang, D.; Li, Y. Isolated Ni Atoms Dispersed on Ru Nanosheets: High-Performance Electrocatalysts toward Hydrogen Oxidation Reaction. *Nano Letters* **2020**, *20* (5), 3442-3448.

(56) Alia, S. M.; Pivovar, B. S.; Yan, Y. Platinum-Coated Copper Nanowires with High Activity for Hydrogen Oxidation Reaction in Base. *Journal of the American Chemical Society* **2013**, *135* (36), 13473-13478.

(57) Ohyama, J.; Sato, T.; Yamamoto, Y.; Arai, S.; Satsuma, A. Size Specifically High Activity of Ru Nanoparticles for Hydrogen Oxidation Reaction in Alkaline Electrolyte. *Journal of the American Chemical Society* **2013**, *135* (21), 8016-8021.

(58) Samanta, R.; Mishra, R.; Barman, S. Interface- and Surface-Engineered PdO−RuO2 Hetero-Nanostructures with High Activity for Hydrogen Evolution/Oxidation Reactions. *ChemSusChem* **2021**, *n/a* (n/a),

(59) Zhou, Y.; Xie, Z.; Jiang, J.; Wang, J.; Song, X.; He, Q.; Ding, W.; Wei, Z. Lattice-confined Ru clusters with high CO tolerance and activity for the hydrogen oxidation reaction. *Nature Catalysis* **2020**, *3* (5), 454-462.

(60) Zheng, J.; Yan, Y. S.; Xu, B. J. Correcting the Hydrogen Diffusion Limitation in Rotating Disk Electrode Measurements of Hydrogen Evolution Reaction Kinetics. *Journal of the Electrochemical Society* **2015**, *162* (14), F1470-F1481.

(61) Weber, D. J.; Janssen, M.; Oezaslan, M. Effect of monovalent Cations on the HOR/HER activity for Pt in alkaline environment. *Journal of The Electrochemical Society* **2019**, *166* (2), F66-F73.

(62) Pearson, R. G. Hard and Soft Acids and Bases. *Journal of the American Chemical Society* **1963**, *85* (22), 3533-3539.

(63) Liu, E.; Li, J.; Jiao, L.; Doan, H. T. T.; Liu, Z.; Zhao, Z.; Huang, Y.; Abraham, K. M.; Mukerjee, S.; Jia, Q. Unifying the Hydrogen Evolution and Oxidation Reactions Kinetics in Base

RuO₂ as promoter in Pt-RuO₂-Nanostructures/Carbon composite, a pH-universal Catalyst for Hydrogen Evolution/Oxidation Reactions

Chapter 3

by Identifying the Catalytic Roles of Hydroxyl-Water-Cation Adducts. *Journal of the American Chemical Society* **2019**, *141* (7), 3232-3239.

RuO₂ as promoter in Pt-RuO₂-Nanostructures/Carbon composite, a pH-universal Catalyst for Hydrogen Evolution/Oxidation Reactions

Chapter 3

Appendix A
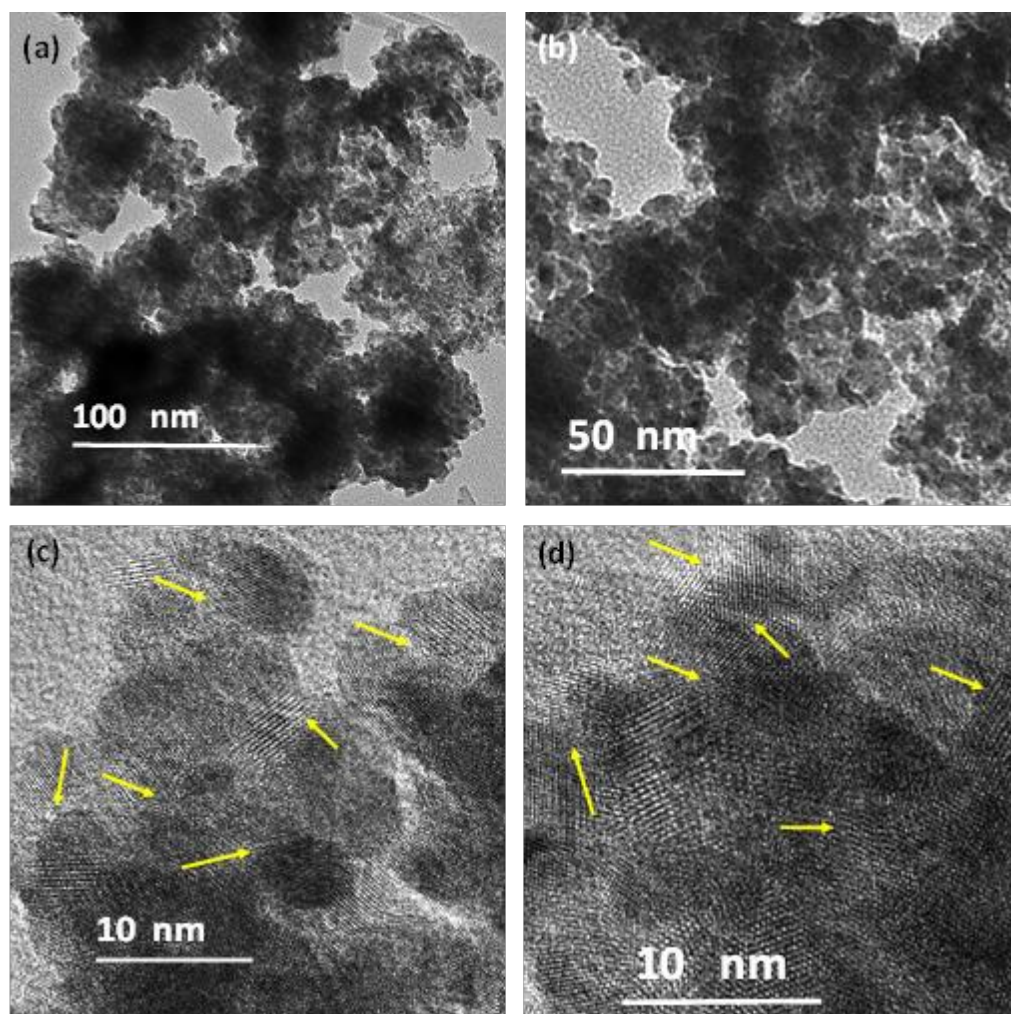
Figure S3.1. (a, b) TEM images, (c, d) HRTEM images of RuO_2-Pt/C (yellow lines show the interfaces of the composite).

RuO₂ as promoter in Pt-RuO₂-Nanostructures/Carbon composite, a pH-universal Catalyst for Hydrogen Evolution/Oxidation Reactions

Chapter 3
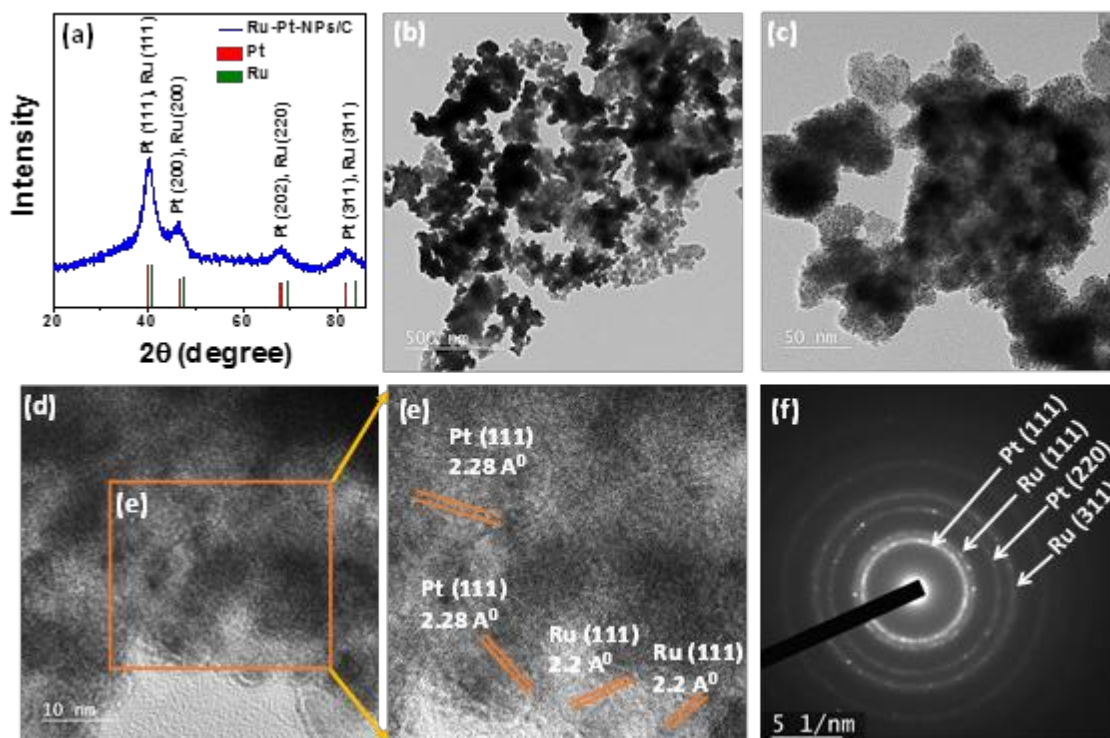
Figure S3.2. (a) p-XRD, (b, c) TEM images, (d, e) HRTEM images, (f) SAED image of Ru-PtNPs/C sample showing the presence of ultra-small Pt, Ru nanoparticles.
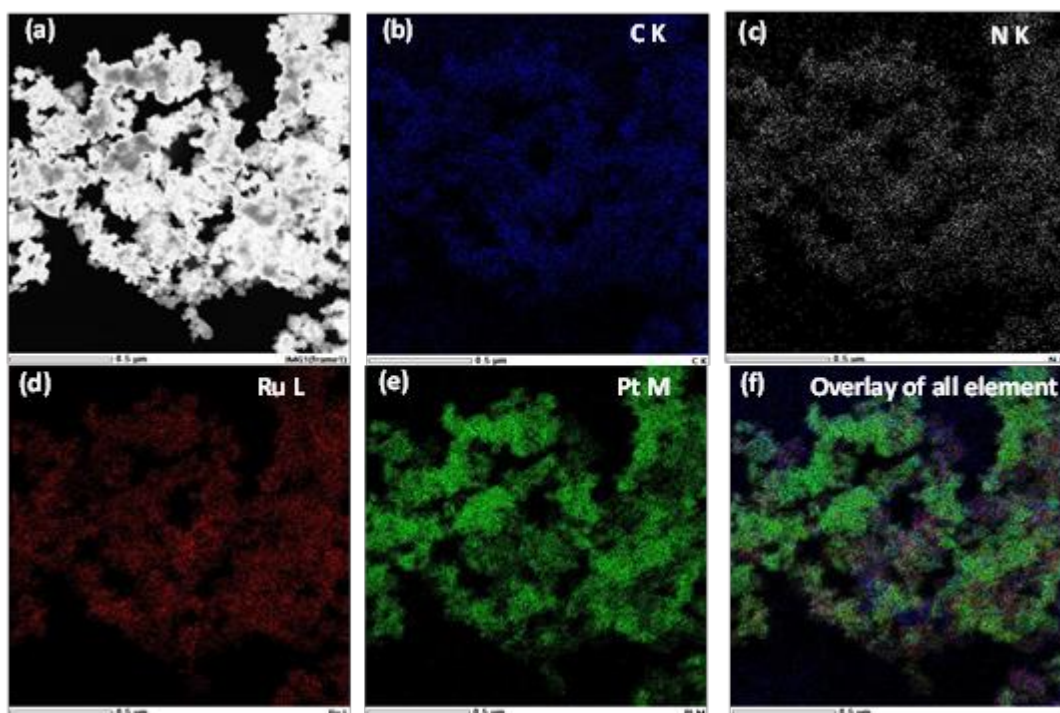
Figure S3.3. (a) STEM, (b-f) elemental mapping of Ru-Pt-NPs/C.

RuO₂ as promoter in Pt-RuO₂-Nanostructures/Carbon composite, a pH-universal Catalyst for Hydrogen Evolution/Oxidation Reactions

Chapter 3
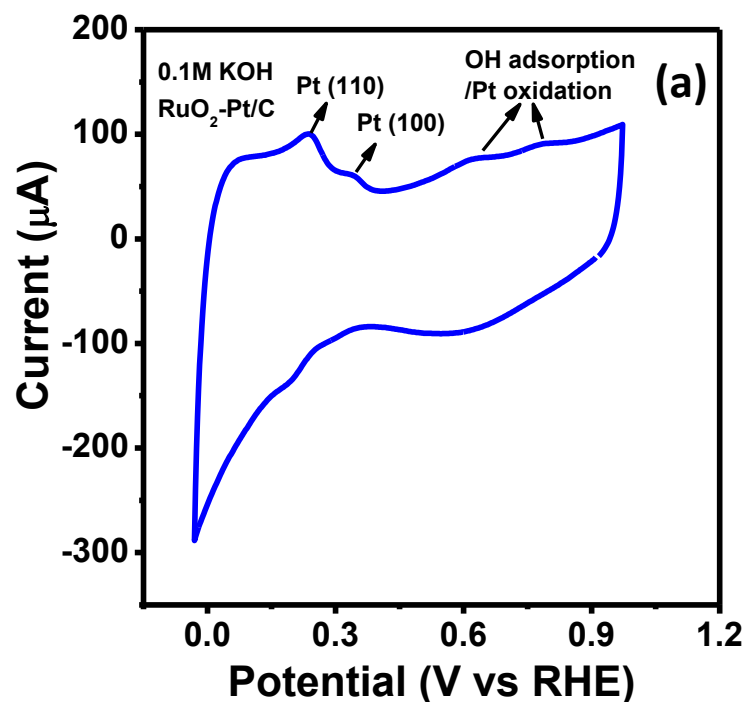
Figure S3.4. CV of RuO$_2$-Pt/C in 0.1M KOH.
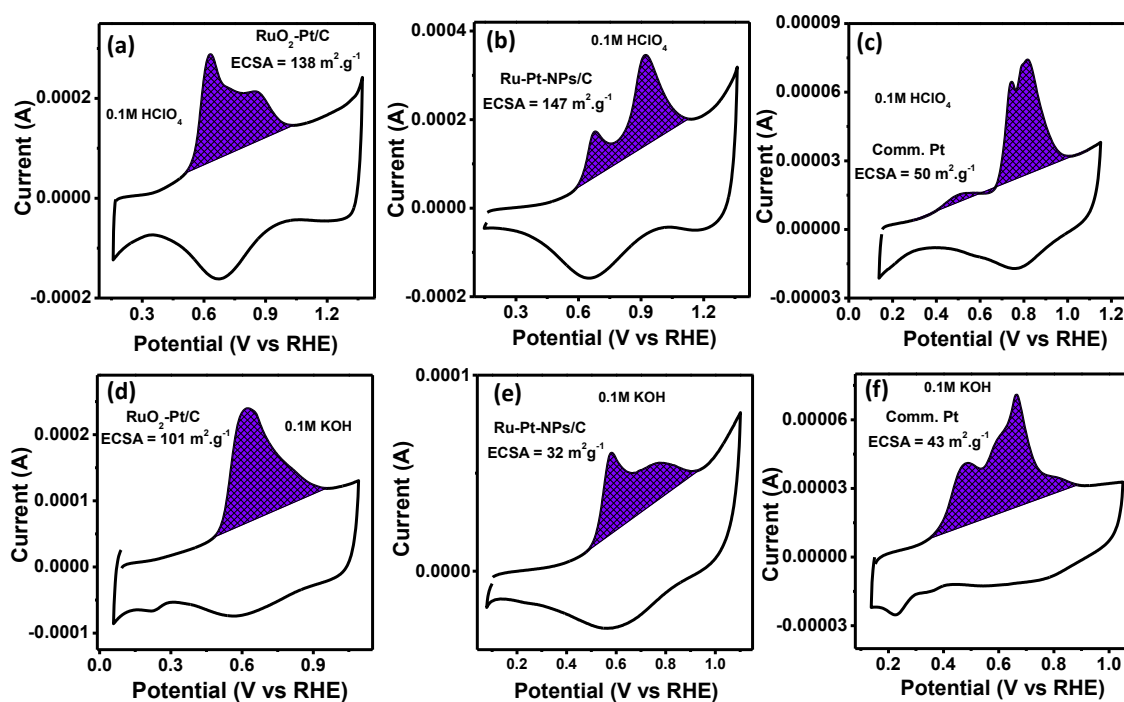
Figure S3.5. ECSA calculation from CO stripping: (a, b, c) CVs of RuO$_2$-Pt/C, Ru-Pt-NPs/C and comm. Pt/C in 0.1M HClO$_4$ and (d, e, f) CVs of RuO$_2$-Pt/C, Ru-Pt-NPs/C and comm. Pt/C in 0.1M KOH respectively.

RuO₂ as promoter in Pt-RuO₂-Nanostructures/Carbon composite, a pH-universal Catalyst for Hydrogen Evolution/Oxidation Reactions

Chapter 3
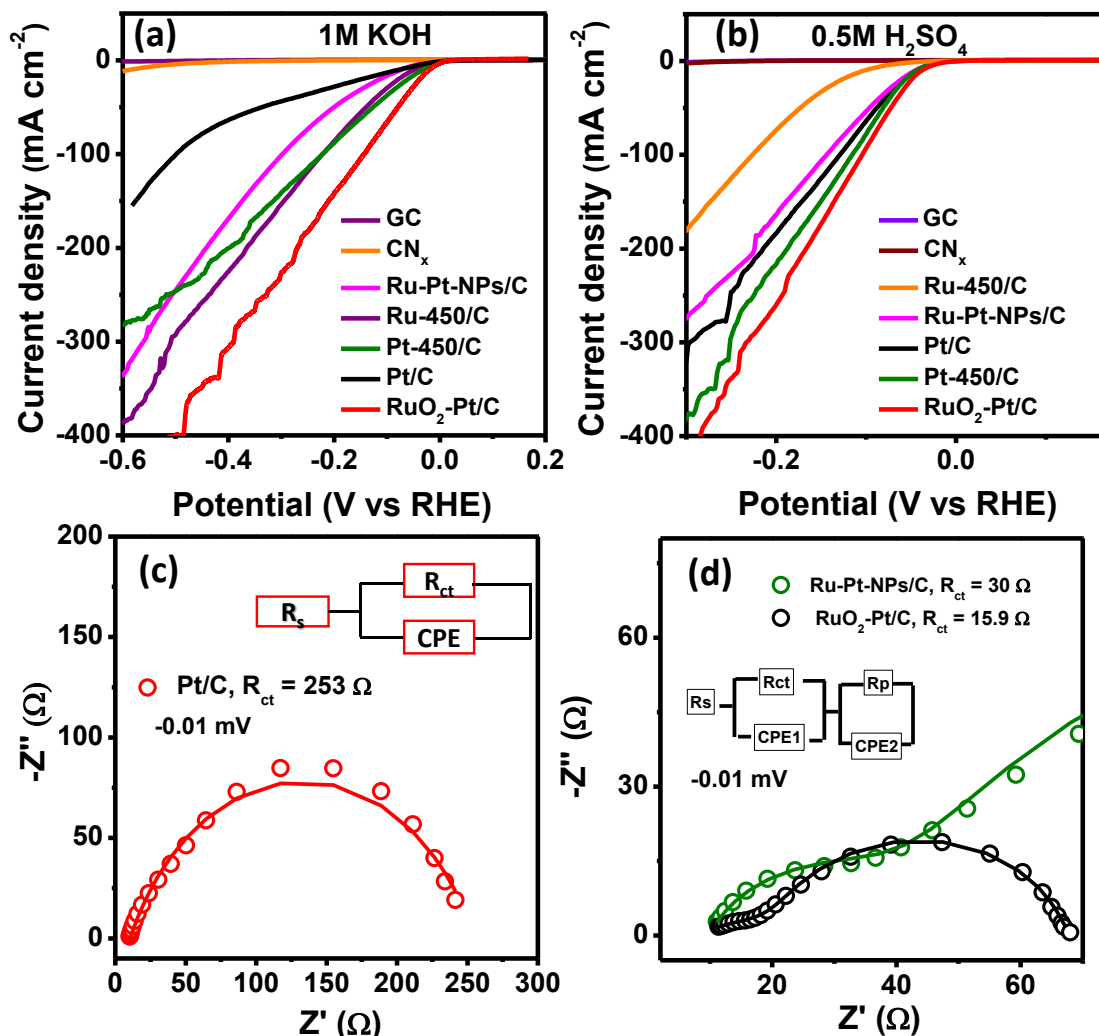
Figure S3.6. (a) Non iR corrected HER activity of RuO_2-PtC, comm. Pt/C and Ru-Pt-NPs/C and other catalyst in 1.0M KOH, (b) Non iR corrected HER activity of RuO_2-Pt/C, comm. Pt/C and Ru-Pt-NPs/C and other catalyst in 0.5M H_2SO_4, (c, d) Nyquist plots of Comm Pt/C and RuO_2-Pt/C, Ru-Pt-NPs/C at 10 mV overpotential respectively.

RuO₂ as promoter in Pt-RuO₂-Nanostructures/Carbon composite, a pH-universal Catalyst for Hydrogen Evolution/Oxidation Reactions

Chapter 3
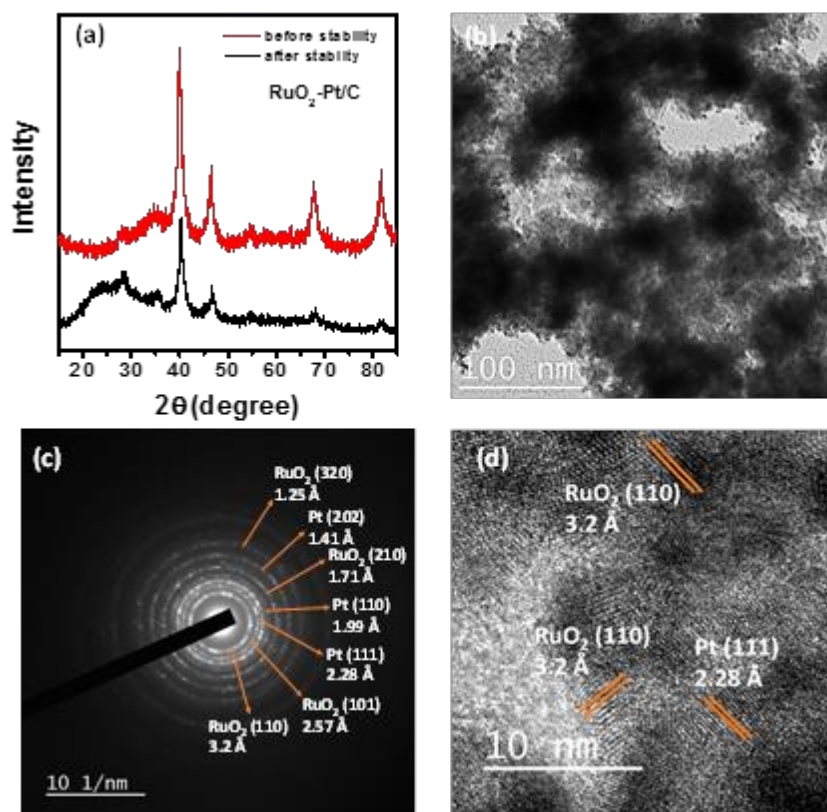
Figure S3.7. (a) p-XRD comparison of RuO_2-Pt/C after and before stability, (b) TEM image, (c) SAED image, (d) HRTEM image of RuO_2-Pt/C after stability.
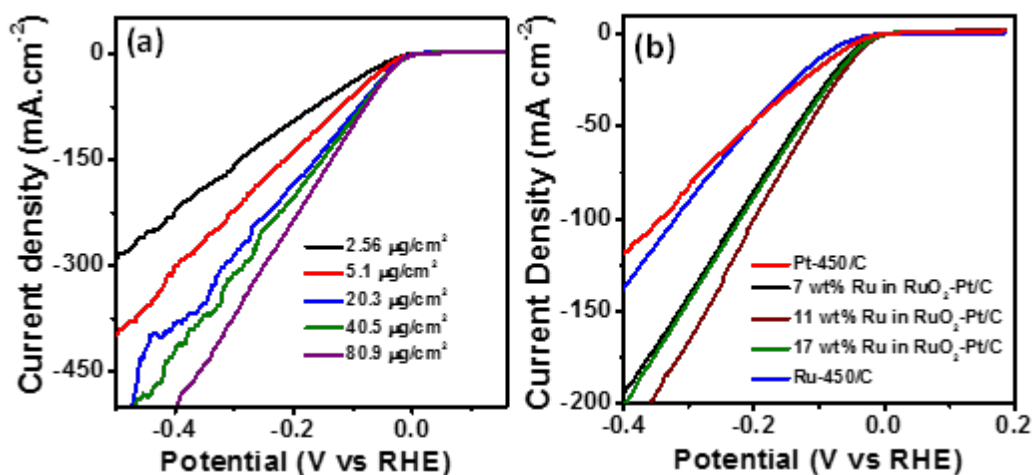
Figure S3.8. (a) HER activity of RuO_2-Pt/C with different loading, (b) HER activity of RuO_2-Pt/C with different Ru, Pt ratio.

RuO₂ as promoter in Pt-RuO₂-Nanostructures/Carbon composite, a pH-universal Catalyst for Hydrogen Evolution/Oxidation Reactions

Chapter 3

Table S3.1. Different HER parameters of RuO$_2$-Pt/C, comm. Pt/C and Ru-Pt-NPs/C catalysts in 1.0M KOH and 0.5M H$_2$SO$_4$ solutions.

Solution	Catalyst	Overpotential (mV) At (10 mA.cm^{-2})	Current density (mA.cm^{-2})	SA (mAcm$^{-2}_{Pt}$)	MA (Amg^{-1})	Tafel slope (mV/dec)
0.5M H$_2$SO$_4$	Commercial Pt/C	39	69*	6.277*	3.39*	29
	RuO$_2$-Pt/C	34	167*	5.944*	8.2*	30
	Ru-Pt-NPs/C	41	57.4*	1.918*	2.82*	31
1.0M KOH	Commercial Pt/C	86	9.5*	1.014*	0.467*	44
	RuO$_2$-Pt/C	20	98.1*	4.77*	4.819*	24
	Ru-Pt-NPs/C	73	11.29*	1.274*	0.554*	42
*at η= -0.07 V.						
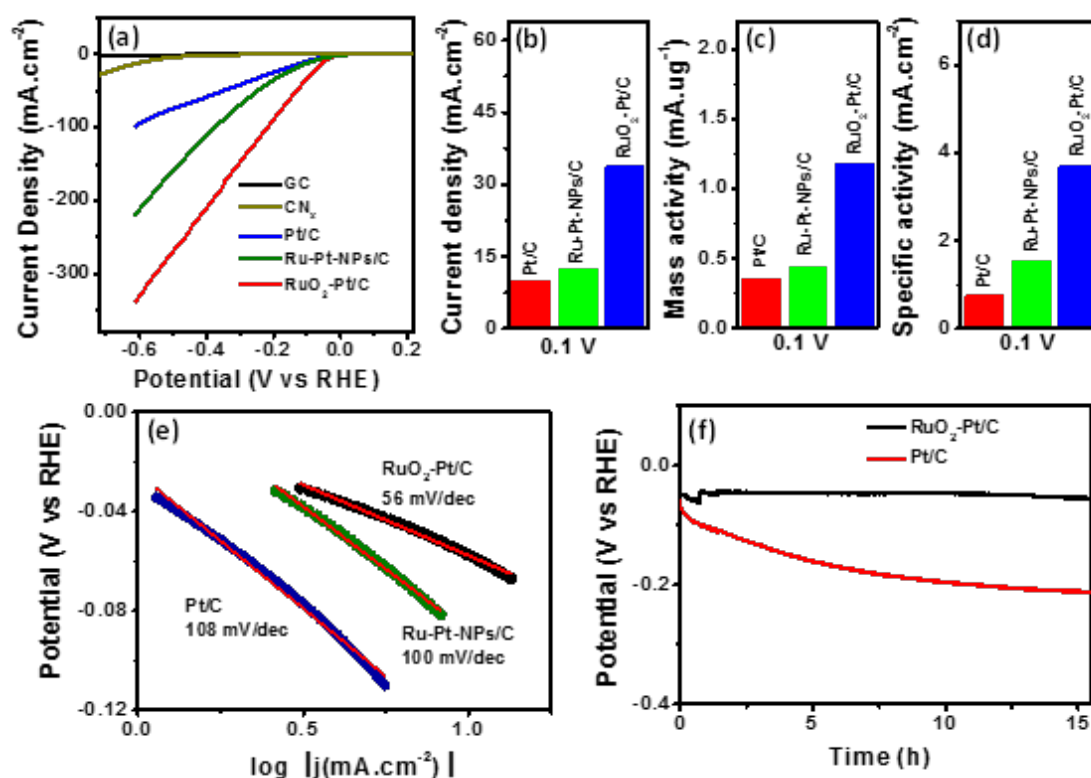
Figure S3.9. (a) HER activity of RuO$_2$-Pt/C, comm. Pt/C and Ru-Pt-NPs/C in 0.5M KOH. (b) Geometric current density (c) MA (d) SA of RuO$_2$-Pt/C, Ru-Pt-NPs/C and

RuO₂ as promoter in Pt-RuO₂-Nanostructures/Carbon composite, a pH-universal Catalyst for Hydrogen Evolution/Oxidation Reactions

Chapter 3

commercial Pt/C (e) Tafel plot of RuO_2-Pt/C, Ru-Pt-NPs/C and comm. Pt/C for 0.5M

KOH (f) Chronopotentiometric stability of RuO_2-Pt/C, commercial Pt/C at 10 $mA.cm^{-2}$.
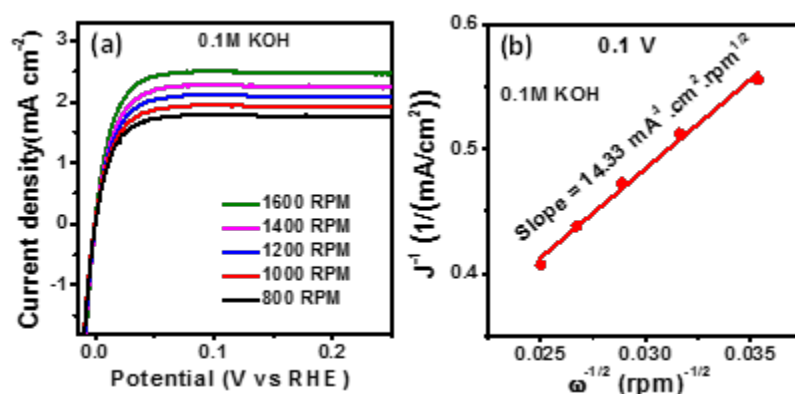
Figure S3.10. (a) HER/HOR polarization curves (going positive direction) RuO_2-Pt/C in

0.1M KOH solution saturated with H_2 (~1 atm) with different rotation speeds at a scan

rate of 10 mV/s, (b) corresponding K-L plot.

Table S3.2. Kinetic parameters of RuO_2-Pt/C, Comm. Pt/C and Ru-Pt-NPs/C catalyst

extracted from the Butler-Volmer fitting for acid and base solutions.

Compound	Solution	Exchange Current density (j_0) ($mAcm^{-2}$)	Mass Specific exchange Current ($mAmg_{Pt}^{-1}$)	Surface Specific exchange Current $i_{0,S}$ ($mAcm_{RuPt}^{-2}$)	Anodic transfer coefficient (α)	Cathodic transfer coefficient (α)
RuO_2-Pt/C	0.1M KOH	11	1833	1.8	0.52	0.48
Ru-Pt-NPs/C	0.1M KOH	0.4	63	0.06	0.5	0.5
Commercial Pt/C	0.1M KOH	1.45	230	0.5	0.52	0.48

RuO₂ as promoter in Pt-RuO₂-Nanostructures/Carbon composite, a pH-universal Catalyst for Hydrogen Evolution/Oxidation Reactions

Chapter 3
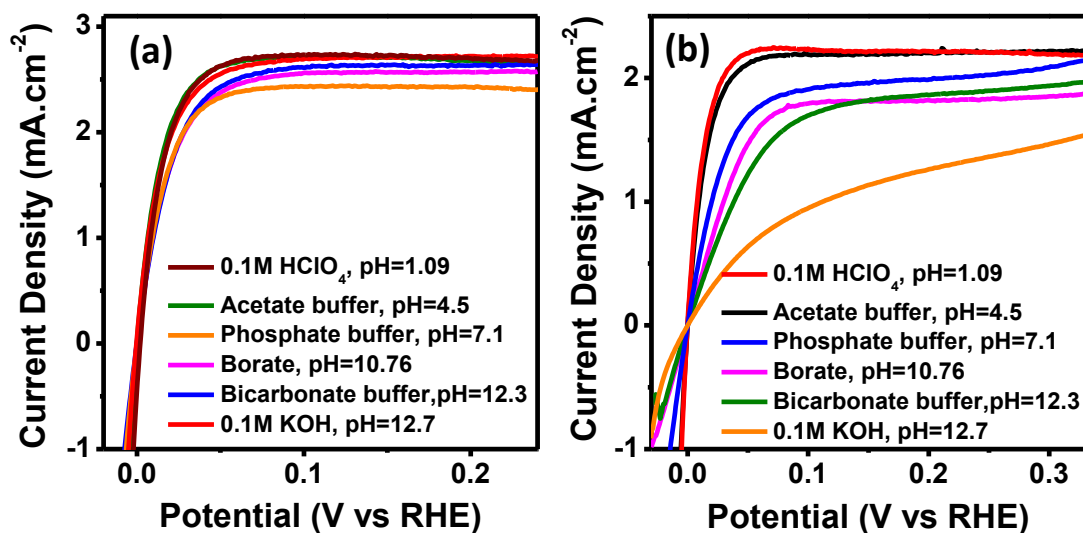
Figure S3.11. (a, b) HOR plots of RuO_2-Pt/C and Ru-Pt-NPs/C in different pH.
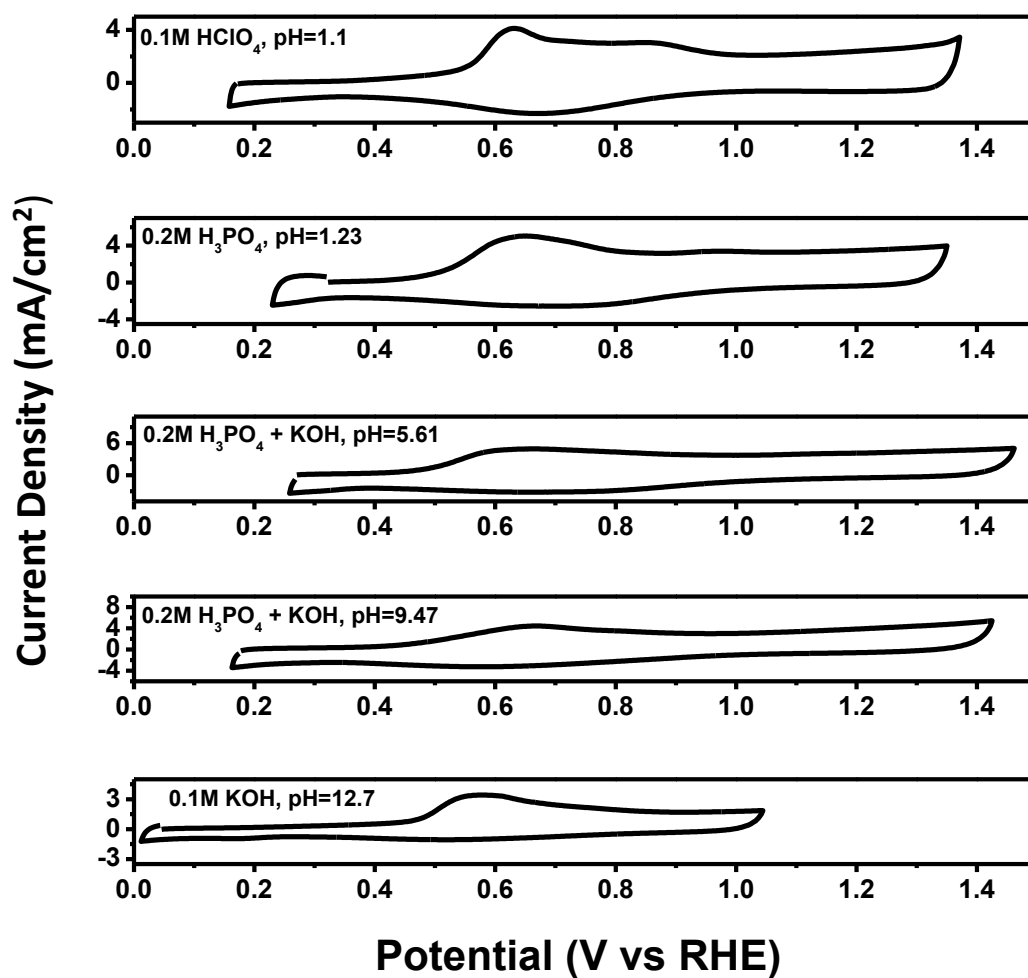
Figure S3.12. CO stripping voltammogram of RuO_2-Pt/C catalyst in different pH solutions.

RuO₂ as promoter in Pt-RuO₂-Nanostructures/Carbon composite, a pH-universal Catalyst for Hydrogen Evolution/Oxidation Reactions

Chapter 3
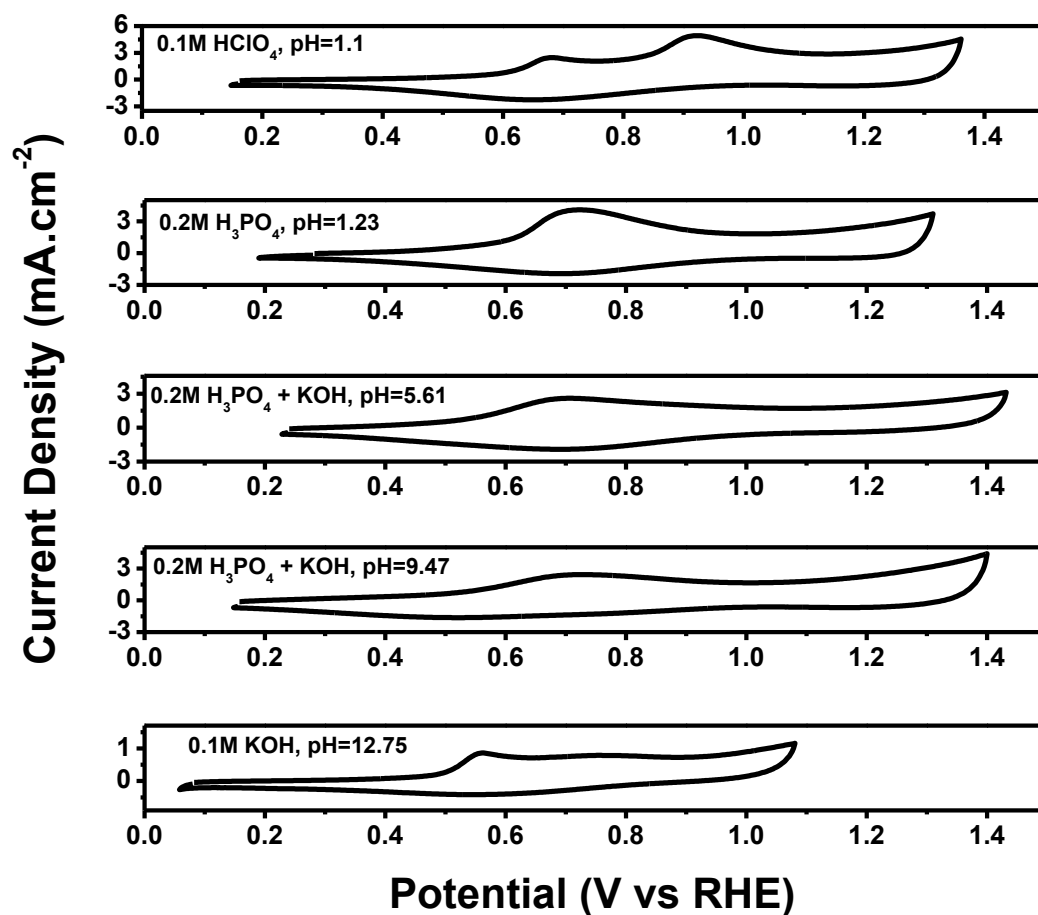
Figure S3.13. CO stripping voltammogram of Ru-Pt-NPs/C in different pH solutions.
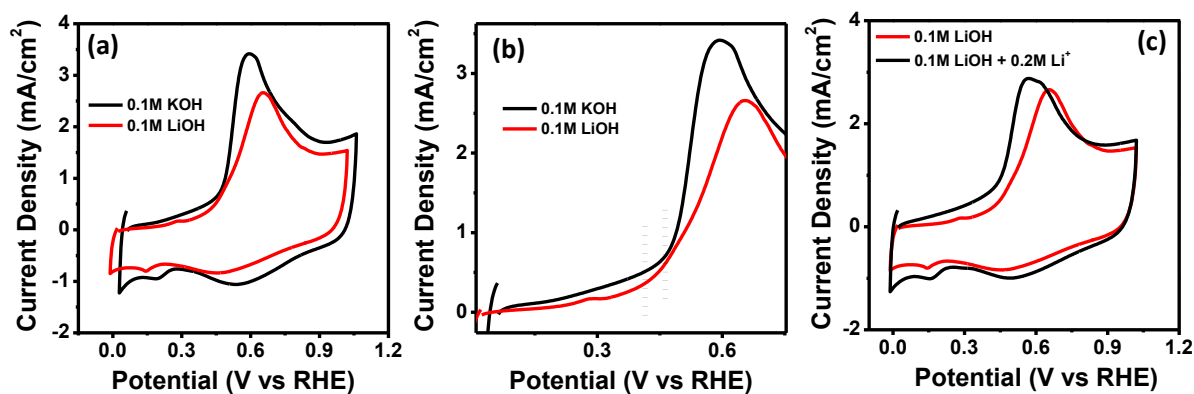
Figure S3.14. (a) CO onset comparison of RuO₂-Pt/C in 0.1M LiOH and 0.1M KOH, (b) Zooming portion of plot c in onset region, (c) CO onset comparison of RuO₂-Pt/C in 0.1M LiOH and 0.1M LiOH + 0.2M Li⁺.

RuO₂ as promoter in Pt-RuO₂-Nanostructures/Carbon composite, a pH-universal Catalyst for Hydrogen Evolution/Oxidation Reactions

Chapter 3

Table S3.3. Comparison of HER activity of RuO$_2$-Pt/C catalyst in alkaline medium

with other reported catalysts.

Catalyst	Electrolytes	Catalyst loading (ug cm^{-2})	Over potential (mV Vs RHE) vs current density (mA cm^{-2})	Tafel slope (mV/dec)	References
P-Ru/C	1 M KOH	30	31 (10 mA cm^{-2})	105	ACS Catal. 2020, 10, 11751−11757
PtRu NCs/BP	1 M KOH	14.8	22 (10 mA cm^{-2}) (ir corrected)	19	ACS Catal. 2019, 9, 10870−10875
PtRu NCs/BP	1 M KOH	14.8	22 (10 mA cm^{-2})	19	ACS Catal. 2019, 9, 10870−10875
PtNi-O	1 M KOH	5.1	39.8 (10 mA cm^{-2})	78.8	J. Am. Chem. Soc., 2018, 140, 9046.
Pt-Co(OH)$_2$/CC	1 M KOH	390	32 (10 mA cm^{-2})	70	ACS Catalysis, 2017, 7, 7131
Pt NWs/SLNi(OH)$_2$	1 M KOH	16	65 (10 mA cm^{-2})		Nat. Commun. 2015, 6, 6430.
Pt$_3$Ni$_2$NWs-S/C	1 M KOH	15.3	50 (10 mA cm-2)	-	Nat. Commun. 2017, 8, 14580.
CoO$_x$@CN	1 M KOH		232 (10 mA cm^{-2})		J. Am. Chem. Soc. 2015, 137, 2688.
Porous Pd-CN$_x$	1 M KOH	43	180 (5 mA cm^{-2})	150	ACS Catal.2016,6, 1929.
Ru@C$_2$N	1 M KOH	285	17 (10 mA cm^{-2})	38	Nature Nanotech., 2017, 12, 441
1D-RuO$_2$-CN$_x$	1 M KOH	12	95 (10 mA cm^{-2})	70	ACS Appl. Mater. Interfaces 2016, 8 (42), 28678.
RuP$_2$@NPC	1 M KOH	233	52 (10 mA cm^{-2})	69	Angew. Chem. Int. Ed., 2017, 129, 11717
Rh nanosheets RhNSs	1 M KOH	15	37 (10 mA cm^{-2}) (iR corrected)	74.7	Chem. Mater. 2017, 29, 5009.
Rh concave tetrahedra (Rh CTs)	1 M KOH	15	66 (10 mA cm^{-2}) (iR corrected)	117.7	Chem. Mater. 2017, 29, 5009.
Rh tetrahedra (Rh THs)	1 M KOH	15	64 (10 mA cm^{-2}) (iR corrected)	79.5	Chem. Mater. 2017, 29, 5009.
Pt-RuO$_2$C	1 M KOH	1.425	20 (10 mA cm^{-2})	41	This work

RuO₂ as promoter in Pt-RuO₂-Nanostructures/Carbon composite, a pH-universal Catalyst for Hydrogen Evolution/Oxidation Reactions

Chapter 3

Table S3.4. Comparison of HOR activity of RuO_2-Pt/C catalyst in alkaline medium with other reported catalysts.

Catalyst	Catalyst loading (ug cm$^{-2}_{disk}$)	Exchange current i_0 (mA/cm^2)	i_0 (A/g$_{metal}$)	ECSA (m^2/g)	Exchange current (mAcm$^{-2}_{metal}$)	References
PtRu/Mo₂C−TaC	13	1.3 at 25 mV	403 ± 25 25 mV	73.9	0.28 ± 0.02 at 25 mV	ACS Catal. 2021, 11, 932−947
Pt₀.₂₅Ru₀.₇₅/N-C	3.5	-	1654	117.3	1.41	*Adv. Mater. Interfaces* **2020**, 2000310
P-Ru/C	6.06		430	56	0.72	ACS Catal. 2020, 10, 11751−11757
Pt/C			203	49.4	0.41	*Small* **2019**, *15*, 1903057.
Pt₇Ru₃	~20		~49	~10.0	0.49	ACS Catal. 2016, 6, 3895−3908
PdO-RuO₂/C	3.55		522	102		Chemsuschem, 2021, https://doi.org/10.1002/cssc.202100200
Pd/CuNWs	12.5		330	32.6	1.01	J. Eclectrochem. Soc., 2015, 162(8), F849-F853
Ru₀.₂₀Pt₀.₈₀	7.09		696	49.0	1.42	J. Phys. Chem. C 2015, 119, 13481−13487
Acid treatment-PtNi/C	10		474	25.1	1.89	J. Am. Chem. Soc. 2017, 139, 5156−5163
Pt/Cu NWs	16		650	35.9	2.1	J. Am. Chem. Soc. 2013, 135, 13473−13478
PtNb/NbOₓ-C	20		360	45.0	0.8	ACS Catal. 2017, 7, 4936−4946
Pt-RuO₂/C	6	11	1833	101	1.8	This Work.

Ag-Pt Nanostructures/Carbon composite for Electrochemical Hydrogen Evolution and Oxygen Reduction Reaction in Alkaline medium

Chapter 4

Chapter 4

Ag-Pt Nanostructures/Carbon composite for Electrochemical Hydrogen Evolution and Oxygen Reduction Reaction in Alkaline medium

4.1 ABSTRACT

The persistent challenge within catalyst development revolves around the intricate task of designing and fabricating catalysts that not only deliver exceptional performance but also exhibit prolonged stability in two vital electrochemical processes: the Hydrogen Evolution Reaction (HER) and the Oxygen Reduction Reaction (ORR). In this chapter, we have discussed about the synthesized catalyst, AgPt-CN$_x$, that emerges as a promising bifunctional solution, catering to both HER and ORR applications. Notably, AgPt-CN$_x$ outperforms the benchmark commercial Pt/C (Comm Pt/C) catalyst in terms of activity for both the HER and ORR. The AgPt-CNx catalyst demonstrates an impressively low overpotential of 78 mV vs RHE for achieving a current density of 10 mA cm^{-2} in the HER while the Comm Pt/C catalyst requires a higher overpotential of 126 mV vs RHE. Furthermore, the ORR onset potentials for both AgPt-CN$_x$ and Comm Pt/C are observed at 0.942 V. Nonetheless, the AgPt-CN$_x$ catalyst exhibits a higher limiting current density than the Comm Pt/C, signifying superior ORR performance, particularly at higher current density. The Koutecky-Levich analysis yields an electron-transfer number of 4.02 for AgPt-CN$_x$, affirming a direct four-electron reduction pathway during ORR. The bifunctional attributes of AgPt-CN$_x$ make it a compelling alternative for integration into fuel cells and electrolyzers, potentially supplanting the conventional Comm Pt/C catalyst.

Ag-Pt Nanostructures/Carbon composite for Electrochemical Hydrogen Evolution and Oxygen Reduction Reaction in Alkaline medium

Chapter 4

4.2 INTRODUCTION

The escalating global energy requirements have incentivized scientists to explore alternative devices for energy conversion and storage.[1] The hydrogen evolution reaction (HER) and the oxygen reduction reaction (ORR) play pivotal roles in various renewable energy technologies, including water electrolyzers, fuel cells, and metal-air batteries.[2-4] Traditional electrocatalysts, such as those based on platinum (Pt) and its alloys, exhibit drawbacks like high expenses and limited stability, despite their low overpotential and rapid reaction kinetics.[5, 6] Consequently, there is a pressing need to tackle the formidable task of designing cost-effective, enduring, and bifunctional electrocatalysts that display exceptional activity for both HER and ORR, even though it presents a substantial challenge.

Hydrogen is regarded as one of the most promising fuels, and electrochemical water splitting provides a method for producing high-purity hydrogen under mild conditions.[7] Proton exchange membrane fuel cells (PEMFCs) exhibit remarkable characteristics such as high energy and power density, as well as high energy conversion efficiency. Pt catalysts are known for their strong activity in the HER within an acidic environment.[8, 9] However, the limited durability of commercial Pt/C catalysts in acidic media presents a major hurdle to their widespread use in PEMFCs and proton exchange membrane electrolyzers (PEMELs).[10] Consequently, it is imperative to develop novel catalysts that offer both high activity and long-term stability for HER in acidic conditions. On the other hand, alkali exchange membrane fuel cells (AEMFCs) and alkali membrane electrolyzers (AEMELs) have emerged as cost-effective alternatives to PEMFCs and PEMELs. This is primarily due to the availability of non-precious catalysts for the ORR[11, 12] and oxygen evolution reaction (OER)[12] that are suitable for alkaline environments. Like acidic media, Pt exhibits strong catalytic performance in HER within alkaline environments.

159

Ag-Pt Nanostructures/Carbon composite for Electrochemical Hydrogen Evolution and Oxygen Reduction Reaction in Alkaline medium

Chapter 4

Nevertheless, the sluggish nature of HER on Pt catalysts in alkaline environments necessitates a significant quantity of Pt for AEMFCs and AEMELs.[13] In fact, Pt catalysts demonstrate 2 to 3 times lower activity for HER in alkaline conditions compared to their performance in acidic media.[14] Hence, it is imperative to develop highly active catalysts specifically tailored for HOR/HER in alkaline environments to enable the practical implementation of AEMFCs and AEMELs.

The commercialization of fuel cells has faced significant challenges due to the inherent sluggishness of ORR, instability of catalysts, and the elevated cost associated with noble-metal catalysts.[15, 16] The rate-determining step in ORR was discovered to involve the formation of O_{ads} and a hydroxide anion derived from the electrochemical splitting of $O_{2,ads}$ species.[17] The alkaline medium proves effective due to the inherently faster kinetics of ORR in alkaline media compared to acidic conditions. Additionally, an alkaline medium offers a less corrosive environment for catalysts and electrodes.[18] Rapid adsorption/desorption processes involving oxygen-containing species such as O, OH^-, O_2^-, HO_2^-, and H_2O_2 are necessary at the catalyst surfaces in an alkaline medium.[19]

Here, in this chapter, we have discussed the electrochemical deposition of Pt in Ag supported on CN_x (AgPt-CN_x) that can act as bifunctional electrocatalyst for hydrogen evolution reaction (HER) and oxygen reduction reaction (ORR). The presence of nitrogen doped carbon sheets provides support and durability to the catalyst. The synthesized AgPt-CN_x catalyst shows less overpotential and excellent durability compared to Commercial Pt/C (Comm Pt/C) to reach 10 mA cm^{-2} current density in 1 M KOH. The potential required to reach 10 mA cm^{-2} current density for AgPt-CN_x is 78 mV vs RHE, whereas for Comm Pt/C catalyst the overpotential required is 126 mV vs RHE. The prepared catalyst showed excellent durability for HER up to 24 hours. The limiting current density for ORR, is higher in the case of AgPt-CN_x catalyst than Comm Pt/C

Ag-Pt Nanostructures/Carbon composite for Electrochemical Hydrogen Evolution and Oxygen Reduction Reaction in Alkaline medium

Chapter 4

catalyst. The O_2 reduction kinetics for AgPt-CN_x follow a direct 4 electron reduction pathway. The prepared bifunctional catalyst can be used in various application to reduce the over usage of Comm Pt/C.

4.3 EXPERIMENTAL SECTION

Materials

Formamide ($HCONH_2$), silver (I) nitrate ($AgNO_3$, 99+% assay), chloroplatinic acid hexahydrate ($H_2PtCl_6 \cdot 6H_2O$), potassium hydroxide (KOH**)** and sodium borohydride ($NaBH_4$) were bought from Sigma Aldrich. Sulfuric acid (H_2SO_4, 98%) was bought from Merck (Germany). These materials were used exactly as they were received, with no further purification. Sigma Aldrich supplied Ar gas (99.99% purity) and O_2 gas. Milli-Q water was prepared using an ultra-filtration system (Milli-Q, Millipore), and the measured conductivity at 25 °C was 35 mho.cm^{-1}.

Synthesis of N-doped carbon (CN_x)

The synthesis of CN_x was done by following our existing method[20]. A brown-colored solution was produced after microwave heating 30 mL of formamide ($HCONH_2$) for two hours at 180°C. A rotating evaporator operating at 180°C evaporated the collected solution. Finally, vacuum drying was used to produce solid N-doped carbon after washing with distilled water.

Synthesis of the AgPt-CN_x composite

The Ag-CN_x composite was synthesized through a series of steps. Initially, 46 mg of silver (I) nitrate was introduced into 5 mL of deionized water and subjected to 30 minutes of sonication using a bath-sonicator. Simultaneously, 5 mg of as-prepared CNx was dispersed in 2 mL of deionized water through 10 minutes of sonication. A homogeneous mixture was achieved by combining the two solutions mentioned above, followed by an

Ag-Pt Nanostructures/Carbon composite for Electrochemical Hydrogen Evolution and Oxygen Reduction Reaction in Alkaline medium

Chapter 4

additional 30 minutes of sonication. Subsequently, 50 mg of $NaBH_4$ was added to the mixture, and the entire solution was subjected to an additional 2 hours of sonication. The resulting dark solution was centrifuged at 1600 rpm and then thoroughly washed with deionized water and ethanol. The black precipitate obtained was collected and subsequently dried under vacuum conditions for further utilization. The prepared Ag-CN_x was coated into a GC and this modified GC has undergo electro reduction of H_2PtCl_6 in PBS solution (pH = 7.4) by potential cycling for 10 cycles by sweeping the potential from -1 V to 1 V vs Ag/AgCl followed by chronoamperometry at-0.6 V vs Ag/AgCl for 300 second to prepare AgPt-CN_x.

4.4 RESULTS AND DISCUSSIONS

Morphology and characterization
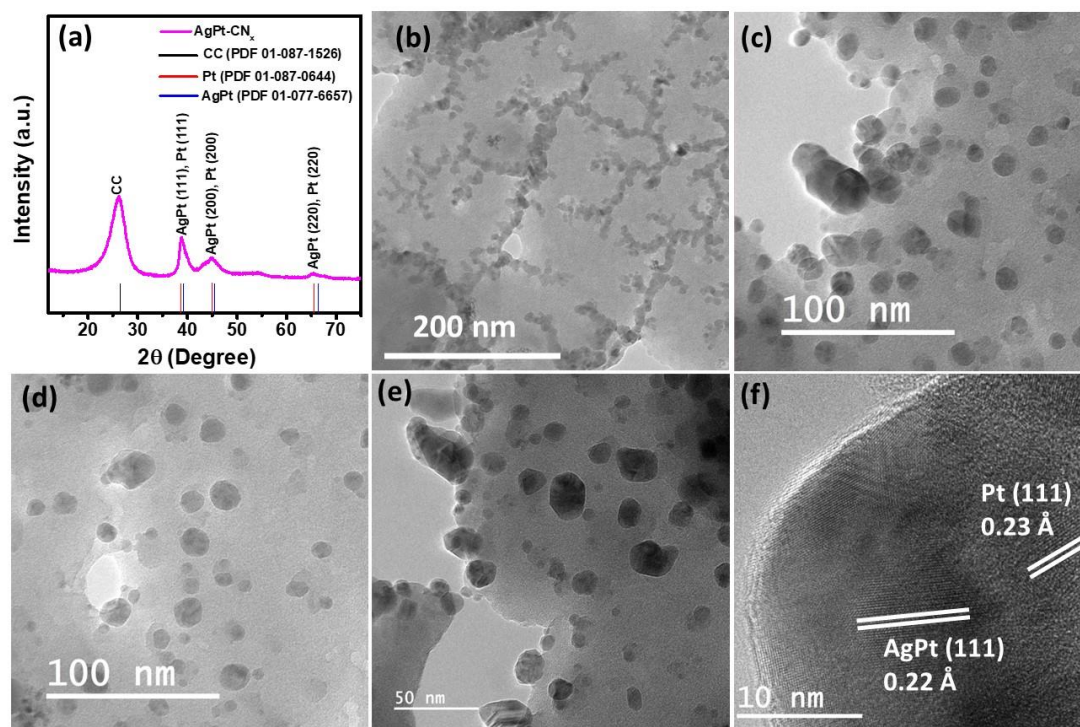
Figure 4.1. (a) *p*-XRD pattern of AgPt-CN_x, (b, c, d, e) TEM images, (f) HRTEM images of AgPt-CN_x.

Ag-Pt Nanostructures/Carbon composite for Electrochemical Hydrogen Evolution and Oxygen Reduction Reaction in Alkaline medium

Chapter 4

The structural analysis of AgPt-CN$_x$ was conducted via powder X-ray diffraction (*p*-XRD), as depicted in Figure 4.1a. The *p*-XRD analysis provides valuable insights into the structural composition of the catalyst, facilitating a precise understanding of its crystalline nature and properties. The observed peak at 26° can be attributed to the presence of the carbon cloth (CC) substrate[21], which is consistent with reference data from standard JCPDS (PDF 01-087-1526). Additionally, the diffraction peaks observed at 39.14°, 45.5°, and 66.32° in the AgPt-CNx composite correspond to the (111), (200), and (220) crystalline planes of both Pt and AgPt. These findings align well with reference data from standard JCPDS (PDF 01-087-0644) and (PDF 01-077-6657), respectively. The morphological analysis of AgPt-CN$_x$ was conducted using Transmission Electron Microscopy (TEM). Based on the TEM image given in Figure 4.1(b-e), it can be observed that small particles are decorated in CN$_x$ sheet. The average diameter of the nano particle were ranging from 20 to 50 nm. The high-resolution transmission electron microscopy (HR-TEM) image of AgPt-CN$_x$ is illustrated in Figure 4.1f. This image reveal a distinct d-spacing value of 0.23 Å, which corresponds to the (111) lattice plane of elemental Pt and the d-spacing value of 0.22 Å corresponds to the (111) lattice plane of AgPt.

Ag-Pt Nanostructures/Carbon composite for Electrochemical Hydrogen Evolution and Oxygen Reduction Reaction in Alkaline medium

Chapter 4
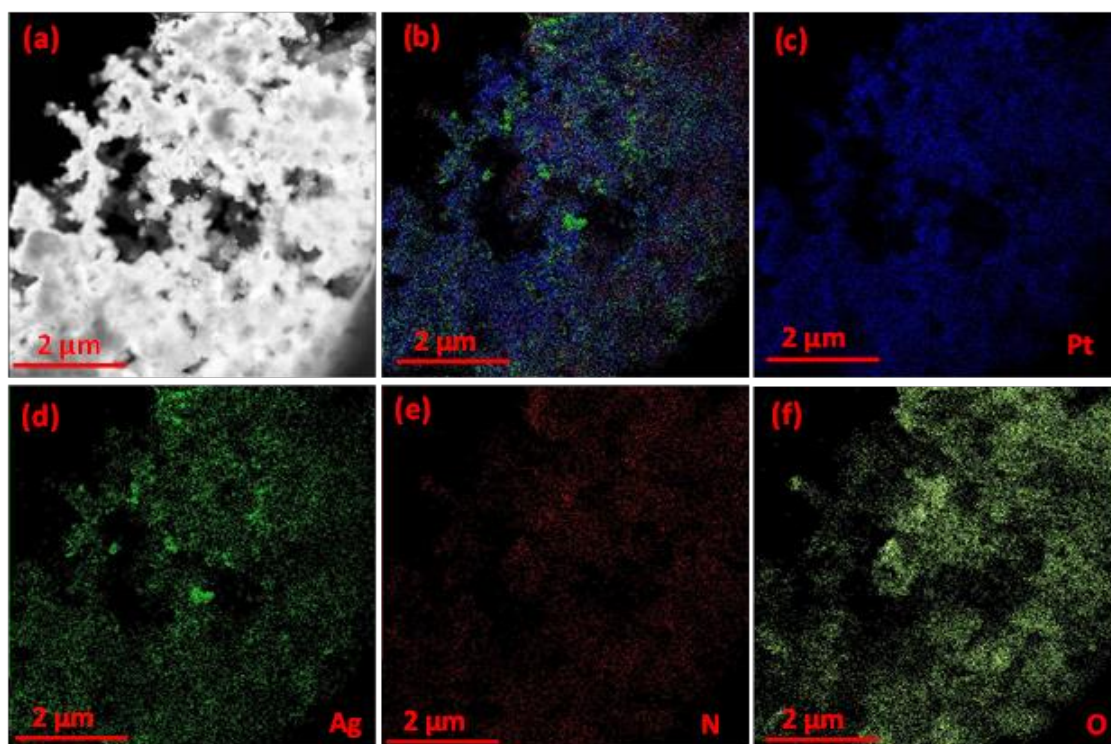
Figure 4.2. (a) STEM image , (b) overlay image, (c-f) elecmental mapping images of AgPt-CN$_x$.

Figure 4.2(a, b) depicts scanning transmission electron microscopy (STEM) image and overlay image, while Figure 4.2(c-f) provides elemental mapping of AgPt-CN$_x$. These images reveal the homogeneous dispersion of atoms and the notable presence of Pt, Ag, Nitrogen, and Oxygen within the composite material. The STEM images offer detailed insights into the structural characteristics of the composite, while the elemental mapping confirms the even distribution of various elements, emphasizing the substantial presence of Pt, Ag, Nitrogen, and Oxygen throughout the material.

Ag-Pt Nanostructures/Carbon composite for Electrochemical Hydrogen Evolution and Oxygen Reduction Reaction in Alkaline medium

Chapter 4

HER studies on the AgPt-CN$_x$ catalyst in alkaline medium
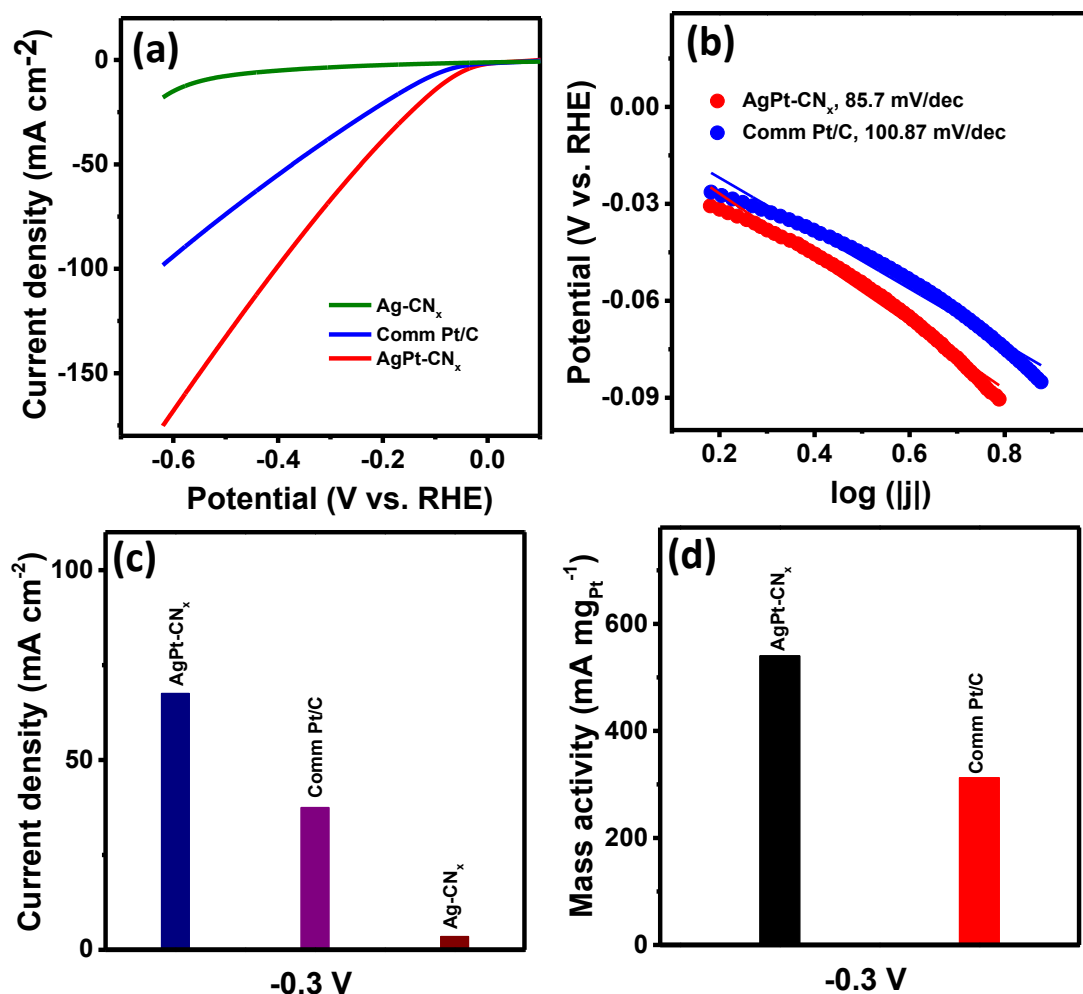
Figure 4.3. (a) Non-iR corrected HER polarisation curve of AgPt-CN$_x$, Comm Pt/C and Ag-CN$_x$ in 1 M KOH, (b) Tafel plots of AgPt-CN$_x$ and Comm Pt/C, (c) current density and (d) mass activity of catalysts at -0.3 V.

The hydrogen evolution reaction (HER) proceeds relatively slowly in alkaline conditions, which poses a hindrance to the efficient production of hydrogen through water splitting. This is because an additional energy input is required for the dissociation of water molecules, as represented by the equation: $H_2O + e^- \rightarrow H^* + OH^-$. In other words, in alkaline media, more energy is needed for the electrolysis of water molecules before hydrogen can be generated, making the process less efficient.[22] HER activity of AgPt-CN$_x$ is investigated in 1 M KOH solution, where a catalyst-coated carbon cloth (1

Ag-Pt Nanostructures/Carbon composite for Electrochemical Hydrogen Evolution and Oxygen Reduction Reaction in Alkaline medium

Chapter 4

cm^2 area) served as the working electrode, platinum wire functioned as the counter electrode, and Ag/AgCl acted as the reference electrode. The Linear Sweep Voltammetry (LSV) polarization curve of AgPt-CN$_x$ is obtained in alkaline medium and it is compared with Comm Pt/C and Ag-CN$_x$ (Figure 4.3a). The overpotential required to reach 10 mA cm^{-2} current density for AgPt-CN$_x$ is 78 mV vs RHE, for Comm Pt/C catalyst 126 mV vs RHE whereas for Ag-CN$_x$ the value is 547 mV. In an alkaline medium, the HER proceeds through two critical stages: 1. The Volmer step, which involves the dissociation of water and the formation of hydrogen intermediates. 2. The desorption of these hydrogen intermediates to produce H$_2$ gas. The determination of the rate-determining step (RDS) for HER can be achieved using the Tafel slope. According to Butler-Volmer kinetics, the RDS can be identified as either the Volmer step, Heyrovsky step, or Tafel step based on the Tafel slope values. Specifically, when the Tafel slope measures 120 mV/dec, the RDS is the Volmer step; when it is 40 mV/dec, it's the Heyrovsky step, and when it's 30 mV/dec, it's the Tafel step.[23] Prior to the adsorption of the intermediate H*, the catalyst needs to overcome the relatively stronger covalent H-O-H bond, a process known as the Volmer step. Because of the substantial energy barrier for water dissociation, achieving a slow HER requires a substantial loading of Pt/C.[24] This increased loading substantially escalates the overall cost of the catalyst. The tafel slope value obtained from Figure 4.3b for AgPt-CN$_x$ (85.7 mV dec^{-1}) is lower than that of Comm Pt/C (100.8 mV dec^{-1}) that indicates HER kinetics occurs faster on the catalyst AgPt-CN$_x$. The current density value at -0.3 V for all the catalysts is shown in Figure 4.3c. The value of current density for AgPt-CN$_x$ at -0.3 V is obtained to be 67.56 mA cm^{-2} and for Comm Pt/C the value obtained to be 37.52 mA cm^{-2} whereas for Ag-CN$_x$ the value is 3.54 mA cm^{-2}. The mass activity of AgPt-CN$_x$ and Comm Pt/C at the same potential is calculated (Figure 4.3d) and the values obtained are 540.48 mA mg$_{Pt}^{-1}$ and

Ag-Pt Nanostructures/Carbon composite for Electrochemical Hydrogen Evolution and Oxygen Reduction Reaction in Alkaline medium

Chapter 4

312.66 mA $\text{mg}_{\text{Pt}}^{-1}$ respectively. This showcases the superior catalytic performance of AgPt-CN$_x$ in driving the HER, making it a promising candidate for various electrochemical applications.
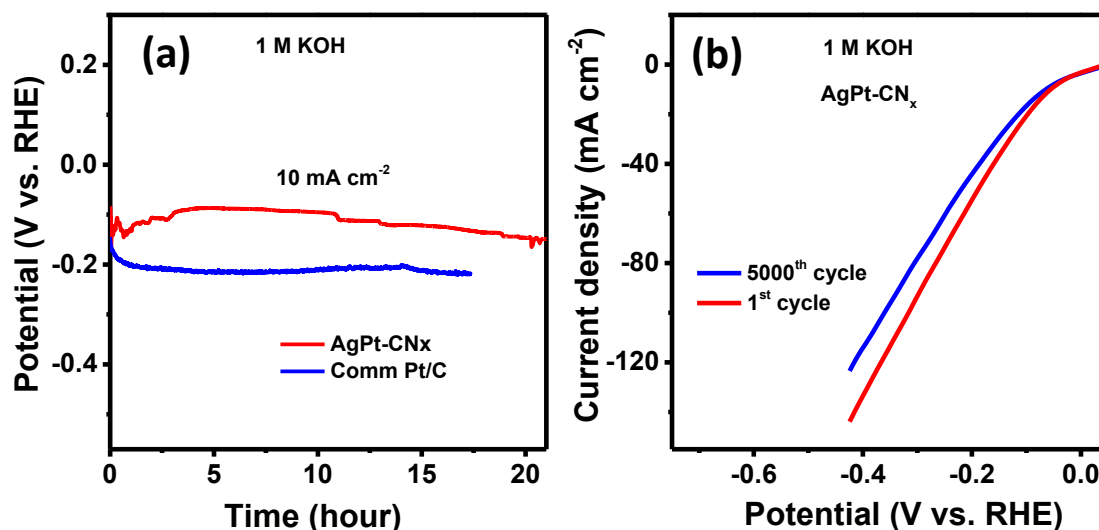
Figure 4.4. (a) Chronopotentiometry stability plot of Comm Pt/C and AgPt-CN$_x$ in 1 M KOH, (b) Cyclic stability of AgPt-CN$_x$ in 1 M KOH.

In order to assess the long-term stability and practical utility of the synthesized AgPt-CN$_x$ catalyst for HER, its durability was systematically examined using a chronopotentiometry experiment. This experiment aimed to provide a thorough evaluation of the catalyst's performance and stability over an extended period of time. The stability curve, as illustrated in Figure 4.4a, was recorded while maintaining a constant current density of 10 mA cm^{-2} for a duration of 24 hours in 1 M KOH electrolyte. Notably, this plot reveals only a minimal increase in overpotential even after the extensive 24-hour testing period. In stark contrast, when the commercial Pt/C catalyst was subjected to the same experimental conditions, a significant increase in overpotential was observed. This discrepancy underscores the exceptional stability of the AgPt-CN$_x$ catalyst compared to the commercial Pt/C catalyst, demonstrating its superior

Ag-Pt Nanostructures/Carbon composite for Electrochemical Hydrogen Evolution and Oxygen Reduction Reaction in Alkaline medium

Chapter 4

performance and robustness under prolonged electrochemical conditions. The cycling stability of AgPt-CN$_x$ was assessed by subjecting it to 5000 cycles in a 1 M KOH electrolyte, shown in Figure 4.4b. Remarkably, after this extensive cycling, the increase in overpotential at a current density of 10 mA cm^{-2} between the first and 5000th cycle was merely 10 mV. This depicts the catalyst's exceptional durability and robust performance over repeated cycling.

ORR studies on AgPt-CN$_x$ catalysts in alkaline medium

The electrocatalytic performance of the AgPt-CN$_x$ catalyst in the ORR was evaluated through a series of experiments. Cyclic voltammetry (CV) was employed to investigate the ORR activity in both Ar and O$_2$-saturated electrolytes, as depicted in Figure 4.5a. These experiments were conducted using a Rotating Disk Electrode (RDE) setup in a 0.1 M KOH solution. In this setup, a catalyst-coated Glassy Carbon (GC) electrode was served as the working electrode, platinum wire served as the counter electrode, and Ag/AgCl functioned as the reference electrode. The CV recorded in the O$_2$-saturated electrolyte reveals a reduction curve around 0.9 V, distinct from the one obtained in the Ar-saturated electrolyte. This observed increase in current at the specified potential signifies the catalyst's good activity, confirming its efficiency in ORR process. Furthermore, the ORR activity of the AgPt-CN$_x$ catalyst was investigated using LSV polarization curves. The LSV analysis involved sweeping the potential within the range of 1.1 to 0.5 V vs. the RHE, as illustrated in Figure 4.5b. These results were then compared with those obtained using Commercial Pt/C as a reference. Notably, both catalysts exhibited a similar onset potential at approximately 0.942 V.

Ag-Pt Nanostructures/Carbon composite for Electrochemical Hydrogen Evolution and Oxygen Reduction Reaction in Alkaline medium

Chapter 4
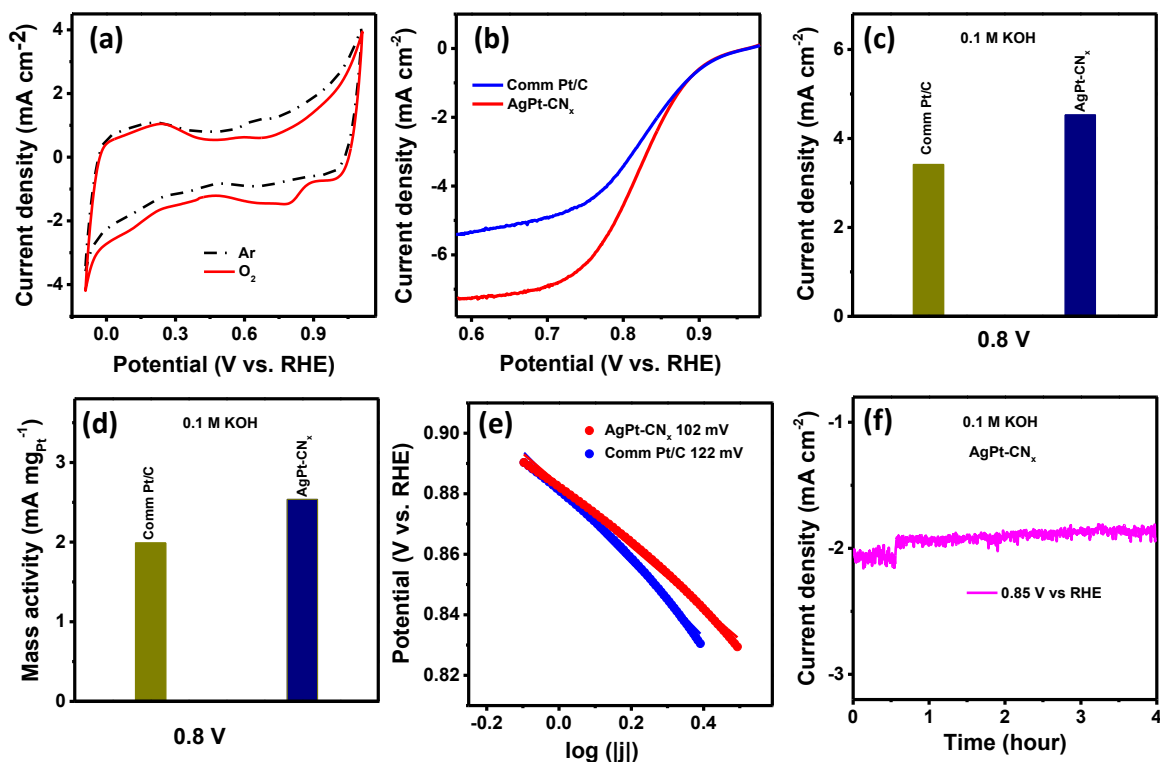
Figure 4.5. (a) CV curve of AgPt-CN$_x$ and Comm Pt/C in Ar and O$_2$ saturated electrolyte, (b) ORR polarization plots in O$_2$ saturated electrolyte, (c) current density, (d) mass activity plot at 0.8 V vs RHE, and (d) tafel plots of AgPt-CN$_x$ and Comm Pt/C in 0.1 M KOH, (e) chronoamperometric response of AgPt-CN$_x$ at 0.85V vs RHE.

However, it is worth highlighting that the AgPt-CN$_x$ catalyst demonstrated a higher limiting current density compared to the Comm Pt/C catalyst. This enhanced performance suggests that the AgPt-CN$_x$ catalyst excels in terms of ORR activity, especially at higher current densities, positioning it as a promising and efficient candidate for electrochemical applications. The current density of AgPt-CN$_x$ catalyst and comm Pt/C at 0.8 V vs RHE was obtained to be 4.53 and 3.417 mA cm^{-2} respectively (Figure 4.5c). Similarly, the mass activity of the AgPt-CN$_x$ catalyst and comm Pt/C at 0.8 V vs RHE was calculated by normalizing kinetic current and is presented in Figure 4.5d. At this potential, the mass activity of AgPt-CN$_x$ was determined to be 2.5368 mA mg$_{Pt}^{-1}$, while comm Pt/C exhibited a value of 1.99 mA mg$_{Pt}^{-1}$. This measurement provides

insights into the catalyst's intrinsic activity and efficiency in promoting ORR at the specified potential. The kinetics of the ORR were further explored using Tafel analysis, a valuable technique for assessing reaction kinetics. The Tafel plot, which reflects the relationship between overpotential and current density, is indicative of reaction kinetics. A lower Tafel plot value signifies faster reaction kinetics. In the case of the AgPt-CN$_x$ catalyst, the Tafel slope value was determined to be 102 mV/dec, while for comm Pt/C, the Tafel slope value was 122 mV/dec, as shown in Figure 4.5e.[25] The lower Tafel slope of AgPt-CN$_x$ than comm Pt/C, indicates that the ORR proceeds more favourably on this catalyst, affirming its superior catalytic performance in facilitating ORR process. In addition to its noteworthy catalytic activity, AgPt-CN$_x$ demonstrates significant stability. When subjected to chronoamperometry in a 0.1 M KOH solution (Figure 4.5f), the catalyst displayed notable stability, maintaining a nearly constant current for up to 4 hours, signifying its enduring performance. This stability is a crucial characteristic for long-term electrocatalytic applications.
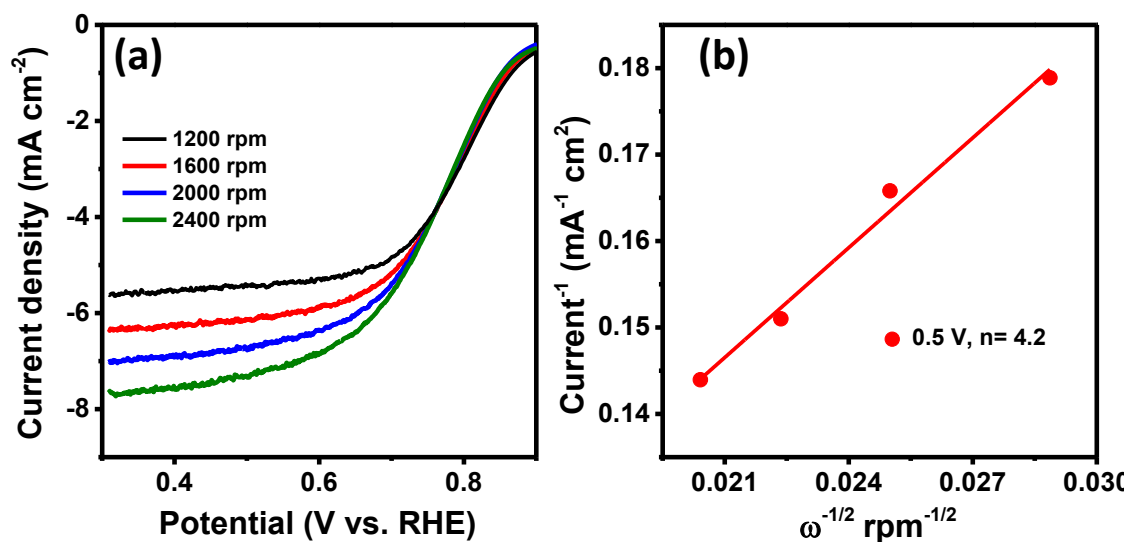
Figure 4.6. (a) LSV polarization curve for ORR of AgPt-CN$_x$ at different rotation in O$_2$ saturated 0.1 M KOH and (b) corresponding K-L plot.

Ag-Pt Nanostructures/Carbon composite for Electrochemical Hydrogen Evolution and Oxygen Reduction Reaction in Alkaline medium

Chapter 4

Figure 4.6a presents the ORR LSV polarization curves for AgPt-CN$_x$ at various rotation speeds. The limiting current density observed at higher overpotentials is primarily governed by diffusion and the increased transport of oxygen at the electrode surface. As the rotation speed increases, the limiting current density also increases, reflecting enhanced oxygen mass transport facilitated by the dynamic electrode rotation. Figure 4.6b illustrates the Koutecky-Levich (K-L) plots, showcasing the inverse current density (j^{-1}) as a function of the inverse square root of the rotation speed ($\omega^{-1/2}$) at different potentials. The linear nature of these K-L plots is indicative of a first-order reaction rate for the reduction of O$_2$.[26] This reveals that the oxygen reduction reaction proceeds at a rate consistent with a first-order reaction. The Koutecky-Levich equation, which can be expressed as follows, is used to model, and analyse electrochemical kinetics:[27]

$$\frac{1}{j_l} = \frac{1}{j_k} + \frac{1}{j_d}$$

Where j_l is limiting current density, j_k is kinetic current density and j_d is diffusion current density. The Levich equation can be used to calculate the total number of electrons transferred during the oxygen reduction process.

$$J_d = 0.62\ nFD_{O2}^{2/3}\ v^{-1/6}\ C_{O2}\ w^{1/2}$$

Where n value gives the total number of electrons that transferred during the reduction process, F indicates Faraday constant (96485 C/mol), v (0.01 cm^2/s) indicates the kinematic viscosity of the electrolyte, D_{O2} (1.9×10^{-5} cm^2/s) indicates the bulk diffusion coefficient of oxygen in the electrolyte, ω indicates the angular velocity of the working electrode and C_{O2} (1.2×10^{-6} mol/cm^3) indicates the concentration of oxygen dissolved in the electrolyte. The K-L plots presented in Figure 4.6b exhibit a good degree of linearity, underscoring the first-order dependency of the O$_2$ reduction process. This linearity reflects a consistent relationship between key parameters, supporting the notion

Ag-Pt Nanostructures/Carbon composite for Electrochemical Hydrogen Evolution and Oxygen Reduction Reaction in Alkaline medium

Chapter 4

of first-order kinetics for O_2 reduction on the AgPt-CN$_x$ electrocatalyst.[28] To further elucidate the reaction mechanism, the slope of these K-L plots is utilized to calculate the electron-transfer number. For AgPt-CN$_x$, this calculation yields a value of 4.02. This finding signifies that a four-electron process predominantly governs the ORR on the AgPt-CN$_x$ electrocatalyst. In other words, the reduction of O_2 proceeds via a direct four-electron pathway on this catalyst.[25] These results obtained from RDE measurements are of significance for fuel cell applications. A four-electron reduction pathway is highly favourable in the context of fuel cells, as it allows for the efficient conversion of oxygen into water, contributing to enhanced electrocatalytic performance and overall efficiency in fuel cell technologies.

4.5 CONCLUSIONS:

The AgPt-CN$_x$ catalyst, synthesized through a two-step process involving NaBH$_4$ reduction of Ag in CN$_x$ followed by electrochemical deposition of Pt in Ag-CN$_x$, demonstrates its versatility as a bifunctional catalyst for both the HER and ORR. In the HER performance in a 1 M KOH electrolyte solution, AgPt-CN$_x$ exhibits superior activity compared to the commercial Pt/C catalyst. This is evidenced by the lower overpotential required to reach a current density of 10 mA cm^{-2}. Specifically, AgPt-CN$_x$ requires an overpotential of 78 mV vs RHE, while the commercial Pt/C catalyst requires a higher overpotential of 126 mV vs RHE. Furthermore, the excellent stability of the AgPt-CN$_x$ catalyst is confirmed through a chronopotentiometry experiment conducted at 10 mA cm^{-2} over 24 hours, where only a minimal increase in overpotential is observed. The ORR performance of AgPt-CN$_x$ and commercial Pt/C showcases an onset potential around 0.942 V. However, the limiting current density of the AgPt-CN$_x$ catalyst surpasses that of the commercial Pt/C catalyst, indicating superior ORR activity, especially at higher current densities. The electron-transfer number calculated from the K-L plot is

Ag-Pt Nanostructures/Carbon composite for Electrochemical Hydrogen Evolution and Oxygen Reduction Reaction in Alkaline medium

Chapter 4

4.02 for AgPt-CNx, demonstrating a direct four-electron reduction pathway for the ORR on this catalyst. This study demonstrates the synthesis of bifunctional catalysts, that can provide a new route to offer versatile solutions for various applications**.**

4.6 REFERENCES:

(1) Barman, B. K.; Sarkar, B.; Ghosh, P.; Ghosh, M.; Mohan Rao, G.; Nanda, K. K. In Situ Decoration of Ultrafine Ru Nanocrystals on N-Doped Graphene Tube and Their Applications as Oxygen Reduction and Hydrogen Evolution Catalyst. *ACS Applied Energy Materials* **2019**, *2* (10), 7330-7339.

(2) Koper, M. T. M. A basic solution. *Nature Chemistry* **2013**, *5* (4), 255-256.

(3) Liu, Y.; Chen, F.; Ye, W.; Zeng, M.; Han, N.; Zhao, F.; Wang, X.; Li, Y. High-Performance Oxygen Reduction Electrocatalyst Derived from Polydopamine and Cobalt Supported on Carbon Nanotubes for Metal–Air Batteries. *Advanced Functional Materials* **2017**, *27* (12), 1606034.

(4) Guo, Y.; Park, T.; Yi, J. W.; Henzie, J.; Kim, J.; Wang, Z.; Jiang, B.; Bando, Y.; Sugahara, Y.; Tang, J.; et al. Nanoarchitectonics for Transition-Metal-Sulfide-Based Electrocatalysts for Water Splitting. *Advanced Materials* **2019**, *31* (17), 1807134.

(5) Liu, J.; Jiao, M.; Lu, L.; Barkholtz, H. M.; Li, Y.; Wang, Y.; Jiang, L.; Wu, Z.; Liu, D.-j.; Zhuang, L.; et al. High performance platinum single atom electrocatalyst for oxygen reduction reaction. *Nature Communications* **2017**, *8* (1), 15938.

(6) Jiang, B.; Li, C.; Tang, J.; Takei, T.; Kim, J. H.; Ide, Y.; Henzie, J.; Tominaka, S.; Yamauchi, Y. Tunable-Sized Polymeric Micelles and Their Assembly for the Preparation of Large Mesoporous Platinum Nanoparticles. *Angewandte Chemie International Edition* **2016**, *55* (34), 10037-10041.

(7) Ma, E.; Shen, T.; Ying, D.; Liu, W.; Zhao, X.; Zhang, L.; Wang, D. Chitin Derived Carbon Anchored Ultrafine Ru Nanoparticles for Efficient Hydrogen Evolution Reaction. *ACS Sustainable Chemistry & Engineering* **2022**, *10* (47), 15530-15537.

Ag-Pt Nanostructures/Carbon composite for Electrochemical Hydrogen Evolution and Oxygen Reduction Reaction in Alkaline medium

Chapter 4

(8) Seh, Z. W.; Kibsgaard, J.; Dickens, C. F.; Chorkendorff, I.; Nørskov, J. K.; Jaramillo, T. F. Combining theory and experiment in electrocatalysis: Insights into materials design. *Science* **2017**, *355* (6321), eaad4998.

(9) Ma, Z.; Chen, C.; Cui, X.; Zeng, L.; Wang, L.; Jiang, W.; Shi, J. Hydrogen Evolution/Oxidation Electrocatalysts by the Self-Activation of Amorphous Platinum. *ACS Applied Materials & Interfaces* **2021**, *13* (37), 44224-44233.

(10) Esposito, D. V.; Hunt, S. T.; Stottlemyer, A. L.; Dobson, K. D.; McCandless, B. E.; Birkmire, R. W.; Chen, J. G. Low-Cost Hydrogen-Evolution Catalysts Based on Monolayer Platinum on Tungsten Monocarbide Substrates. *Angewandte Chemie International Edition* **2010**, *49* (51), 9859-9862.

(11) Zhang, G.; Xu, Y.; Wang, L.; Wang, J.; Kuang, Y.; Sun, X. Rational design of graphene oxide and its hollow CoO composite for superior oxygen reduction reaction. *Science China Materials* **2015**, *58* (7), 534-542.

(12) Lee, G.; Kang, G.-S.; Jang, J.-H.; Yoo, S. J.; Joh, H.-I.; Lee, S. Upcycling waste tires to affordable catalysts for the oxygen reduction reaction. *International Journal of Energy Research* **2022**, *46* (4), 4645-4654.

(13) Jiao, L.; Liu, E.; Hwang, S.; Mukerjee, S.; Jia, Q. Compressive Strain Reduces the Hydrogen Evolution and Oxidation Reaction Activity of Platinum in Alkaline Solution. *ACS Catalysis* **2021**, *11* (13), 8165-8173.

(14) Danilovic, N.; Subbaraman, R.; Strmcnik, D.; Chang, K.-C.; Paulikas, A. P.; Stamenkovic, V. R.; Markovic, N. M. Enhancing the Alkaline Hydrogen Evolution Reaction Activity through the Bifunctionality of Ni(OH)2/Metal Catalysts. *Angewandte Chemie International Edition* **2012**, *51* (50), 12495-12498.

(15) Cao, R.; Lee, J.-S.; Liu, M.; Cho, J. Recent Progress in Non-Precious Catalysts for Metal-Air Batteries. *Advanced Energy Materials* **2012**, *2* (7), 816-829.

(16) Strasser, P.; Koh, S.; Anniyev, T.; Greeley, J.; More, K.; Yu, C.; Liu, Z.; Kaya, S.; Nordlund, D.; Ogasawara, H.; et al. Lattice-strain control of the activity in dealloyed core–shell fuel cell catalysts. *Nature Chemistry* **2010**, *2* (6), 454-460.

Ag-Pt Nanostructures/Carbon composite for Electrochemical Hydrogen Evolution and Oxygen Reduction Reaction in Alkaline medium

Chapter 4

(17) van der Vliet, D. F.; Wang, C.; Tripkovic, D.; Strmcnik, D.; Zhang, X. F.; Debe, M. K.; Atanasoski, R. T.; Markovic, N. M.; Stamenkovic, V. R. Mesostructured thin films as electrocatalysts with tunable composition and surface morphology. *Nature Materials* **2012**, *11* (12), 1051-1058.

(18) Lu, Y.; Jiang, Y.; Gao, X.; Wang, X.; Chen, W. Strongly Coupled Pd Nanotetrahedron/Tungsten Oxide Nanosheet Hybrids with Enhanced Catalytic Activity and Stability as Oxygen Reduction Electrocatalysts. *Journal of the American Chemical Society* **2014**, *136* (33), 11687-11697.

(19) Ge, X.; Sumboja, A.; Wuu, D.; An, T.; Li, B.; Goh, F. W. T.; Hor, T. S. A.; Zong, Y.; Liu, Z. Oxygen Reduction in Alkaline Media: From Mechanisms to Recent Advances of Catalysts. *ACS Catalysis* **2015**, *5* (8), 4643-4667.

(20) Sadhukhan, M.; Barman, S. Bottom-up fabrication of two-dimensional carbon nitride and highly sensitive electrochemical sensors for mercuric ions. *Journal of Materials Chemistry A* **2013**, *1* (8), 2752-2756.

(21) Long, H.; Shi, T.; Hu, H.; Jiang, S.; Xi, S.; Tang, Z. Growth of Hierarchal Mesoporous NiO Nanosheets on Carbon Cloth as Binder-free Anodes for High-performance Flexible Lithium-ion Batteries. *Scientific Reports* **2014**, *4* (1), 7413.

(22) Ali, F. S. M.; Arevalo, R. L.; Vandichel, M.; Speck, F.; Rautama, E.-L.; Jiang, H.; Sorsa, O.; Mustonen, K.; Cherevko, S.; Kallio, T. Hydrogen evolution in alkaline medium on intratube and surface decorated PtRu catalyst. *Applied Catalysis B: Environmental* **2022**, *315*, 121541.

(23) Shinagawa, T.; Garcia-Esparza, A. T.; Takanabe, K. Insight on Tafel slopes from a microkinetic analysis of aqueous electrocatalysis for energy conversion. *Scientific Reports* **2015**, *5* (1), 13801.

(24) Panigrahy, S.; Samanta, R.; Panda, P.; Mishra, R.; Barman, S. RuO2 as promoter in Pt-RuO2-nanostructures/carbon composite, a pH-universal catalyst for hydrogen evolution/oxidation reactions. *International Journal of Energy Research* **2022**, *46* (5), 6406-6420.

Ag-Pt Nanostructures/Carbon composite for Electrochemical Hydrogen Evolution and Oxygen Reduction Reaction in Alkaline medium

Chapter 4

(25) Shi, M.; Tong, X.; Li, W.; Fang, J.; Chen, L.; Ma, C.-a. Enhanced Electrocatalytic Oxygen Reduction on NiWOx Solid Solution with Induced Oxygen Defects. *ACS Applied Materials & Interfaces* **2017**, *9* (40), 34990-35000.

(26) Liang, Y.; Li, Y.; Wang, H.; Zhou, J.; Wang, J.; Regier, T.; Dai, H. Co3O4 nanocrystals on graphene as a synergistic catalyst for oxygen reduction reaction. *Nature Materials* **2011**, *10* (10), 780-786.

(27) Elezović, N. R.; Babić, B. M.; Gajić-Krstajić, L.; Ercius, P.; Radmilović, V. R.; Krstajić, N. V.; Vračar, L. M. Pt supported on nano-tungsten carbide as a beneficial catalyst for the oxygen reduction reaction in alkaline solution. *Electrochimica Acta* **2012**, *69*, 239-246.

(28) Kundu, M. K.; Bhowmik, T.; Barman, S. Gold aerogel supported on graphitic carbon nitride: an efficient electrocatalyst for oxygen reduction reaction and hydrogen evolution reaction. *Journal of Materials Chemistry A* **2015**, *3* (46), 23120-23135.

Carbon-Supported Ag Nanoparticle Aerogel for Electrocatalytic Hydrogenation of 5-(Hydroxymethyl)furfural to 2,5-Hexanedione in Acidic Conditions

Chapter 5

Chapter 5

Carbon-Supported Ag Nanoparticle Aerogel for Electrocatalytic Hydrogenation of 5-(Hydroxymethyl)furfural to 2,5-Hexanedione in Acidic Conditions

5.1 ABSTRACT

A growing interest in the electrochemical conversion of biomass-derived compounds is attributed to the extremely high sustainability of this process, which has the potential to generate value-added products and renewable electricity from biowastes. Design and synthesis of a high surface area interconnected porous network of metal nanomaterials are desirable for their application in the field of catalysis. In this chapter, the synthesis of carbon-supported Ag nanoparticle aerogel (Ag-aerogel-CN_x) for electrocatalytic hydrogenation of 5-(hydroxymethyl)furfural (HMF) is studied. The conversion of HMF to 2,5-hexanedione (HD) via ring-opening using ambient pressure and temperature is demonstrated. Here, water is used as the hydrogen source and silver is used as the metal catalyst, which eliminates the use of H_2 gas and the conventional method of hydrogenation that uses high pressure and temperature, which makes this reduction process more practical and efficient to produce HD. We investigated the most favorable potential for high faradic efficiency and provided a plausible reduction path from HMF to HD. The production of HD is strongly dependent on cathode potential and the nature of the electrolyte. The tuning of cathodic potential can give high Faradic efficiency and suppress the other undesired byproducts like H_2. High faradic efficiency of 78% and selectivity of 77 % are observed for the conversion of HMF to HD on Ag-aerogel-CN_x at -1.1 V vs. Ag/AgCl in 0.5 M H_2SO_4. This direct 6 electron reduction of HMF to HD can provide a new route to produce valuable intermediates from biomass.

Carbon-Supported Ag Nanoparticle Aerogel for Electrocatalytic Hydrogenation of 5-(Hydroxymethyl)furfural to 2,5-Hexanedione in Acidic Conditions

Chapter 5

5.2 INTRODUCTION

As petroleum reserves diminish and global climate change becomes more prevalent, sustainable fuel production pathways must be developed, such as biomass-derived carbohydrates[1-5]. Biomass has emerged as a superior alternative because of its renewability and the possibility of generating a vast number of compounds, many of which have similar or improved properties[4]. One class of dehydration products is the furan compounds that have a high potential to produce fuels and chemicals. Among all, 5-hydroxymethylfurfural (HMF) is one of the essential intermediates for biomass conversion, produced through dehydration of hexoses, primarily glucose and fructose[3]. HMF can be derived from cellulosic matter, which is the most abundant organic material on earth and can generate a wide variety of important chemicals, including polymers, pharmaceuticals, and transportation fuels[6, 7]. HMF can undergo many reactions[8] such as reduction[9], oxidation[10], etherification[2], dimerization[11] and reductive amination[12]. The reduction of HMF can produce a lot of different chemicals through many routes, which have vast applications in various fields.

There are many conventional methods for reducing HMF, but electrocatalytic hydrogenation (ECH) is receiving significant attention[13-15]. ECH is similar to thermo-catalytic hydrogenation, but the key difference is that the adsorbed hydrogen on the electrode surface is electrochemically generated by water reduction (Volmer reaction) rather than the H_2 dissociation. So the large activation barrier for H_2 dissociation can be avoided, and ECH can proceed under mild conditions without the need for external hydrogen supply and conventional hydrogenation catalysts like Pd, Pt, etc. However, hydrogen evolution reaction (HER), being the competitive reaction of ECH that consumes adsorbed hydrogen through Heyrovsky or Tafel reaction can lower the faradic efficiency of ECH.

Carbon-Supported Ag Nanoparticle Aerogel for Electrocatalytic Hydrogenation of 5-(Hydroxymethyl)furfural to 2,5-Hexanedione in Acidic Conditions

Chapter 5

The ECH of HMF can produce several products like 2,5-bis(hydroxymethyl)furan (BHMF), 2,5-Dimethylfuran (DMF), Hydroxy-2,5-hexanedione (HHD), and HD, which has numerous applications. There have been studies on the reduction of HMF to BHMF, where the most common reaction observed is the reduction of aldehyde to alcohol[9, 13, 16-22]. Benito et al. reported the conversion of HMF to BHMF on AgCu bimetallic nanoparticles with more than 80% selectivity and almost 100% conversion[18]. Li et al. reported HMF hydrogenation to BHMF on Ag/C with a yield of 85% and a faradic efficiency of 96.2%[20]. HD is another primary HMF reduction product, which can be obtained by the ring-opening reaction of HMF. Although, very few reports exist for the production of HD by reducing both aldehyde and alcohol groups followed by ring-opening. Choi et al. reported the direct conversion of HMF to HD using zinc as the catalyst and obtained faradic efficiency and selectivity of 72.4% and 81.6%, respectively[23]. In order to form HD from HMF, it has to go through ring-opening and reduction of both terminal functional groups like alcohol and aldehyde group using $6H^+$ and $6e^-$. The conventional conversion of HD from HMF uses precious metals, H_2 gas, and high temperature and pressure[24, 25]. HD is a vital biomass intermediate that can be used as a versatile intermediate to generate various chemicals and biofuels (Figure 5.1). Methylcyclopentane, a promising alternative fuel, can be efficiently produced from HD[26] (Figure 5.1). Apart from the applications of HD in alternative fuels, it can be used to synthesize isocarboxazid, an irreversible monoamine oxidase inhibitor (MAOI) that is used as an antidepressant. Similarly, para-xylene can be produced from HD, which is used as a precursor for producing terephthalic acid for polyethylene terephthalate (PET).

Carbon-Supported Ag Nanoparticle Aerogel for Electrocatalytic Hydrogenation of 5-(Hydroxymethyl)furfural to 2,5-Hexanedione in Acidic Conditions

Chapter 5
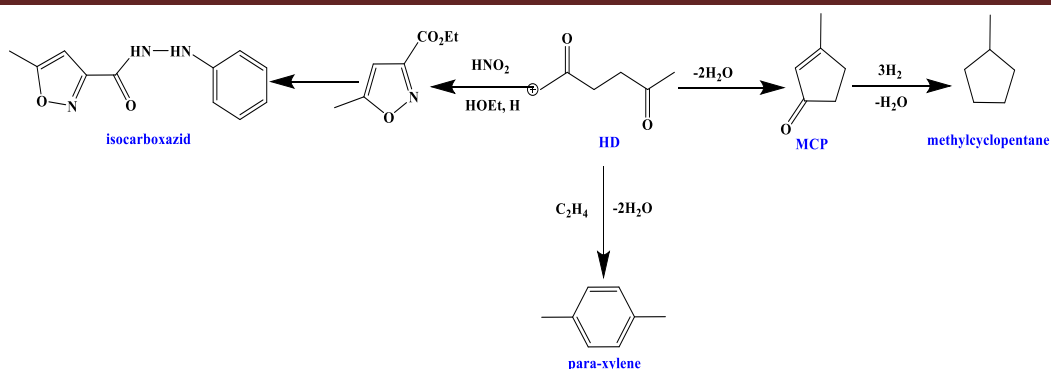
Figure 5.1. Conversion and potential use of HD.

Metal aerogels are unique solid materials with high porosity, extremely low density, and high surface area. It shows high electrical conductivity and catalytic properties[27]. They carry the combined physical and chemical properties of both macroscale and nanoscale materials integrating the behavior of different constituents in a single material, which makes aerogels more suitable in several applications like sensors, piezoelectrics, thermoresistors, and catalysis[28]. The first aerogel was discovered by Kistler in 1931[29] and since then extensive research has been going on to synthesize various aerogels. Several reports are there for the synthesis of silica aerogels[30], carbon aerogels[31], metal oxide aerogels[32], organic-inorganic hybrid aerogels[33], and metal chalcogenide aerogels[34]. For example, Leventis and co-workers synthesized various metallic aerogels of metals like Co, Ni, Cu, and Fe through nanosmelting of metal oxide-polymer hybrid composites[35-38]. While Eychmuller and coworkers reported the preparation method of multimetallic, bimetallic and monometallic noble metal aerogels (Pd, Pt, Ag, Au) and its application in electrocatalysis[28]. Reports on carbon-supported metallic aerogels for electrocatalytic applications are still to be explored. Silver is known as a poor catalyst for HER and shows better activity for electrocatalytic HMF reduction. Carbon-supported silver nanoparticles have been reported to have an intrinsically higher activity than bulk silver[20]. Choi et al. have studied the impact of HMF-metal interaction on the electrochemical reduction pathways of HMF on silver to demonstrate the representative

Carbon-Supported Ag Nanoparticle Aerogel for Electrocatalytic Hydrogenation of 5-(Hydroxymethyl)furfural to 2,5-Hexanedione in Acidic Conditions

Chapter 5

behavior of silver with a high selectivity towards the hydrogenation and discussed that the interaction between silver surface and HMF is very weak. Therefore, the changes in the intramolecular bond lengths in adsorbed HMF relative to free HMF are minimal, which is the optimum condition for hydrogenation[22].

Here, in this chapter, we have demonstrated the synthesis of carbon supported Ag nanoparticle aerogel for electrocatalytic hydrogenation of HMF to produce HD at ambient temperature and pressure using water as the hydrogen source. The pH-dependent behavior and potential-dependent behavior of the catalyst were examined. The reduction involves direct conversion of HMF to HD without producing DMF using $6H^+$ and $6e^-$. The most favorable reduction of HMF involves reduction of aldehyde to alcohol that is HMF to BHMF. However, this study shows a reductive ring opening of HMF to produce HD by reducing both aldehyde and alcohol. The optimal HD production in terms of faradic efficiency is 78% at -1.1 V in 0.5 M H_2SO_4. The high faradic efficiency is sensitive to the nature of the electrolyte and the cathodic potential.

5.3 EXPERIMENTAL SECTION

Materials:

Copper foil was purchased from MTI. Silver (I) nitrate ($AgNO_3$, 99+% assay), sodium borohydride ($NaBH_4$), formamide ($HCONH_2$), potassium sulfate (99+% assay) were purchased from Sigma Aldrich. Sulfuric acid (H_2SO_4, 98%) was purchased from Merck (Germany). 5-hydroxymethylfurfural (99+% assay) and 2,5-hexanedione (98+% assay) were bought from Spectrochem (India). 2,5-bis(hydroxymethyl)furan (BHMF) was purchased from Cayman Chemical Company. All these chemicals were used as they were received without further purification. Ar gas (99.99 % purity) was bought from Sigma Aldrich. Milli-Q water was obtained from an ultra-filtration system (Milli-Q, Millipore) and the measured conductivity was 35 mho.cm^{-1} at 25 °C.

Carbon-Supported Ag Nanoparticle Aerogel for Electrocatalytic Hydrogenation of 5-(Hydroxymethyl)furfural to 2,5-Hexanedione in Acidic Conditions

Chapter 5

Preparation of N-doped carbon:

N-doped carbon (CN_x) was synthesized according to our previously reported method[39]. 30 mL of Formamide ($HCONH_2$) was subjected to microwave heating at temperature of 180°C for 2h which then formed a brown-colored solution. The collected solution was evaporated by a rotary evaporator at a temperature of 180°C. Lastly, solid N-doped carbon was obtained by filtration followed by washing using distilled water and vacuum drying.

Synthesis of the Ag-aerogel-CN_x composite:

Ag-aerogel-CN_x composite was prepared by reducing silver (I) nitrate using $NaBH_4$ followed by ultrasonic treatment. At first, 46 mg of silver (I) nitrate was added in 5 mL of deionised water and sonicated for 30 minutes using a bath-sonicator. On the other side, 5 mg of as-prepared CN_x was dispersed in 2 mL of deionised water by sonicating for 10 minutes. A homogeneous mixture was obtained by mixing the above two solutions and sonicated for 30 minutes. At last, 50 mg of $NaBH_4$ was added to the above mixture and sonicated for additional 2 hrs. The obtained black solution was centrifugated at 1600 rpm and then repeatedly washed with deionized water & ethanol. The black precipitate was collected and dried under vaccum for further use.

Electrode Preparation:

Copper foil (1 cm ×1.5 cm) was used as a current collector to prepare the cathode. To clean the Cu foil, the foil was first washed with 2-propanol and water, then treated with 1 M HCl for 1 minute to remove any oxide layer on the surface followed by washing with water for further use. The stock solution for HMF reduction was prepared by adding 1 mg of Ag-aerogel-CN_x powder to 1 mL of Millipore water and sonicated for 30 minutes.

A

Carbon-Supported Ag Nanoparticle Aerogel for Electrocatalytic Hydrogenation of 5-(Hydroxymethyl)furfural to 2,5-Hexanedione in Acidic Conditions

Chapter 5

300 µL of aqueous stock solution was drop-casted and evaporated on cleaned Cu foil (1 cm ×1 cm) to prepare Ag-aerogel-CN_x electrode.

Electrochemical measurements:

LSV were performed in a conventional three-electrode system at an Autolab 302 N electrochemical station using Ag-aerogel-CN_x on a Cu foil as a working electrode, Pt wire as counter electrode and Ag/AgCl (3M KCl) as reference electrode without stirring. For LSV, 0.02 M HMF is added in 0.5 M H_2SO_4 and the potential is given from 0 to -1.2 V (RHE). For constant potential reduction, a divided H cell is used where the cathodic and anodic compartment is separated by Nafion membrane. By using the general formula $E_{RHE} = E_{Ag/AgCl} + E^0_{Ag/AgCl} + (0.059 \times pH)$, potential obtained from Ag/AgCl reference electrode was converted to RHE, where $E^0_{Ag/AgCl} = 0.1976$ at 25°C (3M KCl) and $E_{Ag/AgCl}$ is the working potential. Before experiment pH was also measured for all electrolytes.

Calculation of TOF:

The TOF is now calculated using the following two assumptions;

Assumptions: (a) Every metal atom present on the electrode are involved in HMF reduction reaction.

(b) It is the lower limit of the TOF value.

The TOF per active site for HMF reduction reaction was calculated by the following equation:

$$TOF\ (s^{-1}) = x = (J * S)/ (z * F * n)$$

J = current density (mA/cm^2) at particular overpotential ($\eta = -1.1$ V), S = Geometrical surface area of the working electrode, F = Faraday's constant (96485.3 coulomb/mol), z = the no. of electron involved in the HMF reduction process, where $z = 6$ for HD, n = Number of moles of active site on the electrode.

Carbon-Supported Ag Nanoparticle Aerogel for Electrocatalytic Hydrogenation of 5-(Hydroxymethyl)furfural to 2,5-Hexanedione in Acidic Conditions

Chapter 5

Characterizations:

Field-emission scanning electron microscope (FESEM) system (Carl Zeiss, Germany make, Model: ∑igma) was used for taking FESEM images. FESEM samples were prepared by casting a drop on a Si-wafer and dried at air around 45°C. The powder x-ray diffraction pattern (p-XRD) of samples was performed by Bruker DAVINCI D8 ADVANCE diffractometer equipped with Cu Kα radiation (λ= 0.15406 nm). NMR spectra were collected by Bruker Avance III 400 MHz NMR spectrometer. Transmission Electron Microscopy (TEM, JEOL F200) operated at 200 kV, was used to investigate surface morphology and also used to take High-Resolution TEM (HRTEM) images. For TEM sample preparation, 10 μL solution was taken from a stock solution of $4x10^{-5}$ mg/L and dried at air around 45°C. CHNS was analysed by using Euro Vector (Euro EA analyser 3000). XPS measurements were done by VG Microtech where monochromatic source was Mg K_α X-ray. XPS was taken from the sample deposited on Si wafer. And all the electrochemical measurements were performed with an Electrochemical Workstation (Autolab, Metrohm, PGSTAT 302N), equipped with rotating disk electrode (RDE). A conventional 3 electrode system, platinum wire as a counter electrode, carbon cloth as a working electrode and Ag/AgCl as a reference electrode were used. Smoothing was applied in chronoamperometric responses where needed to reduce noise in chronoamperometric measurements due to bubble accumulation. pH of the working solution was measured before experiment using Hanna (HI 2209) pH meter.

5.4 RESULTS AND DISCUSSIONS

Morphology and characterization

The Ag-aerogel-CN_x was synthesized by a simple ultra-sonication-assisted BH_4^- reduction of $AgNO_3$ in the presence of CN_x support (details in experimental section). The X-ray diffraction (XRD) pattern of Ag-aerogel-CN_x composite is shown in Figure 5.2a.

Carbon-Supported Ag Nanoparticle Aerogel for Electrocatalytic Hydrogenation of 5-(Hydroxymethyl)furfural to 2,5-Hexanedione in Acidic Conditions

Chapter 5

The diffraction peaks at 38.4°, 44.6°, 64.6°, and 77.6° in Ag-aerogel-CN_x composite are assigned as (111), (200), (220) and (311) crystalline planes of fcc Ag metal, and the obtained data is well matching with the standard JCPDS data of fcc Ag metal (PDF 01-071-4612). The surface area and porosity highly influence the electrocatalytic activity of a catalyst. Large surface area and high porosity are the most desired properties of an electrocatalyst. Figure 5.2b shows nitrogen adsorption/desorption isotherm of Ag-aerogel-CN_x. The specific surface area value was calculated to be 44 m^2 g^{-1} via analysis of the isotherm by the Brunauer−Emmett−Teller (BET) method.
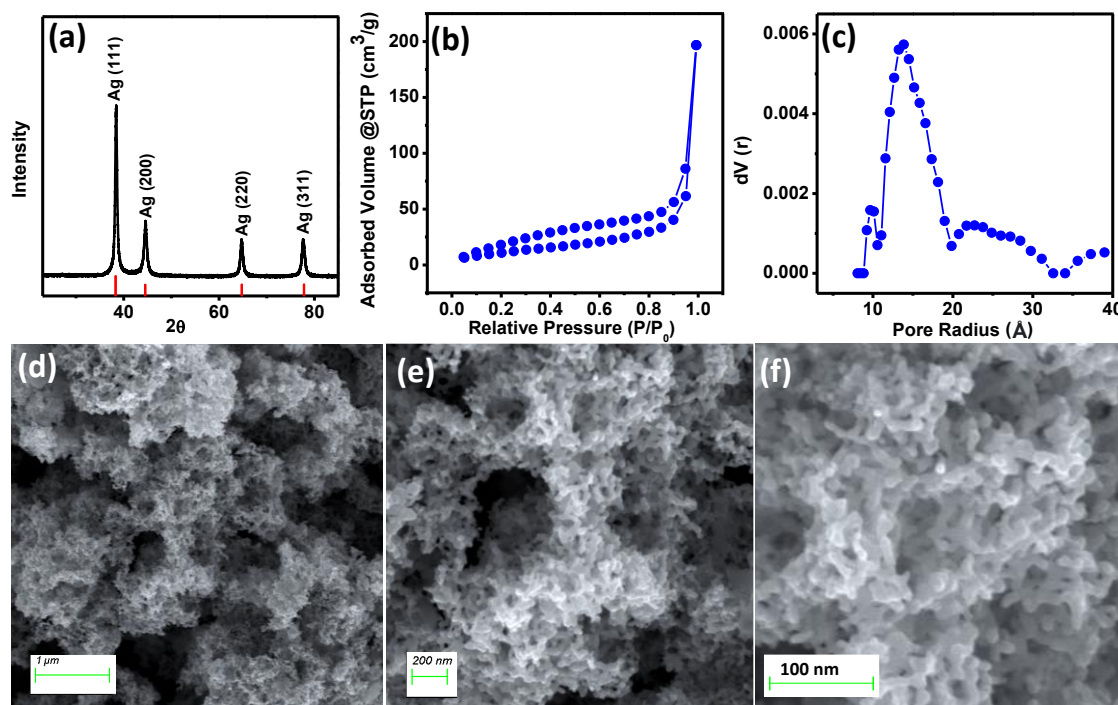
Figure 5.2. (a) p-XRD of Ag-aerogel-CN_x, (b) Nitrogen adsorption/desorption isotherm, (c) Pore size distributions (d, e, f) SEM images of Ag-aerogel-CN_x.

The BET surface areas of the noble metal aerogels are in the range of 32−168 m^2 g^{-1} [28]. The pore size distribution of Ag-aerogel-CN_x is given in Figure 5.2c. The pore size distribution was calculated by the density functional theory (DFT) method. XRD pattern and nitrogen adsorption/desorption isotherm of CN_x are provided in supporting

Carbon-Supported Ag Nanoparticle Aerogel for Electrocatalytic Hydrogenation of 5-(Hydroxymethyl)furfural to 2,5-Hexanedione in Acidic Conditions

Chapter 5

information. The diffraction peak in the XRD pattern of CN_x at around 26.8° can be assigned to (002) plane of graphitic carbon (Figure S5.1a). The specific surface area of CN_x from nitrogen adsorption/desorption isotherm was calculated to be 7 m^2 g^{-1} by BET method (Figure S5.1b).
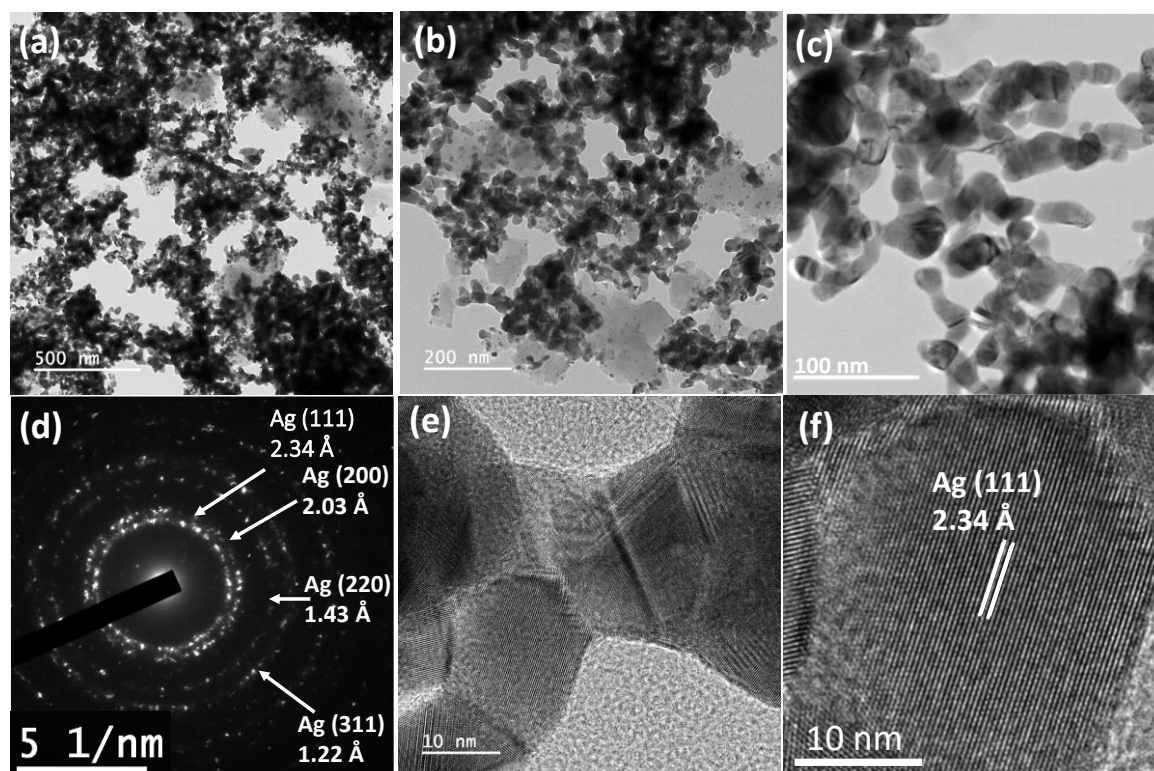
Figure 5.3. (a, b, c) TEM images, (d) SAED image, (e, f) HRTEM image of Ag-aerogel-CN_x.

The morphological characterization of Ag-aerogel-CN_x was studied by Field emission scanning electron microscopy (FESEM) and Transmission Electron Microscopy (TEM). SEM images of Ag-aerogel-CN_x are displayed in Figure 5.2 (d, e, and f). From the SEM images, it is seen that quasi-one-dimensional nanochains are formed. These one-dimensional extended nanochains are interconnected to form three-dimensional network-like structures with a large number of open pores making the Ag aerogel porous. SEM-EDX elemental mapping analysis of Ag-aerogel-CN_x is provided in Figure S5.2. The wt% of Ag metal present in Ag-aerogel-CN_x was found to be 79.9% by SEM-EDX.

Carbon-Supported Ag Nanoparticle Aerogel for Electrocatalytic Hydrogenation of 5-(Hydroxymethyl)furfural to 2,5-Hexanedione in Acidic Conditions

Chapter 5
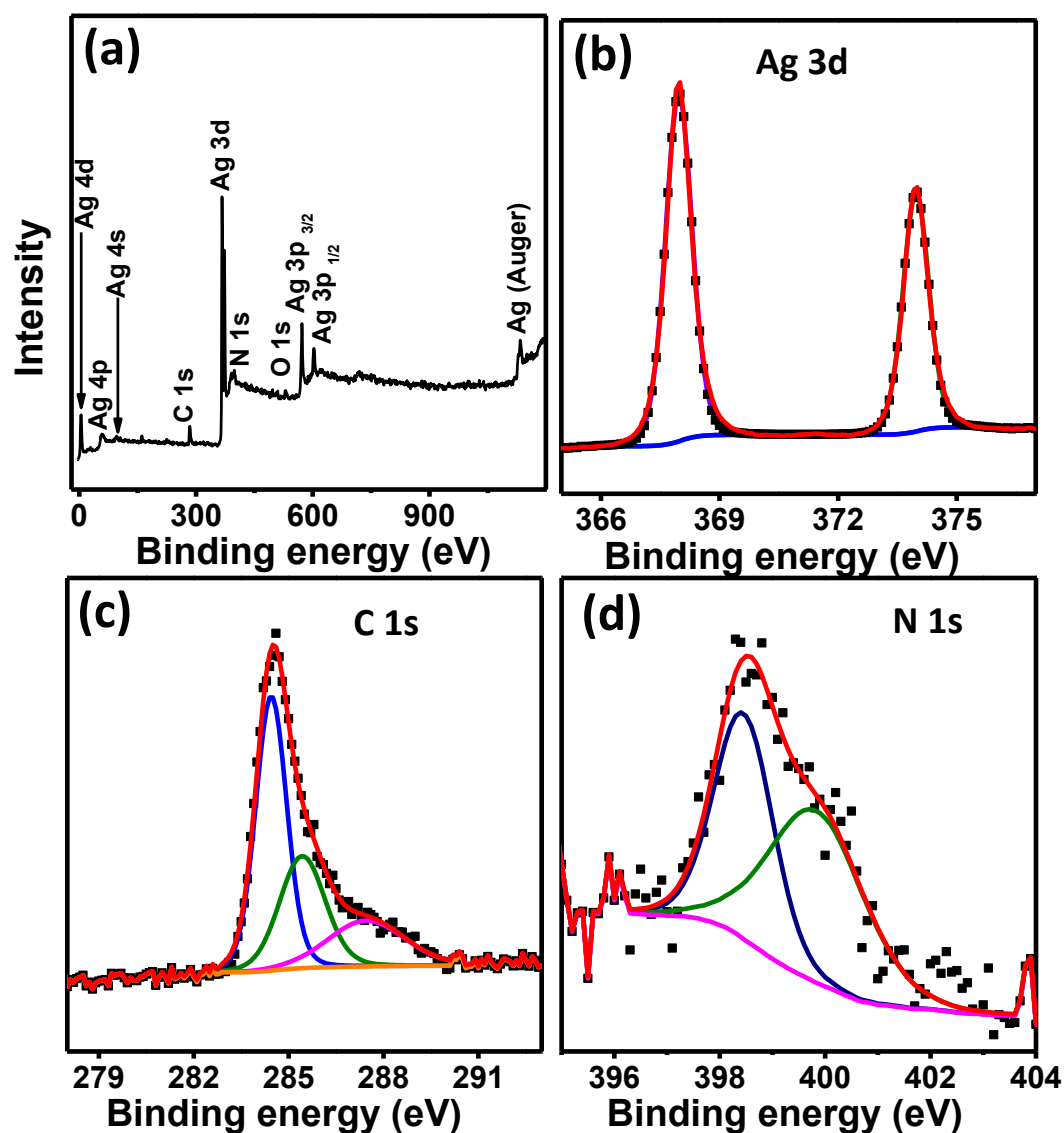
Figure 5.4. (a) XPS survey scan of Ag-aerogel-CN_x, High-resolution XPS spectra of (b) Ag3d, (c) C1s and (d) N1s of Ag-aerogel-CN_x catalyst.

The TEM images of Ag-aerogel-CN_x are displayed in Figure 5.3(a, b, c). The TEM image clearly shows the interconnected porous structure is supported on two-dimensional thin CN_x sheets. The average size of nanoparticles varies from 15 to 18 nm. These nanoparticles are fused to form nanochains of diameter of 15-20 nm and length of 50-

Carbon-Supported Ag Nanoparticle Aerogel for Electrocatalytic Hydrogenation of 5-(Hydroxymethyl)furfural to 2,5-Hexanedione in Acidic Conditions

Chapter 5

150 nm. The TEM images of CN_x are shown in Figure S5.1(c, d). The TEM images show the formation of two-dimensional thin sheets which is beneficial for the mass transfer and also improves the catalytic performance of the electrocatalyst[40]. The SAED image (Figure 5.3d) of Ag-aerogel-CN_x indicates a polycrystalline nature of the catalyst. Further, d-spacings were measured from the SAED image and are found to be 2.34, 2.03, 1.43, and 1.22 Å, corresponding to (111), (200), (220), and (311) planes of Ag respectively, and the obtained results are in good agreement with p-XRD results. Figure 5.3e, f shows the high resolution (HR) TEM image of the Ag-aerogel-CN_x catalyst. In Figure 5.3e, the presence of grain boundary is seen that acts as active site. The d-spacing value of 2.34 Å corresponds to the Ag (111) lattice plane of face-centered cubic Ag (Figure 5.3f). The orientation of these lattice fringes is similar. It suggests the silver aerogel generally grows along the Ag (111) plane. The elemental mapping images of Ag-aerogel-CN_x are also provided in Figure S5.3. From the elemental mapping image Ag nanochains are clearly visible and suggest the uniform distribution of Ag, carbon, and nitrogen in the nanochains. The XPS survey scan spectrum of Ag-aerogel-CN_x was provided in Figure 5.4a. The XPS spectrum clearly indicates the presence of silver (Ag), carbon(C), oxygen (O) and nitrogen (N) atoms. Figure 5.4b depicts the high-resolution Ag3d XPS spectra. Two peaks were used to fit Ag3d XPS spectra of Ag-aerogel-CNx catalyst. The peaks at 367.9 and 373.9 eV can be assigned to $Ag3d_{3/2}$ and $Ag3d_{5/2}$ peaks respectively. High-resolution C1s XPS spectra is shown in Figure 5.4c. The carbon C 1s XPS can be deconvoluted into three peaks as sp^2- bonded carbon at 284 eV, sp^3-bonded carbon at 285.5 eV and C-N bonded carbon at 287.5 eV. The N 1s spectra given in Figure 5.4d, can be deconvoluted into two peaks and can be assigned to pyridinic nitrogen (398.47 eV), pyrrolic nitrogen (399.9 eV) respectively. Heteroatom doping can greatly tune the electrochemical property of electrocatalyst. The presence of N atom in the

composite improves the electrochemical property because of increased charge transfer kinetics[40-44]. Kim and co-workers[45] suggested that presence of the N species improved the electrocatalytic activity of cobalt-doped g-C_3N_4 and also showed that among the different types of N functional groups, graphitic and pyridinic nitrogen species are known to play a more significant role in the improvement of electrocatalytic performance due to superior charge mobility[46].

Product Identification and Quantification:

Detection and quantification of products were done using Bruker Avance III 400 MHz nuclear magnetic resonance (NMR) spectrometer. For quantification, calibration curves were generated for known concentrations of reactant and product using NMR spectroscopy. A series of known concentrations of HMF and HD solutions were analyzed in NMR for the signature peak and compared with the unknown concentrations of HMF and HD to determine their concentration. For NMR analysis, 450 µL of electrolyte solution was taken, to which 50 µL of D_2O was added. The NMR spectra were collected using a water suppression method. The NMR signals of water peak around 4.7 ppm were suppressed, and it did not affect the characteristic peaks of the products. The products were further confirmed by gas chromatography (GC). In GC, the compounds were eluted according to their retention time using Shimadzu GC spectrometer with SH-Rxi-5Sil MS column. The oven temperature was increased from 80 ºC to 300 ºC with a rise of 20 ºC per minute. HMF and HD were eluted first, and then the characteristic peaks were compared to the peaks obtained from the reaction mixture.

Electrochemical HMF reduction:

The main obstacle in achieving high faradic efficiency for HMF hydrogenation is competitive Hydrogen evolution reaction which occurs in the same potential. Choosing

Carbon-Supported Ag Nanoparticle Aerogel for Electrocatalytic Hydrogenation of 5-(Hydroxymethyl)furfural to 2,5-Hexanedione in Acidic Conditions

Chapter 5

a good catalyst for HMF reduction among poor H_2 evolution catalysts is necessary to achieve high faradic efficiency. Silver is known as a poor catalyst for HER hence investigated for HMF hydrogenation. To understand the catalyst-support interaction, the catalytic activities of Ag-aerogel-CN_x catalyst and Ag nanostructure without CN_x support (Ag) were analyzed using Linear Sweep Voltammetry (LSV). LSV was performed in an undivided electrolyte cell with three-electrode system (Ag-aerogel-CN_x on Cu foil as working electrode, Ag/AgCl as reference electrode and Pt wire as counter electrode) without and with 20 mM of HMF in 0.5 M H_2SO_4 (Figure 5.5a). At the outset, the electrolyte was purged with argon prior to the reduction to remove dissolved oxygen in the electrolyte. The potential was scanned from 0 to the negative potential of -1.1V vs Ag/AgCl at 10 mV/s scan rate and LSV was performed without stirring. As shown in Figure 5.5a, Ag-aerogel-CN_x showed less overpotential for reduction of HMF than Ag. Before adding HMF, both Ag-aerogel-CN_x and Ag showed almost same activity but after the addition of HMF, Ag-aerogel-CN_x outperformed Ag. The turnover frequency (TOF) of both the catalysts, Ag-aerogel-CN_x and Ag were also compared. The TOF value at a potential of -1.0 V for Ag-aerogel-CN_x and Ag are calculated to be 75.26 s^{-1} and 51.98 s^{-1} respectively [47](details in supporting information). Similarly, to examine the contribution of the Cu foil, LSVs of Ag-aerogel-CN_x on Cu foil and of only Cu foil was also studied (Figure S5.4a). Cu foil showed a high onset potential and more overpotential for the reduction as compared to Ag-aerogel-CN_x on Cu foil before and after the addition of HMF. This means the contribution of Cu foil in HMF hydrogenation is negligible. The current shown by the catalyst prior to the addition of HMF was purely due to HER for all the catalysts. However, after the addition of HMF, Cu foil does not show any decrease in onset potential and the decrease in onset potential for Ag-aerogel-CN_x on Cu foil was due to HMF reduction.

Carbon-Supported Ag Nanoparticle Aerogel for Electrocatalytic Hydrogenation of 5-(Hydroxymethyl)furfural to 2,5-Hexanedione in Acidic Conditions

Chapter 5
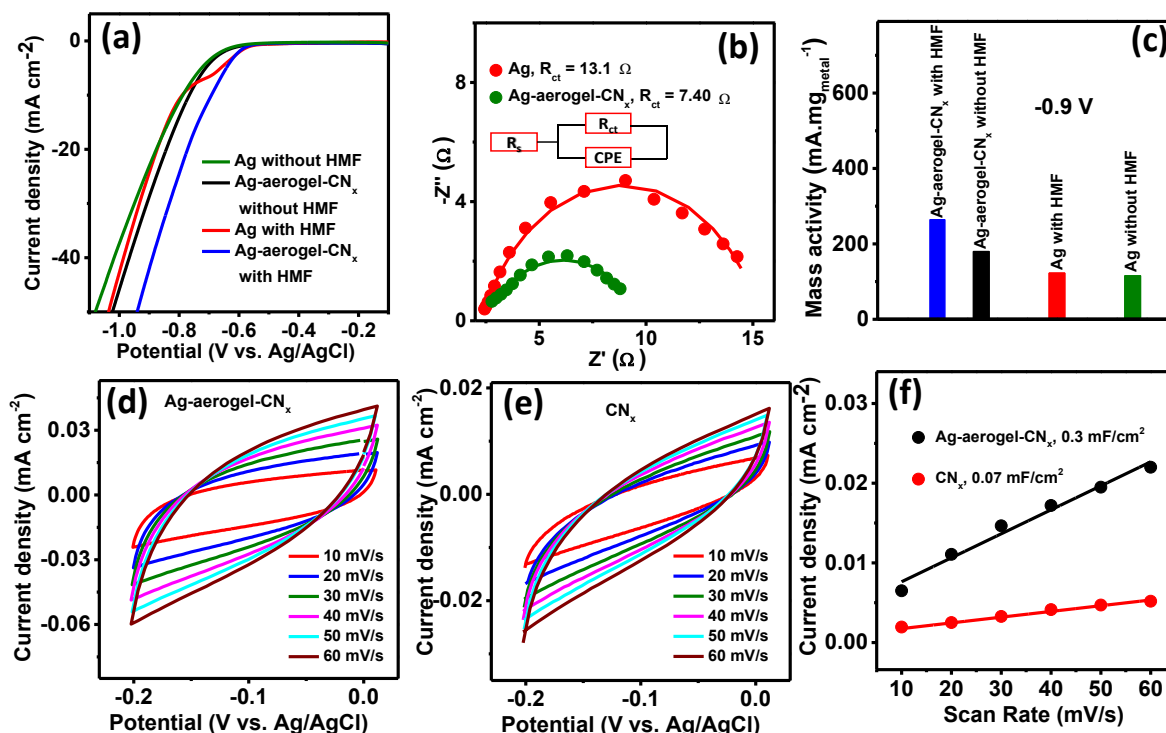
Figure 5.5. (a) Non-iR corrected LSV activity of Ag-aerogel-CN_x and Ag in 0.5 M H_2SO_4 in the presence and absence of 20 mM of HMF, (b) Nyquist plots of Ag-aerogel-CN_x and Ag, (c) Mass activity of different catalysts at -0.9V potential. Electrochemical double-layer capacitance measurements of (d) Ag-aerogel-CN_x, (e) CN_x in 0.5 M H_2SO_4 and (f) C_{dl} value.

The change in potential after the addition of HMF in the presence of Ag-aerogel-CN_x on Cu foil confirms that HMF reduction occurs before HER, which depicts HMF reduction is more favorable than HER for Ag-aerogel-CN_x catalyst. To have a better understanding of the reaction pathway, we also investigated the kinetics of HMF reduction by analyzing electrochemical impedance spectroscopy (EIS) spectra (Figure 5.5b). The spectra were collected in the frequency range of 0.1-100 kHz under open circuit potential with an AC amplitude of 10 mV in 0.5 M H_2SO_4. The EIS of Ag-aerogel-CN_x was compared with Ag after the addition of HMF. The inset shows the circuit using which the EIS data are fitted where R_s depicts solution resistance, diameter of the semicircle depicts charge

Carbon-Supported Ag Nanoparticle Aerogel for Electrocatalytic Hydrogenation of 5-(Hydroxymethyl)furfural to 2,5-Hexanedione in Acidic Conditions

Chapter 5

transfer resistance (R_{ct}) and CPE depicts constant phase element. The EIS spectrum of the catalyst Ag for HMF reduction showed a larger semicircle, however, for Ag-aerogel-CN_x displayed a smaller semicircle. A smaller semicircle depicts the minimum R_{ct} value and better electronic conductivity. R_{ct} values of Ag and Ag-aerogel-CN_x are 13.1 Ω and 7.40 Ω respectively. The EIS spectrum of the catalyst Ag-aerogel-CN_x was also examined before and after the addition of HMF (Figure S5.4b). The R_{ct} value fitted by the circuit after adding HMF is 23Ω and before adding HMF is 67.6 Ω. The lower R_{ct} value of Ag-aerogel-CN_x than only Ag can be attributed to the synergistic effect of catalyst-support interaction, which may be the possible reason behind enhancement of the electrochemical activity of Ag-aerogel-CN_x. The presence of N species in support-CN_x sheet also improves the charge transfer kinetics of the catalyst. The mass activity (MA) of the catalysts in the absence and presence of HMF were evaluated (Figure 5.5c) and the values for Ag-aerogel-CN_x in the presence and absence of HMF at potential value of -0.9 V were calculated to be 264.5 and 180.06 mAmg$_{metal}^{-1}$ respectively. The HMF reduction of Ag catalyst without CN_x support was also measured and MA values in the presence and absence of HMF at potential of 0.9 V were found to be 122.85 and 115.645 mAmg$_{metal}^{-1}$ respectively. The effect of metal loading on the performance of electrocatalyst was also analyzed. Ag-aerogel-CN_x catalysts with varying metal loading (50, 70, 79, and 90 wt%) were also synthesized, and their performance was evaluated using LSV (Figure S5.4c). The activity was found to increase with the increase in metal loading and maximum electrocatalytic activity was achieved with 79 wt% metal loading. The electrochemically active surface area (ECSA) is directly proportional to its electrochemical double-layer capacitance (C_{dl}). The ECSA of Ag-aerogel-CN_x and CN_x was calculated in terms of C_{dl} by recording cycling voltammetry (CV) at the non-faradic region in the range of 10 to 60 mV/s scan rate in 0.5 M H_2SO_4 given in Figure 5.5d and

Carbon-Supported Ag Nanoparticle Aerogel for Electrocatalytic Hydrogenation of 5-(Hydroxymethyl)furfural to 2,5-Hexanedione in Acidic Conditions

Chapter 5

5.5e respectively. The slope of current density and scan rate is given in Figure 5.5f. The obtained C_{dl} value from the slope for Ag-aerogel-CN_x is higher than CN_x. Higher C_{dl} value implies higher ECSA which means more active sites for catalyzing HMF reduction reaction (HMFRR).
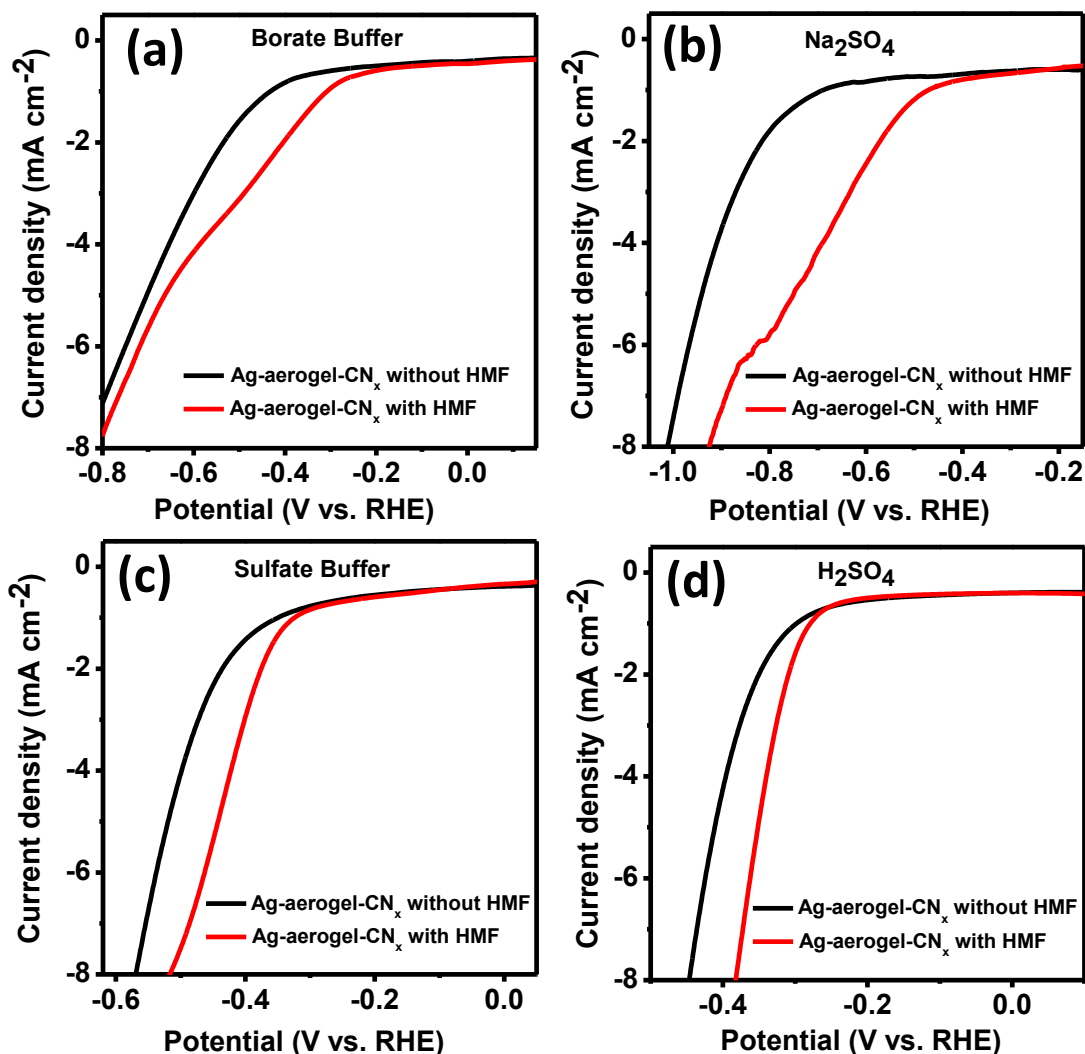
Figure 5.6. LSV polarization curve of Ag-aerogel-CN_x without and with HMF in (a) borate buffer solution, (b) Na_2SO_4 solution, (c) sulfate buffer solution and (d) H_2SO_4 solution.

HMF reduction is pH sensitive. To check the pH sensitivity of the HMF reduction, LSV has been carried out in different solutions of different pH like borate buffer solution (pH = 9.2), Na_2SO_4 solution (pH = 5.8), sulfate buffer solution (pH= 2) and 0.5 M H_2SO_4 (pH

Carbon-Supported Ag Nanoparticle Aerogel for Electrocatalytic Hydrogenation of 5-(Hydroxymethyl)furfural to 2,5-Hexanedione in Acidic Conditions

Chapter 5

= 0.9) as given in Figure 5.6. The onset potential for HMF reduction is less negative than HER for all the media. In acidic media, Ag-aerogel-CN_x is most active and the current obtained for both HER and HMF reduction is the highest; however, the onset potential difference between the HER and HMF reduction is less in acid media. One can assume the initial HMF reduction occurs through water molecules from the electrolyte with only a weak influence of the metal in neutral pH or buffer solutions[13]. HER takes place through the formation of adsorbed H_{ads}, irrespective of its source, whether it is H^+ or H_2O[21], according to equations (1) and (2) :

$$H^+ + e^- \leftrightarrow H_{ads} \tag{1}$$

$$H_2O + e^- \leftrightarrow H_{ads} + OH^- \tag{2}$$

The onset potential for HMF reduction and the onset potential for HER exhibit a close correlation in acidic conditions. Hence it can be observed that the difference in onset potentials for HMF reduction and HER is more in buffer and neutral solutions than in acidic solutions (Figure 5.6). The similarity in onset potential for HER and HMF reduction suggests a weak catalytic effect on the first electron transfer reaction[19]. The onset potential for HMF reduction shifts to more positive potential in acidic electrolytes[21]. The metals are also more active for HER in acidic solutions than in neutral or basic solutions. Koper et al. reported the close correlation between the onset potential of HER and HMF reduction in acidic solution might suggest that the adsorbed hydrogen (H_{ads}) on the electrocatalyst surface is involved in the HMF reduction, at least in acidic solution[21]. Hence, one can assume in an acidic solution; adsorbed hydrogen helps in HMF hydrogenation.

To investigate the product, and to calculate the Faradic efficiency of HMF reduction, the reaction was performed at different applied potentials in divided H-cell to obtain

Carbon-Supported Ag Nanoparticle Aerogel for Electrocatalytic Hydrogenation of 5-(Hydroxymethyl)furfural to 2,5-Hexanedione in Acidic Conditions

Chapter 5

mechanistic insights regarding potential-dependent HMF hydrogenation. The cathodic compartment and anodic compartment in H-cell were separated by a Nafion membrane. The cathodic compartment contains working electrode and reference electrode, and the anodic compartment contains counter electrode. Anodic compartment contained 14 ml of 0.5 M H_2SO_4, whereas the cathodic compartment was charged with 14mL of 0.5 M H_2SO_4 and 20 mM HMF. Throughout the reaction in the cathodic compartment, Argon gas was purged, and rotation of 500 rpm was given with the help of a magnetic stirrer in order to ensure the minimal Faradic loss. The reduction products were analysed and quantified by ^{1}H NMR (Figure S5.5). Based on the results, the Faradic efficiency and the selectivity of HD formation are calculated by using the following equations labelled equations 3 and 4.

$$FE\ (\%) = \frac{mol\ of\ HD\ formed}{total\ charge\ passed\ (c)/\ (F \times n)} \times 100\% \tag{3}$$

$$selectivity\ of\ HD\ (\%) = \frac{mol\ of\ HD\ formed}{mol\ of\ HMF\ consumed} \times 100\% \tag{4}$$

Where n is the number of electrons required to form HD from HMF and F is the Faraday constant (96485 C mol^{-1}). BHMF, which is the most expected product by HMF reduction, was not found in the reduction products in 0.5 M H_2SO_4. HD can be identified by ^{1}H NMR spectra (Figure S5.5). The constant potential HMF reduction was carried out through a range of potential from -0.8 to -1.4V vs. Ag/AgCl. For the catalyst, high faradic efficiency of 78% and selectivity of 77% were found at -1.1V vs. Ag/AgCl. The reduction of HMF to BHMF requires 2e$^-$ and HMF to HD proceeds through the 6e$^-$ process, respectively (Figure 5.7). No DMF was detected through ^{1}H NMR spectra, which means DMF is not formed in the electrochemical conversion of HMF to HD.

Carbon-Supported Ag Nanoparticle Aerogel for Electrocatalytic Hydrogenation of 5-(Hydroxymethyl)furfural to 2,5-Hexanedione in Acidic Conditions

Chapter 5
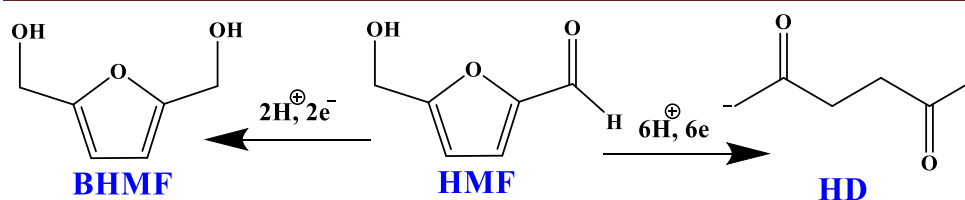
Figure 5.7. Electrochemical reduction of HMF: Route for the formation of BHMF and HD.

Table 5.1. Electrocatalytic hydrogenation of HMF on Ag-aerogel-CN_x at various potentials.

Potential	Average Current density (mA/cm^2)	HD formed (μmol)	FE%	Selectivity%
-0.8	20	11.3	69%	63%
-0.9	23.4	15.6	71%	69%
-1.0	26	18.9	74%	73%
-1.1	32	24	78%	77%
-1.2	40	20	73%	74%
-1.4	96	17.5	67%	60%

The production of HD and H_2 is strongly dependent on cathodic potential. The effect of potential on the Faradic efficiency and selectivity was investigated by varying the reduction potentials, and the results are given in Table 1. On the basis of the FEs and selectivity for HD production, the reduction potential can be divided into three regions. The first region is -0.8V to -1.0V vs. Ag/AgCl. In this range, the Faradic efficiency for HD production is less as the potential was not sufficient to reduce HMF. The second region is -1.1V to -1.3V vs. Ag/AgCl. In this region, both selectivity and FE increase to their maximum value. The maximum Faradic efficiency and selectivity observed for HD formation at -1.1V are 78% and 77%, respectively. This indicates that -1.1V potential is

Carbon-Supported Ag Nanoparticle Aerogel for Electrocatalytic Hydrogenation of 5-(Hydroxymethyl)furfural to 2,5-Hexanedione in Acidic Conditions

Chapter 5

sufficient to reduce HMF molecules, and the other competitive reactions considerably get diminished in this potential window. The third potential region is the region where the reduction potential is more than -1.3V. As the potential increased after -1.3V, the average current density and Faradic efficiency decreased since HER is more favorable at higher potential. The production of HD and Faradic efficiency depends on the nature of the electrolyte as well. We have also tried the reduction of HMF in sulfate buffer (pH=2), Na_2SO_4 (pH=5.61), and borate buffer (pH=9.2). In sulfate buffer, HD and BHMF are produced with less efficiency, whereas at high pH (borate buffer), only BHMF was observed. This suggests nature of the electrolyte plays a vital role in the hydrogenation of HMF.
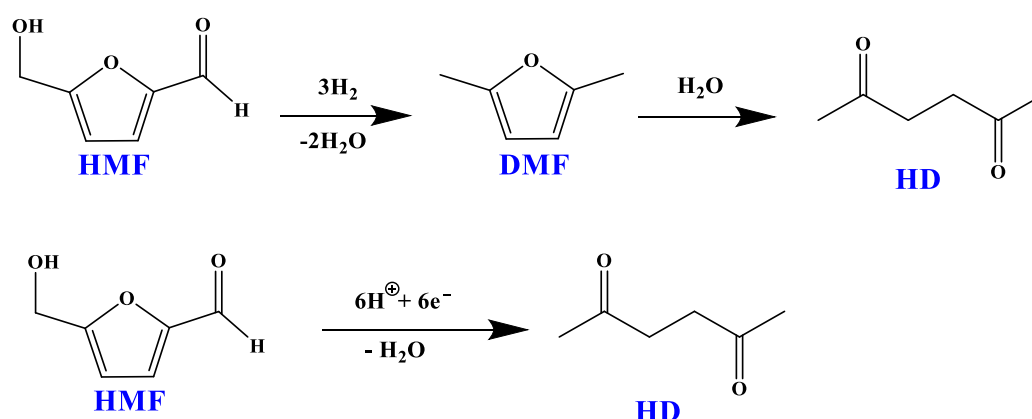
Figure 5.8. The alternative pathways for HD production from HMF.

The conversion of HMF to HD can go through three steps such as the substitution of terminal hydrogen for alcohol, conversion of –CHO group to terminal alkane followed by ring-opening. The production of HD from HMF should go through Clemmensen reduction to convert aldehyde or ketone to hydrocarbon, which consumes 4 electrons and 4 protons, and by removing an H_2O molecule. There are two possible pathways for HD production from HMF are exists which can be seen in Figure 5.8. One possible way is the direct conversion of HMF to HD using 6e⁻ and 6H⁺ and the other possible way is the two-step method which goes through DMF production. In this two-step method, the

197

Carbon-Supported Ag Nanoparticle Aerogel for Electrocatalytic Hydrogenation of 5-(Hydroxymethyl)furfural to 2,5-Hexanedione in Acidic Conditions

Chapter 5

reduction of HMF generally undergoes through the production of DMF followed by hydrolysis of DMF to HD[23]. However, DMF was not detected as an intermediate or as a byproduct. It suggests that the HMF reduction on Ag-aerogel-CN$_x$ in 0.5M H$_2$SO$_4$ is not following the two-step reduction process, that is, the conversion of HMF to DMF followed by hydrolysis to form HD. Herein, these two steps are not occurring in a decoupled sequence. Hence the reductive ring opening of HMF to HD is going through a concerted mechanism; that is, the Clemmensen reaction and acid-catalyzed ring-opening are going through a coupled manner[23]. The ring-opening of HMF should be similar to other established ring-opening mechanisms of furan compounds which consist of the bond breaking of C2 and the furan oxygen through the attack of water molecule, which acts as nucleophile[48]. So the two oxygen atoms of carbonyl groups of HD are one from the furan ring, and another is from the water molecule.
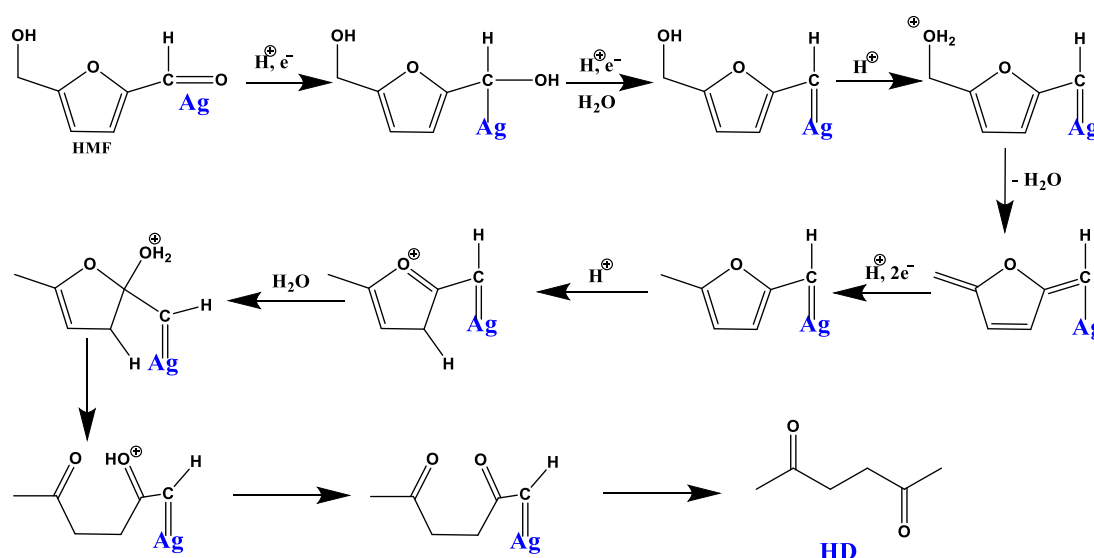
Figure 5.9. The plausible mechanism of conversion of HMF to HD.

To propose a plausible mechanism for electrocatalytic hydrogenation of HMF, the step of substituting terminal hydrogen for alcohol is occurring before, during, or after the Clemmensen reaction should be examined. Recently, Choi et al. reported the formation of HD from 5-methylfurfural (5-MF). Here, 5-MF is similar to 5-HMF, which has a furan

ring and a formyl group; however, it lacks a terminal alcohol group. They showed that HD was detected as the only product from the reduction of 5-MF[23]. This proves lack of an alcohol group is not affecting the reduction and ring-opening process of HMF. By combining all the factors, a predictive mechanism for HD production is proposed and depicted in Figure 5.9. The Clemmensen-like reduction and the ring-opening by the nucleophilic attack were observed from the mechanism. Through the mechanism, it can be easily seen one of the carbonyl oxygens of HD is from water while the other one is from HMF by Clemmensen reduction.

The high activity of the catalyst can be attributed to the following factors, (1) The three-dimensional-network-like porous structure of Ag-aerogel-CN_x is responsible for the enhanced electrochemical surface area. The high electrochemical surface area is crucial for providing an active site for HMF reduction. (2) The presence of a large number of (111) planes in Ag-aerogel-CN_x. It is reported that metal (111) planes are more active for electrochemical performances[27, 49]. An ample amount of Ag (111) planes is visible from p-XRD (Figure 5.2a) and SAED image (Figure 5.3d). From the HRTEM image (Figure 5.3f), it can be suggested that the growth of Ag-aerogel occurred in Ag (111) plane directions. The high catalytic activity of Ag-aerogel-CN_x can also be ascribed to the presence of an adequate amount of Ag (111) planes. (3) The synergistic effect due to metal and support interaction at Ag-aerogel-CN_x efficiently enhances the catalytic activity and leads to fast electron transfer (Figure 5.5).

5.5 CONCLUSIONS:

This chapter demonstrates a simple one-step method for the synthesis of carbon-supported Ag nanoparticle aerogel for electrocatalytic hydrogenation of HMF. The porous network-like structure was formed by the interconnection of Ag nanoparticles on

CN_x sheets. High porosity and large electrochemically active surface area of the catalyst offer adequate active sites for HMF reduction. The Ag-aerogel-CN_x catalyst efficiently reduced HMF to HD by ring-opening using $6e^-$ and $6H^+$. The formation of HD and the Faradic efficiency is highly dependent on both the nature of the electrolyte and the cathode potential. The reduction was performed in the acidic electrolyte under ambient conditions using water as a hydrogen source. High Faradic efficiency of 78% and selectivity of 77% for the production of HD were obtained using Ag-aerogel-CN_x catalyst at -1.1 V vs. Ag/AgCl in 0.5 M H_2SO_4 solution. The synthesized Ag-aerogel-CN_x catalyst is successfully suppressing HER and hydrogenates the HMF to HD at low overpotential with a low R_{ct} value. The direct conversion of HMF to HD can provide a new route to produce valuable intermediates utilizing biomass**.**

5.6 REFERENCES:

(1) Gallo, J. M. R.; Alonso, D. M.; Mellmer, M. A.; Dumesic, J. A. Production and upgrading of 5-hydroxymethylfurfural using heterogeneous catalysts and biomass-derived solvents. *Green Chemistry* **2013**, *15* (1), 85-90.

(2) Balakrishnan, M.; Sacia, E. R.; Bell, A. T. Etherification and reductive etherification of 5-(hydroxymethyl)furfural: 5-(alkoxymethyl)furfurals and 2,5-bis(alkoxymethyl)furans as potential bio-diesel candidates. *Green Chemistry* **2012**, *14* (6), 1626-1634.

(3) van Putten, R.-J.; van der Waal, J. C.; de Jong, E.; Rasrendra, C. B.; Heeres, H. J.; de Vries, J. G. Hydroxymethylfurfural, A Versatile Platform Chemical Made from Renewable Resources. *Chemical Reviews* **2013**, *113* (3), 1499-1597.

(4) Huber, G. W.; Iborra, S.; Corma, A. Synthesis of Transportation Fuels from Biomass: Chemistry, Catalysts, and Engineering. *Chemical Reviews* **2006**, *106* (9), 4044-4098.

(5) Teong, S. P.; Yi, G.; Zhang, Y. Hydroxymethylfurfural production from bioresources: past, present and future. *Green Chemistry* **2014**, *16* (4), 2015-2026.

Carbon-Supported Ag Nanoparticle Aerogel for Electrocatalytic Hydrogenation of 5-(Hydroxymethyl)furfural to 2,5-Hexanedione in Acidic Conditions

Chapter 5

(6) Lee, Y.-C.; Dutta, S.; Wu, K. C. W. Integrated, Cascading Enzyme-/Chemocatalytic Cellulose Conversion using Catalysts based on Mesoporous Silica Nanoparticles. *ChemSusChem* **2014**, *7* (12), 3241-3246.

(7) Peng, W.-H.; Lee, Y.-Y.; Wu, C.; Wu, K. C. W. Acid–base bi-functionalized, large-pored mesoporous silica nanoparticles for cooperative catalysis of one-pot cellulose-to-HMF conversion. *Journal of Materials Chemistry* **2012**, *22* (43), 23181-23185.

(8) Simoska, O.; Rhodes, Z.; Weliwatte, S.; Cabrera-Pardo, J. R.; Gaffney, E. M.; Lim, K.; Minteer, S. D. Advances in Electrochemical Modification Strategies of 5-Hydroxymethylfurfural. *ChemSusChem* **2021**, *14* (7), 1674-1686.

(9) Sanghez de Luna, G.; Ho, P. H.; Lolli, A.; Ospitali, F.; Albonetti, S.; Fornasari, G.; Benito, P. Ag Electrodeposited on Cu Open-Cell Foams for the Selective Electroreduction of 5-Hydroxymethylfurfural. *ChemElectroChem* **2020**, *7* (5), 1238-1247.

(10) Liu, W.-J.; Dang, L.; Xu, Z.; Yu, H.-Q.; Jin, S.; Huber, G. W. Electrochemical Oxidation of 5-Hydroxymethylfurfural with NiFe Layered Double Hydroxide (LDH) Nanosheet Catalysts. *ACS Catalysis* **2018**, *8* (6), 5533-5541.

(11) Kloth, R.; Vasilyev, D. V.; Mayrhofer, K. J. J.; Katsounaros, I. Electroreductive 5-Hydroxymethylfurfural Dimerization on Carbon Electrodes. *ChemSusChem* **2021**, *14* (23), 5245-5253.

(12) Roylance, J. J.; Choi, K.-S. Electrochemical reductive amination of furfural-based biomass intermediates. *Green Chemistry* **2016**, *18* (20), 5412-5417.

(13) Kwon, Y.; de Jong, E.; Raoufmoghaddam, S.; Koper, M. T. M. Electrocatalytic Hydrogenation of 5-Hydroxymethylfurfural in the Absence and Presence of Glucose. *ChemSusChem* **2013**, *6* (9), 1659-1667.

(14) Chadderdon, X. H.; Chadderdon, D. J.; Matthiesen, J. E.; Qiu, Y.; Carraher, J. M.; Tessonnier, J.-P.; Li, W. Mechanisms of Furfural Reduction on Metal Electrodes: Distinguishing Pathways for Selective Hydrogenation of Bioderived Oxygenates. *Journal of the American Chemical Society* **2017**, *139* (40), 14120-14128.

Carbon-Supported Ag Nanoparticle Aerogel for Electrocatalytic Hydrogenation of 5-(Hydroxymethyl)furfural to 2,5-Hexanedione in Acidic Conditions

Chapter 5

(15) Suastegui, M.; Matthiesen, J. E.; Carraher, J. M.; Hernandez, N.; Rodriguez Quiroz, N.; Okerlund, A.; Cochran, E. W.; Shao, Z.; Tessonnier, J.-P. Combining Metabolic Engineering and Electrocatalysis: Application to the Production of Polyamides from Sugar. *Angewandte Chemie International Edition* **2016**, *55* (7), 2368-2373.

(16) Nilges, P.; Schröder, U. Electrochemistry for biofuel generation: production of furans by electrocatalytic hydrogenation of furfurals. *Energy & Environmental Science* **2013**, *6* (10), 2925-2931.

(17) Roylance, J. J.; Kim, T. W.; Choi, K.-S. Efficient and Selective Electrochemical and Photoelectrochemical Reduction of 5-Hydroxymethylfurfural to 2,5-Bis(hydroxymethyl)furan using Water as the Hydrogen Source. *ACS Catalysis* **2016**, *6* (3), 1840-1847.

(18) Sanghez de Luna, G.; Ho, P. H.; Sacco, A.; Hernández, S.; Velasco-Vélez, J.-J.; Ospitali, F.; Paglianti, A.; Albonetti, S.; Fornasari, G.; Benito, P. AgCu Bimetallic Electrocatalysts for the Reduction of Biomass-Derived Compounds. *ACS Applied Materials & Interfaces* **2021**, *13* (20), 23675-23688.

(19) Kwon, Y.; Schouten, K. J. P.; van der Waal, J. C.; de Jong, E.; Koper, M. T. M. Electrocatalytic Conversion of Furanic Compounds. *ACS Catalysis* **2016**, *6* (10), 6704-6717.

(20) Chadderdon, X. H.; Chadderdon, D. J.; Pfennig, T.; Shanks, B. H.; Li, W. Paired electrocatalytic hydrogenation and oxidation of 5-(hydroxymethyl)furfural for efficient production of biomass-derived monomers. *Green Chemistry* **2019**, *21* (22), 6210-6219.

(21) Kwon, Y.; Birdja, Y. Y.; Raoufmoghaddam, S.; Koper, M. T. M. Electrocatalytic Hydrogenation of 5-Hydroxymethylfurfural in Acidic Solution. *ChemSusChem* **2015**, *8* (10), 1745-1751.

(22) Lee, D. K.; Kubota, S. R.; Janes, A. N.; Bender, M. T.; Woo, J.; Schmidt, J. R.; Choi, K.-S. The Impact of 5-Hydroxymethylfurfural (HMF)-Metal Interactions on the Electrochemical Reduction Pathways of HMF on Various Metal Electrodes. *ChemSusChem* **2021**, *14* (20), 4563-4572.

Carbon-Supported Ag Nanoparticle Aerogel for Electrocatalytic Hydrogenation of 5-(Hydroxymethyl)furfural to 2,5-Hexanedione in Acidic Conditions

Chapter 5

(23) Roylance, J. J.; Choi, K.-S. Electrochemical reductive biomass conversion: direct conversion of 5-hydroxymethylfurfural (HMF) to 2,5-hexanedione (HD) via reductive ring-opening. *Green Chemistry* **2016**, *18* (10), 2956-2960.

(24) Chidambaram, M.; Bell, A. T. A two-step approach for the catalytic conversion of glucose to 2,5-dimethylfuran in ionic liquids. *Green Chemistry* **2010**, *12* (7), 1253-1262.

(25) Liu, F.; Audemar, M.; De Oliveira Vigier, K.; Clacens, J.-M.; De Campo, F.; Jérôme, F. Palladium/Carbon Dioxide Cooperative Catalysis for the Production of Diketone Derivatives from Carbohydrates. *ChemSusChem* **2014**, *7* (8), 2089-2093.

(26) Sacia, E. R.; Deaner, M. H.; Louie, Y. L.; Bell, A. T. Synthesis of biomass-derived methylcyclopentane as a gasoline additive via aldol condensation/hydrodeoxygenation of 2,5-hexanedione. *Green Chemistry* **2015**, *17* (4), 2393-2397.

(27) Kundu, M. K.; Bhowmik, T.; Barman, S. Gold aerogel supported on graphitic carbon nitride: an efficient electrocatalyst for oxygen reduction reaction and hydrogen evolution reaction. *Journal of Materials Chemistry A* **2015**, *3* (46), 23120-23135.

(28) Liu, W.; Herrmann, A.-K.; Bigall, N. C.; Rodriguez, P.; Wen, D.; Oezaslan, M.; Schmidt, T. J.; Gaponik, N.; Eychmüller, A. Noble Metal Aerogels—Synthesis, Characterization, and Application as Electrocatalysts. *Accounts of Chemical Research* **2015**, *48* (2), 154-162.

(29) Kistler, S. S. Coherent Expanded Aerogels and Jellies. *Nature* **1931**, *127* (3211), 741-741.

(30) Soleimani Dorcheh, A.; Abbasi, M. H. Silica aerogel; synthesis, properties and characterization. *Journal of Materials Processing Technology* **2008**, *199* (1), 10-26.

(31) Sadekar, A. G.; Mahadik, S. S.; Bang, A. N.; Larimore, Z. J.; Wisner, C. A.; Bertino, M. F.; Kalkan, A. K.; Mang, J. T.; Sotiriou-Leventis, C.; Leventis, N. From 'Green' Aerogels to Porous Graphite by Emulsion Gelation of Acrylonitrile. *Chemistry of Materials* **2012**, *24* (1), 26-47.

(32) Heiligtag, F. J.; Cheng, W.; de Mendonça, V. R.; Süess, M. J.; Hametner, K.; Günther, D.; Ribeiro, C.; Niederberger, M. Self-Assembly of Metal and Metal Oxide Nanoparticles and Nanowires into a Macroscopic Ternary Aerogel Monolith with Tailored Photocatalytic Properties. *Chemistry of Materials* **2014**, *26* (19), 5576-5584.

Carbon-Supported Ag Nanoparticle Aerogel for Electrocatalytic Hydrogenation of 5-(Hydroxymethyl)furfural to 2,5-Hexanedione in Acidic Conditions

Chapter 5

(33) Hoffmann, F.; Cornelius, M.; Morell, J.; Fröba, M. Silica-Based Mesoporous Organic–Inorganic Hybrid Materials. *Angewandte Chemie International Edition* **2006**, *45* (20), 3216-3251.

(34) Mohanan Jaya, L.; Arachchige Indika, U.; Brock Stephanie, L. Porous Semiconductor Chalcogenide Aerogels. *Science* **2005**, *307* (5708), 397-400.

(35) Leventis, N.; Chandrasekaran, N.; Sotiriou-Leventis, C.; Mumtaz, A. Smelting in the age of nano: iron aerogels. *Journal of Materials Chemistry* **2009**, *19* (1), 63-65.

(36) Leventis, N.; Chandrasekaran, N.; Sadekar, A. G.; Mulik, S.; Sotiriou-Leventis, C. The effect of compactness on the carbothermal conversion of interpenetrating metal oxide/resorcinol-formaldehyde nanoparticle networks to porous metals and carbides. *Journal of Materials Chemistry* **2010**, *20* (35), 7456-7471.

(37) Leventis, N.; Chandrasekaran, N.; Sadekar, A. G.; Sotiriou-Leventis, C.; Lu, H. One-Pot Synthesis of Interpenetrating Inorganic/Organic Networks of CuO/Resorcinol-Formaldehyde Aerogels: Nanostructured Energetic Materials. *Journal of the American Chemical Society* **2009**, *131* (13), 4576-4577.

(38) Mahadik-Khanolkar, S.; Donthula, S.; Bang, A.; Wisner, C.; Sotiriou-Leventis, C.; Leventis, Interpenetrating Networks with Iron Oxide and the Carbothermal Synthesis of Highly Porous Monolithic Pure Iron(0) Aerogels as Energetic Materials. *Chemistry of Materials* **2014**, *26* (3), 1318-1331.

(39) Sadhukhan, M.; Barman, S. Bottom-up fabrication of two-dimensional carbon nitride and highly sensitive electrochemical sensors for mercuric ions. *Journal of Materials Chemistry A* **2013**, *1* (8), 2752-2756.

(40) Zhang, S.; Shang, N.; Gao, S.; Meng, T.; Wang, Z.; Gao, Y.; Wang, C. Ultra dispersed Co supported on nitrogen-doped carbon: An efficient electrocatalyst for oxygen reduction reaction and Zn-air battery. *Chemical Engineering Science* **2021**, *234*, 116442.

(41) Wang, Z.; Shang, N.; Wang, W.; Gao, S.; Zhang, S.; Gao, W.; Cheng, X.; Wang, C. Atomically dispersed Co anchored on S,N-riched carbon for efficient oxygen reduction and Zn-air battery. *Journal of Alloys and Compounds* **2022**, *899*, 163225.

Carbon-Supported Ag Nanoparticle Aerogel for Electrocatalytic Hydrogenation of 5-(Hydroxymethyl)furfural to 2,5-Hexanedione in Acidic Conditions

Chapter 5

(42) Shang, N.; Li, S.; Zhou, X.; Gao, S.; Gao, Y.; Wang, C.; Wu, Q.; Wang, Z. Co/nitrogen-doped carbon nanocomposite derived from self-assembled metallogels as efficient bifunctional oxygen electrocatalyst for Zn-air batteries. *Applied Surface Science* **2021**, *537*, 147818.

(43) Hou, B.; Ma, L.; Zang, X.; Shang, N.; Song, J.; Zhao, X.; Wang, C.; Qi, J.; Wang, J.; Yu, R. Design and Construction of 3D Porous Na3V2(PO4)3/C as High Performance Cathode for Sodium Ion Batteries. *Chemical Research in Chinese Universities* **2021**, *37* (2), 265-273.

(44) Xiao, Z.; Xu, X.; Kong, D.; Liang, J.; Zhou, S.; Huang, X.; Yang, Q.; Zhi, L. Chemical tailoring of one-dimensional polypyrene nanocapsules at a molecular level: towards ideal sulfur hosts for high-performance Li–S batteries. *Journal of Materials Chemistry A* **2019**, *7* (5), 2009-2014.

(45) Lee, J. H.; Park, M. J.; Yoo, S. J.; Jang, J. H.; Kim, H.-J.; Nam, S. W.; Yoon, C. W.; Kim, J. Y. A highly active and durable Co–N–C electrocatalyst synthesized using exfoliated graphitic carbon nitride nanosheets. *Nanoscale* **2015**, *7* (23), 10334-10339.

(46) Shang, N.; Wang, C.; Zhang, X.; Gao, S.; Zhang, S.; Meng, T.; Wang, J.; Wang, H.; Du, C.; Shen, T.; et al. Atomically dispersed iron on nitrogen-decorated carbon for high-performance oxygen reduction and zinc-air batteries. *Chemical Engineering Journal* **2021**, *426*, 127345.

(47) Samanta, R.; Mishra, R.; Barman, S. Interface-Engineered Porous Pt–PdO Nanostructures for Highly Efficient Hydrogen Evolution and Oxidation Reactions in Base and Acid. *ACS Sustainable Chemistry & Engineering* **2022**, *10* (11), 3704-3715.

(48) Nikbin, N.; Caratzoulas, S.; Vlachos, D. G. On the Brønsted Acid-Catalyzed Homogeneous Hydrolysis of Furans. *ChemSusChem* **2013**, *6* (11), 2066-2068.

(49) Zhang, J.; Liu, H.; Shi, P.; Li, Y.; Huang, L.; Mai, W.; Tan, S.; Cai, X. Growth of nickel (111) plane: The key role in nickel for further improving the electrochemical property of hexagonal nickel hydroxide-nickel & reduced graphene oxide composite. *Journal of Power Sources* **2014**, *267*, 356-365.

Carbon-Supported Ag Nanoparticle Aerogel for Electrocatalytic Hydrogenation of 5-(Hydroxymethyl)furfural to 2,5-Hexanedione in Acidic Conditions

Chapter 5

Appendix B
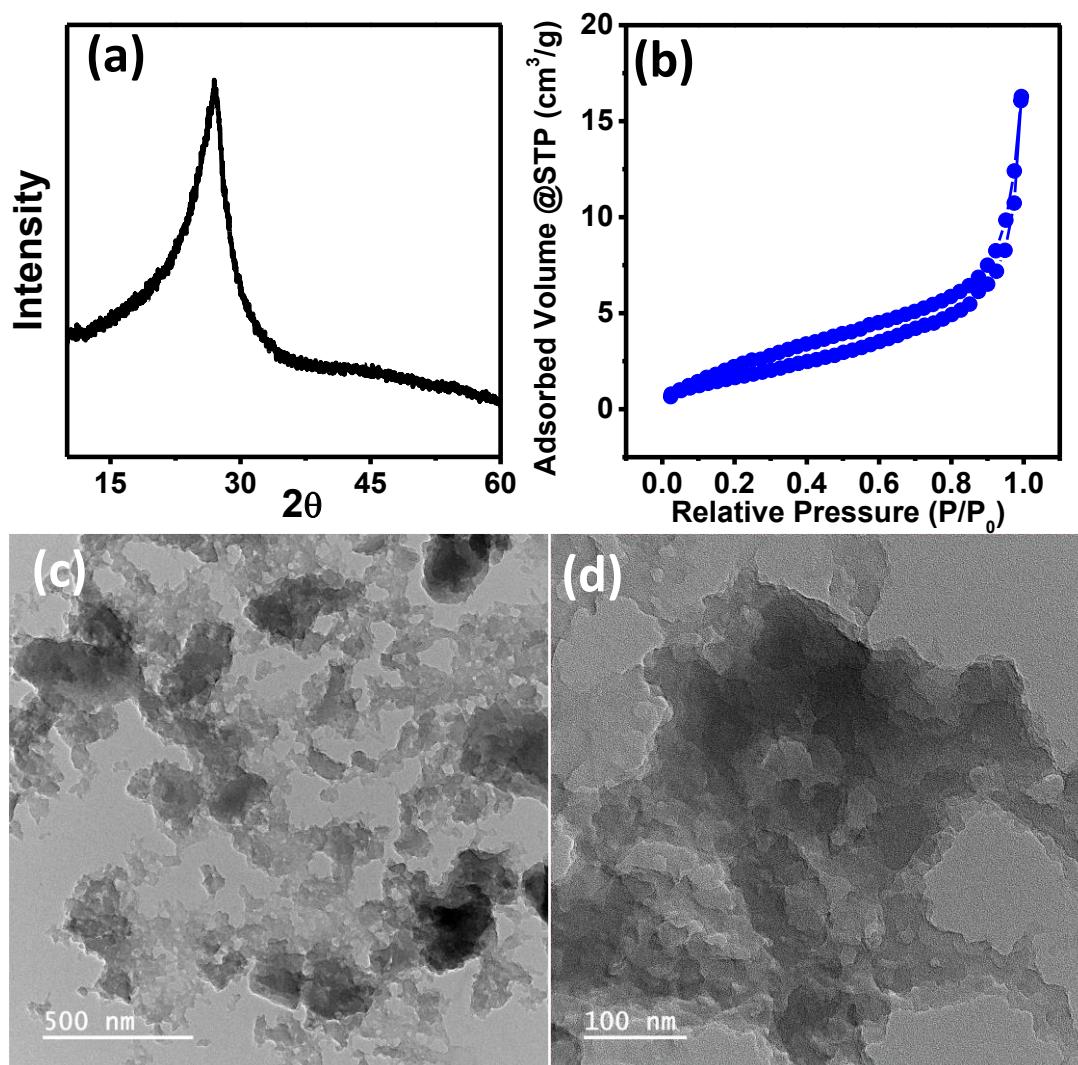
Figure S5.1. (a) p-XRD (b) Nitrogen adsorption/desorption isotherm, (c, d) TEM images of CN_x.

Carbon-Supported Ag Nanoparticle Aerogel for Electrocatalytic Hydrogenation of 5-(Hydroxymethyl)furfural to 2,5-Hexanedione in Acidic Conditions

Chapter 5

Element	Weight %	Atomic %	Error %	Net Int.
C K	9.80	35.70	6.20	69.40
N K	10.30	32.00	15.70	21.60
Ag L	79.90	32.30	2.60	448.90
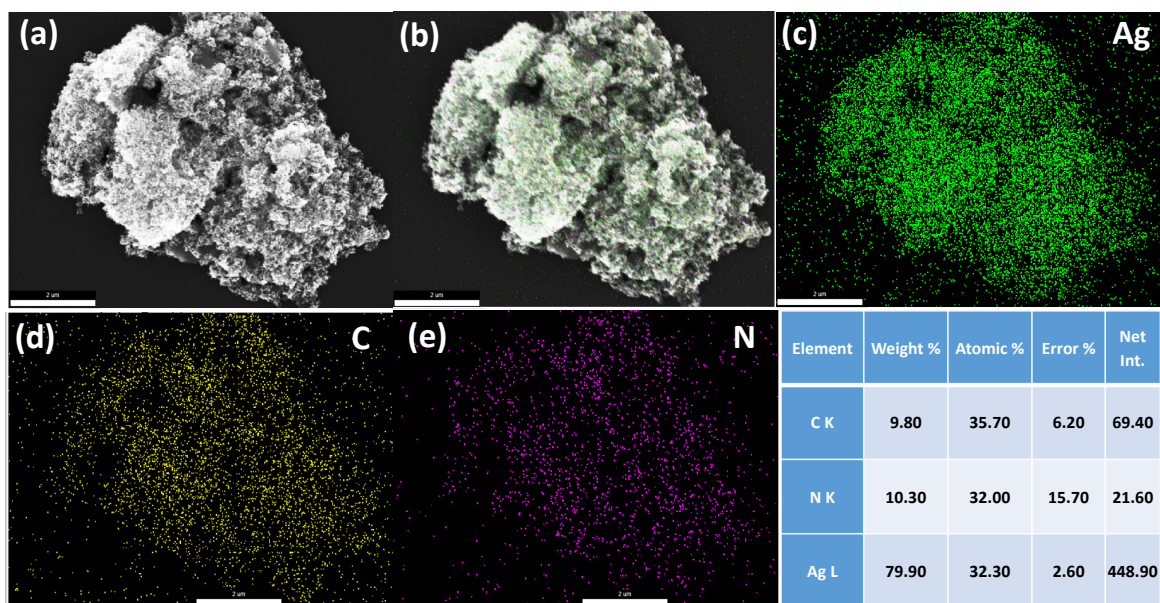
Figure S5.2. SEM-EDAX elemental mapping analysis of Ag-aerogel-CN$_x$.
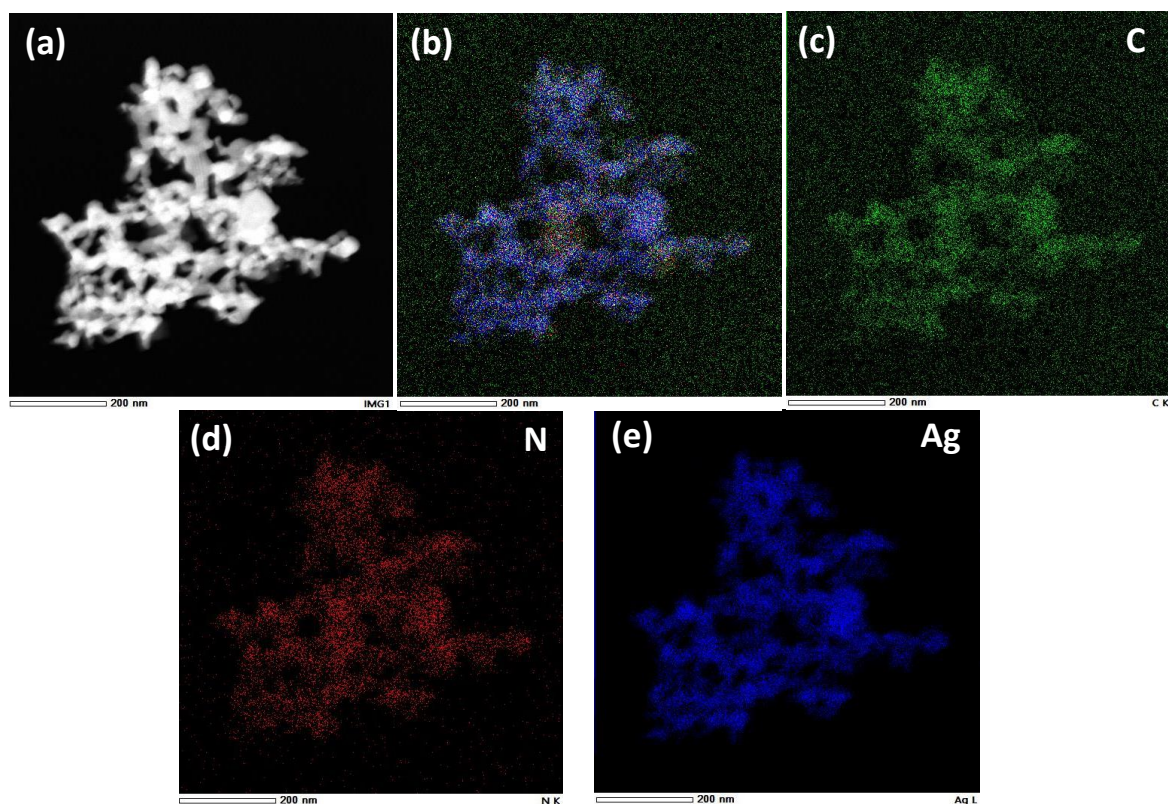
Figure S5.3. (a) STEM, (b-e) elemental mapping of Ag-aerogel-CN$_x$.

Carbon-Supported Ag Nanoparticle Aerogel for Electrocatalytic Hydrogenation of 5-(Hydroxymethyl)furfural to 2,5-Hexanedione in Acidic Conditions

Chapter 5
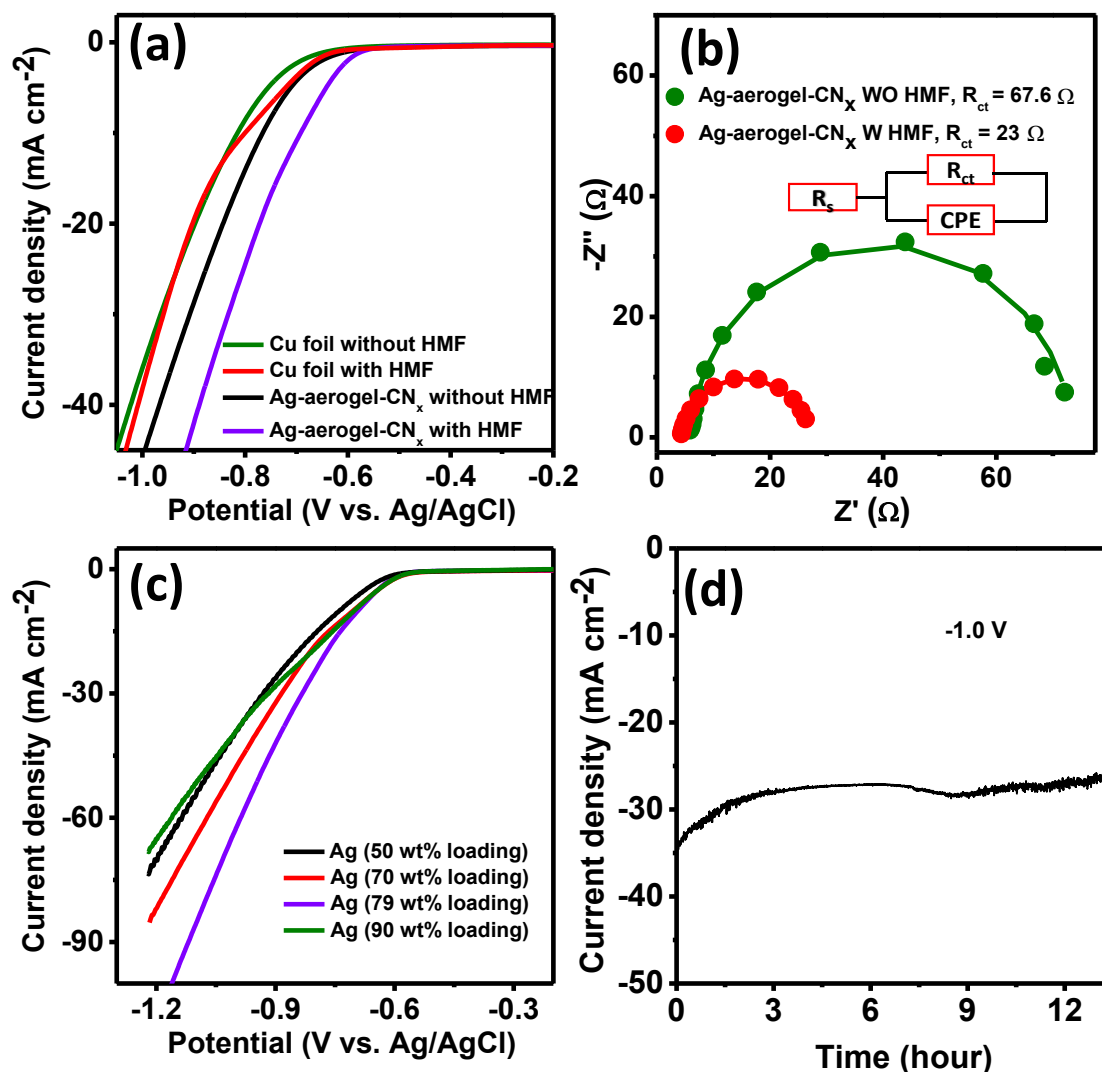
Figure S5.4. (a) Non iR corrected LSV activity of Ag-aerogel-CN$_x$ in Cu foil and only Cu foil in 0.5 M H$_2$SO$_4$ in presence and absence of 20 mM of HMF, (b) Nyquist plots of Ag-aerogel-CN$_x$ with and without HMF at 10 mV overpotential respectively, (c) Non iR corrected LSV activity of Ag-aerogel-CN$_x$ with different metal loading, (d) chronoamperometry stability of Ag-aerogel-CN$_x$.

Carbon-Supported Ag Nanoparticle Aerogel for Electrocatalytic Hydrogenation of 5-(Hydroxymethyl)furfural to 2,5-Hexanedione in Acidic Conditions

Chapter 5
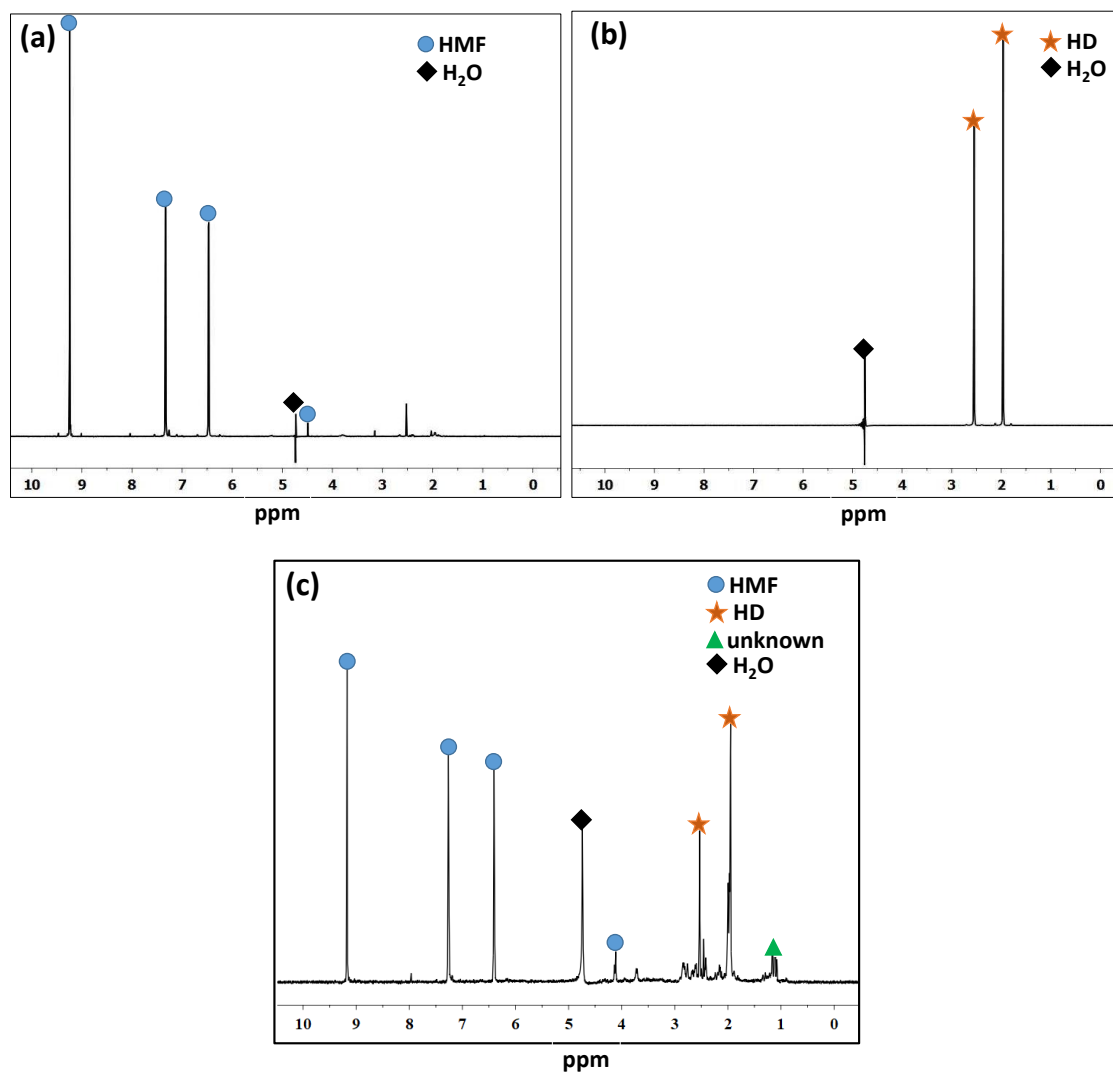
Figure S5.5. ^{1}H NMR spectra for (a) 20 mM HMF in 0.5 M H_2SO_4, (b) 20 mM HD in 0.5 M H_2SO_4, (c) 20 mM HMF in 0.5 M H_2SO_4 after applying potential at -1.1 V for 30 minutes. ^{1}H NMR (400 MHz, 90% H_2O/ 10% D_2O): δ 9.35 (s, 1H), 7.43 (d, 1H), 6.57 (d, 1H), 4.31 (s, 2H), 2.71 (s, 4H), 2.12 (s, 6H). (HMF peaks at 9.35, 7.43, and 6.57 ppm. HD peaks at 2.71 and 2.12 ppm)

Chapter 6

Palladium Oxide Nanoparticle for Electrocatalytic Oxidation of 5-(Hydroxymethyl)furfural to FDCA

6.1 ABSTRACT

A promising platform chemical, 2,5-furandicarboxylic acid (FDCA), is gaining prominence as a substitute for terephthalic acid in the production of various polymeric compounds, such as polyethylene terephthalate (PET). FDCA is derived from the oxidation of 5-hydroxymethylfurfural (HMF), a compound that can be sourced from cellulosic biomass through a series of reactions involving hexose isomerization and dehydration. The principal challenge lies in establishing an electrocatalytic system characterized by an wide potential range, capable of selectively oxidizing HMF to FDCA while achieving high Faradaic efficiencies for FDCA production. This system must effectively suppress water oxidation, which is a major competing reaction in aqueous environments. In this study, we present the electrocatalytic oxidation of HMF in an alkaline environment using palladium oxide supported on carbon (PdO-CN$_x$) as the catalyst. The PdO-CN$_x$ catalyst exhibits a preference for HMF oxidation over water oxidation, leading to the major product, FDCA, in 0.1 M KOH. The highest achieved Faradaic efficiency for FDCA production is 78% at a potential of 1.4 V vs. RHE in 0.1 M KOH for the PdO-CN$_x$ catalyst. By combining the PdO-CN$_x$ catalyst with commercial Pt/C (Comm Pt/C) to create a two-electron system, we compared the overall HMF oxidation with overall water oxidation. Notably, the PdO-CN$_x$ catalyst required significantly less potential to drive the overall HMF oxidation. This study underscores the efficiency of PdO-CN$_x$ as an electrocatalyst for the concurrent generation of clean

hydrogen fuels and value-added chemicals from biomass-derived molecules under ambient conditions.

6.2 INTRODUCTION

A growing amount of work has been put into developing clean, renewable alternative energy sources (such solar and wind) in response to the future global energy needs and climate change challenges brought on by unsustainable fossil fuel consumption.[1] Electrocatalytic water splitting is an optimal process for producing H_2 with no byproducts. Hydrogen produced from water splitting when combined with renewable energy sources, will play a significant role in a future sustainable energy sector.[2] In the water-splitting reaction, however, a large overpotential is required to surmount the high-energy barrier as a result of the sluggish kinetics of oxygen evolution reaction (OER). Therefore, substantial overpotentials are needed to achieve significant catalytic current densities of water splitting.[3] At the moment, the focus is primarily on rationally developing and synthesizing highly active, stable, and affordable catalysts. For instance, the HER catalytic performances of transition metal carbides[4], nitrides[5], phosphides[6], and sulphides[7] have been reported. Several transition metal oxides[8], hydroxides[9], and oxy-hydroxides[10], on the other hand, exhibit good OER capabilities. Recent research has also discovered non-precious bifunctional catalysts with both HER and OER activity.[11] Despite these developments, OER continues to be the water splitting bottleneck, and HER needs additional potential to match its rate.[12] Additionally, oxygen gas (O_2) created by the electrolysis of water can mix with hydrogen gas (H_2) in the electrolyzers headspace, raising safety issues and increasing the cost of gas separation. Substitution of OER with other reaction would be able to create value-added bioproducts and H_2 at both electrodes as well as improve the efficiency of an electrolyzers by substituting OER with thermodynamically more advantageous biomass oxidation processes.[13] Therefore, a

sustainable future depends on the effective conversion of biomass-derived products into high-value liquid fuels and chemicals.

5-hydroxymethylfurfural (HMF) is one of the platform molecules produced from biomass that has been the subject of the most research.[14] HMF, one of the renewable resources obtained from lignocellulosic biomass (LCB) and molecules like d-glucose or d-fructose.[15] The selective oxidation of HMF can yield a number of compounds, such as 2,5-diformylfuran (DFF), 5-hydroxymethyl-2-furancarboxylic acid (HMFCA), maleic anhydride (MA), and 2,5-furandicarboxylic acid (FDCA).[16] Due to its application as a monomer in the polymerization of bio-based polymers like poly(ethylene 2,5-furandicarboxylate) (PEF), FDCA is gaining more attention.[17] Currently, PEF is used in numerous applications in place of the petroleum-derived polymer polyethylene terephthalate (PET). Like PET, PEF's structure substitutes FDCA for terephthalic acid.[14]

The oxidation of HMF, whether in homogeneous or heterogeneous catalytic systems, leads to the formation of multiple oxidized products.[18] In homogeneous catalytic systems, catalysts like Co/Mn/Br are commonly employed; however, they suffer from low yields and pose recycling challenges.[19] Conversely, heterogeneous catalysis requires high-temperature, high-pressure conditions and the presence of expensive metal catalysts.[20-22] Another promising avenue involves the electrochemical oxidation of HMF under ambient conditions, effectively obviating the need for external oxidants.[23] This approach leverages the thermodynamically favorable HMF oxidation reaction to supplant the OER in water-splitting processes, offering increased competitiveness as the cost of renewable energy continues to decrease.[24]

In this study, we demonstrated a straightforward method involving sodium borohydride (NaBH$_4$) reduction to synthesize a carbon-supported palladium oxide catalyst (PdO/CN$_x$). This catalyst was employed for the electrocatalytic oxidation of HMF in a

0.1 M KOH solution. Remarkably, the synthesized PdO/CN$_x$ catalyst exhibited a strong

preference for HMF oxidation over OER. The primary product of the electrocatalytic

oxidation of HMF is FDCA. Importantly, the optimal FDCA production with a notable

faradaic efficiency of 78% is achieved at a potential of 1.4 V vs. RHE. This high faradaic

efficiency is found to be dependent on the electrolyte composition and the cathodic

potential applied. Furthermore, we integrated the PdO/CN$_x$ catalyst as the cathode for

overall HMF oxidation in a full cell configuration, utilizing Pt as the anode. Intriguingly,

the PdO/CN$_x$ catalyst demanded substantially lower potential to drive the overall HMF

oxidation compared to overall water oxidation in 0.1 M KOH, highlighting its remarkable

kinetic favorability for HMF oxidation. Additionally, the catalyst exhibited impressive

durability for overall HMF oxidation, strengthening its potential for practical

applications.

6.3. EXPERIMENTAL SECTION

Materials:

Carbon cloth was purchased from AVCARB. Palladium (II) chloride (PdCl$_2$), sodium

borohydride (NaBH$_4$), formamide (HCONH$_2$) and 2,5-furandicarboxylic acid (FDCA)

were bought from Sigma Aldrich. Sulfuric acid (H$_2$SO$_4$, 98%) was bought from Merck

(Germany). 5-hydroxymethylfurfural (99+% assay) was bought from Spectrochem

(India). All of these materials were utilized exactly as they arrived, with no further

purification. Sigma Aldrich supplied the Ar gas (99.99% purity). Milli-Q water was

produced using an ultra-filtration system (Milli-Q, Millipore), and the measured

conductivity at 25 °C was 35 mho.cm^{-1}.

Preparation of N-doped carbon

The syntheis procedure of N-doped carbon (CN$_x$) was done by using the previously

described process[25]. A brown-colored solution was created by microwave heating 30 mL

of Formamide (HCONH2) for two hours at a temperature of 180°C. A rotating evaporator operating at 180°C evaporated the collected solution. After filtering, washing with distilled water, and hoover drying, solid N-doped carbon was produced.

Synthesis of the PdO/CN$_x$ composite

By using NaBH$_4$ reduction method, palladium (II) chloride was reduced and then subjecting the material to ultrasonic treatment, PdO/CN$_x$ composite was created. First, a bath-sonicator was used to sonicate 35 mg of palladium (II) chloride in 5 mL of deionized water for 30 minutes. On the other hand, 2 mL of deionized water was sonicated for 10 minutes with 5 mg of CN$_x$ in order to disperse it. The two solutions mentioned above were combined, and the mixture was then homogenised using a sonicator for 30 minutes. The aforesaid combination was then given 50 mg of NaBH$_4$ and sonicated for an additional two hours. The resultant black solution was centrifuged at 1600 rpm, followed by many washes with ethanol and deionized water. The dark precipitate was gathered and vacuum-dried for future use.

Instrumentation and Analysis

Surface morphology analysis was done using a field-emission scanning electron microscope (Carl Zeiss, Germany, Model ∑igma). A 0.05 mL of a solution containing 1 mg/mL of material was coated onto a silicon wafer, dried at 45 °C, and then the samples were ready for FE-SEM examination. Utilising a Bruker DAVINCI D8 ADVANCE diffractometer fitted with Cu K radiation (λ= 0.15406 nm), X-ray diffraction (*p*-XRD) patterns were obtained. The surface morphology of the produced materials was examined using high-resolution transmission electron microscopy (HRTEM) at 200 kV. The analysis was carried out using a JEOL F200 instrument. Initially, 10 μL of a 1 mg/mL stock solution was taken for the TEM analysis and dried in the air at a temperature of around 45 °C. By coating the material on a silicon wafer and utilising Mg Kα X-ray as

the monochromatic source, VG Microtech was used to accomplish the X-ray photoelectron spectroscopy experiments. All electrochemical measurements were performed on a workstation for electrochemical measurements (Autolab, Metrohm, PGSTAT 320N). A Hanna (HI 2209) pH meter was used to determine the pH of the electrolyte. Equipment for ultrasonic bath sonication was provided by Genei Laboratories Private Ltd. Bangalore, India. The ^{1}H NMR spectrum was obtained using the water suppression technique on a Bruker 400 MHz instrument.

Electrochemical performances

At first, 1 mg of the prepared catalyst is ultrasonicated for 1 hour to obtain a homogenous slurry in 470 µL of Millipore water along with 30 µL of Nafion (5.0 wt %) solution. The resultant ink was subsequently drop casted on carbon cloth with the help of micropipette and dried at 45 °C for further electrochemical testing. A three-electrode setup connected to the electrochemical workstation (Metrohm Autolab) was used to perform electrochemical performances. Each cathodic and anodic chamber was filled with 40 mL of 0.1 M KOH electrolyte, and these chambers were separated by a anion exchange membrane. The cathodic chamber contained the working electrode (prepared catalyst electrode) and the reference electrode (Ag/AgCl) with a spacing of 0.5 cm between them. In contrast, the anodic chamber included a platinum electrode as the counter electrode. All measurements were referenced to the Ag/AgCl reference electrode and subsequently adjusted to the reversible hydrogen electrode (RHE) using the following equation 1;

$V_{RHE} = V_{Ag/AgCl}$ (saturated 3M KCl) + 0.197 + 0.00592pH ……….…….(1)

Product Identification and Quantification:

Bruker Avance III 400 MHz nuclear magnetic resonance (NMR) spectrometer was used to detect and quantify the products. Using NMR spectroscopy, calibration curves were

produced for known reactant and product concentrations for quantification. To determine their concentration, a series of solutions containing HMF and FDCA at various known concentrations were analysed in NMR for the signature peak. 50 mL of D_2O were added to 450 mL of electrolyte solution for the NMR study. Water suppression was used to collect the NMR spectra. The characteristic peaks of the products were unaffected by the suppression of the water peak in NMR signals, which appears at about 4.7 ppm.

6.4. RESULTS AND DISCUSSION

Morphology and characterization:
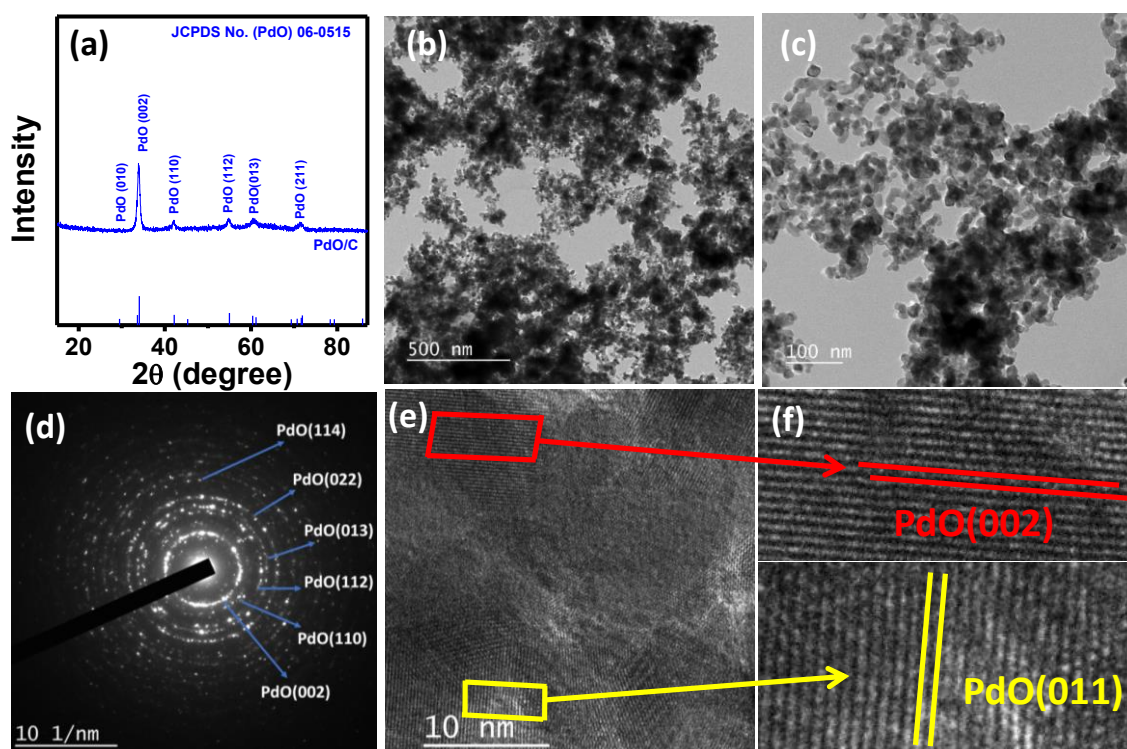
Figure 6.1. (a) p-XRD of PdO/CN$_x$, (b, c) TEM images, (d) SAED image, (e, f) HRTEM image of PdO/CN$_x$.

The PdO/CN$_x$ was synthesized by a simple ultra-sonication-assisted BH_4^- reduction of PdCl$_2$ in the presence of CN$_x$ support followed by heating in furnace at 400°C (details in experimental section). The structural characterization of PdO/CN$_x$ was investigated by

powder X-ray diffraction (p-XRD) pattern. The p-XRD spectra of the prepared catalyst is given is Figure 6.1a. The diffraction peaks at 29.6°, 33.2°, 42.1°, 55.3°, 60.9°, and 72.4° are corresponds to (010), (002), (110), (112), (013), and (211) crystalline planes of PdO/CN_x. The morphological characterization of PdO/CN_x was studied by Transmission Electron Microscopy (TEM). TEM images of PdO/CN_x are displayed in Figure 6.1 (b and c). From the TEM images, it is seen that quasi-one-dimensional nanochains are formed. These one-dimensional extended nanochains are interconnected to form three-dimensional network-like structures with a large number of open pores making the PdO/CN_x catalyst porous. The SAED image of PdO/CN_x is given in Figure 6.1d and HRTEM images are displayed in Figure 6.1(e and f). The SAED image shows the pollycrystalline nature of PdO/CN_x and from the diffraction pattern the planes such as (002), (110), (112), (013), (022), and (114) can be seen in Figure 6.1d. The HRTEM images clearly shows the presence of (002) and (011) planes of PdO in PdO/CN_x which is in accordance with p-XRD data.

Electrochemical HMF oxidation

HMF was electrochemically oxidized in 0.1 M KOH electrolyte using an electrochemical workstation with an H-type electrochemical cell. The electrochemical HMF and water oxidation experiments were carried out in 0.1 M KOH solution with and without HMF at a scan rate of 10 mV/s. Chronopotentiometry was performed at different current density to compute the faradic efficiency of all the catalysts. The cathodic section contained 40 mL of 0.1 M KOH, whereas the anodic section was charged with 40 mL of 0.1 M KOH and 10 mM HMF. In order to ensure minimal Faradic loss, argon gas was purged during the reaction in the anodic compartment, and a magnetic stirrer was used to ensure a rotation rate of 500 rpm. The products formed by HMF oxidation were

Palladium   Oxide   Nanoparticle   for   Electrocatalytic   Oxidation   of
5-(Hydroxymethyl)furfural to FDCA
Chapter 6

identified and quantified by ^{1}H-NMR analysis by water suppression method. The Faradic

efficiency of the products were calculated using the following equation 2.

$$FE\ (\%) = \frac{\text{mol of FDCA formed}}{\text{total charge passed (C)/ (F×n)}} \times 100\% \quad \ldots\ldots\ldots\ldots\ldots\ldots(2)$$

In this equation: *C* stands for the charge passed during the electrolysis at the cathode. *F*

is the Faraday constant, equal to 96485 C mol^{-1}. *n* signifies the number of electrons

required to produce one molecule of the product from HMF.
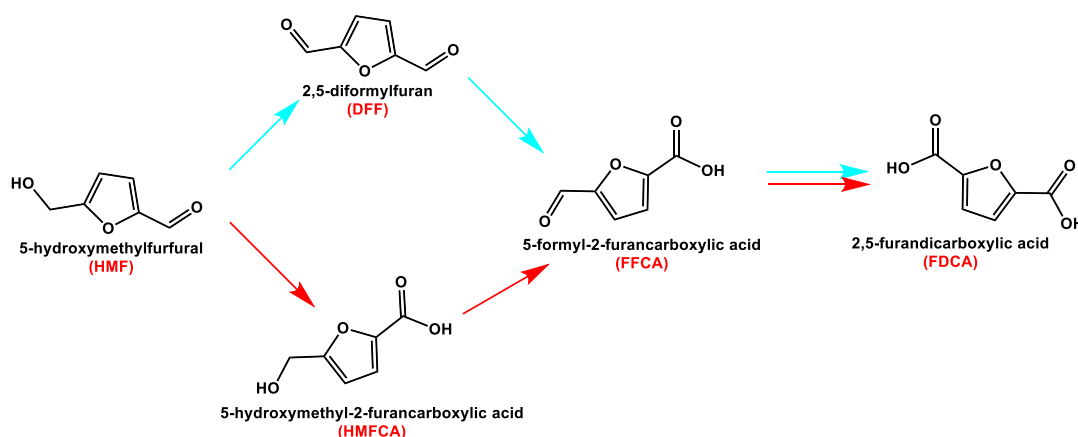
Figure 6.2. Possible ways of HMF oxidation.

FDCA, an important chemical compound, can be synthesized through the oxidation of

5-hydroxymethylfurfural (HMF), which is derived from the conversion of hexoses found

in cellulosic biomass through isomerization and dehydration processes. The

electrocatalytic oxidation of HMF to FDCA primarily comprises a two-step oxidation

process, involving the conversion of an alcohol group and an aldehyde group into a

carboxyl group.[26] This process presents two potential oxidation pathways, leading to the

formation of three distinct reaction intermediates, as illustrated in Figure 6.2. One of

these pathways initiates with the oxidation of the alcohol group, resulting in the

formation of 2,5-diformylfuran (DFF) as an intermediate. In contrast, the alternative

pathway begins with the initial oxidation of the aldehyde group, yielding 5-

hydroxymethyl-2-furancarboxylic acid (HMFCA) as an intermediate product. Both DFF and HMFCA subsequently undergo further oxidation, converging into a shared intermediate molecule, such as 5-formyl-2-furancarboxylic acid (FFCA), which is eventually subjected to further oxidation to yield FDCA.[27, 28]
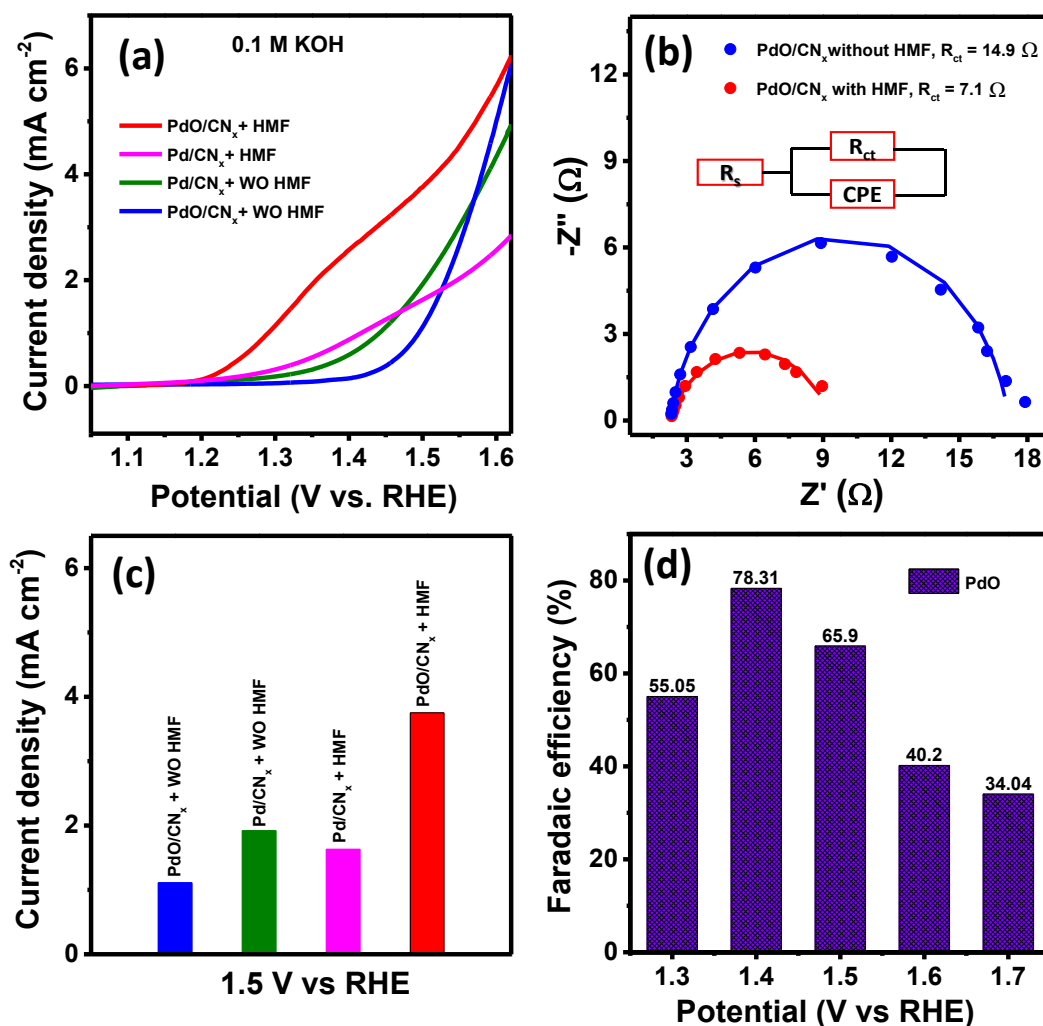
Figure 6.3. (a) LSV polarisation curve, (b) nyquist plots, (c) current density at 1.5 V vs RHE with and without the addition of 10 mM of HMF of PdO/CN$_x$ and Pd in 0.1 M KOH, (d) faradic efficiency of PdO/CN$_x$ at different potentials in 0.1 M KOH.

The LSV polarization curve, as shown in Figure 6.3a, compares PdO/CN$_x$ and Pd/CN$_x$ performance in the presence and absence of HMF. In the absence of HMF, the LSV curve primarily reflects water oxidation. However, upon introducing HMF, a noticeable

variation in overpotential becomes evident, indicating that HMF oxidation is more favourable than water oxidation on the PdO/CN_x catalyst. To gain deeper insights into the reaction pathway, we explored the kinetics of HMF reduction through the analysis of electrochemical impedance spectroscopy (EIS) spectra, as depicted in Figure 6.3b. These spectra were obtained within the frequency range of 0.1-100 kHz in a 0.1 M KOH solution, employing an open circuit potential and an AC amplitude of 10 mV. The inset illustrates the circuit used for fitting the EIS data, wherein "R_s" represents the solution resistance, the semicircle's diameter represents the charge transfer resistance (R_{ct}), and "CPE" signifies the constant phase element. The corresponding R_{ct} value of PdO/CN_x in 0.1 M KOH with HMF is 7.19 Ω and without HMF is 14.9 Ω. A lower R_{ct} value and enhanced electronic conductivity, underscoring the favourable electrocatalytic activity. Figure 6.3c provides current density values at 1.5 V for PdO/CN_x and Pd/CN_x, both with and without the presence of HMF. Following HMF introduction, the current density experiences a substantial increase compared to the condition without HMF. This increase in current density underlines the catalyst's improved performance facilitated by HMF's presence.

Chronopotentiometry measurement was employed to assess the faradic efficiency of each catalyst across varying potential. The experimental setup involved the anodic section containing 40 mL of 0.1 M KOH and 10 mM HMF, while the cathodic section held 40 mL of 0.1 M KOH. Argon gas was continuously introduced into the anodic compartment to minimize Faradic losses, and stirring was maintained at a rate of 300 rpm using a magnetic stirrer. Employing the water suppression method for ^{1}H-NMR analysis, we identified the products generated through HMF oxidation and quantified their concentrations, shown in Figure 6.4. This analysis revealed that in a 0.1 M KOH solution, FDCA emerged as the primary product of HMF oxidation on the PdO/CN_x catalyst.

Palladium   Oxide   Nanoparticle   for   Electrocatalytic   Oxidation   of
5-(Hydroxymethyl)furfural to FDCA
Chapter 6

Faradaic efficiency values for PdO/CN_x were calculated across a range of potentials ranging from 1.3 to 1.7 V vs RHE, and these results are presented in Figure 6.3d. The faradic efficiency of FDCA exhibited a gradual increase as the oxidation potential was elevated, reaching its maximum value at 78.31% when the potential was set at 1.4 V vs RHE. However, subsequent positive shifts in the oxidation potential led to a decrease in the Faradaic efficiency of FDCA. This reduction in Faradaic efficiency at higher potentials can be attributed to the growing predominance of the Oxygen Evolution Reaction (OER) over the HMF oxidation reaction on the PdO/CN_x catalyst. Ultimately, the highest faradic efficiency observed for FDCA production was 78% at 1.4 V in the 0.1 M KOH solution.

ppm
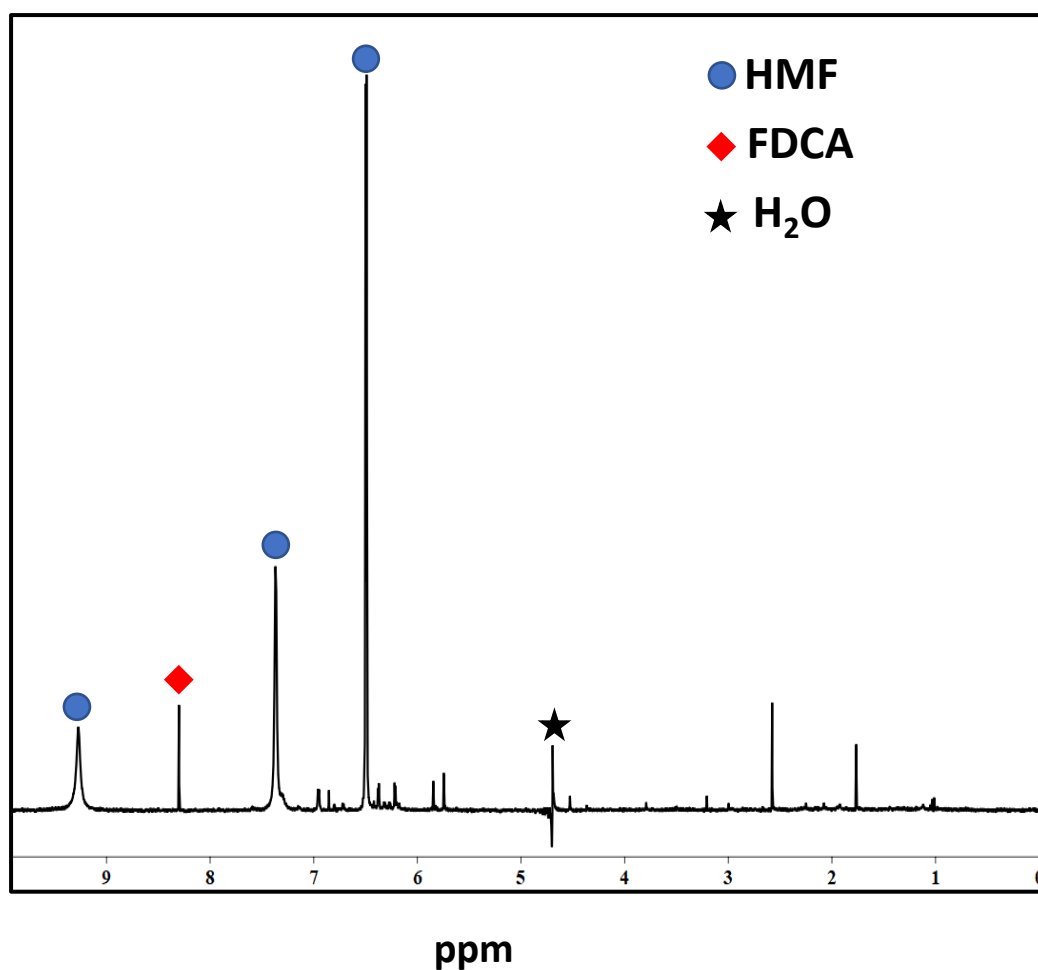
Figure 6.4. ^{1}H NMR spectra for 20 mM HMF in 0.1 M KOH after applying potential at 1.4 V for 30 minutes.^{1}H NMR (400 MHz, 90% H_2O/ 10% D_2O): δ 9.35 (s, 1H), 7.43 (d,

1H), 6.57 (d, 1H), 4.31 (s, 2H), 8.31 (s, 2H). (HMF peaks at 9.35, 7.43, and 6.57 ppm. FDCA peaks at 8.31ppm)

Overall HMF oxidation reaction

The overall HMF oxidation reaction took place within an H-type electrochemical cell utilizing a two-electrode configuration. In this setup, the cathodic electrode is used as commercial Pt/C coated on carbon cloth, while the anodic electrode was coated with PdO/CN$_x$ on carbon cloth. Figure 6.5a illustrates the non-iR-corrected LSV curve for the overall HMF oxidation reaction conducted in a 0.1 M KOH solution with 10 mM HMF in the anodic compartment. The polarization curve clearly indicates that the potential required to drive the overall HMF oxidation is notably lower than that of overall water oxidation for the PdO/CN$_x$ catalyst. This observation suggests that HMF oxidation is considerably more favourable than OER on the synthesized PdO/CN$_x$ in a 0.1 M KOH solution. Figure 6.5b presents the current density values for both overall HMF oxidation and overall water oxidation at a potential of 1.7 V vs RHE for PdO/CN$_x$ in a 0.1 M KOH solution. The plot underscores that the current obtained for overall HMF oxidation substantially surpasses that of water oxidation at this specific potential. Examining the stability of the catalyst is a crucial aspect for assessing its practical viability. To investigate the stability of the system, chronoamperometry measurement was conducted at a potential of 1.7 V vs RHE for an approximate duration of 1 hour, as depicted in Figure 6.5c. Post stabilization, a minor shift in the current is observed, indicating that the system demonstrates remarkable stability. Figure 6.5d provides a digital image illustrating the system while performing the overall HMF oxidation.
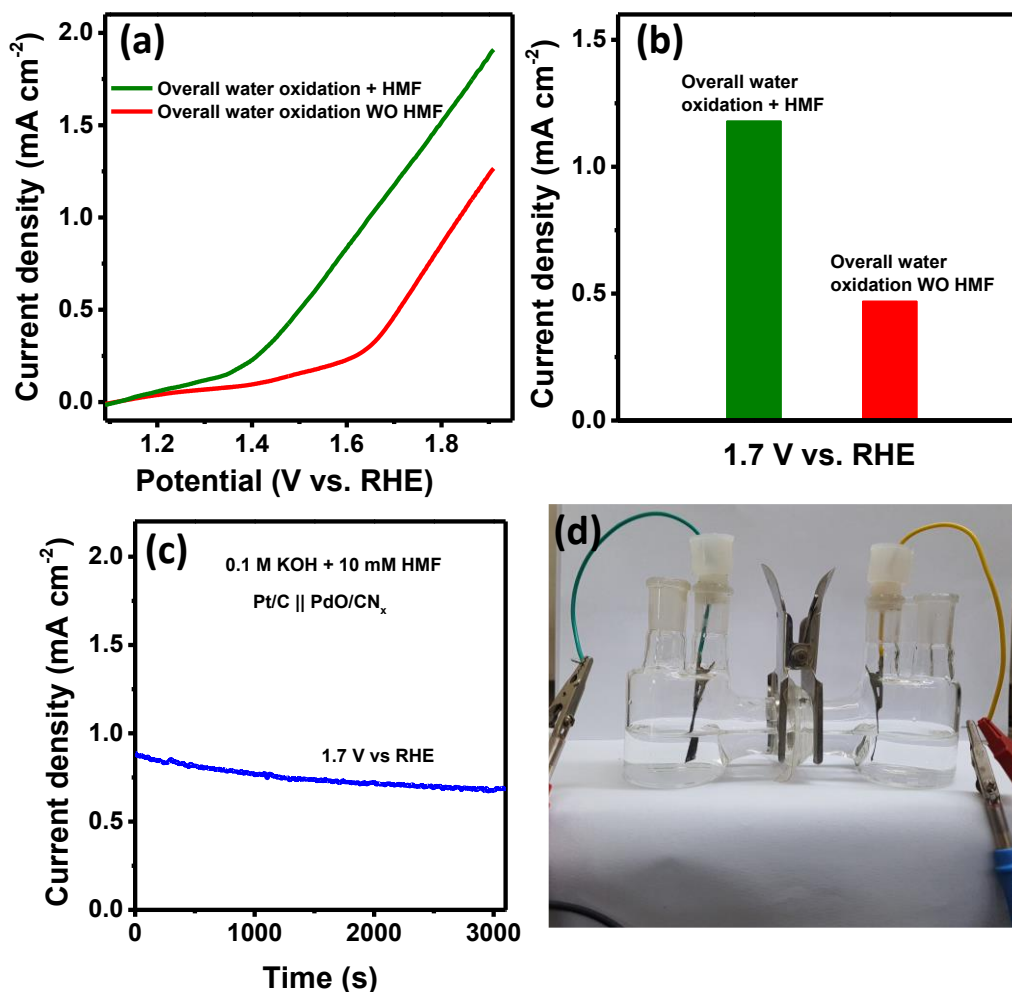
Figure 6.5. (a) Overall water oxidation of PdO/CN$_x$ in 0.1 M KOH with in the presence and absence of 10 mM of HMF, (c) Current density of different catalysts at 1.7 V potential.

6.5. CONCLUSIONS

This study presents a straightforward one-step method for synthesizing PdO nanoparticles supported on carbon (PdO/CN$_x$) to serve as a highly effective catalyst for the electrocatalytic oxidation of HMF. PdO/CN$_x$ proved to be a proficient catalyst for the selective oxidation of HMF to FDCA in a 0.1 M KOH solution. Notably, the onset potential for HMF oxidation on the PdO/CN$_x$ catalyst was considerably lower than that required for OER. This oxidation occurred under ambient conditions in an alkaline

electrolyte, with water serving as the hydrogen source. The primary product of HMF oxidation was identified as FDCA, and a substantial Faradaic efficiency of 78% for FDCA production was achieved using the PdO/CN$_x$ catalyst at an overpotential of 1.4 V vs. RHE in the 0.1 M KOH solution. Furthermore, the PdO/CN$_x$ catalyst effectively suppressed the OER while enabling the oxidation of HMF to FDCA with a low R$_{ct}$ value. Significantly, the PdO/CN$_x$ catalyst required notably lower potential to facilitate the overall HMF oxidation in comparison to overall water oxidation in 0.1 M KOH, signifying the kinetic favorability for HMF oxidation over water oxidation. This efficient conversion of HMF to FDCA presents an innovative pathway for generating valuable chemical intermediates from biomass resources.

6.6. REFERENCES:

(1) Cook, T. R.; Dogutan, D. K.; Reece, S. Y.; Surendranath, Y.; Teets, T. S.; Nocera, D. G. Solar Energy Supply and Storage for the Legacy and Nonlegacy Worlds. *Chemical Reviews* **2010**, *110* (11), 6474-6502.

(2) McCrory, C. C. L.; Jung, S.; Ferrer, I. M.; Chatman, S. M.; Peters, J. C.; Jaramillo, T. F. Benchmarking Hydrogen Evolving Reaction and Oxygen Evolving Reaction Electrocatalysts for Solar Water Splitting Devices. *Journal of the American Chemical Society* **2015**, *137* (13), 4347-4357.

(3) Jiao, Y.; Zheng, Y.; Jaroniec, M.; Qiao, S. Z. Design of electrocatalysts for oxygen- and hydrogen-involving energy conversion reactions. *Chemical Society Reviews* **2015**, *44* (8), 2060-2086, 10.1039/C4CS00470A.

(4) Michalsky, R.; Zhang, Y.-J.; Peterson, A. A. Trends in the Hydrogen Evolution Activity of Metal Carbide Catalysts. *ACS Catalysis* **2014**, *4* (5), 1274-1278.

(5) Cao, B.; Veith, G. M.; Neuefeind, J. C.; Adzic, R. R.; Khalifah, P. G. Mixed Close-Packed Cobalt Molybdenum Nitrides as Non-noble Metal Electrocatalysts for the Hydrogen Evolution Reaction. *Journal of the American Chemical Society* **2013**, *135* (51), 19186-19192.

(6) Popczun, E. J.; McKone, J. R.; Read, C. G.; Biacchi, A. J.; Wiltrout, A. M.; Lewis, N. S.; Schaak, R. E. Nanostructured Nickel Phosphide as an Electrocatalyst for the Hydrogen Evolution Reaction. *Journal of the American Chemical Society* **2013**, *135* (25), 9267-9270.

(7) Shahroudi, A.; Esfandiari, M.; Habibzadeh, S. Nickel sulfide and phosphide electrocatalysts for hydrogen evolution reaction: challenges and future perspectives. *RSC Advances* **2022**, *12* (45), 29440-29468.

(8) Song, F.; Bai, L.; Moysiadou, A.; Lee, S.; Hu, C.; Liardet, L.; Hu, X. Transition Metal Oxides as Electrocatalysts for the Oxygen Evolution Reaction in Alkaline Solutions: An Application-Inspired Renaissance. *Journal of the American Chemical Society* **2018**, *140* (25), 7748-7759.

(9) Zheng, D. J.; Görlin, M.; McCormack, K.; Kim, J.; Peng, J.; Xu, H.; Ma, X.; LeBeau, J. M.; Fischer, R. A.; Román-Leshkov, Y.; et al. Linker-Dependent Stability of Metal-Hydroxide Organic Frameworks for Oxygen Evolution. *Chemistry of Materials* **2023**, *35* (13), 5017-5031.

(10) Han, J.; Guan, J. Multicomponent transition metal oxides and (oxy)hydroxides for oxygen evolution. *Nano Research* **2023**, *16* (2), 1913-1966.

(11) Tsai, F.-T.; Deng, Y.-T.; Pao, C.-W.; Chen, J.-L.; Lee, J.-F.; Lai, K.-T.; Liaw, W.-F. The HER/OER mechanistic study of an FeCoNi-based electrocatalyst for alkaline water splitting. *Journal of Materials Chemistry A* **2020**, *8* (19), 9939-9950.

(12) Shekhawat, A.; Samanta, R.; Panigrahy, S.; Barman, S. Electrocatalytic Oxidation of Urea and Ethanol on Two-Dimensional Amorphous Nickel Oxide Encapsulated on N-Doped Carbon Nanosheets. *ACS Applied Energy Materials* **2023**, *6* (5), 3135-3146.

(13) You, B.; Jiang, N.; Liu, X.; Sun, Y. Simultaneous H2 Generation and Biomass Upgrading in Water by an Efficient Noble-Metal-Free Bifunctional Electrocatalyst. *Angewandte Chemie International Edition* **2016**, *55* (34), 9913-9917.

(14) Nam, D.-H.; Taitt, B. J.; Choi, K.-S. Copper-Based Catalytic Anodes To Produce 2,5-Furandicarboxylic Acid, a Biomass-Derived Alternative to Terephthalic Acid. *ACS Catalysis* **2018**, *8* (2), 1197-1206.

(15) Panigrahy, S.; Mishra, R.; Panda, P.; Kempasiddaiah, M.; Barman, S. Carbon-Supported Ag Nanoparticle Aerogel for Electrocatalytic Hydrogenation of 5-(Hydroxymethyl)furfural to 2,5-Hexanedione Under Acidic Conditions. *ACS Applied Nano Materials* **2022**, *5* (6), 8314-8323.

(16) Woo, J.; Moon, B. C.; Lee, U.; Oh, H.-S.; Chae, K. H.; Jun, Y.; Min, B. K.; Lee, D. K. Collaborative Electrochemical Oxidation of the Alcohol and Aldehyde Groups of 5-Hydroxymethylfurfural by NiOOH and Cu(OH)2 for Superior 2,5-Furandicarboxylic Acid Production. *ACS Catalysis* **2022**, *12* (7), 4078-4091.

(17) Taitt, B. J.; Nam, D.-H.; Choi, K.-S. A Comparative Study of Nickel, Cobalt, and Iron Oxyhydroxide Anodes for the Electrochemical Oxidation of 5-Hydroxymethylfurfural to 2,5-Furandicarboxylic Acid. *ACS Catalysis* **2019**, *9* (1), 660-670.

(18) Zhu, Y.; Shi, J.; Li, Y.; Lu, Y.; Zhou, B.; Wang, S.; Zou, Y. Understanding the surface segregation behavior of bimetallic CoCu toward HMF oxidation reaction. *Journal of Energy Chemistry* **2022**, *74*, 85-90.

(19) Wei, Z.; Li, W.; Yuan, F.; Sun, W.; Zhao, L. Kinetic Modeling of Homogenous Catalytic Oxidation of 5-Hydroxymethylfurfural to 2,5-Furandicarboxylic Acid. *Industrial & Engineering Chemistry Research* **2022**, *61* (50), 18352-18361.

(20) Albonetti, S.; Lolli, A.; Morandi, V.; Migliori, A.; Lucarelli, C.; Cavani, F. Conversion of 5-hydroxymethylfurfural to 2,5-furandicarboxylic acid over Au-based catalysts: Optimization of active phase and metal–support interaction. *Applied Catalysis B: Environmental* **2015**, *163*, 520-530.

(21) Gao, T.; Zhang, H.; Hu, C.; Jing, F.; Fang, W. Base-Free Aerobic Oxidation of 5-Hydroxymethylfurfural on a Ru(0) Center in Cooperation with a Co(II)/Co(III) Redox Pair over the One-Pot Synthesized Ru–Co Composites. *Industrial & Engineering Chemistry Research* **2020**, *59* (39), 17200-17209.

(22) Qu, T.; Hu, J.; Dai, X.; Tan, Q.; Liu, Y.; Chen, Y.; Guo, S.; Liu, Y. Electrospinning Highly Dispersed Ru Nanoparticle-Embedded Carbon Nanofibers Boost CO2 Reduction in a H2/CO2 Fuel Cell. *ACS Applied Materials & Interfaces* **2021**, *13* (20), 23523-23531.

(23) Park, M.; Gu, M.; Kim, B.-S. Tailorable Electrocatalytic 5-Hydroxymethylfurfural Oxidation and H2 Production: Architecture–Performance Relationship in Bifunctional Multilayer Electrodes. *ACS Nano* **2020**, *14* (6), 6812-6822.

(24) Jiang, N.; You, B.; Boonstra, R.; Terrero Rodriguez, I. M.; Sun, Y. Integrating Electrocatalytic 5-Hydroxymethylfurfural Oxidation and Hydrogen Production via Co–P-Derived Electrocatalysts. *ACS Energy Letters* **2016**, *1* (2), 386-390.

(25) Sadhukhan, M.; Barman, S. Bottom-up fabrication of two-dimensional carbon nitride and highly sensitive electrochemical sensors for mercuric ions. *Journal of Materials Chemistry A* **2013**, *1* (8), 2752-2756.

(26) Pang, X.; Bai, H.; Zhao, H.; Fan, W.; Shi, W. Efficient Electrocatalytic Oxidation of 5-Hydroxymethylfurfural Coupled with 4-Nitrophenol Hydrogenation in a Water System. *ACS Catalysis* **2022**, *12* (2), 1545-1557.

(27) Yang, Y.; Mu, T. Electrochemical oxidation of biomass derived 5-hydroxymethylfurfural (HMF): pathway, mechanism, catalysts and coupling reactions. *Green Chemistry* **2021**, *23* (12), 4228-4254.

(28) Zhang, P.; Sheng, X.; Chen, X.; Fang, Z.; Jiang, J.; Wang, M.; Li, F.; Fan, L.; Ren, Y.; Zhang, B.; et al. Paired Electrocatalytic Oxygenation and Hydrogenation of Organic Substrates with Water as the Oxygen and Hydrogen Source. *Angewandte Chemie International Edition* **2019**, *58* (27), 9155-9159.

Chapter 7

One-dimensional Bismuth Nanofibers as an Efficient Cathode Material for Electrochemical CO₂ Conversion to Formate

7.1 ABSTRACT

The electrocatalytic conversion of CO_2 to formate is one of the most practical and technologically advanced processes to produce essential fuels and chemicals. Due to the poor intrinsic activity for the reduction of CO_2 to formate, electron transfer efficiency, adequate active sites are essential to create high-performance electrocatalysts. Numerous studies have been conducted on Bismuth based electrocatalysts in the CO_2 reduction reaction (CO_2RR), due to its high efficiency to produce formate. In this chapter, we are discussing about Bismuth nanofibers, synthesized via electrospinning method (Bi-Bi_2O_3@NF), as an efficient catalyst for the electrocatalytic CO_2 reduction to formate production at high faradic efficiency of 90% at a potential of -0.8 V vs RHE. The catalytic performance of Bi-Bi_2O_3@NF-600 nanocomposites can be attributed to synergistic interactions, higher electrochemical surface area and nitrogen content, and their mixed crystalline and amorphous character. Thus, the outcomes led to an efficient method for increasing the activity and product selectivity of electrocatalysts to facilitate efficient CO_2 conversion.

7.2 INTRODUCTION

The electrochemical reduction reaction of CO_2 (CO_2RR), with the goal of generating energy-intensive compounds or fuels using renewable energy sources, has garnered significant attention in both the academic and business sectors. This approach holds promise for advancing environmental and energy sustainability.[1, 2] Among the various reduction products of CO_2, high-value liquids like formic acid or formate, which are of

particular interest due to their significance as essential feedstocks in chemical manufacturing and their practical utility as energy carriers in fuel cell applications.[3, 4]. Out of the various C1 and C2 products generated through electrochemical CO_2RR, the process that involves a two-electron conversion of CO_2 to formic acid or CO stands out as the most economically viable option when assessing its commercial potential.[5] Formic acid can be treated as a solution for long term energy storage and seasonal intermittency of renewable energy sources, as it can store energy in chemical bonds and it has a high volumetric capacity hydrogen storage media (53.4 g/L at standard temperature and pressure)[6-8]. Several metals catalysts have been explored to produce formic acid by CO_2RR like Hg^9, Ag^{10}, Pd^{11}, Pb^{12}, In^{13}, Sn^{14}. Highly toxic and expensive nature, however, is the obstacle for their large scale application. Sn and Bi catalysts are extensively investigated for formate generation in CO_2RR to tackle the urgent need for non-noble earth-abundant catalysts. However, the poor formic acid selectivity and low conversion rate of Sn-based electrocatalysts, which require considerable energy input, prevent their commercialization[15]. Due to their great selectivity for the production of formic acid, environmentally safe metallic Bi-based electrocatalysts have recently received a lot of interest.

CO_2 molecules are typically inert and thermodynamically stable, therefore it is essential for developing high-efficiency catalysts to enhance the rate of the kinetically sluggish CO_2 reduction process in order to improve the performance of the CO_2 reduction reaction[16]. Numerous methods have been investigated up to this time to enhance the CO_2RR performances of Bi-based electrocatalysts[17] including defect engineering[15], morphology engineering[18], crystal facets tuning[19], and heteroatom doping and alloying[20-22]. Despite these exceptional results, the reported Bi-Bi₂O₃ based catalysts experience large overpotentials because the electrochemical kinetics of CO_2RR are constrained by

the poor electrical conductivity of metallic Bi[22]. In the case of Bi-based electrocatalysts, their capacity to achieve high formic acid productivity in CO_2RR centers on factors such as the accessibility of active sites and their ability in electron transfer. This is particularly important due to their inherent inclination toward formate production.

Herein, the synthesis of highly dispersed $Bi-Bi_2O_3$ nanoparticles embedded in carbon nanofiber ($Bi-Bi_2O_3@NF$) using electrospinning technique, as a catalyst for CO_2 reduction, is reported here. The advantage of this embedded structure is that the Carbon Nano Fiber (CNF) matrix can maintain good electron transfer from the CNF by preventing $Bi-Bi_2O_3$ nanoparticle aggregation. Additionally, due to its porous design, CO_2 molecules can access the $Bi-Bi_2O_3$ surface and participate in the CO_2 reduction reaction. The synthesized $Bi-Bi_2O_3@NF$ shows excellent CO_2 reduction performance with a high faradic effeciency of 90% for formate production at a potential of -1.4 V vs Ag/AgCl and maintained a high FE of over 80% in the potential range of -1.3 to -1.6 V vs Ag/AgCl.

7.3 EXPERIMENTAL SECTION

Materials:

Bismuth (III) nitrate pentahydrate ($Bi(NO_3)_3 \cdot 5H_2O$), polyacrylonitrile (PAN) were bought from Sigma Aldrich. *N,N*-Dimethylformamide (DMF) was purchased from Spectrochem. Potassium bicarbonate ($KHCO_3$) was purchased from CDH. The chemicals and reagents employed in this study are all of analytical grade and have been used without any additional treatment. Carbon cloth (AvCarb 1071 HCB, 7.5 microns diameter) was bought from ASG scientific equipment. We obtained the proton exchange membrane (Nafion 117) from Alfa Aesar. High-purity gases, including CO_2 (99.999%), N_2 (99.998%), and Ar (99.998%), were supplied by Sigma-Aldrich.

Preparation of Bi-Bi₂O₃@NF:

10 mL of DMF was used to dissolve 1 g of $Bi(NO_3)_3 \cdot 5H_2O$ and 0.7 g of PAN. A homogenous precursor solution resulted after 24 hours of vigorous stirring of the above mixture. Using a 22-gauge stainless steel needle, the solution was injected into a syringe and electrospun at a rate of 0.3 mL per hour at a voltage of 20 kV. The distance from the needle to the drum-collector was set at 15 cm. After being stabilized at 250 °C for 2 hours in a muffle furnace, the sample was annealed at 600 °C for additional 2 hours under nitrogen and hydrogen gas atmosphere at the volume ratio of 7:1 %, the desired Bi-coated mesoporous carbon nanofibers (Bi-Bi₂O₃@NF) were produced. In addition, samples were synthesized at different temperatures of 500 °C and 700 °C for comparison.

Instrumentation and Analysis:

Surface morphology analysis was done using a field-emission scanning electron microscope (Carl Zeiss, Germany, Model ∑igma). A 0.05 mL of a solution containing 1 mg/mL of material was coated onto a silicon wafer, dried at 45 °C, and then the samples were ready for FE-SEM examination. Utilising a Bruker DAVINCI D8 ADVANCE diffractometer fitted with Cu K radiation (λ= 0.15406 nm), X-ray diffraction (*p*-XRD) patterns were obtained. The surface morphology of the produced materials was examined using high-resolution transmission electron microscopy (HRTEM) at 200 kV. The analysis was carried out using a JEOL F200 instrument. Initially, 10 μL of a 1 mg/mL stock solution was taken for the TEM analysis and dried in the air at a temperature of around 45 °C. By coating the material on a silicon wafer and utilising Mg Kα X-ray as the monochromatic source, VG Microtech was used to accomplish the X-ray photoelectron spectroscopy experiments. All electrochemical measurements were performed on a workstation for electrochemical measurements (Autolab, Metrohm, PGSTAT 320N). A Hanna (HI 2209) pH meter was used to determine the pH of the

electrolyte. Equipment for ultrasonic bath sonication was provided by Genei Laboratories Private Ltd. Bangalore, India. The ^{1}H NMR spectrum was obtained using the water suppression technique on a Bruker 400 MHz instrument.

Electrochemical performances:

At first, 4 mg of the prepared catalyst is ultrasonicated for 1 hour to obtain a homogenous slurry in 470 µL of Millipore water along with 30 µL of Nafion (5.0 wt %) solution. The resultant ink was subsequently drop casted on carbon cloth with the help of micropipette and dried at 45 °C for further electrochemical testing. A three-electrode setup connected to the electrochemical workstation (Autolab) was used to perform electrochemical performances. Each cathodic and anodic chamber was filled with 60 mL of 0.5 M $KHCO_3$ electrolyte, and these chambers were separated by a Nafion 117 proton exchange membrane. The cathodic chamber contained the working electrode (prepared catalyst electrode) and the reference electrode (Ag/AgCl) with a spacing of 0.5 cm between them. In contrast, the anodic chamber included a platinum electrode as the counter electrode. All measurements were referenced to the Ag/AgCl reference electrode and subsequently adjusted to the reversible hydrogen electrode (RHE) using the following equation 1;

$$V_{RHE} = V_{Ag/AgCl} \text{(saturated 3M KCl)} + 0.197 + 0.00592pH \ldots\ldots\ldots\ldots(1)$$

The CO_2-saturated electrolyte's pH was determined to be 6.85. In order to achieve total saturation, high-purity Ar and CO_2 were used to purge the electrolyte used in the H-cell for at least an hour before each electrochemical measurement.

Product Identification and Quantification:

A gastight H-type cell was used to examine the electrochemical CO_2 reduction under typical environmental circumstances using chronoamperometry experiments. PGSTAT 320N potentiostat (Autolab, Metrohm) was used to apply a fixed potential. To achieve CO_2 saturation, high-purity CO_2 was purged for an hour prior to applying the potential

in a 0.5 M KHCO₃ solution. After 30 minutes of electroreduction, NMR and gas chromatography were used to measure and quantify the liquid and gaseous products, respectively. Gas chromatography (Thermo Scientific Trace 1110 GC), utilizing a 60/80 Carboxen-1000 column outfitted with a thermal conductivity detector (TCD), was used to quantify the gaseous products and high-purity Ar gas is used (99.999%) as the carrier gas. The gaseous products from the headspace were collected and introduced into the GC via a gastight syringe, with each analysis using 1 mL of the gaseous products. To quantify the gaseous products, a standard gas sample containing H_2 (2.04%), CO (2.07%), CO_2 (2.07%), C_2H_6 (2.02%), CH_4 (1.96%), and Ar as the rest of the gas was used. The NMR technique (Bruker 400 MHz spectrometer) was used to identify and measure liquid products resulting from CO_2 reduction, specifically, formate. For NMR analysis, 50 μL of D_2O (Aldrich, 99.9%) were added to 450 μL of electrolyte, and the water suppression technique was used to record the ^1H NMR spectrum. Data obtained from the NMR spectra were processed using the Bruker software TopSpin. The faradaic efficiency of the CO_2 reduced products were calculated using the following equation 2;

$$FE\ (\%) = \frac{\text{mol of product formed (N)}}{\text{total charge passed (C)/ (F×n)}} \times 100\% \ \ldots\ldots\ldots\ldots\ldots\ldots\ldots(2)$$

In this equation: N represents the number of total moles of the product generated. C stands for the charge passed during the electrolysis at the cathode. F is the Faraday constant, equal to 96485 C mol^{-1}. n signifies the number of electrons required to produce one molecule of the product from CO_2.

7.4 RESULTS AND DISCUSSION

Morphology and characterization

The preparation process of Bi-Bi_2O_3@NF-600 is done by using electrospinning technique. At first, the precuassor bismuth (III) nitrate pentahydrate ($Bi(NO_3)_3 \cdot 5H_2O$) is mixed with polymer solution of polyacrylonitrile (PAN) to form a homogenous solution, which subjected to electrospinning to form electrospun fibers composed of PAN and Bi (details in experimental section 2.2.1). The as prepared electrospun fibres were stabilized in air followed by carbonization in presence of N_2/H_2 mixture (7:1) at different temperatures to form Bi-Bi_2O_3@NF uniformly embedded in CNF matrix. The synthesized Bi-Bi_2O_3@NF-600 is analyzed using X-ray diffraction (XRD) pattern, shown in Figure 7.1a. The diffraction peaks at 27.7°, 38.4°, 40°, 44.8°, 46.2°, 49.2°, 56.4°, and 59.5° in Bi-Bi_2O_3@NF-600 composite are assigned as (012), (104), (110), (015), (006), (202), (024), and (107) crystalline planes of Bi metal, and peaks at 28° in Bi-Bi_2O_3@NF-600 composite are assigned as (112) and (004) planes of Bi_2O_3 and the obtained data is well matching with the standard JCPDS data (PDF 00-002-0518) and (PDF 01-075-4627), respectively.
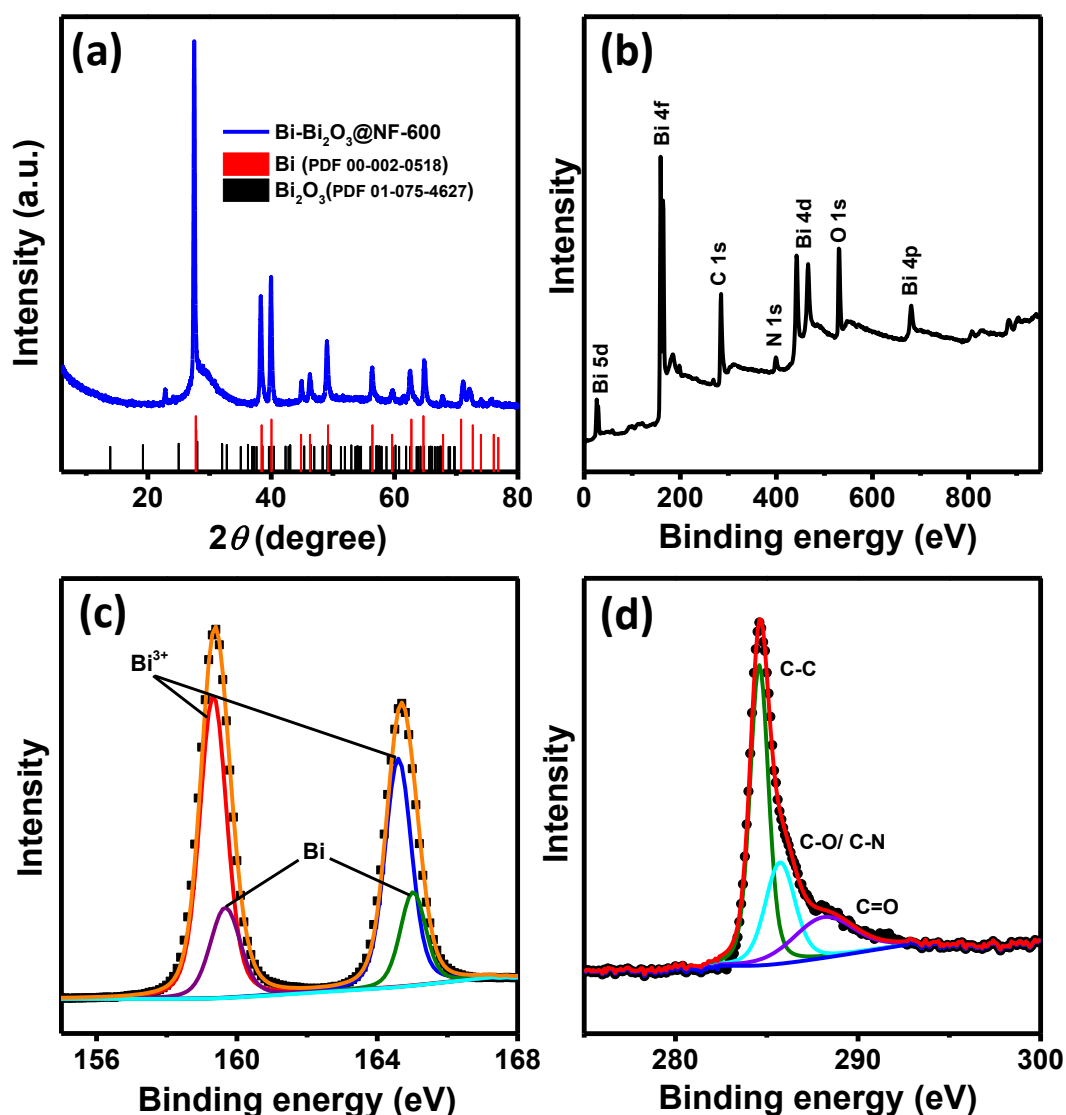
Figure 7.1. (a) p-XRD pattern; XPS (b) survey scan spectra, high resolution XPS spectra of (c) Bi 4f and (d) C 1s of Bi-Bi$_2$O$_3$@NF-600 catalyst.

X-ray photoelectron spectroscopy (XPS) analysis was conducted to gain insights into the chemical composition and structural characteristics of Bi-Bi$_2$O$_3$@NF-600. Figure 7.1b illustrates the survey scan spectra of Bi-Bi$_2$O$_3$@NF-600, providing valuable information about the constituent elements. The spectral data confirms the presence of several elements, namely Bi, C, N, and O within the compound. For a more detailed examination of the Bi component, Figure 7.1c presents the high-resolution Bi XPS spectra. This analysis reveals distinct peaks located at 159.31 and 164.6 eV in the deconvoluted Bi 4f

235

XPS spectrum. These peaks are indicative of the presence of Bi^{3+} within the Bi-Bi_2O_3@NF-600 composite. Two additional peaks at lower binding energies, specifically 159.66 and 164.99 eV, are observed. These lower-energy peaks are attributed to the emergence of metallic Bi within the Bi-Bi_2O_3@NF-600 composite.[15] Figure 7.1d displays the C 1s fitting spectra, shedding light on the carbon (C) component. This spectrum showcases three distinct peaks situated at 284.58, 285.79, and 288.46 eV. The peak at 284.58 eV corresponds to carbon-carbon (C-C) or carbon-carbon double bond (C=C) interactions. The peak at 285.79 eV is attributed to carbon-oxygen (C−O) or carbon-nitrogen (C−N) bonds. Lastly, the peak at 288.46 eV is associated with carbon-oxygen double bonds (C=O). Thus, XPS analysis of Bi- Bi_2O_3@NF-600 provides a comprehensive understanding of its chemical composition, revealing the coexistence of Bi^{3+} and metallic Bi species in the composite.[23]
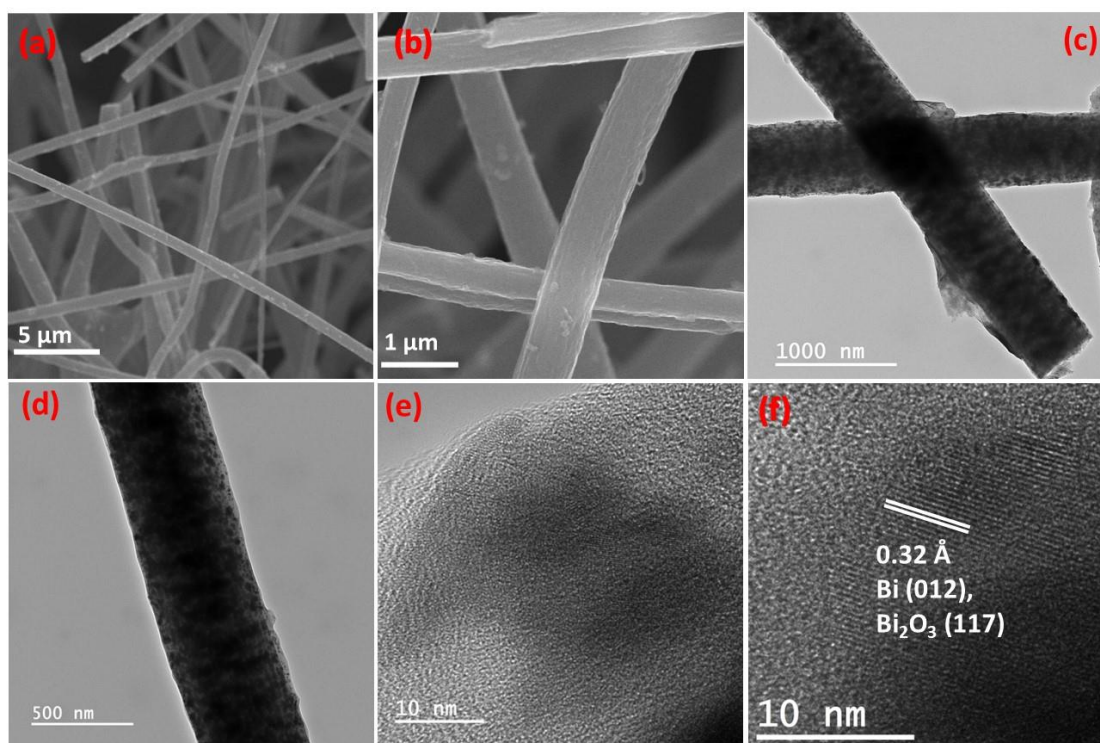
Figure 7.2. (a, b) SEM images, and (c, d) TEM images of Bi-Bi_2O_3@NF-600, (e,f) HRTEM image.

Field emission scanning electron microscopy (FESEM) was employed to investigate the morphological traits of Bi-Bi_2O_3@NF-600. SEM images (Figure 7.2a and b) of Bi-Bi_2O_3@NF-600 clearly reveals the obtained structure and morphology of the catalyst, where a single fiber is seen without any beads of agglomerated Bi on the CNF surface. It indicates that the Bi-Bi_2O_3 nanoparticles were completely incorporated into the CNF matrix. Transmission electron microscopy (TEM) images of Bi-Bi_2O_3@NF-600 are displayed in Figure 7.2 (c and d). From the TEM images, it is seen that one-dimensional nanorods are formed. STEM elemental mapping analysis of Bi-Bi_2O_3@NF-600 is provided in Figure 7.3. The elemental mapping clearly shows the uniform distribution of Bi, N, O and C in the one dimensional rod of Bi-Bi_2O_3@NF-600 which is in accordance with the XRD and XPS data. The high-resolution transmission electron microscopy (HR-TEM) images of Bi-Bi_2O_3@NF-600 are illustrated in Figure 7.2 (e and f). These images reveal a distinct d-spacing value of 0.32 Å, which corresponds to the (012) lattice plane of elemental bismuth (Bi) and the (117) lattice plane of bismuth oxide (Bi_2O_3), as depicted in Figure 7.2f, which is matching with the XRD data.
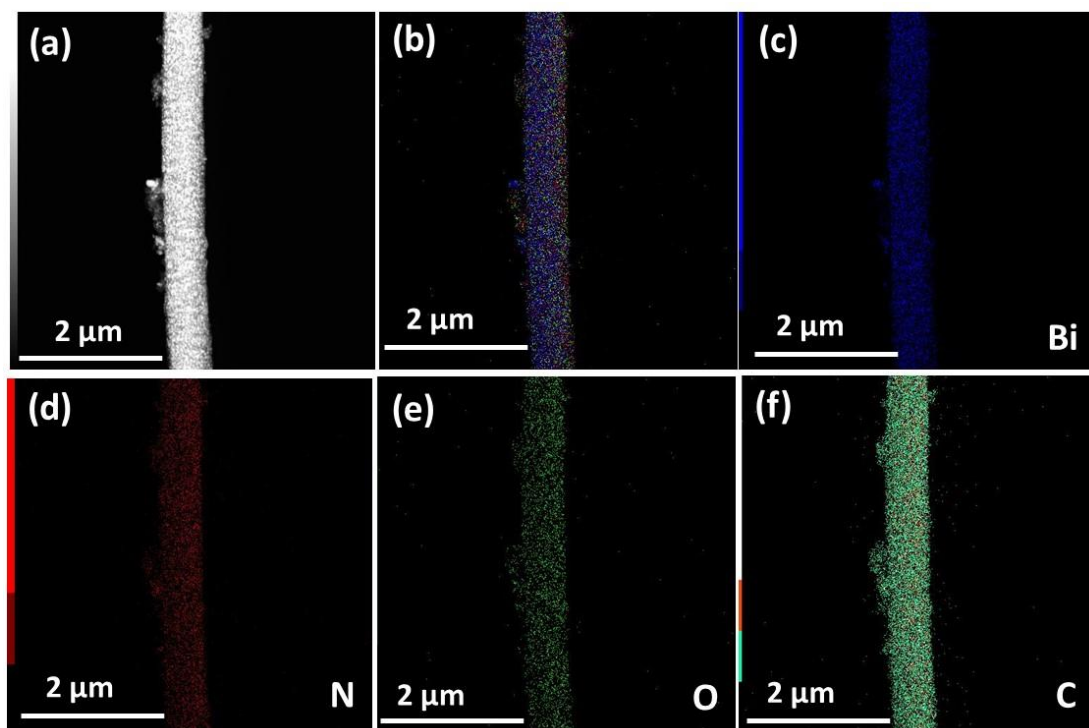
Figure 7.3. (a) STEM images, (b, c, d, e) elemental mapping, (f) Overlay of Bi_2O_3@NF-600.

Electrochemical CO_2 reduction

The electrochemical CO_2 reduction reaction was investigated by Linear Sweep Voltammetry (LSV) plots in undivided three electrode system where Bi-Bi_2O_3@NF was used as working electrode, Ag/AgCl as reference electrode and Pt wire as counter electrode and 0.5 M $KHCO_3$ as electrolyte. The LSV was investigated by purging Ar and CO_2 gas in the electrolyte. The potential was subjected to a scan ranging from -0.5 V to a negative potential of -1.2 V vs RHE, with a scan rate of 10 mV/s during LSV, which was conducted without any stirring. In Ar saturated electrolyte, the LSV current is due to hydrogen evolution reaction. However, in CO_2 saturated electrolye, there is a rise in current and decrese in overpotential is observed for all the samples which depicts CO_2 reduction reaction is more favorable in the electrode surface compared to hydrogen

reduction process. The LSV of all the compounds carbonized at differenet temperatures were investigated which depicts Bi-Bi_2O_3@NF-600 outperformed Bi-Bi_2O_3@NF-500 and Bi-Bi_2O_3@NF-700 composites as shown in Figure 7.4a. Electrochemical impedance spectroscopy (EIS) spectra were employed and analyzed to gain a more comprehensive understanding of the reaction pathway and kinetics involved in CO_2 reduction (Figure 7.4b). These spectra were acquired within a frequency range of 0.1-100 kHz while maintaining an open circuit potential. An alternating current (AC) amplitude of 10 mV was applied in a 0.5 M $KHCO_3$ electrolyte solution. To compare the EIS of Bi-Bi_2O_3@NF-600, measurements were performed in both Ar-saturated and CO_2-saturated electrolytes. The inset illustrates the circuit model utilized for fitting the EIS data, where "Rs" signifies the solution resistance, the semicircle's diameter represents the charge transfer resistance (Rct), and "CPE" represents the constant phase element. The EIS spectrum of the catalyst Bi-Bi_2O_3@NF-600 in Ar saturation showed a larger semicircle, however, for CO_2 saturated electrolyte, displayed a smaller semicircle. The less diameter of the semicircle indicates a reduced Rct value and enhanced electronic conductivity. R_{ct} values of Bi-Bi_2O_3@NF-600 in Ar and CO_2 saturated electrolyte are 44 Ω and 30 Ω respectively. The lower R_{ct} value of Bi-Bi_2O_3@NF-600 in CO_2 saturated electrolyte suggests faster reaction kinetics or charge transfer for CO_2 reduction reaction.
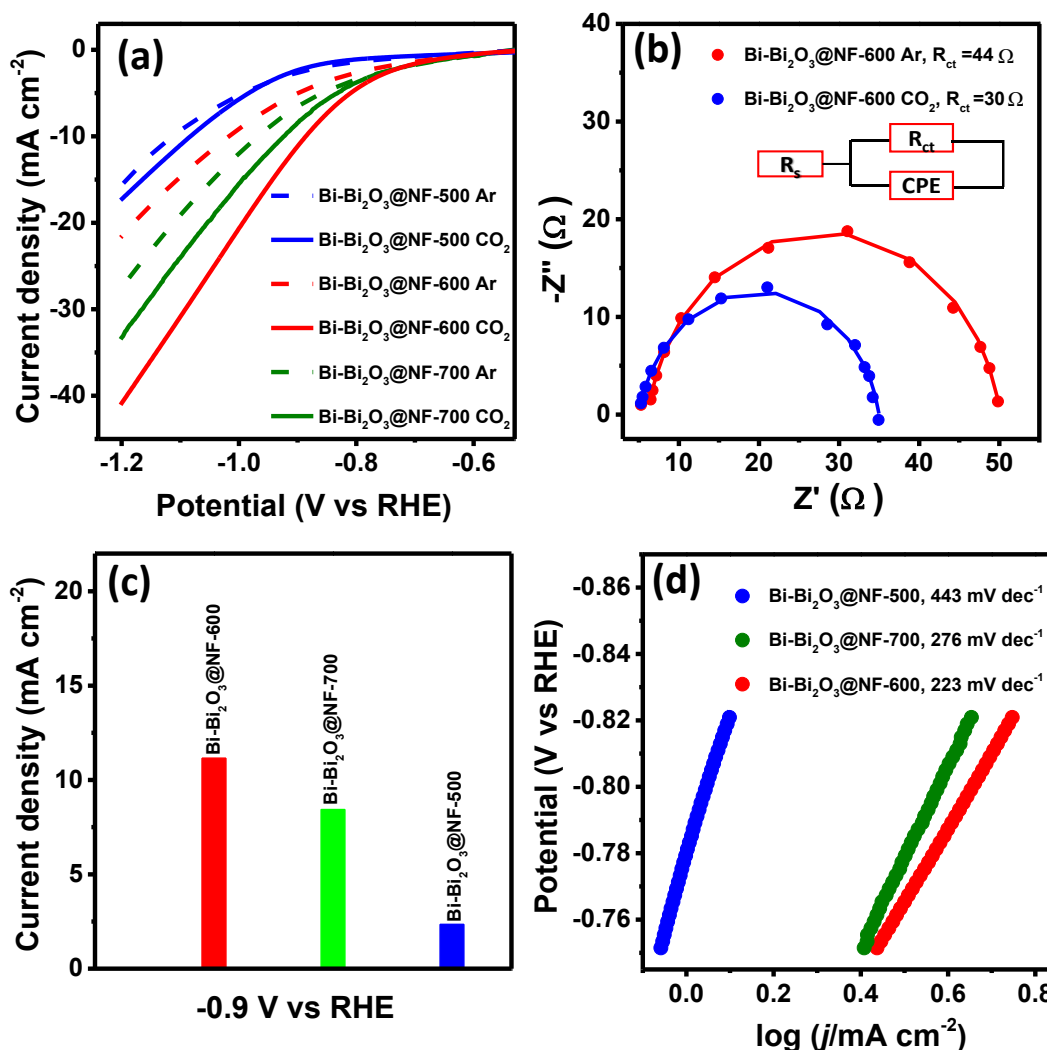
Figure 7.4. (a) Non-iR corrected LSV curves of Bi-Bi_2O_3@NF-500, Bi-Bi_2O_3@NF-600 and Bi-Bi_2O_3@NF-700 in Ar and CO_2 saturated 0.5 M KHCO₃ (b) Nyquist plots of Bi-Bi_2O_3@NF-600, (c) Current density of different catalysts at -0.9 V vs RHE, (d) Tafel slope of Bi-Bi_2O_3@NF-500, Bi-Bi_2O_3@NF-600 and Bi-Bi_2O_3@NF-700 in CO_2 saturated 0.5 M KHCO₃ electrolyte.

The current density (*j*) values of different catalysts at -0.9 V vs RHE potential are given in Figure 7.4c. The *j* vlaues for Bi-Bi_2O_3@NF-500, Bi-Bi_2O_3@NF-600 and Bi-Bi_2O_3@NF-700 are 2.35, 11.16 and 8.44 mA cm^{-2} respectively. The higher current density of Bi-Bi_2O_3@NF-600 proves the highest activity of Bi-Bi_2O_3@NF-600 among all. In addition, to understand the reaction kinetics of the CO_2 reduction reaction, the tafel plots of each catalyst were also calculated using the Tafel equation. The low tafel slope value indicates faster kinetics. The tafel slope values obtained from Figure 7.4d for Bi-

$Bi_2O_3@NF$-500, Bi-$Bi_2O_3@NF$-600 and Bi-$Bi_2O_3@NF$-700 are 443 mV dec^{-1}, 223 mV dec^{-1} and 276 mV dec^{-1} respectively. Comparing different catalysts, Bi-$Bi_2O_3@NF$-600 has the smallest tafel slope value, indicating faster CO_2 reduction reaction on the catalyst.
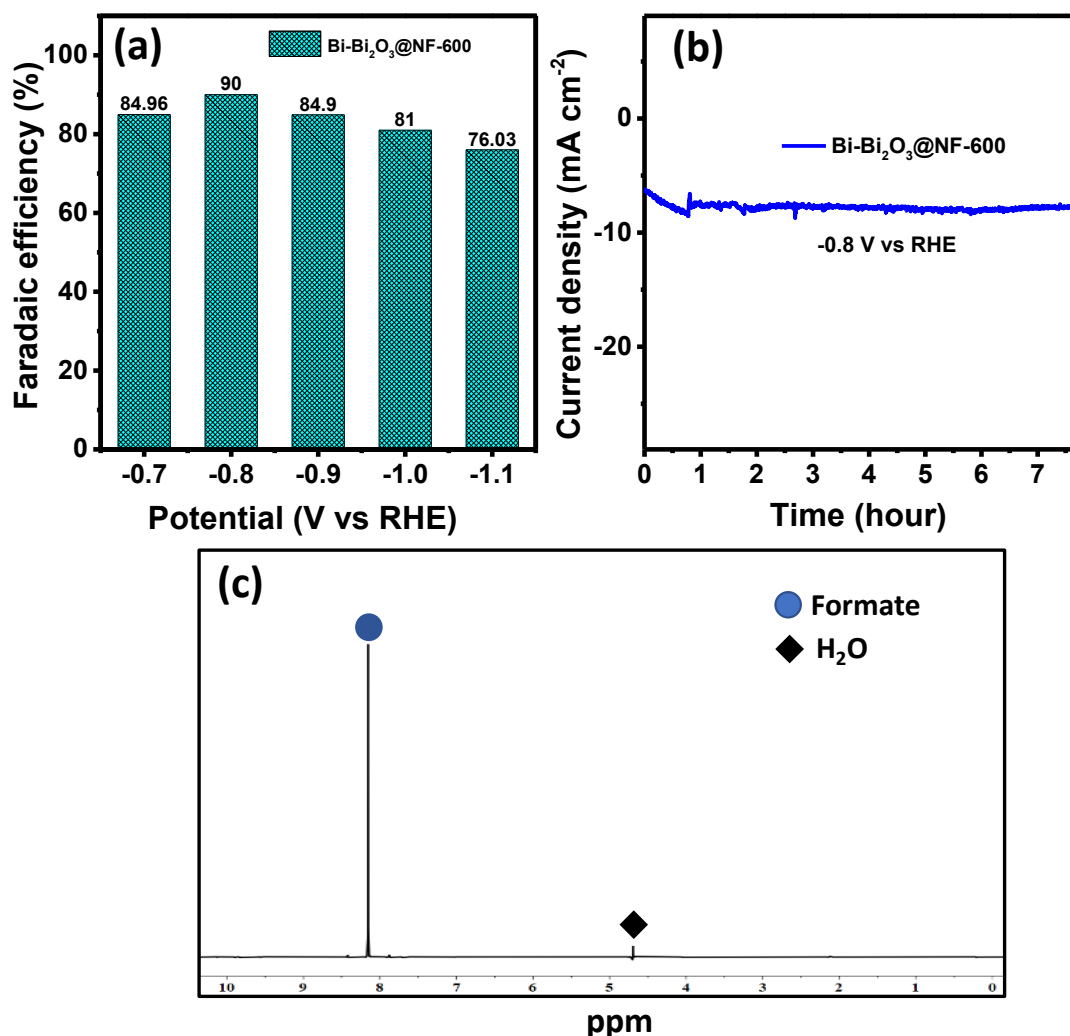
Figure 7.5. (a) Formate faradic efficiency plot, (b) electrochemical stability in CO_2 saturated 0.5 M $KHCO_3$, (c) ^{1}H NMR spectra for electrochemical CO_2 reduction reaction in 0.5 M $KHCO_3$ after applying potential at -0.8 V vs RHE for 30 minutes.^{1}H NMR (400 MHz, 90% H_2O/ 10% D_2O): δ 8.02 (s, 1H). (Formate peak at 8.02 ppm).

Quantitative product analysis for CO_2 reduction reaction was done after 30 mins of chronoamperometry at a constant potential. The gaseous products were analyzed with

the help of GC and the liquid products were analyzed using NMR spectroscopy. The liquid product consists solely of formate across different potentials for the composite material during the products analysis using NMR. From the GC analysis, the presence of slight amount of H_2 was observed. Bi-Bi_2O_3@NF-600 nanocomposite exhibits the maximum faradaic efficiency for $HCOO^-$ ($FE_{formate}$) at each studied potential and inhibits the generation of H_2 (Figure 7.5a). The faradaic efficiency of formate production exhibits a gradual increase with an elevating reduction potential, ultimately peaking at 90% when the potential is set at -0.8 V vs RHE. Further negative shifts in the potential result in a reduction in the faradaic efficiency of formate. This decline in faradaic efficiency at more negative potentials can be attributed to the contributing factor that, at higher overpotentials, the HER prevails over the CO_2RR on the Bi-Bi_2O_3@NF-600 catalyst. The Table 7B.1 presents a comparative analysis of Bi-based catalysts for the electrochemical reduction of CO_2, specifically focusing on their faradaic efficiency in formate production. This demonstrates that the Bi-Bi_2O_3@NF-600 nanocomposite exhibits excellent faradic efficiency for formate production. Chronoamperometry measurements were conducted on Bi-Bi_2O_3@NF-600, maintaining a constant potential of -0.8 V vs RHE. The results, as shown in Figure 7.5b, demonstrate the remarkable stability of the catalyst for up to 8 hours during the CO_2 reduction reaction.

Table 7.1. Comparision of reported Bi-based catalyst for CO_2RR.

Catalyst	Electrolytes	Cell configuration	$FE_{formate}$	Potential (V vs. RHE)	References
SnO_2/Bi_2O_3	**0.1 M KHCO₃**	**H-cell**	**90%**	**-1.0 V**	**24**
Bi_2S_3	**0.5 M KHCO₃**	**H-type cell**	**80%**	**-1.0 V**	**25**
Fractal-Bi_2O_3	**0.1 M KHCO₃**	**H-cell**	**87%**	**−1.2 V**	**19**
Bi/Bi_2O_3-CP	**0.5 M KHCO₃**	**H-cell**	**90.4 %**	**−0.87 V**	**15**

$Bi_2O_3-CeO_x$	1 M KOH	Flow cell	>90%	-0.5 to -1.1 V	26
$Bi-Bi_2O_3@NF$	0.5 M $KHCO_3$	H-cell	90%	-0.8 V	This work
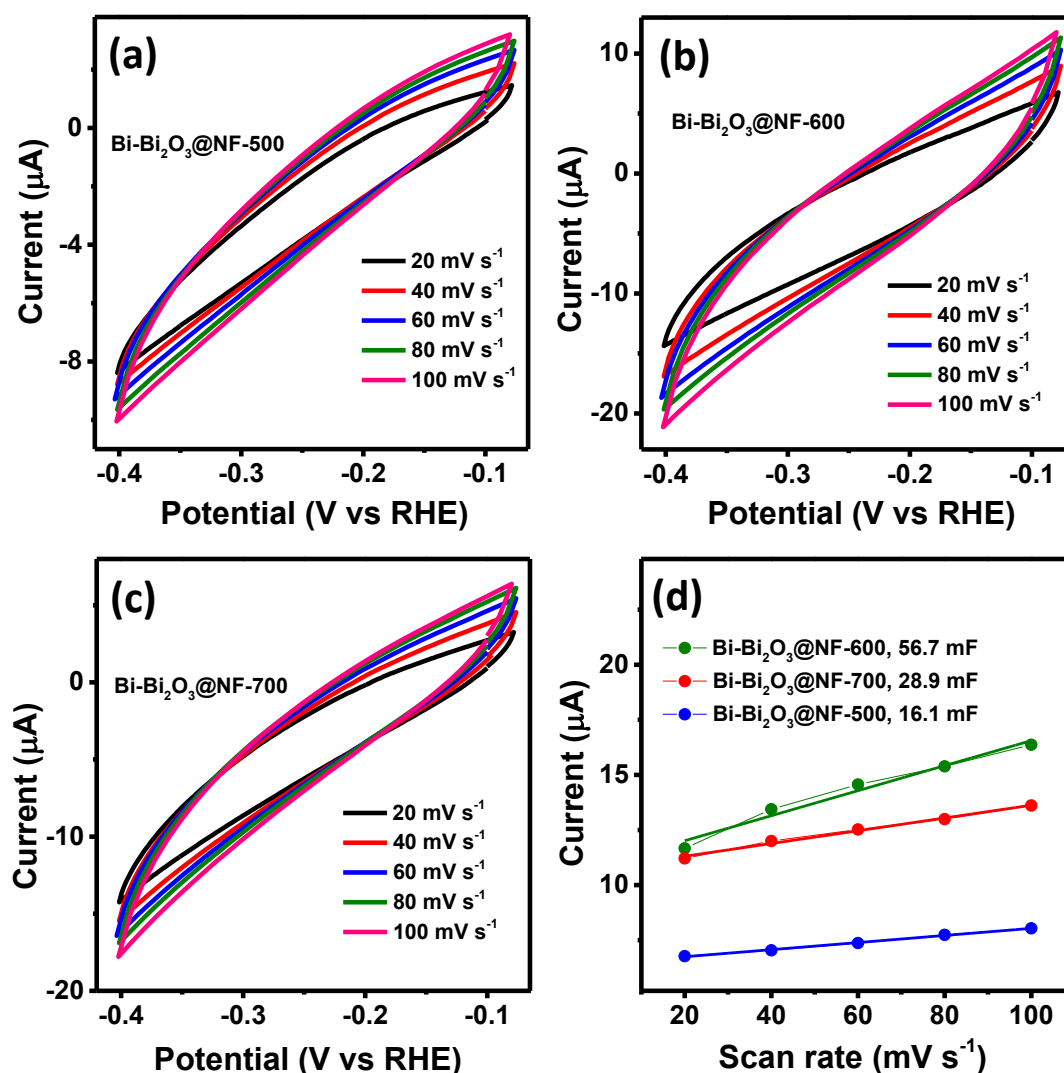
Figure 7.6. (a, b, c) electrochemical double layer measurements of $Bi-Bi_2O_3@NF-500$, $Bi-Bi_2O_3@NF-600$, and $Bi-Bi_2O_3@NF-700$ repectively, (d) corresponding C_{dl} value of catalysts.

To evaluate the influence of surface area and explore the density of active sites on the nanocomposites, we conducted an examination of the electrochemical double-layer capacitance for the catalytic surface of $Bi-Bi_2O_3@NF-500$, $Bi_2O_3@NF-600$, and

Bi_2O_3@NF-700, as shown in Figure 7.6 (a-c). The electrochemically active surface area (ECSA) and the electrochemical double-layer capacitance (C_{dl}) are directly proportional. CV measurements were conducted in a non-faradaic region, employing a scan rate spanning from 20 to 100 mV/s in a 0.5 M $KHCO_3$ electrolyte in order to calculate the C_{dl} of these catalysts (Figure 7.6d). The C_{dl} values from the slope obtained for Bi_2O_3@NF-500, Bi_2O_3@NF-600, and Bi_2O_3@NF-700 are 16.1 mF, 56.7 mF and 28.9 mF respectively. The higher C_{dl} value observed in Bi_2O_3@NF-600 compared to Bi_2O_3@NF-500 and Bi_2O_3@NF-700 indicates a greater electrochemical surface area (ECSA), signifying the presence of more active sites available for catalyzing the CO_2 reduction reaction.

Plausible mechanism for CO₂ reduction to Formic acid
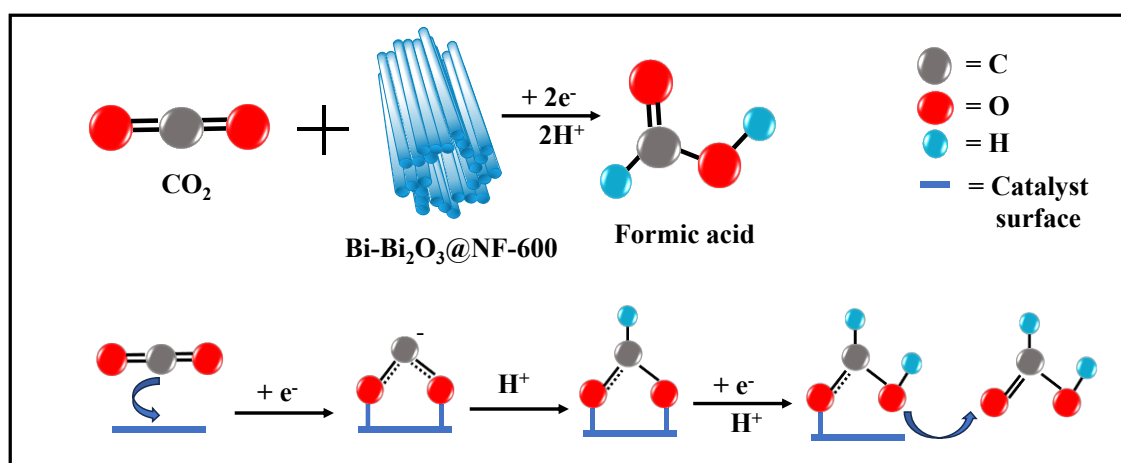
Scheme 7.1. Plausible reduction pathway of CO₂RR to produce Formic acid.

In recent years, bismuth-based catalysts have emerged as promising candidates for enhancing formate production in electrochemical CO_2 reduction. However, despite their potential, the underlying mechanisms governing this reaction have not been thoroughly elucidated. Thus, here a plausible mechanism of electrochemical CO_2 reduction for formate production over bismuth-based catalysts is provided. As depicted in Scheme 7.1, four distinct reaction pathways for the conversion of CO_2 into formate (HCOO− or

HCOOH) was outlined. These pathways shed light on the intricate steps that occur during this electrochemical process. Path I: Initially, CO_2 molecules are adsorbed onto the active sites of the catalyst through interactions with the bismuth-oxygen (Bi-O) bonds. In this step, CO_2 gains an electron, transforming into a $*CO_2^-$ radical anion. Path II: The $*CO_2^-$ radical anion is further involved in a protonation process, leading to the formation of $*OCHO$, a vital intermediate. Path III: $*OCHO$ captures a second electron and an additional proton to evolve into $*HCOOH$ (formic acid). Path IV: Finally, formic acid (HCOOH) is detached from the active sites, completing the reaction cycle.[27]

7.5 CONCLUSIONS:

This chapter showcases a straightforward one-step approach for synthesizing Bi-Bi_2O_3@NF-600 nanofibers intended for use in electrochemical CO_2 reduction. The Bi-Bi_2O_3 embedded CNF matrix was formed by electrospinning method. High porosity and large electrochemically active surface area of the catalyst provides a sufficient number of active sites for CO_2 reduction. Notably, the Bi-Bi_2O_3@NF-600 catalyst's outstanding performance can be attributed to the nitrogen content and the uniformity conferred by the CNF matrix. The synthesized Bi-Bi_2O_3@NF-600 catalyst acts as a cathode material and is successfully suppressing HER and produces formate as major CO_2 reduced product. Bi-Bi_2O_3@NF-600 efficiently reduced CO_2 to formate with a high faradic efficiency of ~90% at -0.8 V vs RHE. Hence, the present study could potentially pave the way for establishing a pathway to generate value-added products through CO_2 reduction with far-reaching implications for sustainable energy applications.

7.6 REFERENCES:

(1) Kibria, M. G.; Edwards, J. P.; Gabardo, C. M.; Dinh, C.-T.; Seifitokaldani, A.; Sinton, D.; Sargent, E. H. Electrochemical CO2 Reduction into Chemical Feedstocks: From Mechanistic Electrocatalysis Models to System Design. *Advanced Materials* **2019**, *31* (31), 1807166,.

(2) Long, C.; Li, X.; Guo, J.; Shi, Y.; Liu, S.; Tang, Z. Electrochemical Reduction of CO2 over Heterogeneous Catalysts in Aqueous Solution: Recent Progress and Perspectives. *Small Methods* **2019**, *3* (3), 1800369.

(3) Zhang, J.; Chen, M.; Li, H.; Li, Y.; Ye, J.; Cao, Z.; Fang, M.; Kuang, Q.; Zheng, J.; Xie, Z. Stable palladium hydride as a superior anode electrocatalyst for direct formic acid fuel cells. *Nano Energy* **2018**, *44*, 127-134.

(4) Natsui, K.; Iwakawa, H.; Ikemiya, N.; Nakata, K.; Einaga, Y. Stable and Highly Efficient Electrochemical Production of Formic Acid from Carbon Dioxide Using Diamond Electrodes. *Angewandte Chemie International Edition* **2018**, *57* (10), 2639-2643,

(5) Huang, Z.; Grim, R. G.; Schaidle, J. A.; Tao, L. The economic outlook for converting CO2 and electrons to molecules. *Energy & Environmental Science* **2021**, *14* (7), 3664-3678.

(6) Grubel, K.; Jeong, H.; Yoon, C. W.; Autrey, T. Challenges and opportunities for using formate to store, transport, and use hydrogen. *Journal of Energy Chemistry* **2020**, *41*, 216-224.

(7) Vo, T.; Purohit, K.; Nguyen, C.; Biggs, B.; Mayoral, S.; Haan, J. L. Formate: an Energy Storage and Transport Bridge between Carbon Dioxide and a Formate Fuel Cell in a Single Device. *ChemSusChem* **2015**, *8* (22), 3853-3858.

(8) Shitrit, Y.; Duraiyarasu, M.; Kumar, J.; Reddy, S.; Ya'akobovitz, A.; Cohen, Y. S.; Edri, E. Deposition of Bismuth Nanoplatelets onto Graphene Foam for Electrocatalytic CO2 Reduction. *ACS Applied Nano Materials* **2022**, *5* (11), 16354-16364.

(9) Abbas, S. A.; Kim, S.-H.; Saleem, H.; Ahn, S.-H.; Jung, K.-D. Preparation of Metal Amalgam Electrodes and Their Selective Electrocatalytic CO2 Reduction for Formate Production. In *Catalysts*, 2019; Vol. 9.

(10) Yang, W.; Chen, S.; Ren, W.; Zhao, Y.; Chen, X.; Jia, C.; Liu, J.; Zhao, C. Nanostructured amalgams with tuneable silver–mercury bonding sites for selective electroreduction of carbon dioxide into formate and carbon monoxide. *Journal of Materials Chemistry A* **2019**, *7* (26), 15907-15912.

(11) Jiang, T.-W.; Qin, X.; Ye, K.; Zhang, W.-Y.; Li, H.; Liu, W.; Huo, S.; Zhang, X.-G.; Jiang, K.; Cai, W.-B. An interactive study of catalyst and mechanism for electrochemical CO2 reduction to formate on Pd surfaces. *Applied Catalysis B: Environmental* **2023**, *334*, 122815.

(12) Pavesi, D.; van de Poll, R. C. J.; Krasovic, J. L.; Figueiredo, M.; Gruter, G.-J. M.; Koper, M. T. M.; Schouten, K. J. P. Cathodic Disintegration as an Easily Scalable Method for the Production of Sn- and Pb-Based Catalysts for CO2 Reduction. *ACS Sustainable Chemistry & Engineering* **2020**, *8* (41), 15603-15610.

(13) Cheng, Q.; Huang, M.; Xiao, L.; Mou, S.; Zhao, X.; Xie, Y.; Jiang, G.; Jiang, X.; Dong, F. Unraveling the Influence of Oxygen Vacancy Concentration on Electrocatalytic CO2 Reduction to Formate over Indium Oxide Catalysts. *ACS Catalysis* **2023**, *13* (6), 4021-4029.

(14) Tsujiguchi, T.; Kawabe, Y.; Jeong, S.; Ohto, T.; Kukunuri, S.; Kuramochi, H.; Takahashi, Y.; Nishiuchi, T.; Masuda, H.; Wakisaka, M.; et al. Acceleration of Electrochemical CO2 Reduction to Formate at the Sn/Reduced Graphene Oxide Interface. *ACS Catalysis* **2021**, *11* (6), 3310-3318.

(15) Wu, D.; Huo, G.; Chen, W.; Fu, X.-Z.; Luo, J.-L. Boosting formate production at high current density from CO2 electroreduction on defect-rich hierarchical mesoporous Bi/Bi2O3 junction nanosheets. *Applied Catalysis B: Environmental* **2020**, *271*, 118957.

(16) Qu, T.; Hu, J.; Dai, X.; Tan, Q.; Liu, Y.; Chen, Y.; Guo, S.; Liu, Y. Electrospinning Highly Dispersed Ru Nanoparticle-Embedded Carbon Nanofibers Boost CO2 Reduction in a H2/CO2 Fuel Cell. *ACS Applied Materials & Interfaces* **2021**, *13* (20), 23523-23531.

(17) Xia, D.; Yu, H.; Xie, H.; Huang, P.; Menzel, R.; Titirici, M. M.; Chai, G. Recent progress of Bi-based electrocatalysts for electrocatalytic CO2 reduction. *Nanoscale* **2022**, *14* (22), 7957-7973.

(18) Melchionna, M.; Moro, M.; Adorinni, S.; Nasi, L.; Colussi, S.; Poggini, L.; Marchesan, S.; Valenti, G.; Paolucci, F.; Prato, M.; et al. Driving up the Electrocatalytic Performance for Carbon Dioxide Conversion through Interface Tuning in Graphene Oxide–Bismuth Oxide Nanocomposites. *ACS Applied Energy Materials* **2022**, *5* (11), 13356-13366.

(19) Tran-Phu, T.; Daiyan, R.; Fusco, Z.; Ma, Z.; Amal, R.; Tricoli, A. Nanostructured β-Bi2O3 Fractals on Carbon Fibers for Highly Selective CO2 Electroreduction to Formate. *Advanced Functional Materials* **2020**, *30* (3), 1906478.

(20) Li, X.; Qian, N.; Ji, L.; Wu, X.; Li, J.; Huang, J.; Yan, Y.; Yang, D.; Zhang, H. Enhanced electrocatalytic reduction of CO2 to formate via doping Ce in Bi2O3 nanosheets. *Nanoscale Advances* **2022**, *4* (10), 2288-2293.

(21) Feng, X.; Zou, H.; Zheng, R.; Wei, W.; Wang, R.; Zou, W.; Lim, G.; Hong, J.; Duan, L.; Chen, H. Bi2O3/BiO2 Nanoheterojunction for Highly Efficient Electrocatalytic CO2 Reduction to Formate. *Nano Letters* **2022**, *22* (4), 1656-1664.

(22) Wang, X.; He, W.; Shi, J.; Junqueira, J. R. C.; Zhang, J.; Dieckhöfer, S.; Seisel, S.; Das, D.; Schuhmann, W. Ag-induced Phase Transition of Bi2O3 Nanofibers for Enhanced Energy Conversion Efficiency towards Formate in CO2 Electroreduction. *Chemistry – An Asian Journal* **2023**, *18* (2), e202201165.

(23) Ouyang, D.; Wang, C.; Zhu, H.; Yu, F.; Yin, J. Bismuth Nanoparticles Encapsulated in Mesoporous Carbon Nanofibers for Efficient Potassium-Ion Storage. *ACS Applied Nano Materials* **2022**, *5* (9), 13171-13179.

(24) Tian, J.; Wang, R.; Shen, M.; Ma, X.; Yao, H.; Hua, Z.; Zhang, L. Bi–Sn Oxides for Highly Selective CO2 Electroreduction to Formate in a Wide Potential Window. *ChemSusChem* **2021**, *14* (10), 2247-2254.

(25) Wang, Y.; Cheng, L.; Liu, J.; Xiao, C.; Zhang, B.; Xiong, Q.; Zhang, T.; Jiang, Z.; Jiang, H.; Zhu, Y.; et al. Rich Bismuth-Oxygen Bonds in Bismuth Derivatives from Bi2S3 Pre-Catalysts Promote the Electrochemical Reduction of CO2. *ChemElectroChem* **2020**, *7* (13), 2864-2868.

(26) Yu, R.; Qiu, C.; Lin, Z.; Liu, H.; Gao, J.; Li, S.; Yao, Y.; Yu, J.; Yang, S. CeOx Promoted Electrocatalytic CO2 Reduction to Formate by Assisting in the Critical Hydrogenation Step. *ACS Materials Letters* **2022**, *4* (9), 1749-1755.

(27) Wang, Y.-H.; Jiang, W.-J.; Yao, W.; Liu, Z.-L.; Liu, Z.; Yang, Y.; Gao, L.-Z. Advances in electrochemical reduction of carbon dioxide to formate over bismuth-based catalysts. *Rare Metals* **2021**, *40* (9), 2327-2353.

Chapter 8

Carbon-Supported Ag Nanostructures for Electrochemical CO₂ Reduction

8.1 ABSTRACT

Electrocatalytic reduction methods hold significant promise in addressing the urgent need to mitigate excessive greenhouse gas emissions, particularly carbon dioxide (CO_2). A highly effective catalyst is essential for achieving the conversion of CO_2 into valuable products due to the complex, multi-electron, and multi-product nature of the CO_2 reduction process. The electrochemical reduction of CO_2, driven by renewable energy sources, presents a valuable opportunity for simultaneously reducing CO_2 emissions while generating valuable chemicals and fuels, with syngas being a noteworthy product. Silver-based electrodes have been the focus of extensive research due to their low overpotential and remarkable selectivity in promoting the generation of carbon monoxide (CO) in the electrocatalytic carbon dioxide reduction reaction (CO_2RR). In this study, we delve into the synthesis of carbon-supported silver nanoparticles ($Ag\text{-}CN_x$), which serve as efficient electrocatalysts for the reduction of CO_2. The as-prepared catalyst, $Ag\text{-}CN_x$, is not only cost-effective but also highly proficient in facilitating the conversion of CO_2 and H_2O into syngas, which is a customizable mixture of hydrogen (H_2) and carbon monoxide (CO). The highest faradic efficiency for production of CO on $Ag\text{-}CN_x$ was calculated to be 56.4% at -1.4 V vs Ag/AgCl. The maximum partial current density for the generation of CO was determined to be -9.4 mA cm^{-2} at a potential of -1.6 V vs Ag/AgCl. This research demonstrates the potential of $Ag\text{-}CN_x$ as an electrocatalyst to enable the sustainable production of syngas, contributing to the reduction of CO_2 emissions and the synthesis of valuable chemical precursors and fuels.

8.2 INTRODUCTION

Significant advancements have occurred in our world since the onset of the industrial revolution, largely driven by the strategic utilization of diverse energy sources. However, as global energy consumption continues to rise and environmental apprehensions, particularly carbon dioxide (CO_2) emissions, escalate, the imperative for pioneering and more effective energy systems becomes inescapable.[1] This imperative is essential for securing dependable, economically viable, and sustainable energy access for all. Electrocatalytic transformations of CO_2 into high-energy fuels and valuable chemicals represent an efficient and environmentally benign approach for achieving sustainable energy utilization.[2, 3] The conversion of CO_2 to carbon monoxide (CO) is of significant importance, as CO can serve as a precursor for various fuels.[4] CO_2 is characterized by its high molecular stability, with a bond energy of 750 kJ mol^{-1}. Reducing CO_2 is a thermodynamically challenging process that necessitates a substantial energy input to break the carbon-oxygen (C=O) bonds.[5]

The electrochemical reduction of CO_2 to CO involves a two-electron reduction mechanism expressed as $CO_2 + 2H^+ + 2e^- = CO + H_2O$, featuring a relatively modest redox potential of -0.53 V compared to the standard hydrogen electrode (SHE). In aqueous electrolytes, the hydrogen evolution reaction (HER) poses a substantial competitive reaction to the CO_2 reduction reaction (CO_2RR), leading to a notable impact on the selectivity for CO and diminishing the efficiency of CO2RR devices.[6] These situations have sparked investigations into the electrochemical simultaneous generation of CO and H_2, known as syngas, through CO_2 reduction. This syngas can be readily employed in the large-scale production of essential chemicals such as dimethyl ether, methanol, synthetic fuels, and acetic acid using established industrial methods.[7, 8] In various downstream processes, the desired syngas composition with varying H_2/CO

ratios is essential.[9] For instance, the production of aldehydes and dimethyl ether necessitates a balanced H_2/CO ratio of $1/1$,[10] while the Fischer−Tropsch process requires a higher H_2/CO ratio of $2/1$.[11] In contrast, syngas fermentation typically utilizes a H_2/CO ratio of approximately $1/3$.[11] Currently, syngas is generated through coal gasification or natural gas reforming processes, and the adjustment of H_2/CO ratios is achieved through the reverse water-gas shift reaction, which heavily relies on the use of fossil fuels. However, the production of syngas via CO_2 reduction using renewable electricity sources, allowing for precise control of syngas composition (such as by adjusting the applied electrode potential), presents a viable and environmentally friendly alternative for large-scale syngas production.[12]

In recent times, there has been a growing interest in the application of electricity for the extraction of carbon dioxide from water, followed by the water-gas shift process to generate syngas. This approach is considered a promising and cost-effective method.[13, 14] Various products are obtained based on the specific metal involved in a distinct reduction pathway. In this context, the creation of an intermediate species known as $CO_2^{\bullet-}$ holds paramount importance as it acts as the rate-determining step. The coordination of this intermediate is pivotal in determining whether the resulting product of the two-electron reduction will be either CO or formate.[15-17] Silver (Ag), gold (Au), and zinc (Zn) exhibit varying degrees of affinity for binding the intermediate $CO_2^{\bullet-}$ but are unable to reduce CO, typically yielding CO as the predominant product.[18] Among these metals, Ag stands out as the most favorable catalyst due to its superior stability compared to Zn or Ga, as well as its significantly lower cost in comparison to Au.[7]

This chapter presents the synthesis of Ag-CN_x as an electrocatalyst for the electrochemical reduction of CO_2. The analysis primarily focused on the production of CO within the potential range of -1.2 to -1.6 V vs Ag/AgCl. Furthermore, the influence

of both loading and time on CO production was investigated. The findings suggest that due to its impressive stability and straightforward fabrication process, the Ag-CN$_x$-based electrode exhibits significant promise for broader-scale applications in the preparation of syngas from CO_2.

8.3 EXPERIMENTAL SECTION

Materials:

Carbon cloth (AvCarb 1071 HCB, 7.5 microns diameter) was bought from ASG scientific equipment. Silver (I) nitrate (AgNO₃, 99+% assay), sodium borohydride (NaBH₄), formamide (HCONH₂), potassium sulfate (99+% assay) were purchased from Sigma Aldrich. Sulfuric acid (H₂SO₄, 98%) was purchased from Merck (Germany). The chemicals and reagents employed in this study are all of analytical grade and have been used without any additional treatment. We obtained the proton exchange membrane (Nafion 117) from Alfa Aesar. High-purity gases, including CO_2 (99.999%), N₂ (99.998%), and Ar (99.998%), were supplied by Sigma-Aldrich. Milli-Q water was obtained from an ultra-filtration system (Milli-Q, Millipore) and the measured conductivity was 35 mho.cm^{-1} at 25 °C.

Preparation of N-doped carbon:

The synthesis of the N-doped carbon material, referred to as CNx, followed a method detailed in our previous publication.[19] In this process, 30 mL of Formamide (HCONH₂) underwent microwave heating at 180°C for 2 hours, resulting in the formation of a solution with a brown hue. Subsequently, the collected solution was evaporated using a rotary evaporator, maintaining a temperature of 180°C. The final product, solid N-doped carbon, was obtained through a sequence of filtration, followed by rinsing with distilled water, and concluding with vacuum drying.

Synthesis of the Ag-CN$_x$ composite

The synthesis of the Ag-CNx composite involved a series of steps. Initially, 46 mg of silver (I) nitrate was combined with 5 mL of deionized water and subjected to 30 minutes of sonication using a bath-sonicator. Simultaneously, 5 mg of the as-prepared CNx was dispersed in 2 mL of deionized water through 10 minutes of sonication. These two solutions were then mixed, which was further sonicated for 30 minutes to achieve a homogeneous mixture. Subsequently, 50 mg of NaBH$_4$ was introduced into the mixture, followed by an additional 2 hours of sonication. The resulting solution appeared black and was subjected to centrifugation at 1600 rpm, followed by multiple washes with deionized water and ethanol. The resulting black precipitate was collected and dried under vacuum for further applications.

Instrumentation and Analysis:

Surface morphology analysis was done using a field-emission scanning electron microscope (Carl Zeiss, Germany, Model ∑igma). A 0.05 mL of a solution containing 1 mg/mL of material was coated onto a silicon wafer, dried at 45 °C, and then the samples were ready for FE-SEM examination. Utilising a Bruker DAVINCI D8 ADVANCE diffractometer fitted with Cu K radiation (λ= 0.15406 nm), X-ray diffraction (*p*-XRD) patterns were obtained. The surface morphology of the produced materials was examined using high-resolution transmission electron microscopy (HRTEM) at 200 kV. The analysis was carried out using a JEOL F200 instrument. Initially, 10 μL of a 1 mg/mL stock solution was taken for the TEM analysis and dried in the air at a temperature of around 45 °C. By coating the material on a silicon wafer and utilising Mg Kα X-ray as the monochromatic source, VG Microtech was used to accomplish the X-ray photoelectron spectroscopy experiments. All electrochemical measurements were performed on a workstation for electrochemical measurements (Autolab, Metrohm,

PGSTAT 320N). A Hanna (HI 2209) pH meter was used to determine the pH of the electrolyte. Equipment for ultrasonic bath sonication was provided by Genei Laboratories Private Ltd. Bangalore, India. The ^{1}H NMR spectrum was obtained using the water suppression technique on a Bruker 400 MHz instrument.

Electrochemical performances:

At first, 1 mg of the prepared catalyst is ultrasonicated for 1 hour to obtain a homogenous slurry in 470 μL of Millipore water along with 30 μL of Nafion (5.0 wt %) solution. The resultant ink was subsequently drop casted on carbon cloth with the help of micropipette and dried at 45 °C for further electrochemical testing. A three-electrode setup connected to the electrochemical workstation (Autolab) was used to perform electrochemical performances. Each cathodic and anodic chamber was filled with 60 mL of 0.1 M $KHCO_3$ electrolyte, and these chambers were separated by a Nafion 117 proton exchange membrane. The cathodic chamber contained the working electrode (prepared catalyst electrode) and the reference electrode (Ag/AgCl) with a spacing of 0.5 cm between them. In contrast, the anodic chamber included a platinum electrode as the counter electrode. All measurements were referenced to the Ag/AgCl reference electrode and subsequently adjusted to the reversible hydrogen electrode (RHE) using the following equation 1;

$$V_{RHE} = V_{Ag/AgCl} \text{ (saturated 3M KCl)} + 0.197 + 0.00592pH \ldots\ldots\ldots\ldots(1)$$

In order to achieve total saturation, high-purity Ar and CO_2 were used to purge the electrolyte used in the H-cell for at least an hour before each electrochemical measurement.

Product Identification and Quantification:

The analysis of gaseous products was carried out using gas chromatography (GC), while the liquid mixture was subjected to analysis and quantification through nuclear magnetic resonance (NMR) spectroscopy techniques. Gas chromatography (Thermo Scientific

Trace 1110 GC), utilizing a 60/80 Carboxen-1000 column outfitted with a thermal conductivity detector (TCD), was used to quantify the gaseous products and high-purity Ar gas is used (99.999%) as the carrier gas. The gaseous products from the headspace were collected and introduced into the GC via a gastight syringe, with each analysis using 1 mL of the gaseous products. TCD detects a significant amount of CO and H_2 product. To quantify the gaseous products, a standard gas sample containing H_2 (2.04%), CO (2.07%), CO_2 (2.07%), C_2H_6 (2.02%), CH_4 (1.96%), and Ar as the rest of the gas, was used. The NMR technique (Bruker 400 MHz spectrometer) was used to identify and measure liquid products resulting from CO_2 reduction. For NMR analysis, 50 µL of D_2O (Aldrich, 99.9%) were added to 450 µL of electrolyte, and the water suppression technique was used to record the ^1H NMR spectrum. Data obtained from the NMR spectra were processed using the Bruker software TopSpin. The faradaic efficiency of the CO_2 reduced products were calculated using the following equation;

$$FE\ (\%) = \frac{\text{mol of product formed (N)}}{\text{total charge passed (c)}/ (F \times n)} \times 100\% \quad \ldots\ldots\ldots\ldots\ldots\ldots.(2)$$

In this equation: *N* represents the number of moles of the product generated. *C* stands for the charge passed during the electrolysis at the cathode. *F* is the Faraday constant, equal to 96485 C mol^{-1}. *n* signifies the number of electrons required to produce one molecule of the product from CO_2.

8.4 RESULTS AND DISCUSSION

Morphology and characterization
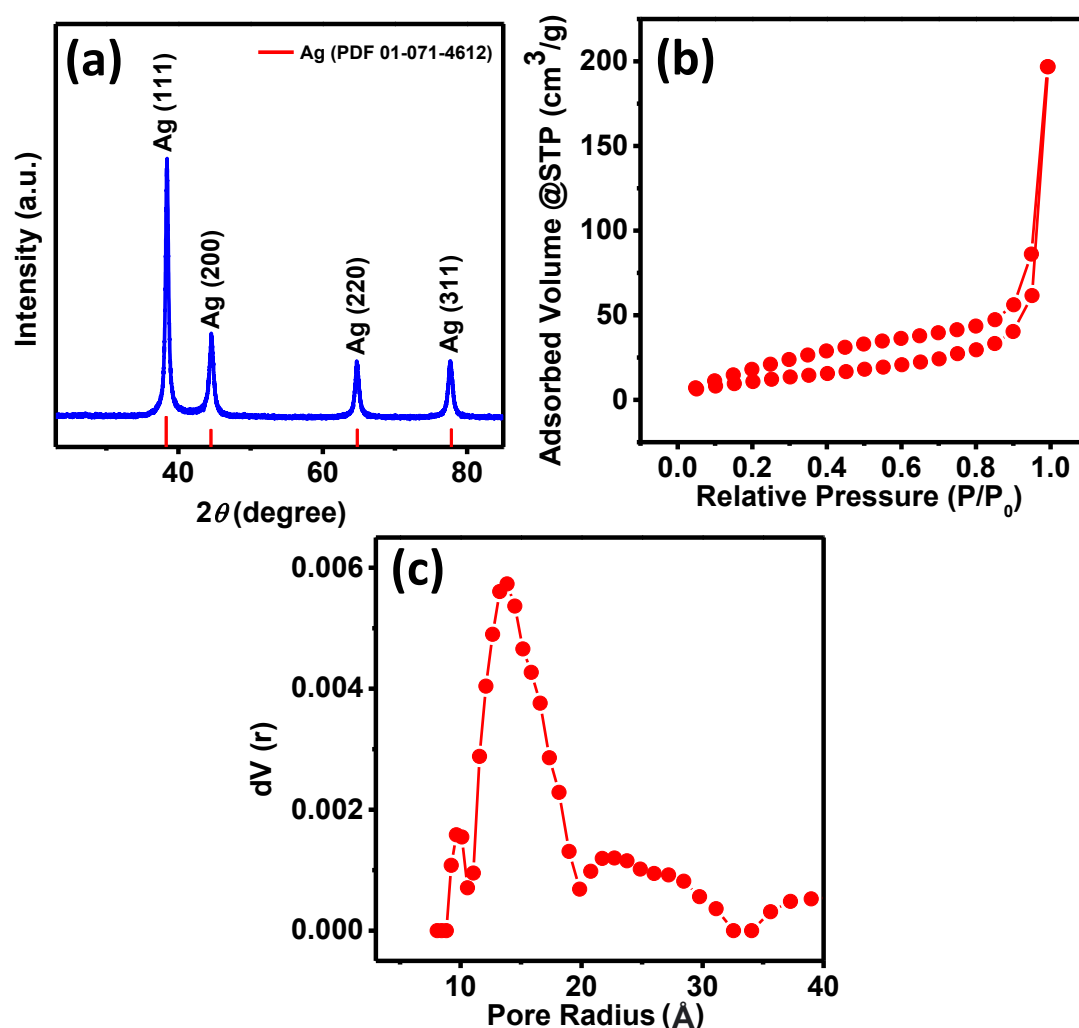
Figure 8.1. (a) p-XRD pattern, (b) Nitrogen adsorption/desorption isotherm, and (c) Pore size distributions of Ag-CN$_x$ catalyst.

The Ag-CN$_x$ composite was synthesized using a facile two step method involving ultrasonication-assisted reduction with BH$_4^-$ of AgNO$_3$ in the presence of a CN$_x$ support, as elaborated in the experimental section. The X-ray diffraction (XRD) pattern of the Ag-CN$_x$ composite is depicted in Figure 8.1a. The distinctive diffraction peaks observed at 38.4°, 44.6°, 64.6°, and 77.6° in the Ag-CN$_x$ composite are attributed to the (111), (200), (220), and (311) crystalline planes of face-centered cubic (fcc) Ag metal. These results

are consistent with the standard JCPDS data for fcc Ag metal (PDF 01-071-4612). The electrocatalytic activity of a catalyst is significantly influenced by its surface area and porosity, making these properties highly desirable. Large surface area and high porosity are key characteristics of an effective electrocatalyst. Figure 8.1b illustrates the nitrogen adsorption/desorption isotherm of the Ag-CNx material. Through the analysis of this isotherm using the Brunauer−Emmett−Teller (BET) method, the specific surface area was determined to be 44 m^2 g^{-1}. The Figure 8.1c represents the pore size distribution of in Ag-CN$_x$. This distribution was determined using the density functional theory (DFT) method.
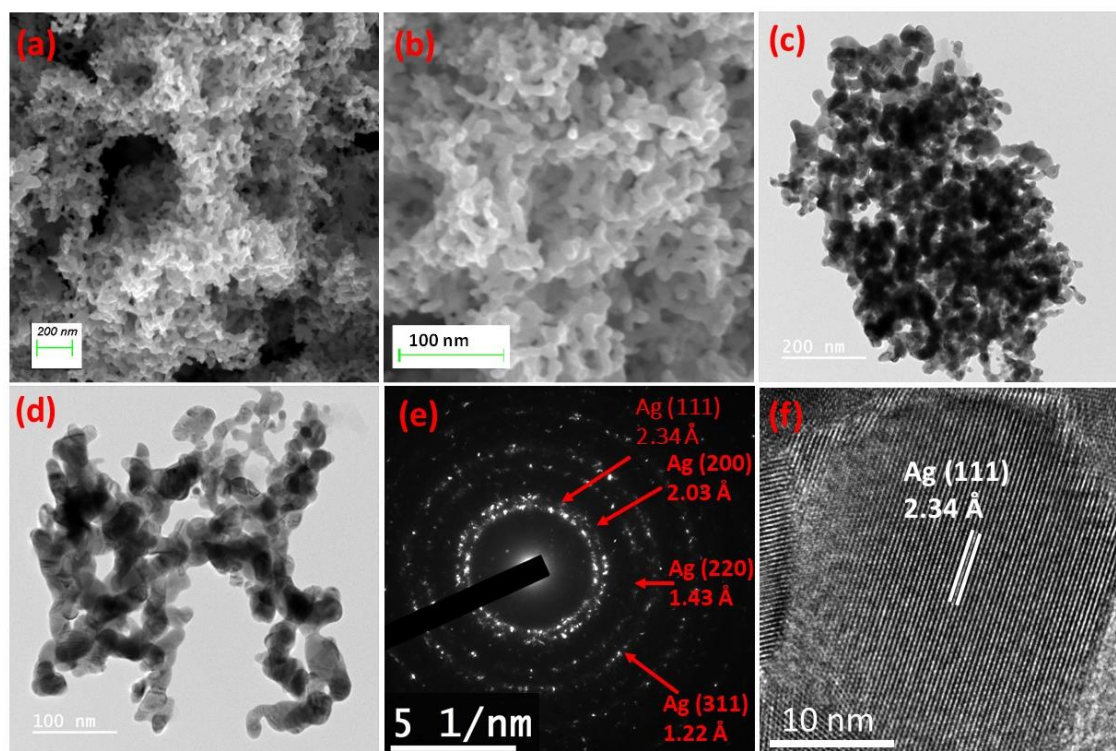
Figure 8.2. (a, b) SEM images, (c, d) TEM images, (e) SAED pattern, (f) HR-TEM image of Ag-CN$_x$ catalyst.

Morphological analysis of Ag-CN$_x$ was done using Field Emission Scanning Electron Microscopy (FESEM) and Transmission Electron Microscopy (TEM). SEM images of Ag-CN$_x$ are presented in Figure 8.2 (a, b). These images reveal the formation of quasi-

one-dimensional nanochains, which interconnect to create a three-dimensional network-like structure with numerous open pores, resulting in a porous Ag-CN_x structure. The TEM images of Ag-CN_x (Figure 8.2 (c, d)) clearly show the interconnected porous structure supported by two-dimensional thin CN_x sheets. The presence of these two-dimensional sheets enhances mass transfer and contributes to the electrocatalyst's catalytic performance.[20] Additionally, the Selected Area Electron Diffraction (SAED) image (Figure 8.2e) indicates the polycrystalline nature of the catalyst. The measured d-spacings from the SAED image correspond to the (111), (200), (220), and (311) planes of Ag, with values of 2.34, 2.03, 1.43, and 1.22 Å, respectively, consistent with the results obtained from XRD. Furthermore, Figure 8.2f displays a high-resolution (HR) TEM image of the Ag-CN_x catalyst, revealing a d-spacing of 2.34 Å, corresponding to the Ag (111) lattice plane of face-centered cubic Ag. The uniform orientation of these lattice fringes suggests the growth of silver primarily along the Ag (111) plane.

The X-ray Photoelectron Spectroscopy (XPS) survey scan spectrum of Ag-CN_x is presented in Figure 8.3a. The XPS survey scan clearly reveals the presence of several elements, including silver (Ag), carbon (C), oxygen (O), and nitrogen (N) atoms. High-resolution Ag3d XPS spectra are depicted in Figure 8.3b. To analyse the Ag3d XPS spectra of Ag-CN_x, two peaks were used for fitting. The peaks observed at 367.9 and 373.9 eV correspond to $Ag3d_{3/2}$ and $Ag3d_{5/2}$ peaks, respectively. Figure 8.3c displays the high-resolution C1s XPS spectra. The C1s XPS spectrum can be deconvoluted into three distinct peaks representing sp^2-bonded carbon at 284 eV, sp^3-bonded carbon at 285.5 eV, and C-N bonded carbon at 287.5 eV.
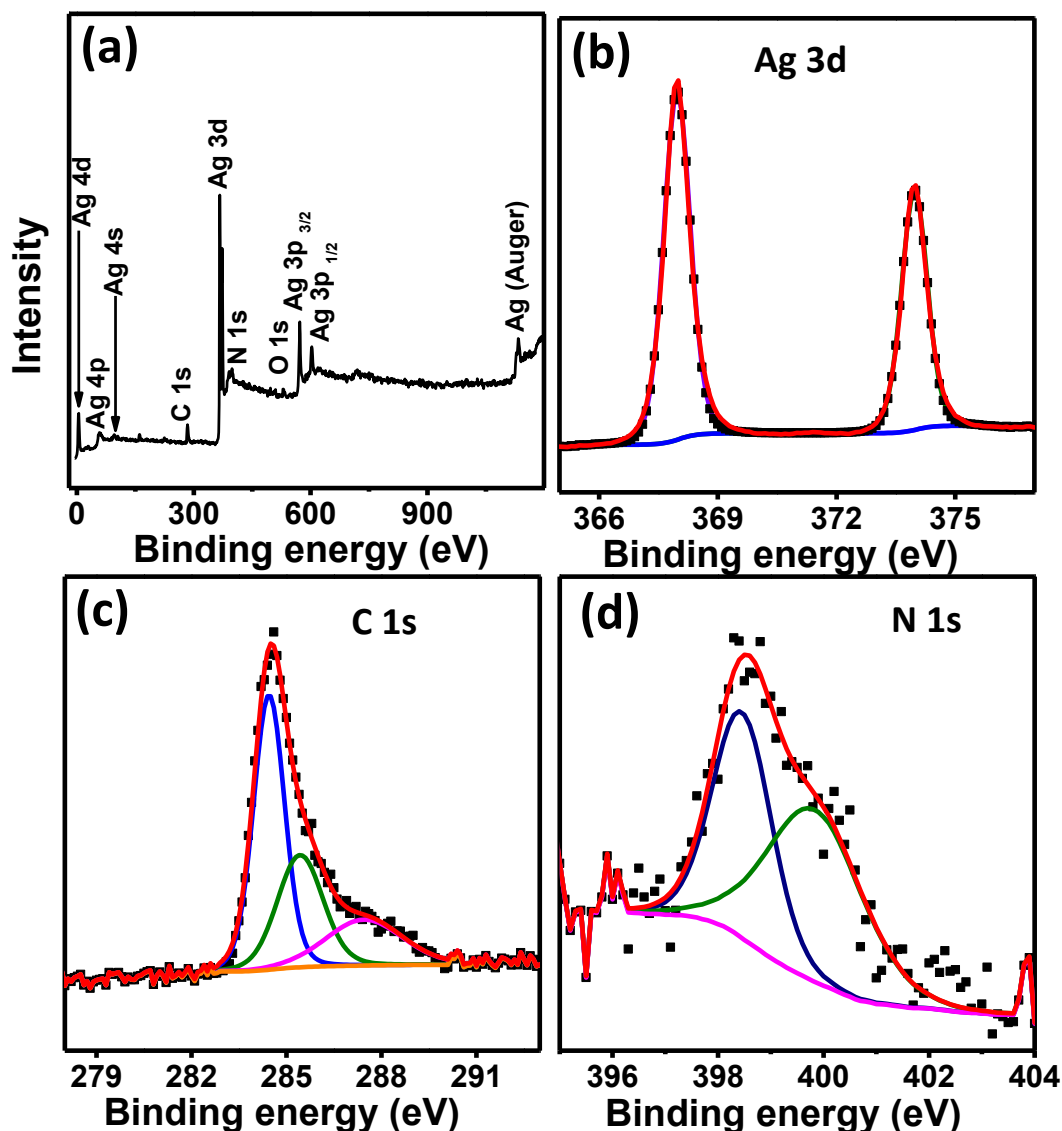
Figure 8.3. (a) XPS survey scan of Ag-CNx, High-resolution XPS spectra of (b) Ag3d, (c) C1s and (d) N1s of Ag-CNx catalyst.

The N 1s high resolution XPS spectra is presented in Figure 8.3d. The N 1s XPS spectra can be deconvoluted into two distinct peaks, which can be attributed to pyridinic nitrogen (398.47 eV) and pyrrolic nitrogen (399.9 eV). The incorporation of nitrogen atoms in the composite significantly influences the electrochemical properties due to enhanced charge transfer kinetics.[20-24] Previous studies have highlighted the positive impact of N species on the electrocatalytic activity of various materials, with graphitic and pyridinic nitrogen

species being particularly noted for their role in improving electrocatalytic performance by enhancing charge mobility.[25, 26]

Electrochemical CO₂ reduction
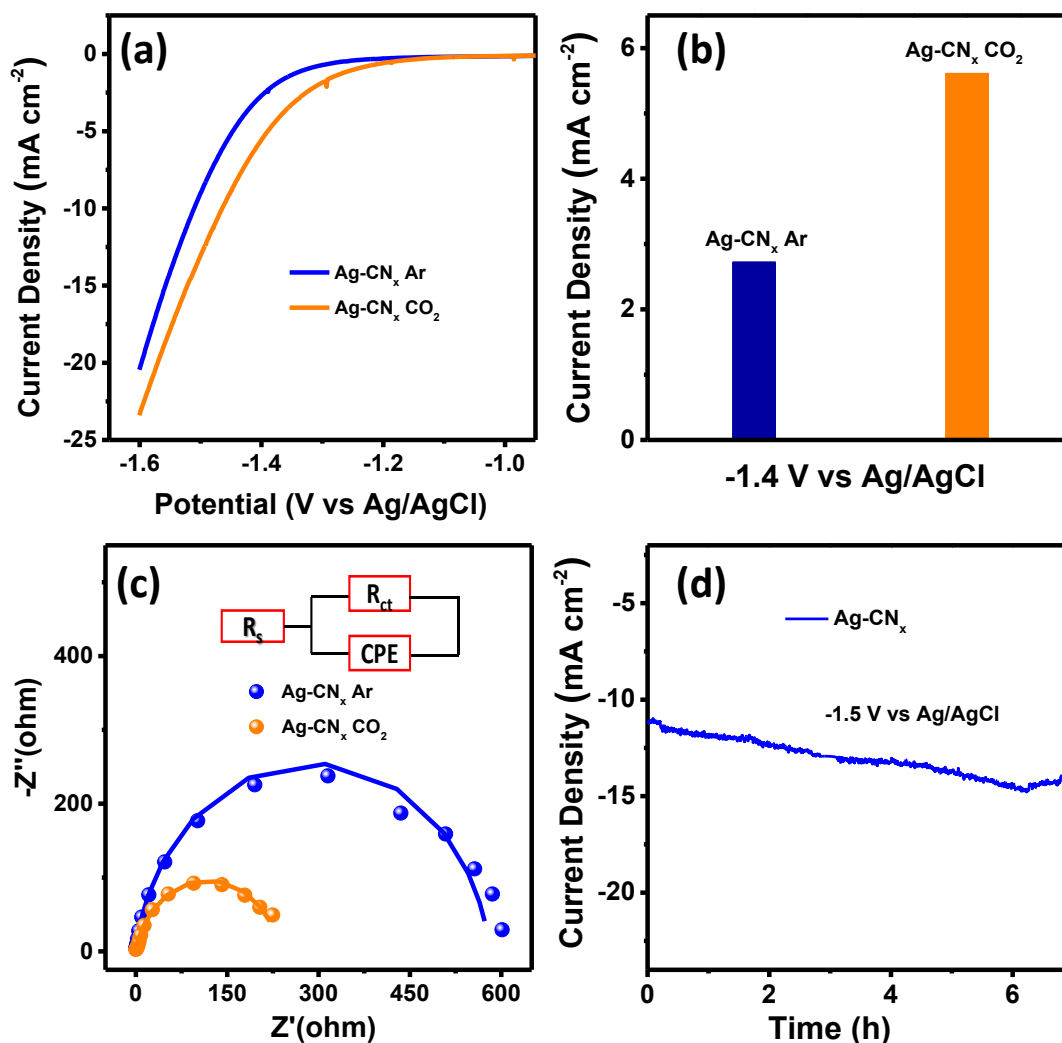
Figure 8.4. (a) LSV polarization curve, (b) current density at -1.4 V potential, and (c) Nyquist plots of Ag-CN$_x$ in Ar and CO₂ saturated electrolyte, (d) chronoamperometry study of Ag-CN$_x$ at a potential of -1.5 V in CO₂ saturated electrolyte.

The electrochemical CO₂ reduction reaction was examined through Linear Sweep Voltammetry (LSV) plots within an undivided three-electrode system (Figure 8.4a). In this setup, the working electrode consisted of Ag-CN$_x$, the reference electrode was Ag/AgCl, and the counter electrode was Pt wire, with a 0.1 M KHCO₃ electrolyte

solution. LSV experiments were conducted under two different gas purging conditions, namely Ar (argon) gas and CO_2 gas, within the electrolyte. The potential was scanned from -0.9 to a negative potential of -1.6 V versus Ag/AgCl at a scan rate of 10 mV/s, and the LSV measurements were performed without any agitation or stirring. In an electrolyte saturated with Ar gas, the observed LSV current was attributed to the hydrogen evolution reaction. However, in an electrolyte saturated with CO_2 gas, an increase in current and a reduction in overpotential were observed for Ag-CN_x. This indicates that the CO_2 reduction reaction is more favorable at the electrode surface when compared to the hydrogen reduction process. The current density of Ag-CN_x was assessed under conditions of both Ar and CO_2 saturation in the electrolyte at a potential of -1.4 V vs Ag/AgCl, as illustrated in Figure 8.4b. At this specific potential, the current density for Ag-CN_x was found to be 2.723 mA cm^{-2} in Ar-saturated conditions, while it increased to 5.613 mA cm^{-2} under CO_2-saturated conditions. This observation demonstrates the significant influence of CO_2 saturation on enhancing the current density, highlighting the electrocatalytic activity of Ag-CN_x in the electroreduction of CO_2.
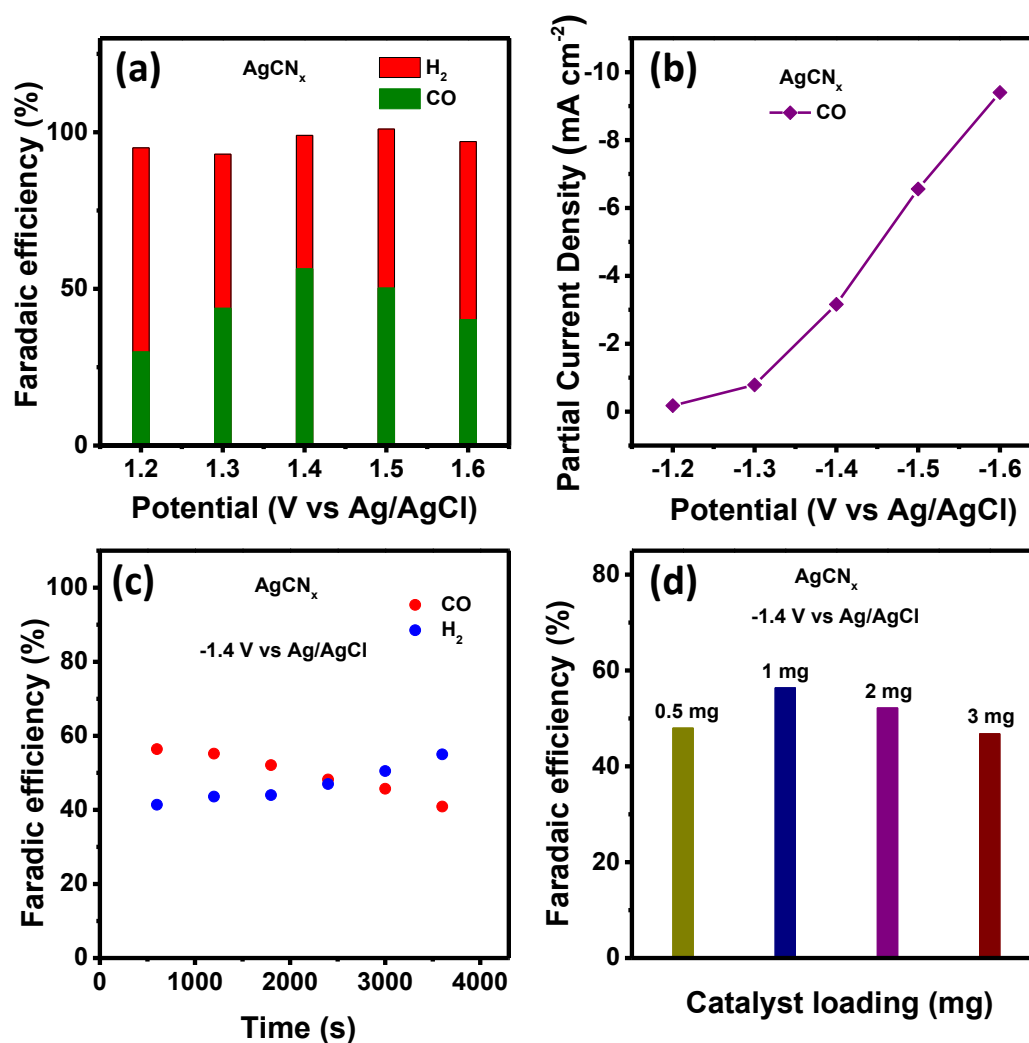
Figure 8.5. (a) Faradic efficiency plot of CO and H_2, (b) partial current density plot of CO, (c) effect of time on faradic efficiency of CO and H_2, (d) effect of catalyst loading on faradic efficiency of CO.

Electrochemical Impedance Spectroscopy (EIS) spectra were systematically investigated and analysed to gain deeper insights into the reaction pathway and kinetics of CO_2 reduction, as depicted in Figure 8.4c. These spectra were acquired across a frequency range of 0.1-100 kHz while operating at the open circuit potential, employing an AC amplitude of 10 mV within a 0.1 M $KHCO_3$ electrolyte. The EIS data for the Ag-CN_x catalyst were compared under two distinct gas saturation conditions, namely Ar-saturated and CO_2-saturated electrolytes. When examining the EIS spectrum of the Ag-CN_x

catalyst in an Ar-saturated electrolyte, a larger semicircle was observed. Conversely, in a CO_2-saturated electrolyte, a smaller semicircle was observed. A smaller semicircle in the EIS spectrum signifies a lower R_{ct} value and enhanced electronic conductivity that suggests faster reaction kinetics or improved charge transfer for the CO_2 reduction reaction. Chronoamperometry measurements were conducted on $Ag\text{-}CN_x$ at a constant potential of -1.5 V over a 7 hours duration, demonstrating the notable stability of the catalyst for up to 7 hours during the CO_2 reduction reaction (Figure 8.4d).

Electrochemical CO_2 reduction products were analysed using a gastight H-type cell, and a PGSTAT 320N potentiostat (Autolab, Metrohm) was employed to maintain a constant electric potential throughout the experiments. To ensure the saturation of CO_2, high-purity CO_2 was introduced into the system for a duration of one hour before applying the desired potential in a 0.1 M $KHCO_3$ solution. The study encompassed chronoamperometric CO_2 electrolysis involving the $Ag\text{-}CN_x$ catalyst, wherein various potentials more negative than -1.2 V vs Ag/AgCl were investigated for a duration of 30 minutes. Potentials ranging from -1.2 V to -1.6 V vs Ag/AgCl was explored in CO_2-saturated 0.1 M $KHCO_3$ to assess the selectivity and faradaic efficiency of major products of CO_2RR. Subsequently, after the 30-minute electrolysis period, both gaseous products in the H-cell headspace and the liquid mixture were meticulously analysed and quantified. The analysis products were carried out using GC and ^{1}H-NMR techniques. The Faradaic efficiencies of CO and H_2 generated during the electrochemical reaction are illustrated in a bar chart (Figure 8.5a). The Faradaic efficiency of CO exhibits a gradual increase with an elevating reduction potential, ultimately peaking at 54.6% when the potential is set at -1.4 V vs Ag/AgCl. Further negative shifts in the reduction potential result in a reduction in the Faradaic efficiency of CO. This decline in Faradaic efficiency at more negative potentials can be attributed to several contributing factors. These factors

include limitations in the mass transport of CO_2 and local changes in pH due to higher reaction rates.[27] Additionally, at higher overpotentials, the HER prevails over the CO_2RR on the Ag-CN_x catalyst. No liquid reaction products were observed during NMR measurements. A partial current density plot was generated with respect to the production of CO in the potential range from -1.2 to -1.6 V vs Ag/AgCl (Figure 8.5b). The highest value for the partial current density of CO, which amounted to -9.4 mA cm^{-2}, was recorded at -1.6 V vs Ag/AgCl. The impact of time and the catalyst loading on the faradaic efficiency of CO was also examined. As demonstrated in Figure 8.5c, an increase in time led to a reduction in the Faradaic efficiency of CO. This phenomenon can be attributed to the diminishing concentration of CO_2 in the electrolyte over time. Furthermore, the catalyst loading was examined to assess its influence on CO production (Figure 8.5d). It was determined that a catalyst loading of 1 mg on carbon cloth represented the optimal loading for CO production. A lower loading was deemed insufficient to cover the entire active surface area, while a higher loading was found to obstruct the active surface area, impeding the CO_2RR process.

Plausible mechanism for CO₂ reduction to CO
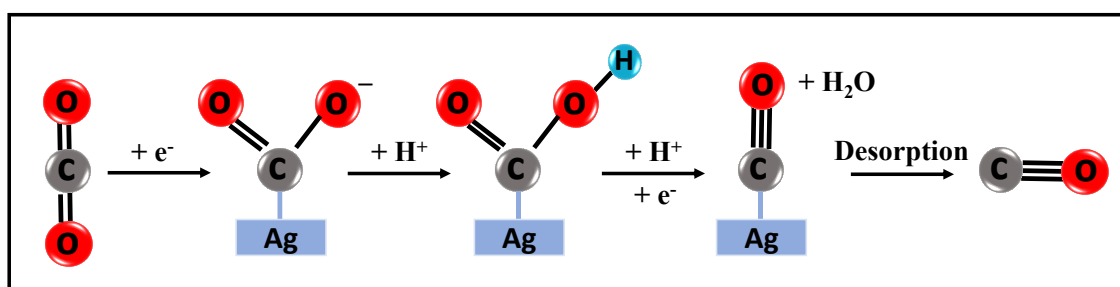
Scheme 8.1. Plausible reduction pathway of CO_2RR to produce CO.

A mechanism involving a two-electron transfer process in the electrochemical reduction of CO_2 to CO, as depicted in Scheme 8.1 has been proposed by Hori.[28, 29] Moreover, many computational investigations into the reaction pathways for CO_2 reduction are

rooted in the Computational Hydrogen Electrode (CHE) model, which posits that a proton-coupled electron transfer (PCET) occurs at each step of the reaction sequence. In this framework, it is assumed that the formation of a COOH* intermediate represents the initial CO_2 activation step in Density Functional Theory (DFT) simulations.[30, 31] However, it is worth noting that certain experimental findings offer an alternative perspective. In this context, it is postulated that an adsorbed $*CO_2^-$ radical anion intermediate is created on the active sites of the metal surface via a one-electron transfer process with a CO_2 molecule. Subsequently, the COOH* intermediate forms after gaining a proton.[32, 33] Furthermore, there is evidence suggesting that the first proton donation originates from HCO_3^-. Following this, the COOH* intermediate located on the surface acquires both another electron and proton to yield CO and a water (H_2O) molecule.[34]

8.5 CONCLUSIONS:

This chapter employed $Ag\text{-}CN_x$, synthesized via a one-step $NaBH_4$ reduction process, as a catalyst for the electrochemical CO₂RR. The resultant structure exhibited a porous network-like morphology due to the interconnected Ag nanoparticles on CN_x sheets. This unique morphology endowed the catalyst with exceptional porosity and a substantial electrochemically active surface area, providing abundant active sites for the electrocatalytic conversion of CO_2. $Ag\text{-}CN_x$ demonstrated remarkable efficiency in reducing CO_2 to generate CO as a major product. Notably, the highest faradic efficiency for CO production on $Ag\text{-}CN_x$ was achieved, reaching 56.4%, at a potential of -1.4 V vs Ag/AgCl. The study also investigated the impact of reduction time and catalyst loading on CO production. The optimal conditions were determined to be a catalyst loading of 1 mg and a reduction time of 20 minutes. These findings underscore the potential of Ag-

CN_x as a robust catalyst for CO₂RR and highlight the importance of fine-tuning experimental parameters to optimize CO production efficiency.

8.6 REFERENCES:

(1) Gan, K.; Li, H.; Li, R.; Niu, J.; He, J.; Jia, D.; He, X. Electroreduction of CO2 to syngas with controllable H2/CO ratios in a wide potential range over Ni–N co-doped ultrathin carbon nanosheets. *Inorganic Chemistry Frontiers* **2023**, *10* (8), 2414-2422.

(2) Gao, F.-Y.; Bao, R.-C.; Gao, M.-R.; Yu, S.-H. Electrochemical CO2-to-CO conversion: electrocatalysts, electrolytes, and electrolyzers. *Journal of Materials Chemistry A* **2020**, *8* (31), 15458-15478.

(3) Wu, J.; Sharifi, T.; Gao, Y.; Zhang, T.; Ajayan, P. M. Emerging Carbon-Based Heterogeneous Catalysts for Electrochemical Reduction of Carbon Dioxide into Value-Added Chemicals. *Advanced Materials* **2019**, *31* (13), 1804257.

(4) Wei, L.; Li, H.; Chen, J.; Yuan, Z.; Huang, Q.; Liao, X.; Henkelman, G.; Chen, Y. Thiocyanate-Modified Silver Nanofoam for Efficient CO2 Reduction to CO. *ACS Catalysis* **2020**, *10* (2), 1444-1453.

(5) Aparna, R. K.; Surendran, V.; Roy, D.; Pathak, B.; Shaijumon, M. M.; Mandal, S. Silver Nanoparticle-Decorated Defective Zr-Based Metal–Organic Frameworks for Efficient Electrocatalytic Carbon Dioxide Reduction with Ultrahigh Mass Activity. *ACS Applied Energy Materials* **2023**, *6* (7), 4072-4078.

(6) Rakowski Dubois, M.; Dubois, D. L. Development of Molecular Electrocatalysts for CO2 Reduction and H2 Production/Oxidation. *Accounts of Chemical Research* **2009**, *42* (12), 1974-1982.

(7) Xi, W.; Ma, R.; Wang, H.; Gao, Z.; Zhang, W.; Zhao, Y. Ultrathin Ag Nanowires Electrode for Electrochemical Syngas Production from Carbon Dioxide. *ACS Sustainable Chemistry & Engineering* **2018**, *6* (6), 7687-7694.

(8) Sheng, W.; Kattel, S.; Yao, S.; Yan, B.; Liang, Z.; Hawxhurst, C. J.; Wu, Q.; Chen, J. G. Electrochemical reduction of CO2 to synthesis gas with controlled CO/H2 ratios. *Energy & Environmental Science* **2017**, *10* (5), 1180-1185.

(9) Kang, P.; Chen, Z.; Nayak, A.; Zhang, S.; Meyer, T. J. Single catalyst electrocatalytic reduction of CO2 in water to H2+CO syngas mixtures with water oxidation to O2. *Energy & Environmental Science* **2014**, *7* (12), 4007-4012.

(10) He, R.; Zhang, A.; Ding, Y.; Kong, T.; Xiao, Q.; Li, H.; Liu, Y.; Zeng, J. Achieving the Widest Range of Syngas Proportions at High Current Density over Cadmium Sulfoselenide Nanorods in CO2 Electroreduction. *Advanced Materials* **2018**, *30* (7), 1705872.

(11) Ross, M. B.; Dinh, C. T.; Li, Y.; Kim, D.; De Luna, P.; Sargent, E. H.; Yang, P. Tunable Cu Enrichment Enables Designer Syngas Electrosynthesis from CO2. *Journal of the American Chemical Society* **2017**, *139* (27), 9359-9363.

(12) Xie, H.; Chen, S.; Ma, F.; Liang, J.; Miao, Z.; Wang, T.; Wang, H.-L.; Huang, Y.; Li, Q. Boosting Tunable Syngas Formation via Electrochemical CO2 Reduction on Cu/In2O3 Core/Shell Nanoparticles. *ACS Applied Materials & Interfaces* **2018**, *10* (43), 36996-37004.

(13) Ouyang, T.; Huang, H.-H.; Wang, J.-W.; Zhong, D.-C.; Lu, T.-B. A Dinuclear Cobalt Cryptate as a Homogeneous Photocatalyst for Highly Selective and Efficient Visible-Light Driven CO2 Reduction to CO in CH3CN/H2O Solution. *Angewandte Chemie International Edition* **2017**, *56* (3), 738-743.

(14) Takeda, H.; Cometto, C.; Ishitani, O.; Robert, M. Electrons, Photons, Protons and Earth-Abundant Metal Complexes for Molecular Catalysis of CO2 Reduction. *ACS Catalysis* **2017**, *7* (1), 70-88.

(15) Bai, X.; Chen, W.; Zhao, C.; Li, S.; Song, Y.; Ge, R.; Wei, W.; Sun, Y. Exclusive Formation of Formic Acid from CO2 Electroreduction by a Tunable Pd-Sn Alloy. *Angewandte Chemie International Edition* **2017**, *56* (40), 12219-12223.

(16) Xu, J.; Li, X.; Liu, W.; Sun, Y.; Ju, Z.; Yao, T.; Wang, C.; Ju, H.; Zhu, J.; Wei, S.; et al. Carbon Dioxide Electroreduction into Syngas Boosted by a Partially Delocalized Charge in

Molybdenum Sulfide Selenide Alloy Monolayers. *Angewandte Chemie International Edition* **2017**, *56* (31), 9121-9125.

(17) Zhu, G.; Li, Y.; Zhu, H.; Su, H.; Chan, S. H.; Sun, Q. Enhanced CO2 electroreduction on armchair graphene nanoribbons edge-decorated with copper. *Nano Research* **2017**, *10* (5), 1641-1650.

(18) Lu, Q.; Jiao, F. Electrochemical CO2 reduction: Electrocatalyst, reaction mechanism, and process engineering. *Nano Energy* **2016**, *29*, 439-456.

(19) Sadhukhan, M.; Barman, S. Bottom-up fabrication of two-dimensional carbon nitride and highly sensitive electrochemical sensors for mercuric ions. *Journal of Materials Chemistry A* **2013**, *1* (8), 2752-2756.

(20) Zhang, S.; Shang, N.; Gao, S.; Meng, T.; Wang, Z.; Gao, Y.; Wang, C. Ultra dispersed Co supported on nitrogen-doped carbon: An efficient electrocatalyst for oxygen reduction reaction and Zn-air battery. *Chemical Engineering Science* **2021**, *234*, 116442.

(21) Wang, Z.; Shang, N.; Wang, W.; Gao, S.; Zhang, S.; Gao, W.; Cheng, X.; Wang, C. Atomically dispersed Co anchored on S,N-riched carbon for efficient oxygen reduction and Zn-air battery. *Journal of Alloys and Compounds* **2022**, *899*, 163225.

(22) Shang, N.; Li, S.; Zhou, X.; Gao, S.; Gao, Y.; Wang, C.; Wu, Q.; Wang, Z. Co/nitrogen-doped carbon nanocomposite derived from self-assembled metallogels as efficient bifunctional oxygen electrocatalyst for Zn-air batteries. *Applied Surface Science* **2021**, *537*, 147818.

(23) Hou, B.; Ma, L.; Zang, X.; Shang, N.; Song, J.; Zhao, X.; Wang, C.; Qi, J.; Wang, J.; Yu, R. Design and Construction of 3D Porous Na3V2(PO4)3/C as High Performance Cathode for Sodium Ion Batteries. *Chemical Research in Chinese Universities* **2021**, *37* (2), 265-273.

(24) Xiao, Z.; Xu, X.; Kong, D.; Liang, J.; Zhou, S.; Huang, X.; Yang, Q.; Zhi, L. Chemical tailoring of one-dimensional polypyrene nanocapsules at a molecular level: towards ideal sulfur hosts for high-performance Li–S batteries. *Journal of Materials Chemistry A* **2019**, *7* (5), 2009-2014.

(25) Lee, J. H.; Park, M. J.; Yoo, S. J.; Jang, J. H.; Kim, H.-J.; Nam, S. W.; Yoon, C. W.; Kim, J. Y. A highly active and durable Co–N–C electrocatalyst synthesized using exfoliated graphitic carbon nitride nanosheets. *Nanoscale* **2015**, *7* (23), 10334-10339.

(26) Shang, N.; Wang, C.; Zhang, X.; Gao, S.; Zhang, S.; Meng, T.; Wang, J.; Wang, H.; Du, C.; Shen, T.; et al. Atomically dispersed iron on nitrogen-decorated carbon for high-performance oxygen reduction and zinc-air batteries. *Chemical Engineering Journal* **2021**, *426*, 127345.

(27) Luan, C.; Shao, Y.; Lu, Q.; Gao, S.; Huang, K.; Wu, H.; Yao, K. High-Performance Carbon Dioxide Electrocatalytic Reduction by Easily Fabricated Large-Scale Silver Nanowire Arrays. *ACS Applied Materials & Interfaces* **2018**, *10* (21), 17950-17956.

(28) Hori, Y. Electrochemical CO2 Reduction on Metal Electrodes. In *Modern Aspects of Electrochemistry*, Springer New York, 2008; pp 89-189.

(29) Hori, Y.; Wakebe, H.; Tsukamoto, T.; Koga, O. Electrocatalytic process of CO selectivity in electrochemical reduction of CO2 at metal electrodes in aqueous media. *Electrochimica Acta* **1994**, *39* (11), 1833-1839.

(30) Kortlever, R.; Shen, J.; Schouten, K. J. P.; Calle-Vallejo, F.; Koper, M. T. M. Catalysts and Reaction Pathways for the Electrochemical Reduction of Carbon Dioxide. *The Journal of Physical Chemistry Letters* **2015**, *6* (20), 4073-4082.

(31) Peterson, A. A.; Abild-Pedersen, F.; Studt, F.; Rossmeisl, J.; Nørskov, J. K. How copper catalyzes the electroreduction of carbon dioxide into hydrocarbon fuels. *Energy & Environmental Science* **2010**, *3* (9), 1311-1315.

(32) Lu, Q.; Rosen, J.; Zhou, Y.; Hutchings, G. S.; Kimmel, Y. C.; Chen, J. G.; Jiao, F. A selective and efficient electrocatalyst for carbon dioxide reduction. *Nature Communications* **2014**, *5* (1), 3242.

(33) Lu, Q.; Rosen, J.; Jiao, F. Nanostructured Metallic Electrocatalysts for Carbon Dioxide Reduction. *ChemCatChem* **2015**, *7* (1), 38-47.

(34) Ma, M.; Trześniewski, B. J.; Xie, J.; Smith, W. A. Selective and Efficient Reduction of Carbon Dioxide to Carbon Monoxide on Oxide-Derived Nanostructured Silver Electrocatalysts. *Angewandte Chemie International Edition* **2016**, *55* (33), 9748-9752.

One-Dimensional Ni-MIL-77 Metal-Organic Framework as An Efficient Electrode Nanomaterial for Asymmetric Supercapacitor

Chapter 9

Chapter 9

One-Dimensional Ni-MIL-77 Metal-Organic Framework as An Efficient Electrode Nanomaterial for Asymmetric Supercapacitor

9.1 ABSTRACT

The design and synthesis of one-dimensional (1D) metal-organic framework (MOF) with a high surface area are crucial for their potential usage in supercapacitor applications. 1D-Ni-MIL-77 MOF, synthesized by a one-step solvothermal method, is discussed in this chapter, to investigate its activity in supercapacitor applications. High surface-to-volume ratios and short ion diffusion path lengths in 1D structured nanomaterials result in high charge/discharge rates. 1D-Ni-MIL-77 MOF nanobelts show a high surface area of 93.48 m^2 g^{-1} that gives ample active electrochemical sites. 1D-Ni-MIL-77 shows a specific capacitance (C) value of 1376 F g^{-1} under the current of 1 A g^{-1}. Additionally, an asymmetric supercapacitor (ASC) was assembled by employing activated carbon (AC) as the negative electrode and a 1D-Ni-MIL-77 nanobelt as the positive electrode. With the assembled ASC, at a power density (PD) of 750 W kg^{-1}, an energy density (ED) of 25 W h kg^{-1} was attained with a voltage ranging from 0 to 1.5 V. The cyclic durability of the asymmetric supercapacitor was examined and exhibited excellent retention of 95% of its initial capacitance after 5000 cycles.

9.2 INTRODUCTION

The problem of global climate change and the extensive usage of fossil fuels is progressively growing worse[1]. It has become a prominent topic to discuss how to deal with severe environmental pollution and energy shortages using clean renewable energy sources, including solar, wind, tidal, and hydrogen[2]. An important obstacle to the effective consumption of various renewable energy sources is the intermittent nature of

One-Dimensional Ni-MIL-77 Metal-Organic Framework as An Efficient Electrode Nanomaterial for Asymmetric Supercapacitor

Chapter 9

the energy supply[3]. Thus, it is crucial to create energy storage systems that are effective[4, 5]. Between all the energy storage systems like conventional capacitors and batteries, supercapacitors fill the gap[6]. Due to their good sustainability, and environmental friendliness, supercapacitors have emerged as attractive contenders in the field of electrochemical energy storage[7]. Supercapacitors, having several advantages like high PD, short discharge/charge time, and exceptional cycling capability, are considered as efficient renewable energy storage devices compared to other conventional energy storage devices[8-10]. Low energy density, however, continues to be an obstacle to the widespread usage of supercapacitors[11]. The performance of supercapacitors is expected to be most significantly enhanced by electrode materials. Although conductive polymers and carbon materials exhibit outstanding rate performance, their applications are constrained by their low specific capacitance[12]. Owing to their impressive specific capacitance and high energy density, much research has been done on metal sulfides and oxides as positive electrodes for supercapacitors[13]. However, there are challenges in synthesizing metal oxide-based high-performance supercapacitors due to their low rate performances, less electrical conductivity, and volume expansion during cycling[14-16]. As a result, current research challenges involve examining electrode materials that can deliver enhanced specific capacity, high stability as well as high energy density.

A new family of porous crystalline material has drawn significant interest in the area of energy storage owing to their high specific surface area (SSA), compositions, and diverse structures. These new porous crystalline materials are made up of organic linkers and metal nodes and are described as Metal-organic frameworks (MOFs)[17, 18]. In recent years, MOFs have become more widely used in energy storage devices, such as supercapacitors, battery-supercapacitor hybrid devices, and rechargeable batteries due to their impressive features like tailorable pore size and shape, high surface area, diverse

One-Dimensional Ni-MIL-77 Metal-Organic Framework as An Efficient Electrode Nanomaterial for Asymmetric Supercapacitor

Chapter 9

functionalization, and controllable chemical composition[19-22]. However, the limited practical applicability of MOFs in the area of energy storage is because of their poor intrinsic electrical conductivity and low exposed electroactive sites[23]. Therefore, designing and fabricating highly efficient energy storage devices using pure MOFs is a major challenge. Ni-MOFs have drawn much attention among the different transition metal-based MOFs (Co-, Zn-, Mn-, and Fe-MOFs, etc.). Ni-MOFs can be employed as a new kind of electrode material with different structures since there are several advantages like excellent electrolyte penetrability, low steric hindrance, and conjugated π bonds, which potentially allow the fast electrons transfer and electrolyte diffusion in the course of the electrochemical reaction, and thus may show high electrochemical activity[24]. Additionally, Ni-MOFs also possess high specific capacitance and exceptional cyclic stability[25]. These advantages may be significant when designing and developing nickel-based MOFs for applications in energy storage. For instance, Cong-Huan Wang et al. reported an ultrathin nanosheet-assembled nickel-based MOF microflowers by using terephthalic acid (BDC) as organic ligand for supercapacitor applications. This MOF exhibited C value of 1093 F g^{-1} under a current of 1 A g^{-1} [26]. Similarly, Kang et al. synthesized Ni-BTC MOF using 1,3,5-benzentricarboxylic acid as their organic linker, giving a C value of 726 Fg^{-1} under a current of 1 Ag^{-1} [27]. Recently, Ruibin Liang et al. reported a Ni-MOF/NC electrode material using P-Phthalic acid as their organic linker and improved the surface area and uniformity of the catalyst. This Ni-MOF/NC delivered a high C value of 848 F/g under the current of 1 Ag^{-1}. Also, this material exhibited excellent capacitance retention[2]. Recent advancements in the search for an effective material for its application in supercapacitors led us to focus on nickel-based MOFs with high surface area and excellent capacitance retention. To date, Ni-MIL-77 nanobelts have been synthesized and used in the field of electrolysis for determination of glucose in

One-Dimensional Ni-MIL-77 Metal-Organic Framework as An Efficient Electrode Nanomaterial for Asymmetric Supercapacitor

Chapter 9

human serum[28], determination of urea in human body fluids[29], as a bifunctional oxygen catalyst[30], for electrocatalytic urea evolution[10], for high sensitive detection of nitrite[31], etc. However, the activity of Ni-MIL-77 is still not much explored in supercapacitor applications.

Here, in this chapter, we discuss ribbon strip like 1D-Ni-MOF nanobelts that shows high electrocatalytic activity because of their vast surface-to-volume ratio and highly active surface[29]. This 1D nickel-based metal-organic framework (1D-Ni-MIL-77) nanobelts, synthesized by solvothermal method, is used as the cathode material in supercapacitors. 1D-Ni-MIL-77 nanobelts achieved a high surface area of 93.48 m^2 g^{-1}. It demonstrated a C value of 1376 F g^{-1} under a current of 1 A g^{-1} in 3 M KOH and a good rate capacity of 81% up to 4000 cycles. The assembled asymmetric supercapacitor using 1D-Ni-MIL-77 as positive and activated carbon (AC) as a negative electrode obtained 25 W h kg^{-1} energy density at a power density of 750 W kg^{-1} in a potential range of 1.5 V and showed excellent capacitive retention even after 5000 cycles.

9.3 EXPERIMENTAL SECTION

Materials:

Glutaric acid ($HOOC(CH_2)_3COOH$) and Nickel acetate tetrahydrate ($Ni(CH_3COO)_2 \cdot 4H_2O$) were bought from Sigma Aldrich. Sodium hydroxide (NaOH) and potassium hydroxide (KOH) were purchased from Merk. All of these chemicals were used without any additional purification. At 25 °C, the measured conductivity of Milli-Q water, which was obtained from an ultra-filtration system (Milli-Q, Millipore), was 35 mho.cm^{-1}.

Preparation of Ni-MIL-77:

One-Dimensional Ni-MIL-77 Metal-Organic Framework as An Efficient Electrode Nanomaterial for Asymmetric Supercapacitor

Chapter 9

Ni-MIL-77 MOF was synthesized using a facile hydrothermal method[10, 29]. Nickel acetate (988 mg), glutaric acid (792 mg) and potassium hydroxide (460 mg) were dissolved in a solution of 40 mL containing 1:1 ratio by volume of ethanol and deionized water. 4 mL of 0.4 M of NaOH solution was added to this solution under continuous stirring. This mixture was put into a 100 mL autoclave lined with Teflon after around 30 minutes of stirring and the reaction was set to 180 °C for 48 hours then cooled down to ambient temperature. By centrifuging at 16000 rpm and repeatedly washing with water and ethanol, the green precipitate was produced. Lastly, solid product was obtained by vacuum drying.

Electrode preparation:

In order to create a homogeneous slurry, the obtained products are used as active electrode material (80 weight %) and combined with acetylene black (10 weight %), polyvinylidene fluoride (10 weight %), and 1-methyl-2-pyrrolidinone (NMP). The nickel foam (1 cm ×1 cm) is then coated with the slurry and dried under a vacuum. The active substance has an average mass loading of 1 mg cm^{-2}. On a Corrtest electrochemical workstation with a three-electrode system in 3 M KOH solution, the modified nickel foam is utilized as the working electrode, and the electrochemical parameters of the electrode are examined. The platinum wire is used as the counter electrode and the Hg/HgO electrode as the reference electrode respectively. Electrochemical tests are carried out using cyclic voltammetry (CV), galvanostatic charge-discharge (GCD), and electrochemical impedance spectroscopy (EIS). The negative electrode (anode) for the design of the ASC was the AC, the positive electrode (cathode) was the active material, and the separator was cellulose paper. The weight loading ratio was calculated to be 0.27 for positive and negative electrodes (weight loading for positive and negative electrodes was 1 mg and 3.7 mg, respectively).

One-Dimensional Ni-MIL-77 Metal-Organic Framework as An Efficient Electrode Nanomaterial for Asymmetric Supercapacitor

Chapter 9

Characterizations:

Ultrasound treatment was carried out by SINEO UWave-1000 (Shanghai, China) with 28 kHz frequency. Field-emission scanning electron microscope (FESEM) system (Carl Zeiss, Germany make, Model: ∑igma) was used for taking FESEM images. FESEM samples were prepared by casting a drop on a Si-wafer and dried at air around 45°C. The powder x-ray diffraction pattern (p-XRD) of samples was performed by Bruker DAVINCI D8 ADVANCE diffractometer equipped with Cu kα radiation (λ= 0.15406 nm). Transmission Electron Microscopy (TEM, JEOL F200) operated at 200 kV, was used to investigate surface morphology and also used to take High-Resolution TEM (HRTEM) images. For TEM sample preparation, 10 μL solution was taken from a stock solution of 4×10^{-5} mg/L and dried at air around 45°C. XPS measurements were done by VG Microtech where monochromatic source was Mg K_α X-ray. XPS was taken from the sample deposited on Si wafer. All electrochemical measurements were performed by using CorrTest Electrochemical Workstation [Model: CS350]. A conventional 3 electrode system, platinum wire as a counter electrode, glassy carbon as a working electrode and Hg/HgO as a reference electrode were used. pH of the working solution was measured before experiment using Hanna (HI 2209) pH meter. Quantachrome Instruments (AutosorbiQ-XR-XR (2 Stat.) Viton was used to determine the Specific surface area by N_2 adsorption-desorption isotherm.

9.4 RESULTS AND DISCUSSION

Morphology and characterization:

1D-Ni-MIL-77 is prepared using a simple one-step solvothermal method[28, 29] (detailed synthesis procedure is given in Supplementary information). Scheme 9.1 shows the schematic preparation procedure of 1D-Ni-MIL-77. During the synthesis method, a

One-Dimensional Ni-MIL-77 Metal-Organic Framework as An Efficient Electrode Nanomaterial for Asymmetric Supercapacitor

Chapter 9

neutralization reaction between KOH and the ligand glutaric acid occurs to produce glutarate. Under high-temperature conditions, the produced glutarate and the added Ni^{2+} combine to grow continuously in a fixed direction to form 1D-Ni-MIL-77 nanobelts[10].
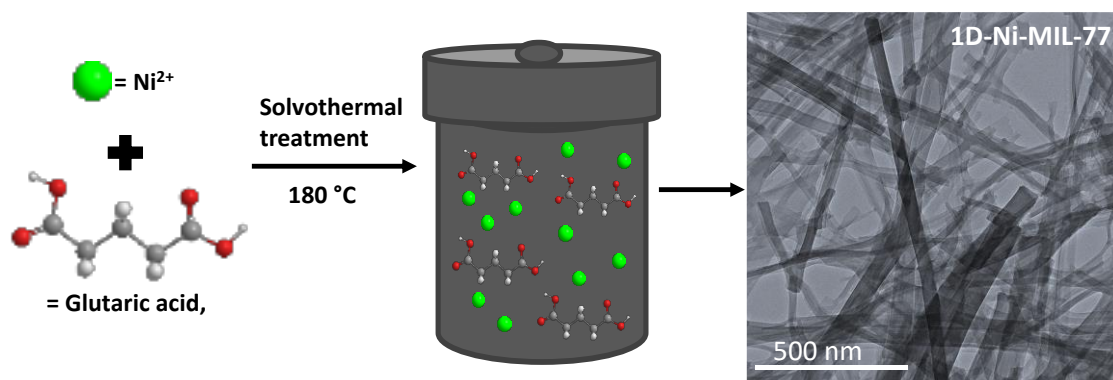
Scheme 9.1. Synthesis scheme of 1D-Ni-MIL-77.

Powder X-ray diffraction (p-XRD) was used to characterize the 1D-Ni-MIL-77. The characteristic peak of 1D-Ni-MIL-77 is the prominent peak between 5 and 10°, as seen in Figure 9.1a. The intense peak located at the 2θ value of around 9° corresponds to the (111) plane of the MOF[32]. 1D-Ni-MIL-77 was further characterized with the help of FT-IR and Brunauer-Emmett-Teller (BET) method. After examining the products FT-IR spectra (Figure 9.1b), a wide peak is observed at 3392 cm^{-1} due to the stretching mode of the hydroxyl group (O-H). The peak observed at 2933 cm^{-1} can be attributed to the stretching mode of C-H. The alkene bond stretching (C=C) contributed to the intense peak at 1600 cm^{-1}. The three absorption peaks centered at 1454, 1398, and 1312 cm^{-1} are due to the bending mode of C-H, and the observations are consistent with the previous report[29].

One-Dimensional Ni-MIL-77 Metal-Organic Framework as An Efficient Electrode Nanomaterial for Asymmetric Supercapacitor

Chapter 9
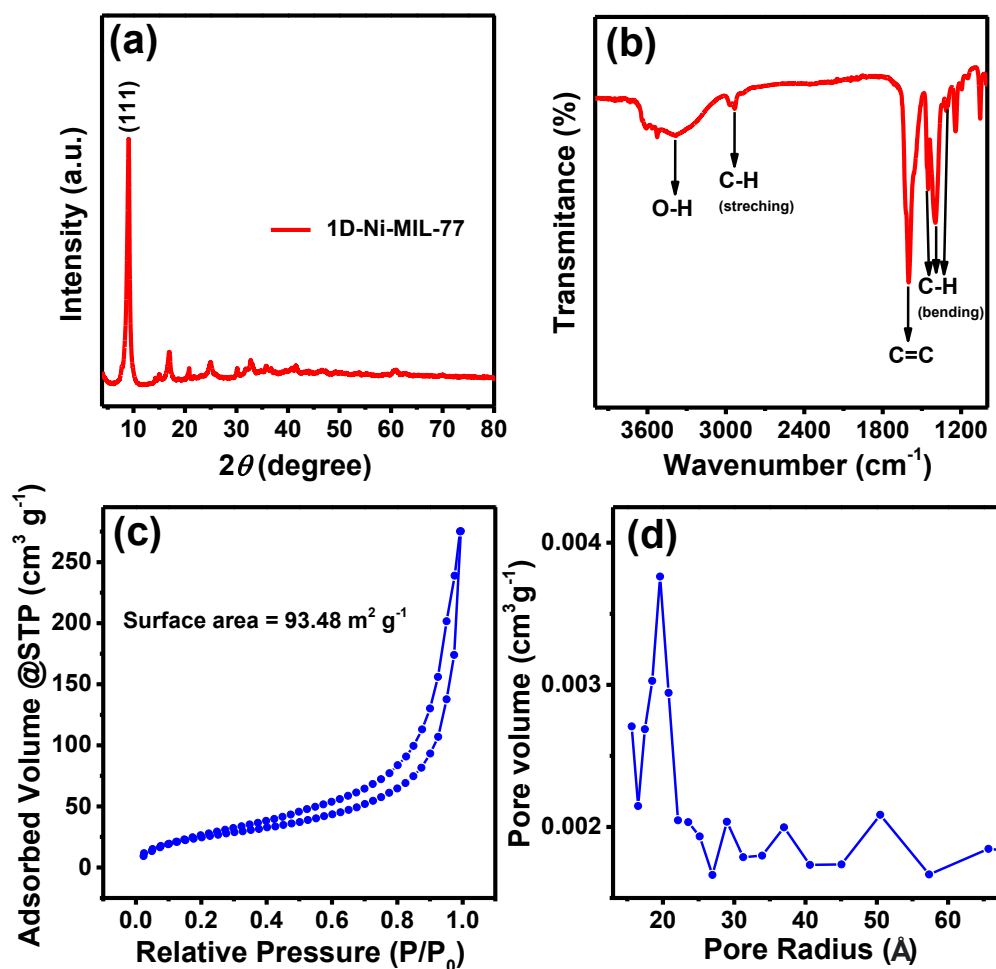
Figure 9.1. (a) p-XRD, (b) FT-IR spectrum, (c) N_2 desorption/adsorption isotherm, (d) Pore size distributions of 1D-Ni-MIL-77.

N_2 desorption/adsorption isothermal curves are used to calculate the SSA of 1D-Ni-MIL-77, and the Barrett-Joyner-Halenda (BJH) distribution is used to determine the pore size distribution (PSD). The type IV isotherms are observed in Figure 9.1c and it exhibit hysteresis loop that range from ~0.4 to 1.0 (P/P$_0$), which denotes a structure with high porosity. According to the experimental findings, 1D-Ni-MIL-77 has a SSA of 93.48 m^2 g^{-1}. By the BJH method (Figure 9.1d), the pore radius is found to be 20 Å which proves

One-Dimensional Ni-MIL-77 Metal-Organic Framework as An Efficient Electrode Nanomaterial for Asymmetric Supercapacitor

Chapter 9

the structure to be mesoporous. Ion/mass diffusion is facilitated by having enough

mesopores and a large SSA in addition to a high electrochemical active area[10].
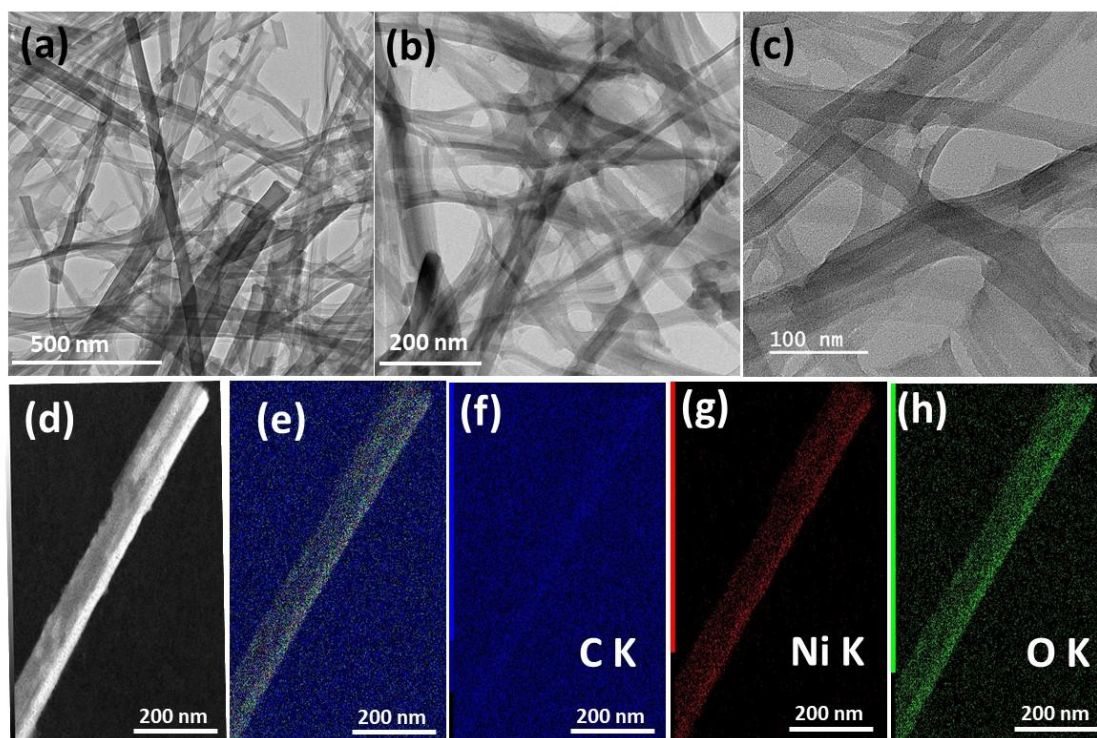
Figure 9.2. (a, b, c) TEM images of 1D-Ni-MIL-77, (d) STEM image, (e) overlay image, (f-h) elemental mapping of 1D-Ni-MIL-77.

The structural composition of the synthesized MOF is characterized by Transmission

electron microscopy (TEM), Field Emission Scanning Electron Microscopy (FESEM),

High-resolution transmission electron microscopy (HRTEM) and Scanning

Transmission Electron Microscopy (STEM). Figure 9.2 (a-c) displays the TEM images

of 1D-Ni-MIL-77 composite at different magnifications. It shows the nanobelt-like

architecture of the synthesized 1D-Ni-MIL-77 MOF with smooth surfaces and some of

them intertwined into bundles. It can be observed that the ultrathin nanobelts show a

relatively uniform width of around ~40 to 60 nm. This nanobelt structure offers high

surface area and excellent electrical conductivity and hence improving the

electrochemical properties and cyclic stability in supercapacitor applications[33]. Figure

9.2 (d, e) shows the STEM and overlay images, respectively. Figure 9.2 (f-h) displays

One-Dimensional Ni-MIL-77 Metal-Organic Framework as An Efficient Electrode Nanomaterial for Asymmetric Supercapacitor

Chapter 9

the elemental mapping of 1D-Ni-MIL-77, indicating uniform distribution atoms and the presence of a significant amount of Nickel, Carbon, and Oxygen in the composite. The FESEM images of 1D-Ni-MIL-77 MOF are presented in Figure S9.1. The crystalline nature of 1D-Ni-MIL-77 can be clearly seen from the HRTEM images (Figure S9.2). The elemental composition of 1D-Ni-MIL-77 is characterized by SEM-EDX (Energy Dispersive X-Ray) to find out the exact metal content in catalyst. The weight percentage of Nickel, Carbon, and oxygen present in catalyst is obtained are 38.8, 39.8, and 21.4 respectively from SEM-EDX data.

The composition of functional groups and the fundamental form of 1D-Ni-MIL-77 can be identified through X-ray photoelectron spectroscopy (XPS). The XPS spectra are displayed in Figure 9.3. The survey scan of the 1D-Ni-MIL-77 in the binding energy range of 0–1200 eV is depicted in Figure 9.3a. The survey scan spectra indicates the presence of Ni, C, and O in the 1D-Ni-MIL-77 composite, which is in accordance with the element distribution by STEM data. Figure 9.3b shows two major peaks visible in the high-resolution Ni 2p spectra, centered at 855.4 eV (Ni $2p_{3/2}$) and 872.9 eV (Ni $2p_{1/2}$), with an interval of 17.5 eV of spin energy. This suggests the existence of nickel in the form of Ni^{2+} in 1D-Ni-MIL-77. The satellite peak of Ni $2p_{3/2}$ can be attributed to the broad peak at around 859.5 eV, and the satellite peak of Ni $2p_{1/2}$ is observed at 877.6 eV[29]. Figure 9.3c shows the high resolution spectra of C 1s. The peak is deconvoluted into two peaks. The C-C bond is responsible for the peak observed at 284.6 eV, and the peak centered at 288.1 eV is due to the presence of the O=C−O bond. The high-resolution spectra of O 1s (Figure 9.3d) shows a broad peak that can be deconvoluted into two peaks. The peak centered at 530.8 eV can be attributed to the metal−oxygen (Ni−O) bond and the peak at 531.5 is due to the O element in the ligand, which is in accordance with literature reports[2].

One-Dimensional Ni-MIL-77 Metal-Organic Framework as An Efficient Electrode Nanomaterial for Asymmetric Supercapacitor

Chapter 9
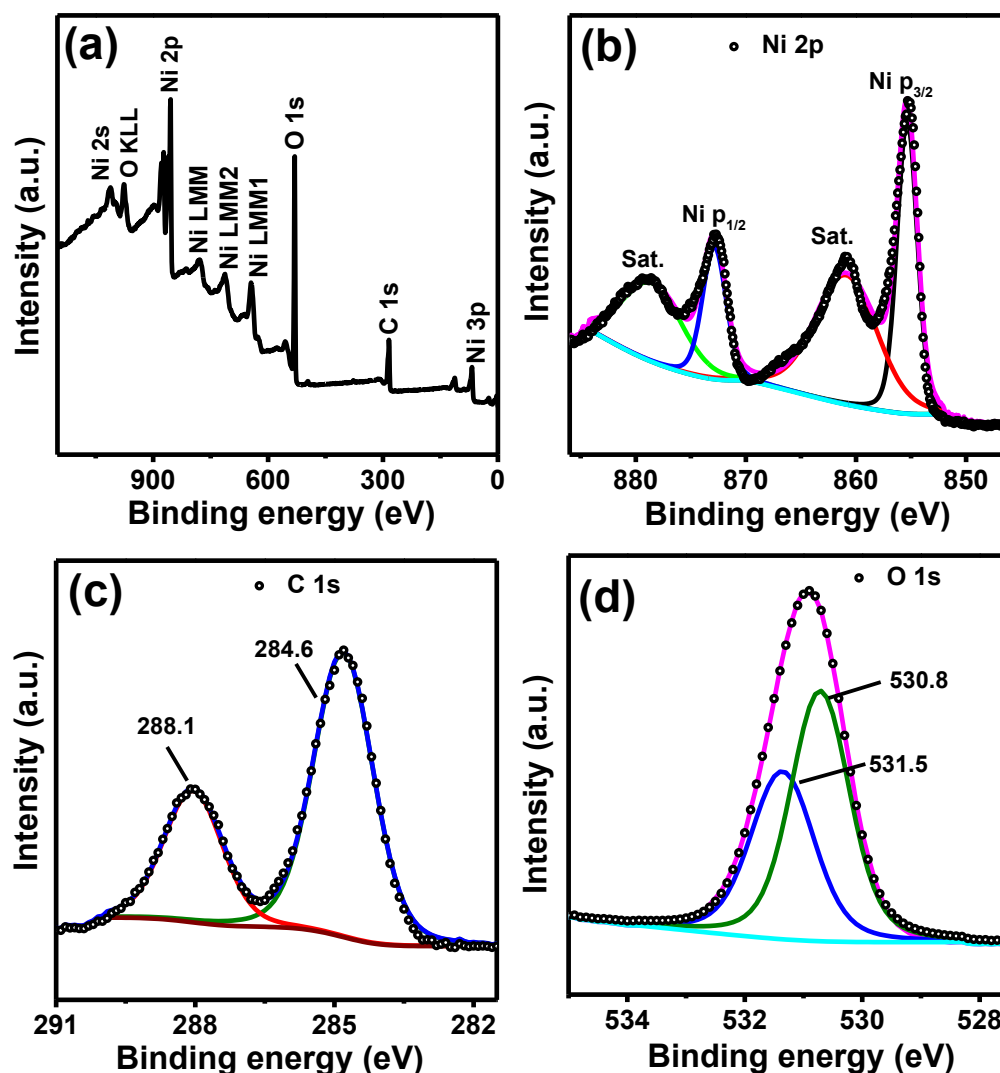
Figure 9.3. (a) XPS survey scan of 1D-Ni-MIL-77, High-resolution XPS spectra of (b) Ni 2p, (c) C1s and (d) O1s of 1D-Ni-MIL-77.

Electrochemical performance:

The electrochemical activity of 1D-Ni-MIL-77 was studied using Cyclic voltammetry (CV) and galvanostatic charge−discharge curve (GCD) experiments. The experiments were done in a 3 M KOH solution as an electrolyte at ambient temperature in a three-electrode system. Platinum wire, Hg/HgO, and 1D-Ni-MIL-77 coated on 1×1 cm^2 Ni foam were used in the half-cell configuration as the counter, reference, and working

One-Dimensional Ni-MIL-77 Metal-Organic Framework as An Efficient Electrode Nanomaterial for Asymmetric Supercapacitor

Chapter 9

electrode, respectively. The optical image of the electrode and the electrical connectivity of 1D-Ni-MIL-77 is shown in Figure S9.3. The specific capacitance (C) was obtained from the CV and GCD plots respectively by following equations[1, 16]

$$C = \frac{\int I \, dV}{2m\Delta V \upsilon} \tag{1}$$

$$C = \frac{I \times \Delta t}{m \times \Delta V} \tag{2}$$

Where $\int I \, dV$ is the area under the CV plot, m is the mass of the catalyst (mg), ΔV is the voltage range, υ represents scan rate, I represent current, and Δt is discharging time.

For the Asymmetric supercapacitor (ASC) device denoted as 1D-Ni-MIL-77//AC, 1D-Ni-MIL-77 acts as the cathode, and activated carbon (AC) acts as the anode. The mass ratio of 1D-Ni-MIL-77 and AC should be balanced for the charge storage in ASC. The ratio of mass is balanced by the following equation[34]

$$\frac{m^-}{m^+} = \frac{C^+ \Delta V^+}{C^- \Delta V^-} \tag{3}$$

Where m^- denotes the mass of negative electrode, m^+ denotes the mass of positive electrode, C^+ and C^- denotes specific capacitance value of cathode and anode, respectively, and ΔV^+ and ΔV^- denotes the potential range for the cathode and anode, respectively. According to calculations, the weight loading ratio for the positive and negative electrodes is 0.27. The weight loading of the positive electrode was 1 mg, and that of the negative electrode was 3.7 mg.

The power density (PD) and energy density (ED) are obtained by using equations 4 and 5 [1, 34]

$$ED = \frac{C \times \Delta V^2}{7.2} \tag{4}$$

One-Dimensional Ni-MIL-77 Metal-Organic Framework as An Efficient Electrode Nanomaterial for Asymmetric Supercapacitor

Chapter 9

$$PD = \frac{3600 \times E}{\Delta t} \qquad (5)$$

Here ΔV is the voltage range of the ASC, C is the specific capacitance of ASC, and Δt is the discharge time.

Figure 9.4a represents the CV plot profiles of 1D-Ni-MIL-77 between the voltage varying from 0-0.5 V (vs Hg/HgO) and sweep rate ranging from 5 to 100 mV s^{-1}. All the CV curves possess a pair of redox peaks, which appears due to the Faradic reaction occurring between Ni^{2+} and Ni^{3+} in alkaline electrolyte according to the following equation[2]

$$Ni^{3+} + 3OH^- \leftrightarrow NiOOH + H_2O + e^- \qquad (6)$$

The C value for 1D-Ni-MIL-77 is obtained by integrating the area under the CV plot using equation 1 and is obtained to be 716 and 383 F g^{-1} at 5 and 10 mV s^{-1} scan rate, respectively. Figure 9.4b shows the GCD curve of 1D-Ni-MIL-77 in the same potential range (0 to 0.5 V) under 1 to 20 A g^{-1} current density. As shown in the GCD plots, all the cycles show almost equal charging and discharging time. The shape of the GCD plots shows a non-linear curve indicating the typical pseudocapacitive nature of the electrode materials that come from faradaic redox reactions. The symmetrical nature of the discharging/charging curves shows good electrochemical activity and a reversible redox process. The highest C value of 1376 F g^{-1} was obtained under 1 A g^{-1} current using equation 2. The C values obtained from the GCD curve are 1160, 1008, 944, 880, 760, and 640 F g^{-1} under the current of 2, 3, 4, 5, 10, and 20 A g^{-1}, respectively. This shows a capacitance retention of 53.48% from its initial value after 20 A g^{-1} current density. Figure 9.4c represents the C value (F g^{-1}) of 1D-Ni-MIL-77 for a corresponding current ranging from 1 to 20 A g^{-1}. The GCD curve of bare Nickel foam at a current of 1 mA is shown in Figure S9.4 for comparison, demonstrating the negligible contribution of Ni

One-Dimensional Ni-MIL-77 Metal-Organic Framework as An Efficient Electrode Nanomaterial for Asymmetric Supercapacitor

Chapter 9

foam on electrochemical performance. The electrochemical activity of 1D-Ni-MIL-77 MOF is compared with previously reported MOFs, and the comparison table is shown in Table 8.1. The capacitance value of 1D-Ni-MIL-77 is on par with or higher than that of the most of the reported literatures. The reproducibility of 1D-Ni-MIL-77 was investigated by preparing five different electrodes. The specific capacitance value obtained for all five electrodes is presented as a bar plot in SI (Figure S9.5), demonstrating good reproducibility[35]. To investigate the cyclic stability of 1D-Ni-MIL-77, GCD under the current of 10 A g^{-1} was obtained for 4000 cycles, given in Figure 9.4d. The plot shows that even after 4000 cycles of GCD, 1D-Ni-MIL-77 retained 81% of its initial capacitance value. This implies the high stability of 1D-Ni-MIL-77 under a current of 10 A g^{-1} in 3 M KOH. The post-stability characterization, that is, p-XRD and SEM of 1D-Ni-MIL-77, is given in SI (Figure S9.6).

One-Dimensional Ni-MIL-77 Metal-Organic Framework as An Efficient Electrode Nanomaterial for Asymmetric Supercapacitor

Chapter 9
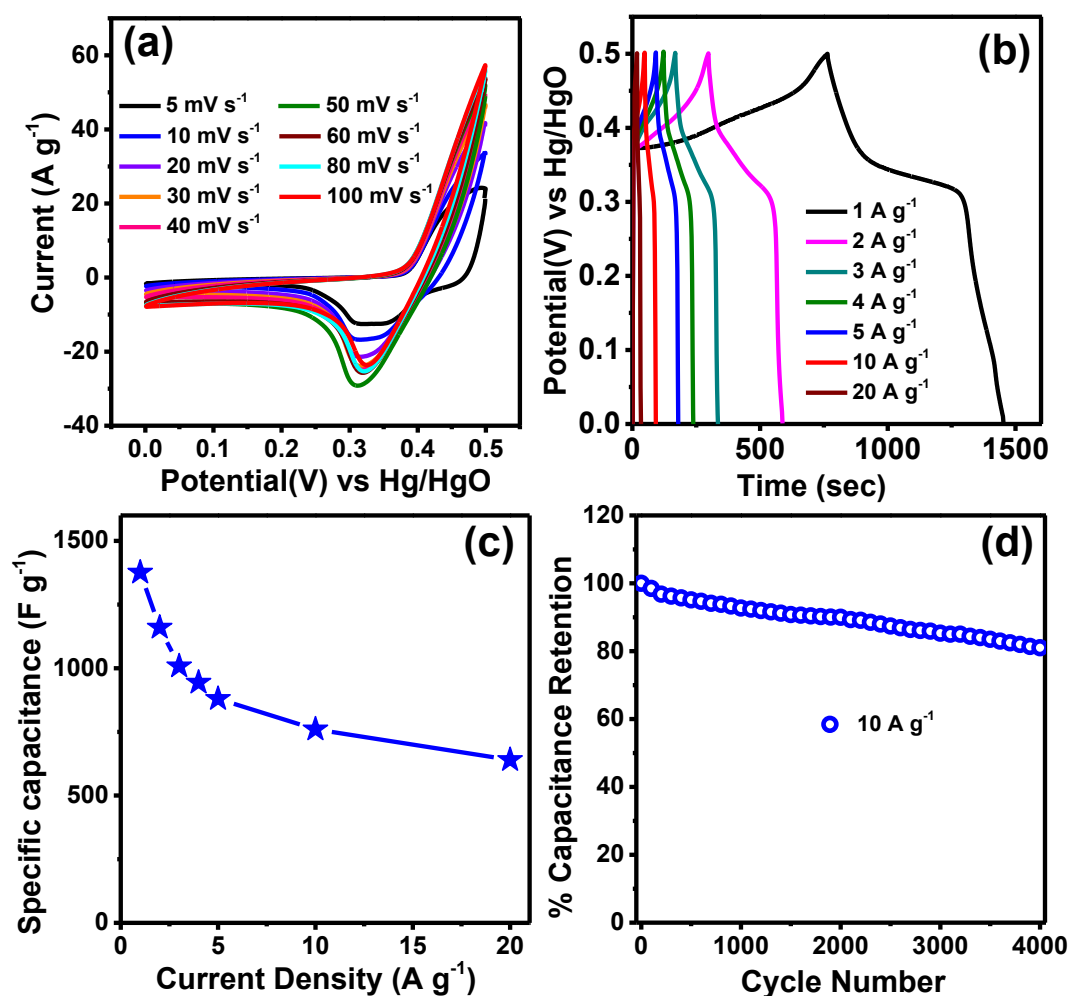
Figure 9.4. (a) CV curve, (b) GCD curve, (c) Specific capacitance at different current densities, and (d) cyclic stability of 1D-Ni-MIL-77 under the current of 10 A g^{-1}.

The post-stability p-XRD pattern indicates the presence of the characteristic peak, that is (111) plane of 1D-Ni-MIL-77, however intensity of the peaks are decreased, and the peaks at 45° and 52° correspond to the (111) and (200) planes of nickel foam (ICDD #04-0850)[36]. The post-stability SEM image reveals the 1D nature of 1D-Ni-MIL-77 is retained and the structure remained almost same. The CV curve for the three-electrode configuration at sweep rates in the range of 1 to 10 mV s^{-1} is investigated to comprehend the mechanism of charge storage of the electrode material. The following equation investigates the kinetics and energy storage mechanism of 1D-Ni-MIL-77

One-Dimensional Ni-MIL-77 Metal-Organic Framework as An Efficient Electrode Nanomaterial for Asymmetric Supercapacitor

Chapter 9

$$i = av^b \tag{7}$$

Where i denotes current, v represents sweep rate, and a and b are variables that represent intercept and slope of the linear plot of log current (i in A g^{-1}) versus log scan rate (v in mV s^{-1}). Figure 9.5a represents the plot of log i vs. log v, and the fitted slope shows the value of b. The value of b can be 1 or 0.5. When the value of b is equal to 1, that represents the supercapacitor behavior to be non-diffusion controlled which includes pseudocapacitance and Electric double layer capacitor (EDLC) type. When the value of b is equal to 0.5, that indicates the redox reaction is limited by diffusion-controlled behavior. From the plot (Figure 9.5a), the slope (b) for the oxidation peak is found to be 0.43, and for the reduction peak, b value is 0.56. Both the values are close to 0.5, that implies charge-discharge process of 1D-Ni-MIL-77 is dominated by diffusion-controlled behavior. Dunn and coworkers[37] proposed a method by which the contributions of surface capacitance effects and diffusion-controlled process can be quantified by studying the dependence of the CV plots on the sweep rates[38]. The ratio can be obtained by a method which is described in the equation 8, that is applicable to determine the current (i) when the voltage (V) is fixed.

$$i(v) = k_1\, v + k_2\, v^{1/2} \tag{8}$$

where v is the sweep rate, and k_1 and k_2 are constants. The diffusion-controlled current and capacitive current are denoted by $k_2 v^{1/2}$ and $k_1 v$, respectively. The CV curve can be used to calculate k_1 and k_2. Using equation 8, i versus $v^{1/2}$ can be plotted to obtain the slope (k_1). The percentage of capacitive contribution at a slow scan rate can be calculated using the aforementioned calculation. The CV plot of 1D-Ni-MIL-77 at 1 mV s^{-1} is given in Figure 9.5b, with the shaded area representing capacitive contribution. The capacitive contribution for 1D-Ni-MIL-77 at different scan rates was also calculated by using Dunn's method. The capacitive contribution values obtained for 1, 2, and 3 mV s^{-1}

One-Dimensional Ni-MIL-77 Metal-Organic Framework as An Efficient Electrode Nanomaterial for Asymmetric Supercapacitor

Chapter 9

scan rates are 28.3, 30.25, and 32.8, respectively, as presented in Figure 9.5c. Figure 9.5d

shows the Nyquist plot of 1D-Ni-MIL-77 in 3 M KOH electrolyte at frequencies ranging

from 0.1 and 100 kHz with an open circuit voltage with three electrodes and an AC

amplitude of 10 mV. The Nyquist plot consists of 2 parts, one of which is the quasi-

semicircular part in the high-frequency region. The other part is linear in the low-

frequency region. The Nyquist plot of 1D-Ni-MIL-77 was fitted using an equivalent

circuit (inset of Figure 9.5d), and from the fitting results, 1D-Ni-MIL-77 was found to

have a charge transfer resistance (R_{CT}) of 1.28 Ω, showing improved electrical

conductivities. The Nyquist plot showing the increased overall conductivity of the

composite yielded an equivalent series resistance (R_s) of 1.67 for 1D-Ni-MIL-77, which

was obtained by equivalent circuit fitting[1].

Table 9.1. Comparison of C values of 1D-Ni-MIL-77 with previously reported MOFs.

Catalysts	C (F g^{-1})	Current load/ scan rate	Electrolyte	Reference
Ni-MOF/NC	828	1 A g^{-1}	3 M KOH	[2]
GM-LEG@Ni-MOF	987.6	0.5 A g^{-1}	3 M KOH	[34]
PPNF@Co−Ni MOF	1096.2	1 A g^{-1}	3 M KOH	[39]
CoNi$_{0.5}$-MOF	663.6	1 A g^{-1}	2 M KOH	[16]
Co$_1$Ni$_{20}$-MOF	597	0.5 A g^{-1}	3 M KOH	[40]
ZnCo-MOF/GS	695	1 A g^{-1}	3 M KOH	[41]
NiO/Ni-MOF-25	1176.6	1 A g^{-1}	2 M KOH	[42]
NiCo-MOF	1202.1	1 A g^{-1}	2 M KOH	[43]
Ni$_3$S$_4$/NiS/NC-12	323.0	1 A g^{-1}	2 M KOH	[44]
NO16	1065.9	1 A g^{-1}	2 M KOH+0.4 M NaCl	[45]
1D-Ni-MIL-77	1376	1 A g^{-1}	3 M KOH	This work

One-Dimensional Ni-MIL-77 Metal-Organic Framework as An Efficient Electrode Nanomaterial for Asymmetric Supercapacitor

Chapter 9

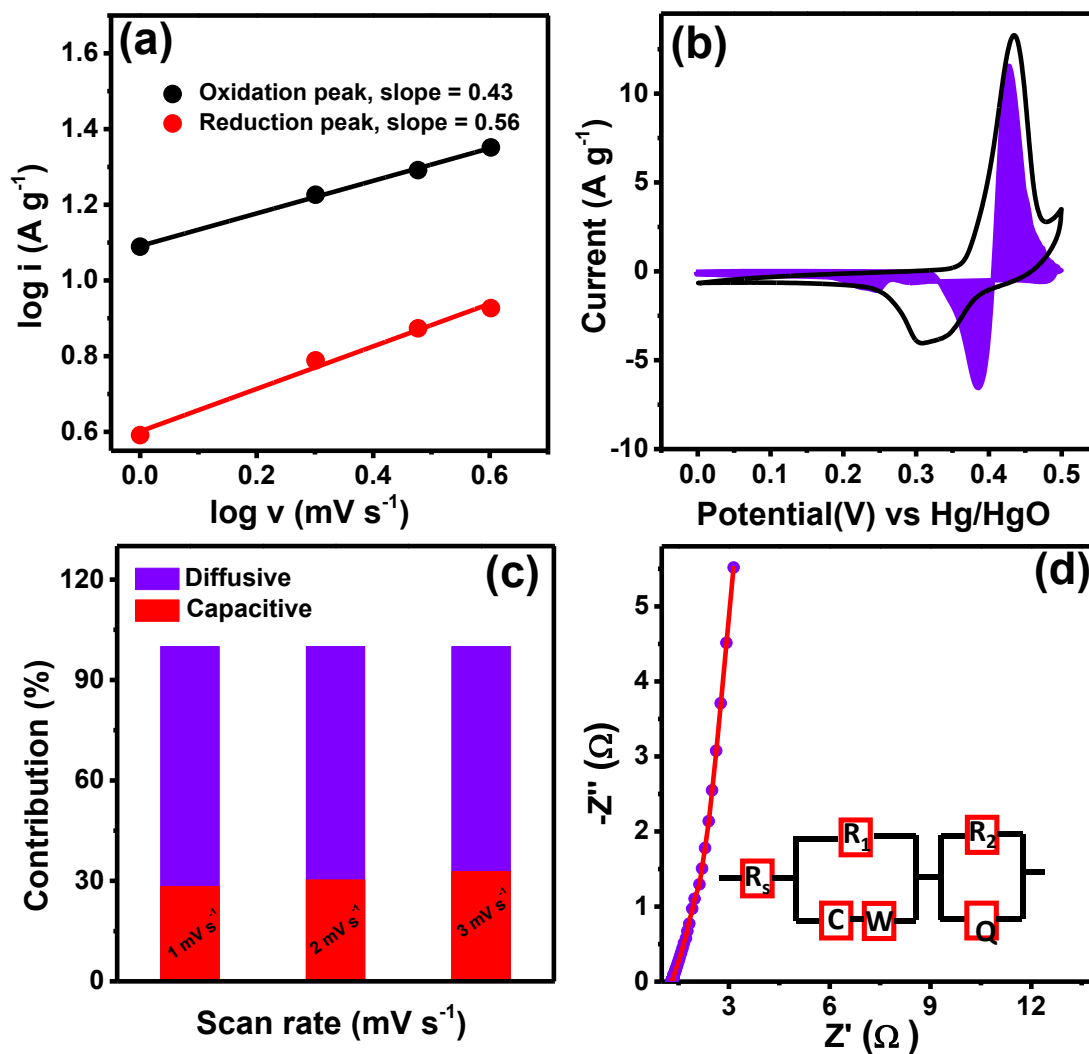**Figure 9.5**. (a) plot of log(i) and log(v), (b) CV curve of 1D-Ni-MIL-77 showing contribution area of the pseudocapacitance at a sweep rate of 1 mV s^{-1}, (c) Pseudocapacitive contribution of 1D-Ni-MIL-77 by varying sweep rates, (d) EIS fitting of 1D-Ni-MIL-77 in 3 M KOH.

One-Dimensional Ni-MIL-77 Metal-Organic Framework as An Efficient Electrode Nanomaterial for Asymmetric Supercapacitor

Chapter 9

Asymmetric supercapacitor (ASC) device:

To evaluate the potential applications of 1D-Ni-MIL-77, an asymmetric supercapacitor device 1D-Ni-MIL-77//AC was assembled consisting of 1D-Ni-MIL-77 as cathode, AC as the anode and the electrolyte is 3 M KOH. The electrochemical test of AC was conducted in a three-electrode system using AC as the working electrode, platinum wire as the counter electrode, and Hg/HgO as the reference electrode. The CV curves of AC between the potential range of 0 to −1 V in 3 M KOH at different sweep rate ranging from 10 to 100 mV s^{-1} is displayed in Figure S9.7a, and the GCD curve of AC ranging from 1 to 5 A g^{-1} current is given in Figure S9.7b. The GCD curve of AC is symmetric, and the CV curve is rectangular in nature, which does not show any oxidation or reduction peaks, which is a clear indication of the EDLC-type nature of the AC. The C value for AC is found to be 184 F g^{-1} (−1.0 to 0.0 V) under a current of 1 A g^{-1}.
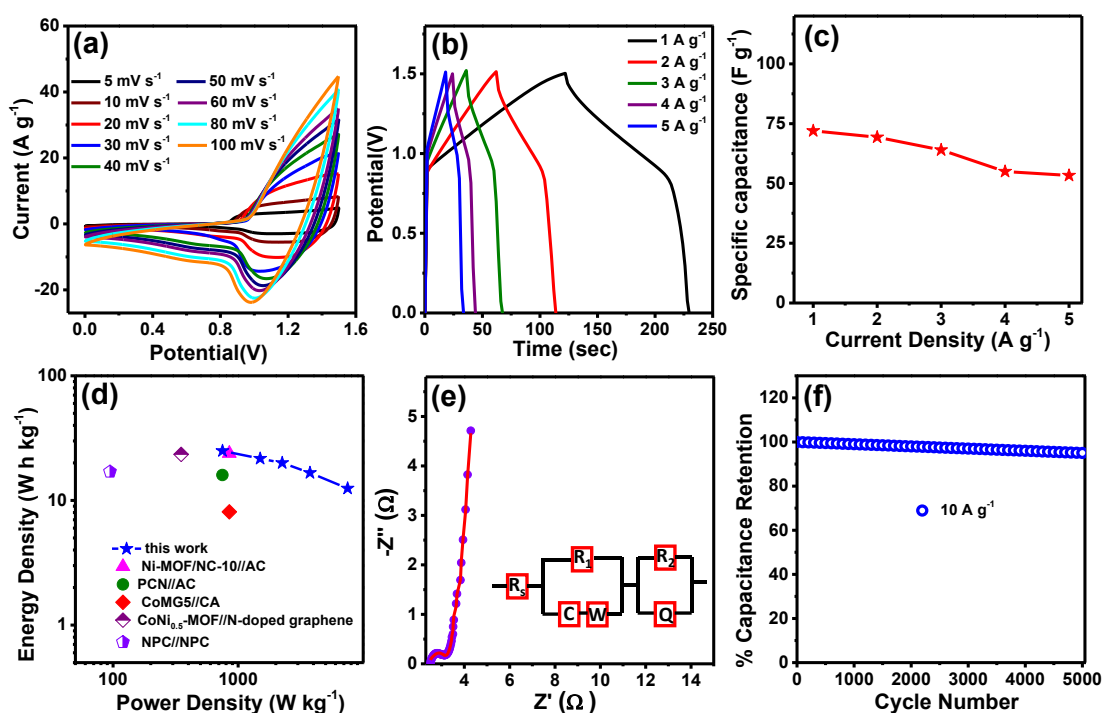

Figure 9.6. (a) CV curve, (b) GCD curve of 1D-Ni-MIL-77//AC, (c) C at different current, (d) Ragone plot of the 1D-Ni-MIL-77//AC, (e) EIS spectra, and (f) stability plot of 1D-Ni-MIL-77//AC.

One-Dimensional Ni-MIL-77 Metal-Organic Framework as An Efficient Electrode Nanomaterial for Asymmetric Supercapacitor

Chapter 9

The CV curves of 1D-Ni-MIL-77 and AC is given in Figure S9.8a. The voltage window of AC is -1 to 0 V, and that of 1D-Ni-MIL-77 is 0 to 0.5 V. The combined contributions of the positive and negative materials were used to determine the voltage range of the ASC. To examine the stable potential windows of ASC, CV up to different potentials were recorded (Figure S9.8b), indicating 1.5 V is the maximum voltage window within which ASC will be stable with no polarization deformation. The CV plot of the assembled ASC with varied sweep rates of 10 to 100 mV s^{-1} is displayed in Figure 9.6a with a potential range of 0-1.5 V. Additionally, the CV plots show the traits of the double layer and faradaic redox behaviors when 1D-Ni-MIL-77 and AC are used as cathode and anode to assemble the ASC. By increasing the sweep rate from 10 to 100 mV s^{-1}, no significant change is seen on the curves, indicating that the assembled ASC has strong electrochemical reversibility. The GCD curve of the assembled ASC under the current from 1 to 10 A g^{-1} is shown in Figure 9.6b. The assembled ASC, in the GCD test, can reach up to a large potential range of 0 to 1.5 V, which is consistent with CV results. The C value with respect to the current density of the ASC (Figure 9.6c) is calculated to be 72, 69.33, 64, 55, and 53.33 F g^{-1} at 1, 2, 3, 4, and 5 A g$^{-1,}$ respectively. Figure 9.6d represents the Ragone plot of the 1D-Ni-MIL-77//AC ASC device. The ED and PD were obtained by using equation 4 and 5, respectively. The obtained maximum ED for the assembled ASC is 25 W h kg^{-1} at a PD of 750 W kg$^{-1,}$ and it even delivered high ED of 12.5 W h kg^{-1} at 7500 W kg^{-1} PD. The ED of 1D-Ni-MIL-77//AC ASC is compared with some recently published results and given in Figure 9.6d. The plot clearly shows that the prepared ASC outperformed Ni-MOF/NC-10//AC[2], PCN//AC[46], CoMG5//CA[47], CoNi$_{0.5}$-MOF//N-doped graphene[16], and NPC//NPC[48] in terms of electrochemical performance. EIS plots of 1D-Ni-MIL-77//AC ASC were obtained (Figure 9.6e) to calculate the resistance offered in charge transfer during charging-discharging. The R$_s$

One-Dimensional Ni-MIL-77 Metal-Organic Framework as An Efficient Electrode Nanomaterial for Asymmetric Supercapacitor

Chapter 9

and R_{CT} were calculated to be 0.73 Ω and 2.45 Ω, respectively. This suggests the ASC offers low resistance and high conductivity. Cycling stability is an crucial factor to evaluate the electrochemical activity of supercapacitors. To examine the cyclic stability of the as-prepared ASC, 5000 GCD cycles at 10 A g^{-1} current were performed, as displayed in Figure 9.6f. The 1D-Ni-MIL-77//AC ASC device showed good cyclic durability, and a capacitive retention of 95% of its initial value is observed.

The following factors can be used to explain the high electrochemical performance of the 1D-Ni-MIL-77 MOF:

1. The good porosity of 1D-Ni-MIL-77 might be a factor for the high capacitance value. The porous network helps in higher ion diffusion and improved electrochemical interactions. The high surface area helps in adsorption and different catalytic processes. The buildup of electrostatic charge at the electrode/electrolyte contact rises with increasing specific surface area[1]. For example, Puja et al. suggested the increment of specific capacitance and stability of catalysts with increment in porosity of the catalyst[49]. Figure 9.1c shows the BET data of the catalyst, and from the plot, the SSA is calculated to be 93.48 m^2/g indicating the good porosity of 1D-Ni-MIL-77.

2. The 1D nature of the material may be one of the reasons for the high capacitance value of 1D-Ni-MIL-77. Generally, 1D nanostructured materials have a high surface-to-volume ratio, excellent surface activities, and crystallographic orientation[50]. For example, Shinde et al. reported a cobalt phosphate electrode material having 1D nanobelts for excellent supercapacitors[33]. They reported a maximum C value of 1766 F g^{-1} at a low sweep rate of 5 mV s^{-1} in an electrolyte of 1 M KOH. Figure 9.2 displays the 1D nature of the 1D-Ni-MIL-77 catalyst.

One-Dimensional Ni-MIL-77 Metal-Organic Framework as An Efficient Electrode Nanomaterial for Asymmetric Supercapacitor

Chapter 9

3. Low R_{CT} value of 1D-Ni-MIL-77 might be a reason for increased capacitance. When the synthesized 1D-Ni-MIL-77 was employed as a cathode in ASC for supercapacitor application, the R_{CT} value was obtained to be 2.45 Ω (Figure 9.6e). Typically, the specific capacitance of a supercapacitor is indirectly inversely correlated with the R_{CT} value; the greater the R_{CT} value, the lower the specific capacitance[51]. The decreased electronic and diffusion resistance of 1D-Ni-MIL-77, as indicated by the low R_{CT} value (2.45 Ω), leads to improved charge mobility at the interface of electrode/electrolyte and high electronic conductivity, both of which might increase the electrochemical activity of 1D-Ni-MIL-77.

9.5 CONCLUSIONS:

In summary, the synthesis of 1D-Ni-MIL-77 composite was discussed by a facile one-step solvothermal method that shows a high SSA of 93.48 m^2 g^{-1}. This mesoporous structure with highly porous architecture offers ample active sites of metal with fast mass transfer and excellent electron transfer for electrocatalytic reactions. The 1D-Ni-MIL-77 electrode delivers a high C value of 1376 F g^{-1} under a current of 1 A g^{-1} and 81% retention of its initial capacity value after 4000 cycles. The ASC device 1D-Ni-MIL-77/AC delivered high ED of 25 W h kg^{-1} at PD of 750 W kg^{-1} with capacitance retention of 95% after 5000 cycles. The high electrochemical activity of the 1D-Ni-MIL-77 composite is owing to its unique 1D structure and high SSA, which provides easy electrolyte/ion diffusions and electron conduction. This work offers a good strategy for developing 1D MOFs with high conductivity and a large number of active sites for energy storage applications.

One-Dimensional Ni-MIL-77 Metal-Organic Framework as An Efficient Electrode Nanomaterial for Asymmetric Supercapacitor

Chapter 9

9.6 REFERENCES:

(1) Panda, P.; Mishra, R.; Panigrahy, S.; Barman, S. 3D Assembly of CoAl2O4 Spinel Nanosheets for Energy Storage. *ACS Applied Nano Materials* **2022**, *5* (4), 5176-5186.

(2) Liang, R.; Du, Y.; Lin, J.; Chen, J.; Xiao, P. Facile-Synthesized Ni-Metal–Organic Framework/Nano Carbon Electrode Material for High-Performance Supercapacitors. *Energy & Fuels* **2022**, *36* (13), 7115-7120.

(3) Liang, R.; Du, Y.; Xiao, P.; Cheng, J.; Yuan, S.; Chen, Y.; Yuan, J.; Chen, J. Transition Metal Oxide Electrode Materials for Supercapacitors: A Review of Recent Developments. *Nanomaterials*, 2021, *11*, 1248.

(4) Xiao, S.; Li, X.; Zhang, W.; Xiang, Y.; Li, T.; Niu, X.; Chen, J. S.; Yan, Q. Bilateral Interfaces in In2Se3-CoIn2-CoSe2 Heterostructures for High-Rate Reversible Sodium Storage. *ACS Nano* **2021**, *15* (8), 13307-13318.

(5) Xie, Y.; Cao, J.; Wang, X.; Li, W.; Deng, L.; Ma, S.; Zhang, H.; Guan, C.; Huang, W. MOF-Derived Bifunctional Co0.85Se Nanoparticles Embedded in N-Doped Carbon Nanosheet Arrays as Efficient Sulfur Hosts for Lithium–Sulfur Batteries. *Nano Letters* **2021**, *21* (20), 8579-8586.

(6) Panda, P.; Mishra, R.; Panigrahy, S.; Barman, S. Design of Co1Al3(OH)m/carbon nitride hybrid nanostructures for enhanced capacitive energy storage in an alkaline electrolyte. *Materials Advances* **2021**, *2* (23), 7671-7680.

(7) Panda, P.; Mishra, R.; Barman, S. In-situ nano-engineering of amorphous MoS2 nanosheets with carbon dots for enhanced supercapacitor performances. *International Journal of Energy Research* **2022**, *46* (12), 17576-17589.

(8) Xiong, D.; Li, X.; Bai, Z.; Lu, S. Recent Advances in Layered Ti3C2Tx MXene for Electrochemical Energy Storage. *Small* **2018**, *14* (17), 1703419,

(9) Cai, P.; Liu, T.; Zhang, L.; Cheng, B.; Yu, J. ZIF-67 derived nickel cobalt sulfide hollow cages for high-performance supercapacitors. *Applied Surface Science* **2020**, *504*, 144501.

One-Dimensional Ni-MIL-77 Metal-Organic Framework as An Efficient Electrode Nanomaterial for Asymmetric Supercapacitor

Chapter 9

(10) Xiao, X.; Zhang, G.; Wang, J.; Wang, X.; Pang, H. Ultrathin One-Dimensional Ni-MIL-77 Nanobelts for High-Performance Electrocatalytic Urea Evolution. *Crystal Growth & Design* **2021**, *21* (7), 3639-3644.

(11) Chen, Y.; Yang, R.; Chen, C.; Li, Y.; Wei, M. Construction of hierarchical Mn2O3 hollow microspheres derived from metal–organic frameworks for high performance supercapacitors. *Journal of Power Sources* **2021**, *505*, 230077.

(12) Sahu, P.; Mishra, R.; Panigrahy, S.; Panda, P.; Barman, S. Constructing micropore-rich nitrogen-doped carbon for high-performance supercapacitor and adsorption of carbon dioxide. *International Journal of Energy Research* **2022**, *46* (10), 13556-13569.

(13) Mishra, R.; Panda, P.; Barman, S. Synthesis of a Co3V2O8/CNx hybrid nanocomposite as an efficient electrode material for supercapacitors. *New Journal of Chemistry* **2021**, *45* (13), 5897-5906.

(14) Jha, S.; Mehta, S.; Chen, Y.; Renner, P.; Sankar, S. S.; Parkinson, D.; Kundu, S.; Liang, H. NiWO4 nanoparticle decorated lignin as electrodes for asymmetric flexible supercapacitors. *Journal of Materials Chemistry C* **2020**, *8* (10), 3418-3430.

(15) Wang, L.; Xu, H.; Gao, J.; Yao, J.; Zhang, Q. Recent progress in metal-organic frameworks-based hydrogels and aerogels and their applications. *Coordination Chemistry Reviews* **2019**, *398*, 213016.

(16) Zhang, W.; Guo, X.; Wang, Y.; Zheng, Y.; Zhao, J.; Xie, H.; Zhang, Z.; Zhao, Y. Self-Assembly of Ni-Doped Co-MOF Spherical Shell Electrode for a High-Performance Supercapacitor. *Energy & Fuels* **2022**, *36* (3), 1716-1725.

(17) Shekhawat, A.; Samanta, R.; Barman, S. MOF-Derived Porous Fe3O4/RuO2-C Composite for Efficient Alkaline Overall Water Splitting. *ACS Applied Energy Materials* **2022**, *5* (5), 6059-6069.

(18) Kuyuldar, S.; Genna, D. T.; Burda, C. On the potential for nanoscale metal–organic frameworks for energy applications. *Journal of Materials Chemistry A* **2019**, *7* (38), 21545-21576.

One-Dimensional Ni-MIL-77 Metal-Organic Framework as An Efficient Electrode Nanomaterial for Asymmetric Supercapacitor

Chapter 9

(19) Chen, D. D.; He, Z. Q.; Wang, M.; Wu, D.; Chen, X. Y.; Zhang, Z. J. Boron doping and structure control of carbon materials for supercapacitor application: the effect of freeze-drying and air-drying for porosity engineering. *Journal of Solid State Electrochemistry* **2020**, *24* (3), 641-654.

(20) Sundriyal, S.; Kaur, H.; Bhardwaj, S. K.; Mishra, S.; Kim, K.-H.; Deep, A. Metal-organic frameworks and their composites as efficient electrodes for supercapacitor applications. *Coordination Chemistry Reviews* **2018**, *369*, 15-38.

(21) Liang, Z.; Zhao, R.; Qiu, T.; Zou, R.; Xu, Q. Metal-organic framework-derived materials for electrochemical energy applications. *EnergyChem* **2019**, *1* (1), 100001.

(22) Shao, Y.; El-Kady, M. F.; Sun, J.; Li, Y.; Zhang, Q.; Zhu, M.; Wang, H.; Dunn, B.; Kaner, R. B. Design and Mechanisms of Asymmetric Supercapacitors. *Chemical Reviews* **2018**, *118* (18), 9233-9280.

(23) Pan, Y.; Shi, C.; Chen, Y.; Li, D.; Tian, Z.; Guo, L.; Wang, Y. Fishbone-like Ni3S2/Co3S4 integrated with nickel MOF nanosheets for hybrid supercapacitors. *Applied Surface Science* **2021**, *566*, 150744.

(24) Jiao, Y.; Pei, J.; Yan, C.; Chen, D.; Hu, Y.; Chen, G. Layered nickel metal–organic framework for high performance alkaline battery-supercapacitor hybrid devices. *Journal of Materials Chemistry A* **2016**, *4* (34), 13344-13351.

(25) Yang, C.; Li, X.; Yu, L.; Liu, X.; Yang, J.; Wei, M. A new promising Ni-MOF superstructure for high-performance supercapacitors. *Chemical Communications* **2020**, *56* (12), 1803-1806.

(26) Wang, C.-H.; Zhang, D.-W.; Liu, S.; Yamauchi, Y.; Zhang, F.-B.; Kaneti, Y. V. Ultrathin nanosheet-assembled nickel-based metal–organic framework microflowers for supercapacitor applications. *Chemical Communications* **2022**, *58* (7), 1009-1012.

(27) Kang, L.; Sun, S.-X.; Kong, L.-B.; Lang, J.-W.; Luo, Y.-C. Investigating metal-organic framework as a new pseudo-capacitive material for supercapacitors. *Chinese Chemical Letters* **2014**, *25* (6), 957-961.

One-Dimensional Ni-MIL-77 Metal-Organic Framework as An Efficient Electrode Nanomaterial for Asymmetric Supercapacitor

Chapter 9

(28) Xiao, X.; Zheng, S.; Li, X.; Zhang, G.; Guo, X.; Xue, H.; Pang, H. Facile synthesis of ultrathin Ni-MOF nanobelts for high-efficiency determination of glucose in human serum. *Journal of Materials Chemistry B* **2017**, *5* (26), 5234-5239.

(29) Bao, C.; Niu, Q.; Chen, Z.-A.; Cao, X.; Wang, H.; Lu, W. Ultrathin nickel-metal–organic framework nanobelt based electrochemical sensor for the determination of urea in human body fluids. *RSC Advances* **2019**, *9* (50), 29474-29481.

(30) Xiao, X.; Li, Q.; Yuan, X.; Xu, Y.; Zheng, M.; Pang, H. Ultrathin Nanobelts as an Excellent Bifunctional Oxygen Catalyst: Insight into the Subtle Changes in Structure and Synergistic Effects of Bimetallic Metal–Organic Framework. *Small Methods* **2018**, *2* (12), 1800240.

(31) Meng, X.; Xiao, X.; Pang, H. Ultrathin Ni-MOF Nanobelts-Derived Composite for High Sensitive Detection of Nitrite. *Frontiers in Chemistry* **2020**, *8*, 330.

(32) Guillou, N.; Livage, C.; Chaigneau, J.; Férey, G. Structural investigation of the nickel 3-methylglutarate from powder diffraction demonstrating adaptability of the inorganic skeleton of MIL-77. *Powder Diffraction* **2005**, *20* (4), 288-293.

(33) Shinde, S. K.; Jalak, M. B.; Karade, S. S.; Majumder, S.; Tamboli, M. S.; Truong, N. T.; Maile, N. C.; Kim, D.-Y.; Jagadale, A. D.; Yadav, H. M. A Novel Synthesized 1D Nanobelt-like Cobalt Phosphate Electrode Material for Excellent Supercapacitor Applications. *Materials*, 2022, *15*, 8235.

(34) Xiao, Y.; Wei, W.; Zhang, M.; Jiao, S.; Shi, Y.; Ding, S. Facile Surface Properties Engineering of High-Quality Graphene: Toward Advanced Ni-MOF Heterostructures for High-Performance Supercapacitor Electrode. *ACS Applied Energy Materials* **2019**, *2* (3), 2169-2177.

(35) Qiao, Y.; Liu, Q.; Lu, S.; Chen, G.; Gao, S.; Lu, W.; Sun, X. High-performance non-enzymatic glucose detection: using a conductive Ni-MOF as an electrocatalyst. *Journal of Materials Chemistry B* **2020**, *8* (25), 5411-5415,

(36) Mulik, S. V.; Dhas, S. D.; Moholkar, A. V.; Parale, V. G.; Park, H.-H.; Koyale, P. A.; Ghodake, V. S.; Panda, D. K.; Delekar, S. D. Square-Facet Nanobar MOF-Derived Co3O4@Co/N-doped CNT Core–Shell-based Nanocomposites as Cathode Materials for High-Performance Supercapacitor Studies. *ACS Omega* **2023**, *8* (2), 2183-2196.

One-Dimensional Ni-MIL-77 Metal-Organic Framework as An Efficient Electrode Nanomaterial for Asymmetric Supercapacitor

Chapter 9

(37) Wang, J.; Polleux, J.; Lim, J.; Dunn, B. Pseudocapacitive Contributions to Electrochemical Energy Storage in TiO2 (Anatase) Nanoparticles. *The Journal of Physical Chemistry C* **2007**, *111* (40), 14925-14931.

(38) Jiang, Y.; Liu, J. Definitions of Pseudocapacitive Materials: A Brief Review. *ENERGY & ENVIRONMENTAL MATERIALS* **2019**, *2* (1), 30-37.

(39) Tian, D.; Song, N.; Zhong, M.; Lu, X.; Wang, C. Bimetallic MOF Nanosheets Decorated on Electrospun Nanofibers for High-Performance Asymmetric Supercapacitors. *ACS Applied Materials & Interfaces* **2020**, *12* (1), 1280-1291.

(40) Hang, X.; Xue, Y.; Cheng, Y.; Du, M.; Du, L.; Pang, H. From Co-MOF to CoNi-MOF to Ni-MOF: A Facile Synthesis of 1D Micro-/Nanomaterials. *Inorganic Chemistry* **2021**, *60* (17), 13168-13176.

(41) Erçarıkcı, E.; Dağcı Kıranşan, K.; Topçu, E. Three-Dimensional ZnCo-MOF Modified Graphene Sponge: Flexible Electrode Material for Symmetric Supercapacitor. *Energy & Fuels* **2022**, *36* (3), 1735-1745.

(42) Wang, G.; Yan, Z.; Wang, N.; Xiang, M.; Xu, Z. NiO/Ni Metal–Organic Framework Nanostructures for Asymmetric Supercapacitors. *ACS Applied Nano Materials* **2021**, *4* (9), 9034-9043.

(43) Wang, Y.; Liu, Y.; Wang, H.; Liu, W.; Li, Y.; Zhang, J.; Hou, H.; Yang, J. Ultrathin NiCo-MOF Nanosheets for High-Performance Supercapacitor Electrodes. *ACS Applied Energy Materials* **2019**, *2* (3), 2063-2071.

(44) Wei, W.; Guo, Z.; Xu, J.; Fang, Z.; Zhang, J.; Jia, Y.; Mi, L. Novel Ni3S4/NiS/NC composite with multiple heterojunctions synthesized through space-confined effect for high-performance supercapacitors. *International Journal of Extreme Manufacturing* **2023**, *5* (1), 015504.

(45) Wei, W.; Chen, W.; Mi, L.; Xu, J.; Zhang, J. High-rate performance aqueous-based supercapacitors at −30 °C driven by novel 1D Ni(OH)2 nanorods and a two-solute electrolyte. *Journal of Materials Chemistry A* **2021**, *9* (42), 23860-23872.

One-Dimensional Ni-MIL-77 Metal-Organic Framework as An Efficient Electrode Nanomaterial for Asymmetric Supercapacitor

Chapter 9

(46) Wang, K.; Bi, R.; Huang, M.; Lv, B.; Wang, H.; Li, C.; Wu, H.; Zhang, Q. Porous Cobalt Metal–Organic Frameworks as Active Elements in Battery–Supercapacitor Hybrid Devices. *Inorganic Chemistry* **2020**, *59* (10), 6808-6814.

(47) Azadfalah, M.; Sedghi, A.; Hosseini, H.; Kashani, H. Cobalt based Metal Organic Framework/Graphene nanocomposite as high performance battery-type electrode materials for asymmetric Supercapacitors. *Journal of Energy Storage* **2021**, *33*, 101925.

(48) Yue, Y.; Huang, Y.-L.; Bian, S.-W. Nitrogen-Doped Hierarchical Porous Carbon Films Derived from Metal–Organic Framework/Cotton Composite Fabrics as Freestanding Electrodes for Flexible Supercapacitors. *ACS Applied Electronic Materials* **2021**, *3* (5), 2178-2186.

(49) De, P.; Halder, J.; Gowda, C. C.; Kansal, S.; Priya, S.; Anshu, S.; Chowdhury, A.; Mandal, D.; Biswas, S.; Dubey, B. K.; et al. Role of porosity and diffusion coefficient in porous electrode used in supercapacitors – Correlating theoretical and experimental studies. *Electrochemical Science Advances* **2022**, *3*, e2100159.

(50) Zheng, F.-L.; Li, G.-R.; Ou, Y.-N.; Wang, Z.-L.; Su, C.-Y.; Tong, Y.-X. Synthesis of hierarchical rippled Bi2O3 nanobelts for supercapacitor applications. *Chemical Communications* **2010**, *46* (27), 5021-5023.

(51) Bhujun, B.; Tan, M. T. T.; Shanmugam, A. S. Evaluation of aluminium doped spinel ferrite electrodes for supercapacitors. *Ceramics International* **2016**, *42* (5), 6457-6466.
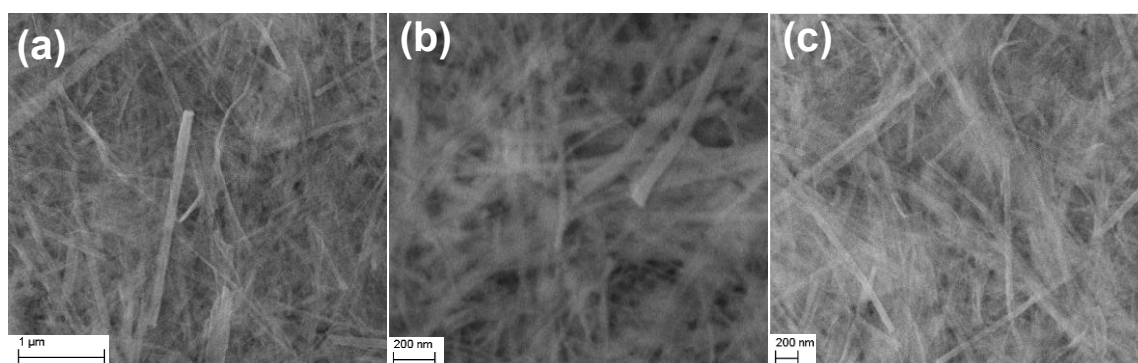
One-Dimensional Ni-MIL-77 Metal-Organic Framework as An Efficient Electrode Nanomaterial for Asymmetric Supercapacitor

Chapter 9

Appendix B

Figure S9.1. (a, b, c) FESEM images of 1D-Ni-MIL-77.
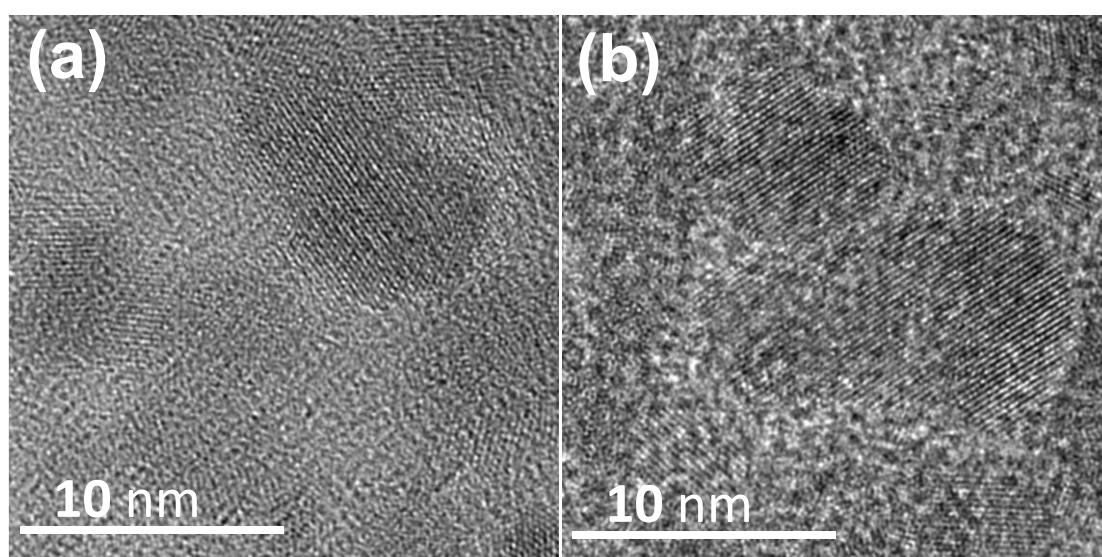
Figure S9.2. (a, b) HRTEM images of 1D-Ni-MIL-77.

One-Dimensional Ni-MIL-77 Metal-Organic Framework as An Efficient Electrode Nanomaterial for Asymmetric Supercapacitor

Chapter 9
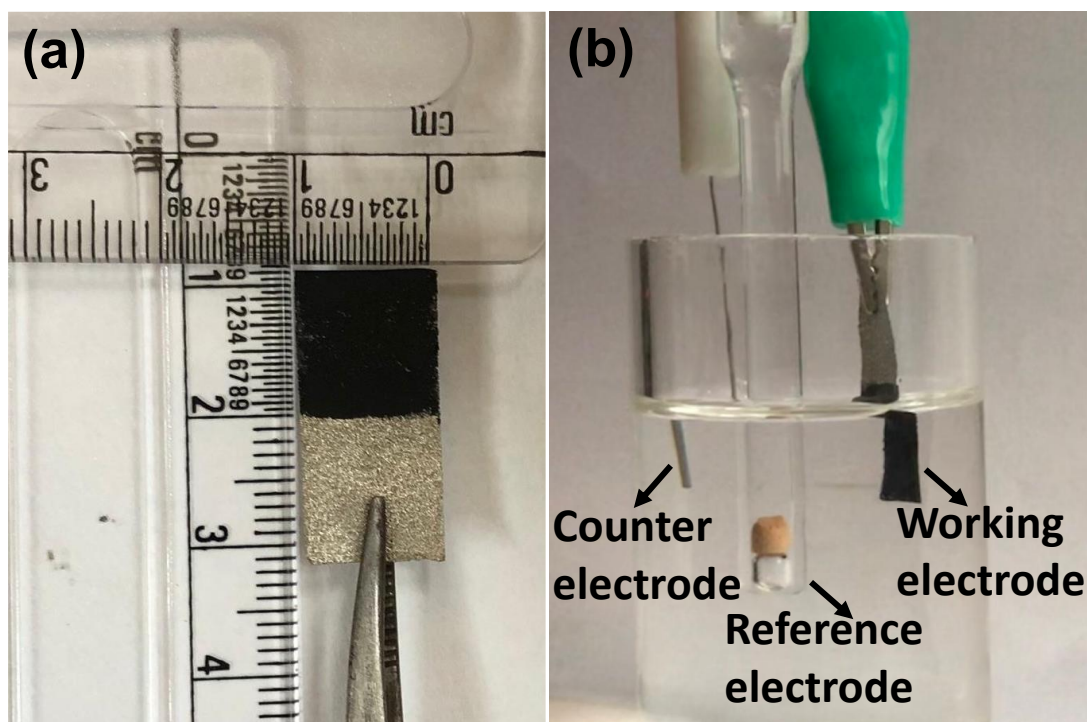
Figure S9.3. (a, b) Optical image for the electrical connectivity of 1D-Ni-MIL-77.
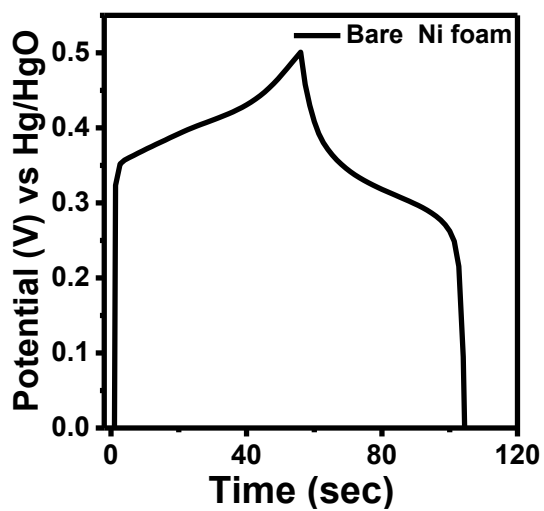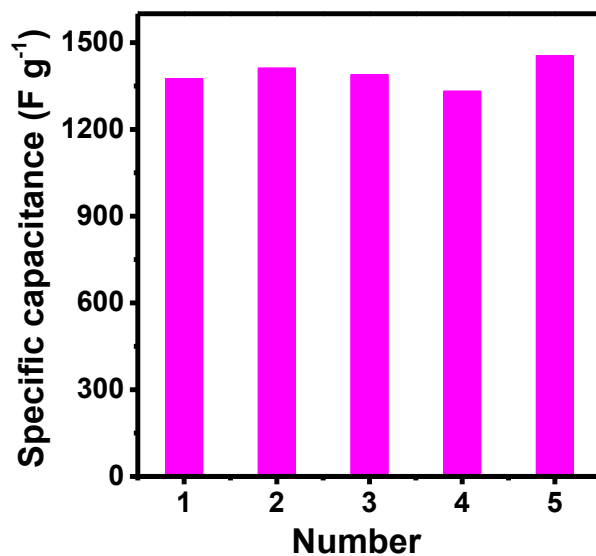

Figure S9.4. GCD curve of bare Ni foam.

One-Dimensional Ni-MIL-77 Metal-Organic Framework as An Efficient Electrode Nanomaterial for Asymmetric Supercapacitor

Chapter 9

Figure S9.5. Reproducibility of 5 different electrodes of 1D-Ni-MIL-77.
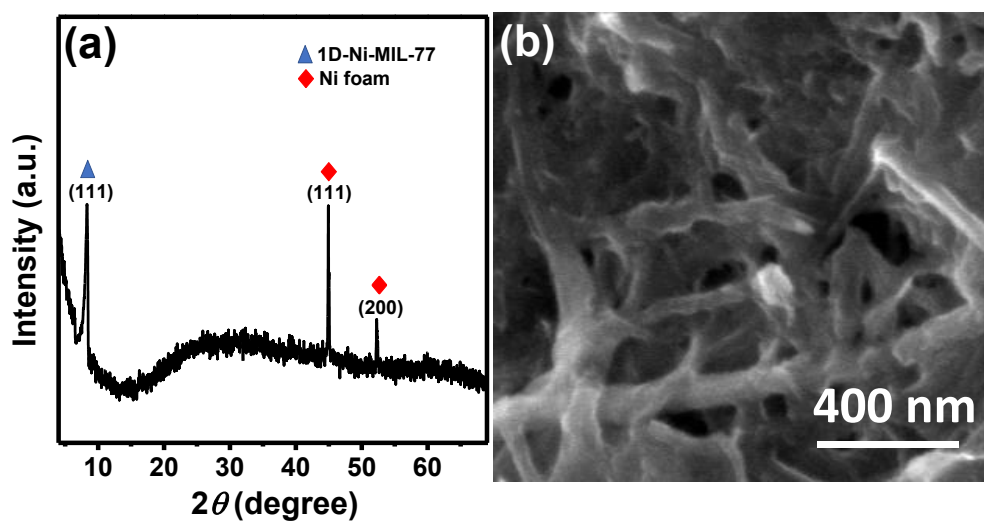
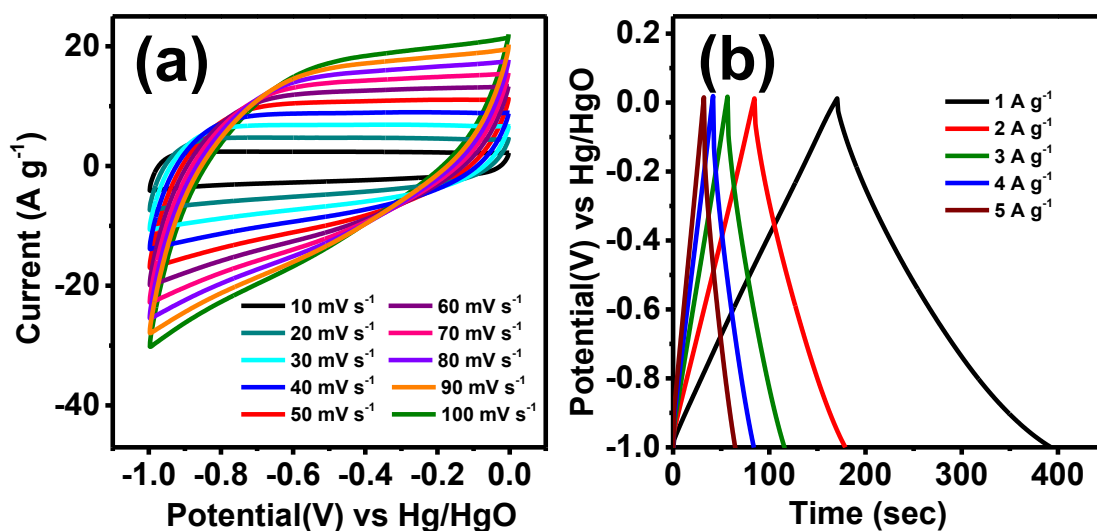**Figure S9.6.** Post stability (a) p-XRD and (b) SEM image of 1D-Ni-MIL-77.

One-Dimensional Ni-MIL-77 Metal-Organic Framework as An Efficient Electrode Nanomaterial for Asymmetric Supercapacitor

Chapter 9

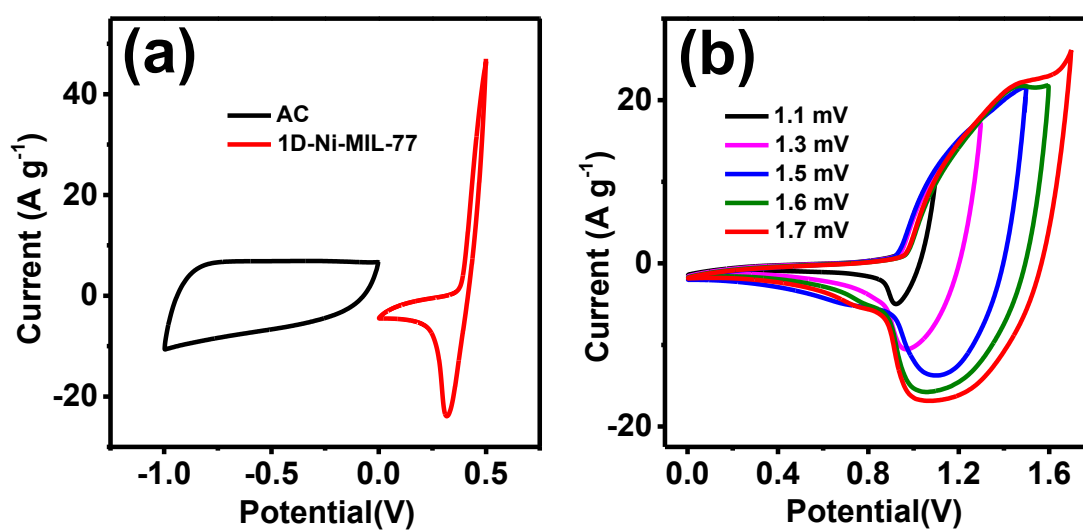**Figure S9.7.** (a) CV curve, (b) GCD curve of AC.

Figure S9.8. (a) CV curve of AC and 1D-Ni-MIL-77 at 30 mV/s; (b) CV curve of the

1D-Ni-MIL-77//AC ASC at 30 mV/s with different potential windows.